Identification of Cancer-specific Therapeutic Targets and Tumor Suppressor Genes in Glioblastoma Multiforme by Functional Genetics

Chad M. Toledo

A dissertation

Submitted in partial fulfillment of the

Requirements for the degree of

Doctor of Philosophy

University of Washington

2015

Reading Committee:

Patrick Paddison, Chair

Susan Biggins

Robert Bradley

Program Authorized of Offer Degree:

Molecular and Cellular Biology

University of Washington

Abstract

Identification of Cancer-specific Therapeutic Targets and Tumor Suppressor genes in Glioblastoma Multiforme by functional genetics

Chad M. Toledo

Chair of the Supervisory Committee:
Affiliated Associate Professor Patrick Paddison
Department of Genome Sciences

Glioblastoma Multiforme (GBM) is the most common and aggressive form of brain cancer. ~90% of adult GBM patients receiving standard of care therapies die within 2 years of diagnosis due to ineffective therapies. To identify new therapeutic targets for GBM, we performed lethal genome-wide short-hairpin RNA (shRNA) and RNA-guided clustered regularly interspaced short palindromic repeats-Cas9 (CRISPR-Cas9) knockout screens in patient-derived GBM stem-like cells (GSCs) and also non-transformed human neural stem cells (NSCs), non-neoplastic tissue of origin controls. Previous experiments with RNA interference (RNAi) identified multiple molecular vulnerabilities specific to GSCs in processes that include

kinetochore regulation and 3' pre-messenger RNA splice site recognition. It is likely that additional genes contributing to these or other biological processes could yield similar or superior cancer-lethal effects.

From an unbiased RNAi viability screen to putative transcription factors in GSCs and NSCs, we identified a new kinetochore protein, *BuGZ*/*ZNF207,* that is differentially required for expansion in the GSCs, but not in NSCs. Inhibition of *BuGZ* results in loss of both BUB3 and BUB1 from kinetochores, reduction of BUB1-dependent phosphorylation of centromeric histone H2A, attenuation of kinetochore-based Aurora B kinase activity, and chromosome congression defects in cancer cells. From genome-wide CRISPR-Cas9 knockout screens, we identified multiple GSC-sensitive genes, including the WEE1-like kinase protein *PKMYT1*, which is essential to most GBM isolates, but not NSCs. Molecular and mechanistic studies revealed that PKMYT1 acts redundantly with WEE1 to inhibitory phosphorylate CDK1-Y15 and to promote timely completion of mitosis in NSCs, but that this redundancy is lost in most GBM isolates and in NSCs harboring activated alleles of *EGFR* and *AKT1*. *PKMYT1* depletion in GSCs and genetically altered NSCs requiring *PKMYT1* lead to cytokinesis failure and cell death during mitosis. In addition, CRISPR-Cas9 knockout screens revealed multiple genes required for *in vitro* expansion of NSCs, including: *ARID1A, ARID1B, CREBBP, EP300, NF2, PDCD10, PTPN14, TAOK1, TGFBR2,* and *TP53*. Knockout of these genes caused shortened cell cycle transit times and drastic growth advantages in NSCs, and in the case of *CREBBP* knockout, caused precocious entry into S-phase and deregulation of cell cycle gene expression. Together, these functional genetic studies identify novel cancer therapeutic targets and growth suppressor genes in human GBM isolates and NSCs that will direct the development of therapeutics to these cancer-specific cellular targets and complexes for cancer patients.

Table of Contents

List of figures

List of tables

Abbreviations and Acronyms

ABK	Aurora B Kinase
AKT	v-akt murine thymoma viral oncogene homolog 1; Alias: AKT1
AKT1	v-akt murine thymoma viral oncogene homolog 1; Alias: AKT
APC/C	Anaphase promoting complex/cyclosome
ARID1A	AT rich interactive domain 1A (SWI-like)
ARID1B	AT rich interactive domain 1B (SWI-like)
ATP	Adenosine triphosphate
B56A	PPP2R5A: protein phosphatase 2, regulatory subunit B', alpha
B-RAF	B-Raf proto-oncogene, serine/threonine kinase
BrdU	Bromodeoxyuridine
BUB1	Budding uninhibited by benzimidazole 1 mitotic checkpoint serine/threonine kinase
BUB3	Budding uninhibited by benzimidazole 3 mitotic checkpoint protein
BUBR1	Budding uninhibited by benzimidazole 1 mitotic checkpoint serine/threonine kinase
BuGZ	Bub3 interacting GLEBS and Zinc finger domain containing protein; Alias: ZNF207
C2H2	$Cysteine_2$ $Histidine_2$
CAB39	Calcium binding protein 39; Alias: MO25
CAK	Cyclin-dependent kinase-activating kinase
Cas	CRISPR associated gene
Cas9	CRISPR associated gene 9
c-MYC	v-myc avian myelocytomatosis viral oncogene homolog
CCNB1	Cyclin B1; Alias: CCNB (cyclin B)
CCND1	Cyclin D1
CDC20	Cell division cycle 20
CDC25	Cell division cycle 25
CDC25A	Cell division cycle 25A
CDC25B	Cell division cycle 25B
CDC25C	Cell division cycle 25C
CDH1	Cell division cycle 20 related 1; Alias: FZR1 (homo sapiens)
CDK	Cyclin-dependent kinase
CDK1	Cyclin-dependent kinase 1
CDK2	Cyclin-dependent kinase 2
CDK4	Cyclin-dependent kinase 4
CDKN1A	Cyclin-dependent kinase inhibitor 1A; Alias: p21
CDKN2A	Cyclin-dependent kinase inhibitor 2A; Alias: p16, $p16^{INK4A}$
CDKN2B	Cyclin-dependent kinase inhibitor 2B
CENP-A	Centromere protein A
CENP-C	Centromere protein C

CENP-E	Centromere protein E
CHI3L1	Chitinase 3-like 1
ClaNC	Classification to nearest centroids
CLSPN	Claspin
CMV	Cytomegalovirus
CNV	Copy number variation
COP9	Constitutive photomorphogenesis 9
Cre	Cre recombinase
CREBBP	CREB binding protein; Alias: CBP
CRISPR	Clustered regularly interspaced short palindromic repeats
crRNA	CRISPR RNA array
DLL3	Delta-like 3
DMEM	Dulbecco/Vogt modified Eagle's minimal essential medium
DNA	Deoxyribonucleic acid
dsDNA	Double-stranded deoxyribonucleic acid
E2F1	E2F transcription factor 1
EGFR	Epidermal growth factor receptor
EP300	E1A binding protein p300
ERBB	Erythroblastic leukemia viral oncogene
ERK	Mitogen-activated protein kinase 1; Alias: MAPK1, ERK2
ERK1/2	Mitogen-activated protein kinase 3; Alias: MAPK3 / Mitogen-activated protein kinase 1; Alias: MAPK1
FANCI/D2	Fanconi anemia, complementation group I; Alias: KIAA1794 / Fanconi anemia, complementation group D2; Alias: FAD2, FANCD
FBS	Fetal bovine serum
FDA	Food and drug administration
FDR	False discovery rate
FPKM	Fragments per kilobase of exon per million fragments mapped
FRET	Fluorescence resonance energy transfer
G1	Gap phase 1
GAF	Global allele frequency
GATK	Genome Analysis Toolkit
GBM	Glioblastoma multiforme
GeCKO	Genome-scale CRISPR knock out
GFAP	Glial fibrillary acidic
GFP	Green Fluorescent Protein
GLEBS	Gle2-binding-sequence
GSC	Glioma stem-like cell
GSEA	Gene set enrichment analysis
H2A	Histone 2A
HDAC2	Histone deacetylase 2
HEATR1	HEAT repeat containing 1; Alias: UTP10

HEC1	NDC80 kinetochore complex component; Alias: NDC80
HIV	Human immunodeficiency virus
HRAS	Harvey rat sarcoma viral oncogene homolog
hTERT	Human telomerase reverse transcriptase
HTSeq	High-throughput sequencing
IDH1	Isocitrate dehydrogenase 1 (NADP+)
IgG	Immunoglobulin G
IKD	Inter-kinetochore distances
INDEL	Insertion/deletion
KIF11	Kinesin family member 11; Alias: EG5
KMN	Composed of KNL-1, the MIS12 complex, and the NDC80 complex
KNL-1	Kinetochore null protein 1; Alias: CASC5 (homo sapiens), Blinkin, AF15q14, Spc105
KO	Knock out
KT	Kinetochore
LKB1	Serine/threonine kinase 11; Alias: STK11
logFC	Log fold change
MAD1	MAD1 mitotic arrest deficient-like 1; Alias: MAD1L1 (homo sapiens)
MAD2	MAD2 mitotic arrest deficient-like 1; Alias: MAD2L1 (homo sapiens)
MAD2L1	MAD2 mitotic arrest deficient-like 1; Alias: MAD2
MAP	Mitogen-activated protein
MAPK	Mitogen-activated protein kinases
MCC	Mitotic checkpoint complex
MCM2	Minichromosome maintenance complex component 2
MDC1	Mediator of DNA-damage checkpoint 1
MDM2	Mouse double minute 2 homolog (MDM2 proto-oncogene, E3 ubiquitin protein ligase)
MDM4	Mouse double minute 4 homolog (p53 regulator)
MEF	Murine embryonic fibroblasts
MEK	Mitogen-activated protein kinase kinase
MELT	Met-Glu-Leu-Thr motifs (MELT) on the KT scaffold KNL-1
MET	MET proto-oncogene receptor tyrosine kinase
MIS12	Mis-segregation 12 complex
MO25	Calcium binding protein 39; Alias: CAB39
MPS1	Monopolar spindle 1;Alias: TTK (homo sapiens)
mRNA	Messenger RNA
MSigDB	The molecular signatures database
MT	Microtubule
MTT	Mitotic transit time
MYC	v-myc avian myelocytomatosis viral oncogene homolog
Myt1	Protein kinase, member associated tyrosine/threonine 1; Alias: PKMYT1
NANOG	Nanog homebox transcription factor

NDC80	Nuclear division cycle 80
NEFL	Neurofilament, light polypeptide
NES	Nestin
NESTIN	Alias: NES
NHEJ	Nonhomologous end joining
NF-κB	Nuclear factor of kappa light polypeptide gene enhancer in B-cells
NF1	Neurofibromin 1
NF2	Neurofibromin 2 (merlin)
NKX2-2	NK2 homeobox 2
NSC	Neural stem cell
NUP98	Nucleoporin 98kDa
OCT4	POU class 5 homeobox 1; Alias: POU5F1
OLIG2	Oligodendrocyte lineage transcription factor 2
ORF	Open reading frame
$p16^{INK4A}$	Cyclin-dependent kinase inhibitor 2A; Alias: CDKN2A, ARF, INK4A,
p21	Cyclin-dependent kinase inhibitor 1A; Alias: CDKN1A
PAF1	Paf1 RNA polymerase II associated factor complex component (PAF1 homolog)
PAM	Protospacer adjacent motif
PCR	Polymerase chain reaction
PDCD10	Programmed cell death 10
PDGFRA	Platelet-derived growth factor rector, alpha polypeptide
PHF5A	PHD finger protein 5A
PI3K	Phosphatidylinositol-3-OH kinase
PIK3CA	Phosphatidylinositol-4,5-biphosphate 3-kinase, catalytic subunit alpha
PKM2	Pyruvate kinase M2
PKMYT1	Protein kinase, member associated tyrosine/threonine 1; Alias: MYT1
PLK1	Polo-like kinase 1
PP1	Protein phosphatase 1
PP2A	Protein phosphatase 2A
PTEN	Phosphatase and tensin homolog
PTPN14	Protein tyrosine phosphatase, non-receptor type 14
qRT-PCR	Real-Time quantitative reverse transcription polymerase chain reaction
RAE1	Ribonucleic acid export 1
RAS	Rat sarcoma viral oncogene homolog
RB	Retinoblastoma 1: Alias: RB1
RB1	Retinoblastoma 1: Alias: RB
rDNA	Ribosomal DNA
RFP	Red fluorescent protein
RNA	Ribonucleic acid
RNAi	RNA interference
RNase III	Ribonuclease III

RTK	Receptor tyrosine kinase
S-phase	DNA synthesis phase
SAC	Spindle assembly checkpoint
shRNA	Short-hairpin RNA
sgRNA	Single guide RNA
SIK3	Salt-inducible kinase 3
SLC12A5	Solute carrier family 12 (potassium/chloride transporter), member 5
SOX2	SRY (sex determining region Y)-box2
SREBF2	Sterol regulatory element binding transcription factor 2
SREBP	Sterol regulatory element binding transcription factor 1; Alias: SREBP1
SSEA1	Stage-specific embryonic antigen 1; Alias: CD15, LeX
STRADA	STE20-related kinase adaptor alpha
SV40	*Simian virus* 40
SYT1	Synaptotagmin I
T14	Threonine residue 14 of CDK1
T161	Threonine residue 161 of CDK1
TAOK1	TAO kinase 1
TCF4	Transcription factor 4
TCGA	The Cancer Genome Atlas
TERT	Telomerase reverse transcriptase
Tet	Tetracycline-inducible
TFAP2C	Transcription factor AP-2 gamma (activating enhancer binding protein 2 gamma)
TGFBR2	Transforming growth factor, beta receptor II
TMM	Trimmed mean of M-values
TP53	Tumor protein p53
tracrRNA	Trans-activating CRISPR RNA
TTK	TTK protein kinase; Alias: MPS1 (Monopolar spindle 1)
TUJ1	Neuronal class III beta-tubulin; Alias: TUBB3
WD40	Repeats have a region of variable length followed by a core of more or less constant length bracketed by two characteristic pattern elements, Gly-His and Trp-Asp (WD)[1]; Alias: beta-transducin repeat
WEE1	WEE1 kinase
Y15	Tyrosine residue 15 of CDK1
ZF	Zinc finger
ZFP	Zinc finger protein
ZFP207	Zinc finger protein 207(*Mus musculus*); Alias ZNF207 (homo sapiens), BuGZ (homo sapiens)
ZNF207	Zinc finger protein 207; Alias: BuGZ

Acknowledgements

My thesis work wouldn't have been possible without the great support of so many good people in my life. I am truly blessed and extremely grateful to everyone who has helped me along the way.

I first want to thank my lab mates in the Paddison lab. I am appreciative of Xiaoji Chen, who helped me learn the ways of the Paddison lab and was always available to help with experiments. I am appreciative of my former bench mate, Yu Ding, for his patience, guidance on difficult problems, and teachings. Thanks to Phil Corrin who was always there to assist with my experiments, listen to me ramble about my crazy ideas, and support me in everything I do. I am extremely appreciative of my former lab mate Chris Hubert, who always gave me his time, patience, and support. Chris went above and beyond to guide me through my first few years of graduate school, and taught me many valuable lab techniques, how to critically think about science, how to be a good mentor, and always found ways to challenge my scientific ideas. A special thanks goes to Dan Kuppers for his continual guidance, advice, and of course our daily sports talk. A huge thanks goes to Pia Hoellerbauer for her assistance with experiments, humor, grace, and encouragement. Lastly, I like to thank Pam Lindberg for all of her help with paper work, budgets, ordering, etc., and for our nice weekly conversations.

My biggest thanks goes to my advisor, Patrick Paddison, for taking me on as his graduate student and joining me in the roller coaster ride during graduate school. Patrick provided me with tremendous support and encouragement, and placed situations into perspective, which I needed to hear to counter my personal strive for perfection. He always challenges me to expand my scope of scientific thinking, and to critically think through all of my scientific ideas. I'm grateful that he provided me with the opportunity to pursue almost all of my ideas in graduate school, and entrusted me with many important projects for the lab. I also truly enjoyed our stimulating scientific conversations, and appreciate all of his time he provided me. I will always be thankful to Patrick for molding me into the scientist I am today.

I also like to thank everyone in the Olson lab. They have always provided me with support, advice, and encouragement throughout my graduate studies. A thanks goes to Sally Ditzler for her patience and guidance in introducing and teaching me how to perform brain surgeries in mice. A special thanks goes to Emily Girard for all of her help, time, and advice with my mouse experiments. A special thanks goes to Jim Olson for all of his time, support, and guidance throughout graduate studies. He always made time for me whenever I needed to talk to him regarding science or personal items. He also always encourages me to think in a broader perspective, and how my research impact cancer patients, which is why I decided to conduct cancer research. Jim has really been a second mentor to me, and I will always be grateful for everything he has done.

I want to thank my thesis advisory committee members: Sue Biggins, Robert Bradley, Jon Cooper, and Robert Hevner, for their time, useful advice, and encouragement. A special thanks goes to Sue Biggins for helping us establish a dialogue with Yixian Zheng, which allowed

us to co-submit our BuGZ articles. I particularly want to thank Sue Biggins and Robert Bradley for taking the time to read and comment on my thesis.

I like to thank all of my friends, especially my close friends Nic Branshaw, Mike Zhang, and Akash Kumar. These gentlemen, who are like brothers to me, were always there to provide support, encouragement, and discuss scientific or personal items. They always lifted my sprits, and made sure I maintained a balance in my life. I'm extremely blessed that we were able to go through our graduate and life journeys together, and I can't imagine life without them.

I want to thank my family who has supported me throughout my graduate studies. There is not enough space to properly thank them. I like to thank my father for teaching me all of life's principles, and most importantly, teaching me to give my full effort in everything I do. I also like to thank my mother for all of her sacrifices in life, and for putting me first before herself ever since I can remember. I pursued the sciences because of my mother, as she always encouraged me that I could succeed in anything that I do if I put all of my effort into it. I'm truly thankful and blessed for my wonderful parents.

Saving the best for last, I like to thank my wife, Christina Toledo. I can't begin to explain all of the things she has helped me with throughout my graduate studies. I truly cherished all of the times she would come to lab in the late evenings and the weekends to assist with my experiments or to just make sure I didn't go insane from being isolated in lab. She has always provided me with the encouragement and love I needed, and always told me to keep moving forward. She endured listening to all of my practice talks, and listening to me ramble about science. She truly takes care of me each and everyday, and I have made it through my graduate studies because of her.

Chapter 1-Introduction

I. Glioblastoma multiforme characterization

Glioma stem cells

Glioblastoma multiforme (GBM), grade IV astrocytoma, is the most malignant variant of diffuse glioma[2]. The average 5-year survival rate for this notorious drug and radiation resistant cancer is less than 5%[3-5]. Unfortunately, the current standard of care therapy for GBM patients results in a median survival of 12-15 months upon diagnosis[3,6]. The current standard of care for GBM, which is rather ineffective, is surgery followed by radiation and adjuvant chemotherapy using temozolomide[7]. The hallmarks of GBM are its uncontrollable cellular proliferation, aggressive growth, diffuse infiltration, robust angiogenesis, resistance to apoptosis, genomic instability, and recurrence, which is typically 1-2 cm a way from the original tumor border[8,9]. GBM is composed of a heterogeneous cell population derived from glioma stem-like cells (GSCs)[4,10-12].

GSCs, referred here as tumor-initiating and tumor-propagating cells, are consistent with a stem cell origin, and retain the multipotent, self-renewing potential, and molecular signatures found in the patient's brain tumor[10,12,13]. GSCs have also shown resistance to temozolomide, as a small population of GSCs can exist in a quiescent state and re-propagate the tumor following chemotherapy[14]. Currently, there is strong evidence to support the notion that GSCs are derived from neural stem cells (NSCs), which are mostly quiescent in the adult[14,15]. NSCs are restricted to the subgranular zone in the dentate gyrus of the hippocampus and the subventricular zone of the lateral ventricles in an adult[8,16,17]. However, GSCs may also arise from neural progenitor cells or differentiated cells such as astrocytes[5,17]. Nonetheless, it is a challenge to target GSCs

with therapeutics since they are protected by the blood-brain barrier. The blood-brain barrier is a multicellular vascular structure composed of astrocytes, endothelial cells, pericytes, and extracellular matrix that provide both structural and functional support[18]. The blood-brain barrier regulates the influx and efflux transport across the barrier and maintains brain homeostasis; and thus, it is difficult to penetrate the barrier with potential GBM therapeutics[18,19].

GSCs and NSCs can be cultured *in vitro* on laminin coated plates and neural basal media containing basic fibroblast growth factor and epidermal growth factor[10,12,20]. NSCs can only be passage for ~40 passages before they experience replicative senescence, while GSCs can be passage for over 70 passages[10]. More importantly, GSCs retain most of the patient's molecular signatures after 70 passages, making GSCs an ideal model for functional genetic and chemical screens in order to identify new therapeutic targets[10,12]. In contrast, GSCs maintained under serum conditions begin to diverge from the patient's characteristics after passage 10 [10]. Interestingly, numerous stem cell associated genes are found to be similarly expressed and regulated in both GSCs and NSCs, such as *SOX2*, *NESTIN*, and *GFAP* [4,12,21]. However, in contrast to NSCs, GSCs also have an activated gene expression signature that is representative of the mesodermal and endodermal lineages[21]. In addition, GSCs and embryonic stem cells share similarities at the molecular levels, as they both express OCT4 and NANOG[21].

Glioblastoma multiforme alterations

Three important genetic events commonly occur in GBM: 1) deregulation of growth factor signaling via amplification and mutational activation of receptor tyrosine kinase (RTK) genes; 2) activation of phosphatidylinositol-3-OH kinase (PI3K) pathway; and 3) inactivation of the TP53 and retinoblastoma (RB) tumor suppressor pathways[22-24]. Altering these pathways fuels cancer cells proliferation and enhances their survival while allowing them to escape cell-cycle

checkpoints, senescence, and apoptosis[4]. In 91 GBM samples analyzed for somatic alterations, 88%, 87%, and 78% of the samples had signaling altered in the RTK/RAS/PI3K, TP53, and RB pathways, respectively[25], which is similar to a more recent study analyzing 251 GBM samples[23]. One of the most common alterations in GBM is the homozygous deletion of *CDKN2A/B,* which disrupts RB function. *CDKN2A/B* is altered in 55% and 53%, respectively, of GBM samples[25]. Interestingly, *RAS* is only altered in 1-2% of the samples, but the negative inhibitor of RAS, *NF1*, is genetically altered in 10-18% of the samples[23,25]. In addition, *EGFR*, a member of the erbB family of tyrosine kinase receptors that can activate downstream signaling RAS and PI3K pathways upon receptor dimerization[26], is altered in 45-57% of GBM samples[23,25]. Similarly, *PI3K* is genetically altered in 15-25% of the samples, while its negative regulator, *PTEN*, is altered in 36-41% of the samples[23,25]. 74% of the samples harbored aberrations in all three pathways, which suggest deregulation of these pathways is a core requirement in GBM pathogenesis[25].

Glioblastoma multiforme subtypes

GBM is typically divided into four molecular signatures (also known as subtypes): Classical, Mesenchymal, Neural, and Proneural[27,28]. These subtypes are associated with prognostic values, activation of signaling pathways, and gene expression changes that commonly accompany recurrence[27,28]. The Classical subtype is associated with amplification of chromosome 7 paired with loss of chromosome 10, which is the chromosomal location of *EGFR* and the tumor suppressor *PTEN* respectively[28]. Homozygous deletion of *CDKN2A*, which encodes both *p16INK4A* and *p14ARF* (components of the RB pathway), and expression of the NSC and neural precursor marker, NESTIN, are also associated with this subtype[28]. The Mesenchymal subtype is associated with hemizygous deletion of *NF1*, a tumor suppressor that

negatively regulates the RAS signaling pathway[29], and many Mesenchymal samples have lower expression of *NF1*[28]. Tumors in this subtype express mesenchymal markers *CHI3L1* and *MET*, and have elevated expression of genes involved in the tumor necrosis factor superfamily pathway and NF-κB pathway[28]. The Proneural subtype contains alterations in *PDGFRA*, specifically concomitant focal amplification in conjunction with high levels of *PDGFRA* gene expression, and point mutations in *IDH1*[28]. This subtype is associated with high expression of oligodendrocytic developmental genes, such as *PDFGRA, NKX2-2, and OLIG2*, which has been shown to down-regulate the tumor suppressor *p21* (*CDKN1A*)[28]. The Proneural subtype is also associated with proneural developmental genes such as the *SOX* genes, *DLL3*, and *TCF4*[28]. The Neural subtype is classified based upon expression of neuronal markers, such as *NEFL, SYT1,* and *SLC12A5*[28]. Mesenchymal subtypes usually have a poorer survival outcome compared to proneural subtypes, 0.6 year versus 1 year respectively[27]. However, mesenchymal subtypes are more sensitive to combinational therapy consisting of radiation and chemotherapy[27].

Recently, it has been shown by single cell transcriptome analysis of GBM patient isolates that GBM tumors can contain a mixture of all GBM subtype classifiers[30]. However, one subtype will act predominantly within the tumor[30]. More importantly, these studies demonstrate that each GBM patient isolate is comprised of an intratumoral heterogeneous cell population, which helps explain the challenges of treating this deadly disease[30]. For example, therapeutically targeting one subtype of GBM may give rise to another subtype within the tumor that is resistant to the treatment. Interestingly, tumors that contain high tumor heterogeneity were associated with a poorer survival outcome when compared to tumors containing low tumor heterogeneity and one subtype (Proneural) only[30].

II. Glioblastoma multiforme models

Mouse models

Genetically engineered mouse models play a key role in the study of cancer. Genetically engineered mouse models allow for comparative onco-genomic studies that can identify additional altered genes during the course of tumorigenesis[31]. They also provide a tool to validate the functionality of specific genes in tumorigenesis[31]. Genetic models of glioma have permitted molecular studies on tumor initiation, progression, metastasis, cell-of-origin, microenvironment, therapeutic responses, and others, since they are able to mirror and resemble human GBM[4,17,31]. In addition, GBM mouse models are vital for preclinical trials because they help determine effective therapeutics before they are given to patients in clinical trials. GBM mouse models are created by a variety of methods, including: germline mutations, tet-regulatable or cre-inducible alleles of genes, and retroviral and adenoviral vectors[31]. Many GBM mouse models disrupt the RTK/PI3K pathway, TP53 pathway, and/or RB pathway[4,5,17,31,32].

GBM mouse models have shown that the induction of high-grade astrocytomas require the deletion of *TP53* in conjunction with the deletion of *NF1, PTEN*, *RB*, or the deletion of both *PTEN* and *RB* [17]. Interestingly, *PTEN/TP53* conditional knockout mice contained tumors that showed amplification of RB regulators, demonstrating that deregulation of RB signaling is a critical event in gliomagenesis[17]. Tumors did not arise when the tumor suppressors *NF1, PTEN,* and *RB* were altered alone[5,17].

Multiple mouse models have also provided evidence that NSCs can be the cell of origin for GSCs[5,17,32,33]. A mouse model constructed by temporally deleting *TP53*, *NF1*, and *PTEN* tumor suppressors using both genetic and stereotactic injection methods demonstrated that embryonic, early postnatal, and adult neural stem/progenitor cells can give rise to malignant

glioma formation with 100% penetrance[5]. However, more mature cells types could not produce tumors[5]. In addition, these tumors rose from the subventricular zone. In contrast, a mouse model disrupting the PI3K-TP53-RB pathways in a *GFAP*-tamoxifen-dependent *Cre* recombinase background, which allowed for the induction of widespread tumor suppressor deletion in astrocytes and less than 1% of progenitor cells in the adult brain, demonstrated that GBMs can arise from mature astrocytes, locally resident progenitor cells, or progenitor cells that escaped from proliferative niches[17]. Intriguingly, there was a higher frequency of tumors that were associated with proliferative niches, which is consistent with the notion that NSCs/progenitor cells have a greater tendency for malignant transformation[17]. In addition, these tumors are believed to arise from both the subventricular zone and subgranular zones of the brain, which is also where adult NSCs reside.[5,8,16,17,32].

Drosophila models

A glioma model in *Drosophila* has also been developed in order to facilitate genetic analysis of gliomagenesis[34]. *Drosophila* is a great model organism since it offers multiple tools for precise cell-type specific genetic modifications, cell lineage tracing, and dissection of multigene interactions[34,35]. *Drosophila* also has a rapid life cycle, which allows for relatively short *in vivo* experiments[35]. Interestingly, 70% of known human disease genes have functional *Drosophila* orthologs[34]. In addition, the main classes of central nervous system glia in *Drosophila* - cortex, neuropil, surface, and peripheral glia- exhibit many morphological and functional similarities to the mammalians' glia - astrocytes, oligodendrocytes, microglia, and Schwann cells, respectively[36]. Moreover, though *Drosophila* and mammalian blood-brain barriers are morphologically distinct, they are thought to function in similar ways[36].

Glial-specific co-activation of *Drosophila* orthologs *EGFR* and *PIK3CA* give rise to glial neoplasia[34]. These *Drosophila* glia tumor-like growths contain small, highly proliferative glia and polyploidy glia[34]. Similar results are seen when *EGFR* is co-expressed with the *Drosophila* ortholog *AKT* or $PTEN^{dsRNA}$, which knocks down *PTEN* expression[34]. However, glia overgrowth from co-activation of *Drosophila* orthologs *EGFR* and *PIK3CA* is suppressed when *Drosophila* ortholog *PTEN* is overexpressed[34]. Contrary to glioma mouse models[37], the expression of *Drosophila* ortholog *EGFR* results in a slight induction of glial growth[34]. Nevertheless, expression of *Drosophila* orthologs *RB, PIK3CA, AKT, or* $PTEN^{dsRNA}$ alone does not result in glial growth[34]. Interestingly, overexpression of active *EGFR* and constitutively active *RAS* in a *PTEN* null allele results in highly invasive tumor-like growths that penetrate deep into the brain, a phenotype that is reminiscent of human GBM[34]. This is consistent with GBM genetically engineered mouse models that give rise to tumors following alterations in the following combination of genes[4]: $HRAS^{G12V}$/$EGFR^{delvII}$ [38], $HRAS^{G12V}$/*PTEN* loss[38], $KRAS^{G12D}$/constitutively active *AKT* [39], and $HRAS^{G12V}$/ constitutively active *AKT*[40]. In addition, altering the PI3K-RB pathways in conjunction with expression of activated *EGFR* in *Drosophila* give rise to profound glial neoplasia and a substantial increase in small anaplastic-like glia throughout the central nervous system[34]. Nonetheless, these *Drosophila* studies did not examine the *Drosophila* ortholog *TP53*, which has been shown to regulate apoptosis[41].

In vitro models

GBM models have also been established *in vitro* by transforming NSCs, a non-neoplastic cell of origin for GSCs, into glioma-like stem-like cells[42,43]. Early transformation studies took advantages of a variety of tumor viruses in order to transform a normal cell into a cancer-like cell. For example, the monkey virus SV40 encodes the viral protein large-T antigen targeting

TP53 and RB, which disrupt these respective pathways[44]. It was later shown that ectopic expression of both the telomerase reverse transcriptase (*TERT*) catalytic subunit and oncogenic *RAS* (*H-RAS*^{V12}) in conjunction with the expression of the large-T antigen transforms normal human embryonic kidney cells and human BJ fibroblasts into human tumor cells[45]. Ectopic expression of *TERT* prevents replicative senescence and allows for an unlimited replications for the cells, and expression of oncogenic *RAS* results in a factor-independent cellular proliferation, cell survival, invasion, angiogenesis, and metastasis[46]. One caveat of the expression of the large-T antigen is that it binds to additional proteins besides TP53 and RB, such as the histone acetyltransferases and tumor suppressors CREBBP and EP300[47]. However, disruption of the TP53 and RB pathways in human derived cells are required in order to avoid RAS-induced senescence, a cell-cycle arrest involving TP53 and p16^{INK4A} that is indistinguishable from cellular senescence[48,49]. To circumvent the large-T antigen, TP53 can be impeded by expression of its dominant-negative form, *TP53*^{DD}, and RB can be disrupted by overexpression of both *CCND1* and activation mutants of *CDK4*^{R24C} [46]. Non-transformed human mammary epithelial cells, human myoblasts, and human embryonic kidney cells have been transformed by transduction with *TP53*^{DD} + *CCND1* + *CDK4*^{R24C} + *TERT* in combination with constitutively active *RAS*^{G12V} and a T58A stabilization mutant of *c-MYC* [46].

We recently transformed NSCs into glioma-like stem-like cells using a variety of oncogenic alterations in different combinations[42,43] (unpublished). NSCs require the disruption of both the TP53 and RB pathways in order to bypass RAS-induced senescence[42,43]. Transformed NSCs give rise to brain tumors *in vivo* when they express constitutively active *RAS*^{G12V} or constitutively active *RAS*^{G12V} + oncogenic *c-MYC*^{T58A} in the presence of altered TP53 and RB pathways[43] (unpublished). However, oncogenic *c-MYC*^{T58A} alone, which is not

commonly mutated in GBM[25], in the presence of disrupted TP53 and RB pathways does not give rise to tumors *in vivo* (unpublished). Interestingly, NSCs expressing constitutively active *EGFR* and *AKT*, which are commonly altered signaling pathways in GBM[23,25], in the presence of altered TP53 and RB pathways undergo a dramatic morphology change that resembles the proneural GSC patient isolate, GSC-0827 (Figure 1.1). The successful transformation of NSCs into glioma-like stem-like cells demonstrates that NSCs can be a cell-of-origin for GSCs, as they can give rise to brain tumors after they have been genetically altered with common GBM oncogenic alterations. More importantly, these studies provide an *in vitro* GBM model to study gliomagenesis, as it allows for comparative genomic, transcriptome, and pathway analyses of each commonly altered gene in GBM alone or in combination with other commonly altered genes in GBM. These relative analyses can lead to new candidate GBM therapeutic targets by identifying genes that are differentially required in GSCs, but not NSCs.

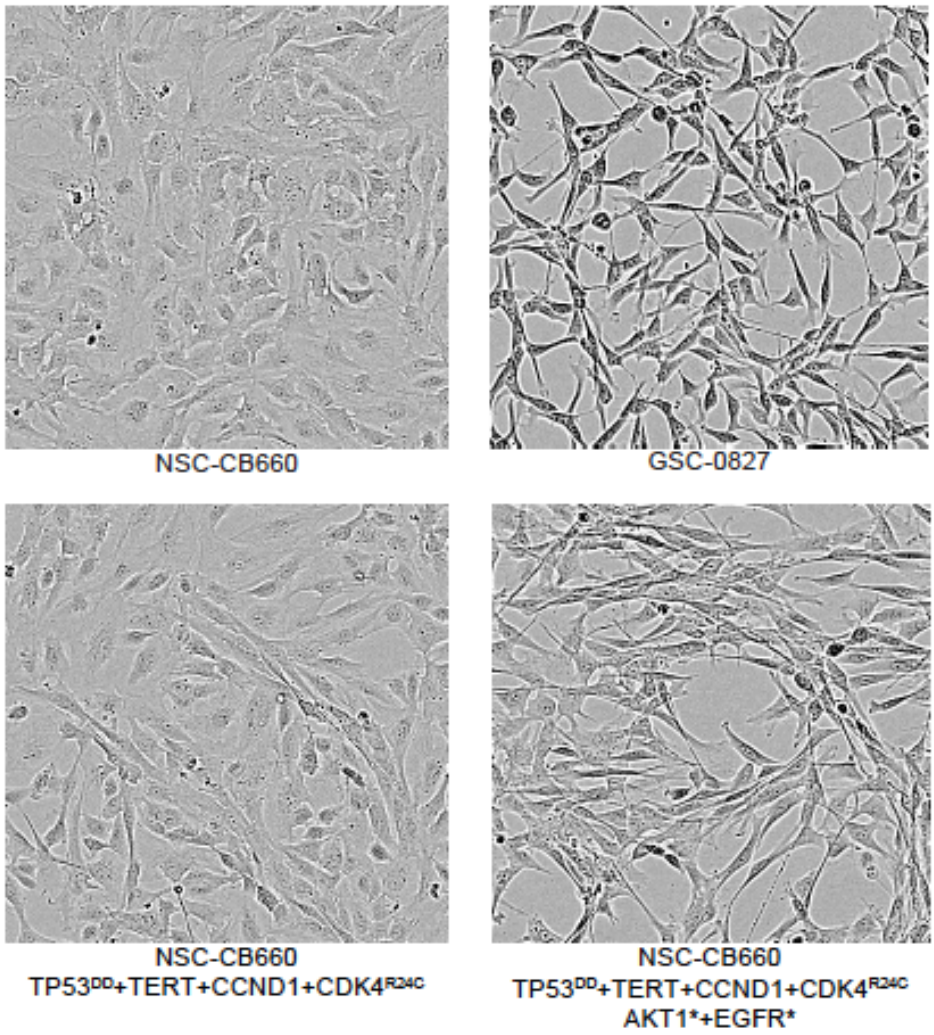

Figure 1.1. Representative images of non-transformed NSC-CB660, genetically modified NSC-CB660, and GSC-0827.

III. Applying functional genetics in glioblastoma multiforme

During the course of tumorigenesis, cells accumulate somatic genetic alterations, such as chromosome translocations, point mutations, and copy number alterations, which provide cells with a growth and/or survival advantage[50]. A subset of these alterations are known as "driver events" that promote malignant transformation by activating oncogenes or inactivating tumor suppressors[50]. The remaining alterations are known as "passenger events," which occurs in

cancer due to genomic instability[50]. Although these oncogenic alterations provide cancer cells with growth and survival advantages, these same oncogenic alterations lead to cancer specific vulnerabilities. Cancer specific vulnerabilities arise due to alterations in surveillance mechanisms and multiple cellular processes that allow cancer cells to escape cell-cycle checkpoints, senescence, and apoptosis. One strategy to target cancer cells is to identify the genes that are required to overcome these functional impairments and cancer-specific stressors[50], but have redundant and non-essential activities in non-transformed cells, a concept originally proposed by Hartwell *et al.* for cancer cells[51].

The discovery of RNA interference (RNAi) technology, which provides a tool to silence gene expression, was a groundbreaking opportunity for cancer biology[52]. Soon after, large-scale libraries of RNAi-inducing short-hairpin RNA (shRNA) expression vectors targeting human and mouse genes were made available, providing functional genetic tools for mammalian cells[53]. For cancer biology, shRNA pool libraries provide a tool to identify genes that are differentially required in cancer cells, but dispensable in non-transformed cells, which could lead to new candidate cancer therapeutic targets. However, many shRNA screens conducted in cancer cells fail to perform a non-neoplastic tissue of origin control, which makes it difficult to determine if the proposed candidate cancer-lethal gene is truly cancer-specific[54,55]. In GBM, screens have been limited to a subset of genes, such as to transcription factors, the kinome, and the phosphatome, and have not been conducted in NSCs or neural progenitor cells[56-59].

GBM is an ideal *in vitro* modeling system to identify novel therapeutic targets by functional genetics due to: 1) the ability to isolate, culture, and genetically manipulate GSCs and non-neoplastic cell-of-origin controls, NSCs; 2) fairly similar doubling time between GSCs and NSCs (28-36 hours vs. 45-55 hours respectively); 3) overlapping expression profiles between

GSCs and NSCs; and 4) similar development potential, such as differentiating into astrocytes, oligodendrocytes, and neuronal cells[12,20,42,43,60]. Genome-wide or focused shRNA high throughput screens provide an unbiased and systematic approach to discover new therapeutic targets. High throughput screens can be conducted in an array or pooled format. However, the array format has limitations since array screens are typically performed using multi-well plates with each well of the plate representing a single shRNA; thus, the scale of the screen is limited to the number of plates that can be processed at a given time. Though the array format provides a direct readout of the desired phenotype, pooled screens utilizing shRNA-expressing lentiviruses can target thousands of genes in parallel. For pooled screens, cells are transduced in a one-to-one ratio of one shRNA-expressing virion to one cell in order to ensure that only one shRNA is incorporated into a cell. In order to decrease biological, experimental, and random noise, and produce reproducible data, each shRNA is represented by 500-1,000 cells during transduction (500-1,000 fold representation). In addition, multiple biological replicates are performed. Following chemical selection for successfully transduced cells containing a shRNA, cells are expanded for 14-21 days. The initial fold representation is maintained during the entire screening process in order to ensure a technically successful screen. At the end time point, genomic DNA is harvested, and the shRNA is PCR amplified from the entire genomic DNA. During this step, it is critical that the PCR amplifications are within the exponential phase ("linear range") in order to reduce PCR noise[61]. Each shRNA present in the population is then typically identified using next generation sequencing[62].

Our lab has conducted multiple functional genetic high throughput screens in both the GSCs and NSCs in order to identify novel GBM candidate therapeutic targets[42,43,60]. Two candidate novel therapeutic targets, *BUBR1*[60] (budding uninhibited by benzimidazole 1 mitotic

checkpoint serine/threonine related kinase) and *PHF5A*[42], were identified as GBM-specific lethal hits following focused shRNA screens to the kinome and putative transcription factors, respectively. Knockdown of these genes causes lethality in GSCs, but not in NSCs[42,60]. We found that *BUBR1* and *PHF5A* are differentially required by GSCs due to their roles in the kinetochore (KT) and RNA splicing, respectively. Thus, the KT and RNA splicing are sources of GBM vulnerability[42,43,60].

IV. Glioblastoma multiforme and the kinetochore

Kinetochore

The KT is a large, complex structure composed of over 100 proteins that assembles on centromeric DNA during mitosis[63]. Mature KTs only exist during mitosis in vertebrates, and have multiple roles during mitotic progression in order to ensure error-free chromosome segregation of the replicated sister chromatids into two daughter cells[63,64]. KTs are composed of an inner and outer plate[64]. The inner KT plate is located at the periphery of centromeric chromatin and comprised of many proteins, including the constitutive centromere-associated network, which is composed of CENP-A, CENP-C, and others[63-65]. The outer KT plate is comprised of many proteins as well, including the "KMN network," which is composed of KNL-1 (CASC5 in homo sapiens), the MIS12 complex, and the NDC80 (also known as HEC1) complex[63,64,66]. The KMN network is the core attachment factor that binds to the dynamic plus-ends of the mitotic spindle microtubules (MTs)[63,66,67]. Together, the inner and outer plates of the KTs link centromeric DNA to spindle MTs, and thus, orchestrate and power chromosome movements by the MT dynamic forces[63,65,66,68].

Following nuclear envelop breakdown, KTs lack spatial organization and arbitrarily bind to MTs[66]. This can lead to monotelic (condition where only one sister KT in a pair of sister KTs are attached to KT-MTs), syntelic (condition where both pair of sister KTs are attached to KT-MTs from the same spindle pole), or merotelic (condition where one sister KT in a pair of sister KTs are attached to KT-MTs from both spindle poles) attachments during prometaphase[64,66]. To prevent such erroneous attachments and to promote the correct stable bi-orientated KT-MT attachments, the essential mitotic kinase Aurora B (ABK) phosphorylates multiple KT proteins early in mitosis, including members of the KMN network, to increase KT-MT turnover[63,64,66]. At unattached or monotelic KTs, ABK concentrates at centromeres and is believed to be activated by the lack of tension between the sister chromatids[64]. As mitosis progresses, ABK activity decreases and phosphatase activity from phosphatases, such as protein phosphatase-1 and -2A[63], increases, resulting in low levels of ABK-dependent KT phosphorylation[66]. The decreased NDC80 complex phosphorylation increases its MT-binding activity, which results in stabilized KT-MT attachments[66].

Defects in the ABK regulatory system can lead to chromosome segregation errors and chromosome instability, which are observed in many cancers[66,69]. Nonetheless, syntelic erroneous attachments can be detected by the cell's surveillance mechanism, the spindle assembly checkpoint (SAC), which prevents chromosome mis-segregation and aneuploidy by ensuring that proper KT-MT attachments have been formed, chromosomes are aligned, and KTs are under proper tension at the metaphase plate before the cell enters anaphase[64,70]. Interestingly, certain cancers and mouse models have shown a partial or complete loss of a SAC response, suggesting that a loss of SAC activity may promote tumorigenesis[66,71-73]. On the contrary, other cancers do not contain loss-of-function mutations in SAC genes, and many late-stage cancers

exhibit high SAC gene expression, suggesting hyperactivity[66,73,74]. Therefore, it is likely that SAC proteins become increasingly required by cancer cells in order to support mitotic defects in KT-MT attachments as low-grade tumors transition to more aggressive malignancies, such as GBM[66,74].

Glioblastoma multiforme and BUBR1

BUBR1 is a critical mitotic checkpoint kinase that is highly expressed in many late stage cancers[60]. *BUB1B* encodes a highly conserved BUB1-like pseudo kinase, BUBR1, and is a component of the mitotic checkpoint complex (MCC), which is a core component of the SAC[64]. BUBR1 has multiple functional domains that have been implicated in mitotic timing and regulating KT-MT attachments[66]. In addition, BUBR1 acts as a pseudo-substrate inhibitor of the anaphase promoting complex/cyclosome (APC/C) during G2 and pre-anaphase mitosis to prevent premature anaphase by directly binding to CDC20[75].

Kinetochore-microtubule (KT-MT) dynamics are fundamentally altered in GSCs to favor KT-MT detachment, which BUBR1 is required to suppress[60]. Oncogenic MAPK signaling by expression of $HRAS^{G12V}$ or MEK^{DD} alters KT regulation, resulting in short inter-kinetochore distances (IKD), the maximum distance achieved between sister KTs when stable end-on MT attachment has occurred during metaphase, and KT-MT instability[60,76]. IKD distances serve as an indirect measure of the pulling forces generated by dynamic MTs bound to KTs, such that stronger attachments lead to longer IKDs and weaker attachments lead to shorter IKDs[66,76]. GBM patient isolates with short inter-KT distances require BUBR1's localization to the KT during prometaphse in order to recruit protein phosphotase 2A (PP2A) to KTs[60,66,76]. PP2A then counteracts ABK phophorylation of outer KT substrates, which allows for stable KT-MT attachments[60,66,76-78]. This suggests that BUBR1-dependent KT recruitment of PP2A is not

necessarily essential in normal KT-MT dynamics, perhaps due to functional redundancy with other KT phosphatases, or alternative PP2A recruitment mechanism(s).[60,66,76]

Specifically, BUBR1's Gle2-binding-sequence (GLEBS) domain activity is essential for KT-MT attachments in GSCs[60], as the GLEBS domain is necessary for BUBR1's localization to the KT during mitosis[60,66,76,79]. In cells harboring short IKDs, knockdown of *BUBR1* or GLEBS domain inhibition results in profound loss of KT-MT attachments and cell death[60]. *BUBR1* depletion in GSCs or RAS-transformed cells leads to chromosome alignment defects independent of its essential role in the SAC[60,76]. In addition, *BUBR1* knockdown in GSCs causes significant reduction in mitotic transit times[60]. Though expression of the altered GLEBS^{E406K} allele restores mitotic timing, the altered GLEBS^{E406K} allele does not rescue viability or KT-MT attachment defects, suggesting that the requirment for BUBR1's GLEBS domain activity is distinct from BUBR1-dependent APC regulation in GSCs[60]. In contrast, recent studies suggest that BUBR1's GLEBS domain and KT localization are not required for KT-MT attachment in normally dividing somatic cells, such as neural stem cells and astrocytes[60,66].

V. Research aims

It is likely that additional genes contributing to GBM vulnerabilites at the KT or during RNA splicing could yield similar or superior cancer-lethal effects compared to *BUBR1* and *PHF5A*. Moreover, employing alternate functional genetic techniques could identify additional vulnerablities in GBM and novel GBM therapeutic targets. Here, we have identified a third lethal functionally unknown zinc finger gene, *ZNF207*, from a putative transcription factor shRNA screen[43]. We found that *ZNF207* is specifically required for GSCs' survival, but not NSCs[43]. In addition, I employed CRISPR-Cas9 technology, a new functional genetic tool that

knocks out a gene in a cell[80], in our *in vitro* GBM modeling system in order to identify candidate GBM-specific therapeutic targets, such as *PKMYT1*, and tumor supressor genes, such as *CREBBP*.

In chapter 2, I tested the hypothesis that *ZNF207* is differentially required in human brain tumors and genetically transformed cells due to its functional role at the KT, a source of GBM vulnerability. Briefly, from coimmunoprecipitation (co-IP) tandem mass spectrometry studies, we found that ZNF207 is a kinetochore protein that binds to and stabilizes the KT protein BUB3. Extensive immunofluorescence and genetic studies demonstrated that ZNF207 contains a GLEBS domain, which is required for its localization to the KT. Knockdown of *ZNF207* in GSCs causes chromosomes to misalign, resulting in the cell death of GSCs. Moreover, suppression of *ZNF207* expression compromises GBM tumor formation *in vivo*, demonstrating that *ZNF207* is a candidate GBM therapeutic target[43].

In chapter 3, I used CRISPR-Cas9 technology to determine genes that are differentially required in GSCs, but not NSCs, upon knockout. We performed genome-wide CRISPR-Cas9 screens to identify multiple essential and GSC-sensitive targets, as well as tumor suppressor genes. I tested the hypothesis that the GSC-sensitive target *PKMYT1* has a functional mitotic role in GSCs. Mechanistic studies revealed that *PKMYT1* depletion in GSCs results in a drastic increase in mitotic transit time, which leads to cytokinesis failure and cell death during mitosis. I also demonstrated that NSCs containing disruptions in the TP53 and RB pathways and harboring activated alleles of *EGFR* and *AKT*, which are commonly altered signaling pathways in GBM, differentially require *PKMYT1*. In addition to lethal genes, knockouts promoting *in vitro* NSCs' expansion were examined, and compared to pediatric and adult glioma/GBM alteration datasets from the Pediatric Cancer Genome Project and The Cancer Genome Atlas, respectively. These

analyses revealed that 42 of the 272 candidate growth-limiting genes are altered in glioma/GBM. From validation studies, I identified multiple growth-limiting genes, and found that inhibition of these growth-limiting genes shortens NSC cell cycle transit times and cause growth advantages. Since NSCs spend the majority of their time in G1 of the cell cycle, I tested the hypothesis that the growth-limiting genes regulate entry into S-phase. Using *CREBBP* as a test case, I found that depletion of *CREBBP* leads to drastic deregulation of cell cycle gene expression and precious entry into S-phase. Taken together, these data establish that employing functional genetics by the use of CRISPR-Cas9 technology can identify new essential genes, candidate cancer therapeutic targets, and tumor-suppressor genes in GBM patient isolates and NSCs.

Chapter 2-An RNAi screen in glioblastoma multiforme identifies a novel kinetochore protein BuGZ.

Note: This work was published in *Developmental Cell* as "BuGZ is Required for Bub3 Stability, Bub1 Kinetochore Function, and Chromosome Alignment."

Chad M. Toledo[1,3]*, Jacob A. Herman[4]*, Jonathan B. Olsen[5], Yu Ding[1], Philip Corrin[1], Emily J. Girard[2], James M. Olson[2], Andrew Emili[5], Jennifer G. DeLuca[4†], and Patrick J. Paddison[1,3†]

[1]Human Biology Division, [2]Clinical Research Division, Fred Hutchinson Cancer Research Center, Seattle, WA 98109, USA; [3]Molecular and Cellular Biology Program, University of Washington, Seattle, WA 98195, USA; [4]Department of Biochemistry and Molecular Biology, Colorado State University, Fort Collins, CO 80523, USA; [5]Donnelly Centre for Cellular and Biomolecular Research, University of Toronto, ON, M5S 3E1, Canada.

*These authors contributed equally to this work.

[†]Correspondence: Patrick Paddison (paddison@fhcrc.org) or Jennifer DeLuca (Jennifer.Deluca@ColoState.edu).

Key words: BuGZ, ZNF207, BUB3, spindle assembly checkpoint, kinetochore, cancer stem cells, Glioblastoma multiforme

Abstract

During mitosis, the spindle assembly checkpoint (SAC) monitors the attachment of kinetochores (KTs) to the plus ends of spindle microtubules (MTs) and prevents anaphase onset until chromosomes are aligned and KTs are under proper tension. Here, we identify a novel kinetochore protein, *BuGZ/ZNF207*, from an RNAi viability screen in human Glioblastoma multiforme (GBM) brain tumor stem cells. BuGZ binds to and stabilizes BUB3 during interphase and mitosis through a highly conserved GLE2p-binding sequence (GLEBS) domain. Inhibition of *BuGZ* results in loss of both BUB3 and its binding partner BUB1 from KTs, reduction of BUB1-dependent phosphorylation of centromeric histone H2A, attenuation of KT-based Aurora kinase B activity, and lethal chromosome congression defects in cancer cells. Phylogenetic analysis indicates that *BuGZ* orthologs are highly conserved among eukaryotes, but are conspicuously absent from budding and fission yeasts. These findings suggest *BuGZ* has evolved to facilitate BUB3 activity and chromosome congression in higher eukaryotes.

Introduction

During mitosis, the spindle assembly checkpoint (SAC) monitors the attachment of kinetochores (KTs) to the plus ends of spindle microtubules (MTs) and prevents anaphase onset until all chromosomes have proper KT-MT attachments, chromosomes are aligned, and KTs are under proper tension[67,70]. The SAC machinery contains multiple KT proteins (i.e., BUB1, BUBR1, BUB3, MAD1, MAD2, and MPS1) that monitor MT attachment and regulate anaphase progression[67,70]. During prometaphase, all SAC proteins concentrate at KTs[64]. The SAC proteins MAD2, BUBR1, and BUB3 comprise the soluble Mitotic Checkpoint Complex (MCC) and prevent the activation of the ubiquitin ligase anaphase promoting complex/cyclosome

(APC/C) by targeting APC/C's co-factor CDC20[64]. Following proper chromosome alignment and tension at the KT, CDC20 inhibition is released to activate the APC/C, which begins the cascade of events that lead to anaphase[64]. Specifically, the activation of APC/C leads to the polyubiquitylation of anaphase substrates such as cyclin B (also known as CCNB1), which activates CDK1's kinase activity upon binding, and securin, the stoichiometric inhibitor of the protease called separase[64]. Polyubiquitylation of cyclin B, securin, and others lead to their proteolytic destruction by the proteasome, causing the inactivity of CDK1 and the activation of separase[64]. Separase then targets the cohesion ring that holds the sister chromatids together, which results in the loss of sister-chromatid cohesion and the separation of sister chromatids[64].

In addition, BUB1, BUBR1, and BUB3 have been implicated in promoting chromosome alignment through regulation of Aurora B kinase (ABK) activity at KTs during chromosome congression[81-83]. During the onset of mitosis, the SAC kinase MPS1 is recruited to unattached and tensionless KTs[84,85]. MPS1 then phosphorylates multiple Met-Glu-Leu-Thr (MELT) motifs on the KT scaffold KNL-1 (also known as Blinkin and SPC105)[84-87]. BUB3 reads and binds the phosphorylated MELT motifs of KNL-1[86]. BUB3 is required to recruit both BUB1 and BUBR1 to KTs[79,88], and BUB3 inhibition results in chromosome congression defects consistent with loss of BUB1 function at KTs[83]. In prometaphase, BUB1 kinase phosphorylates threonine 120 of centromere-bound Histone 2A (pH2A-T120), which facilitates recruitment of ABK to the KT[89-91]. ABK, in turn, phosphorylates KT-MT attachment proteins, which reduces their binding affinity for MTs and prevents the premature stabilization of KT-MT attachments[92-95]. In contrast to BUB1, BUBR1 activity opposes ABK dependent phosphorylation of KT binding factors by recruiting PP2A phosphatase to the KT[77,78], which promotes the recruitment of PP1 to KTs[85]. PP1 reverses MPS1-mediated phosphorylation on KNL-1 at KTs, which releases BUB3 from the

KT, and turns off the SAC once KTs make proper bi-oriented attachments and are under proper tension[85,87]. The interplay between these opposing activities regulates the formation of stable-end on KT-MT attachments[77,78,82,85].

BUBR1 and BUB1 both interact with BUB3, a MCC adapter protein, at the KT through highly conserved GLEBS domains[79,90,96]. These are short disordered regions of about 40 amino acids that form a series of salt bridges between the WD40 domains of BUB3 and two glutamate residues in the GLEBS domain[97]. As a result of BUB3 binding, the GLEBS domain undergoes a conformational shift from a disordered to a well-ordered structure with fixed interaction points on the top face of BUB3's WD40 propeller[97]. This interaction is critical for BUB3-dependent recruitment of BUB1 and BUBR1 to KTs during prometaphase[79,88,90]. For example, a single amino-acid change in BUBR1's GLEBS domain (E406K) is sufficient to prevent BUB3 interaction and BUBR1's KT localization[88].

We have previously found that human GBM brain tumors, the most common and lethal form of brain cancer, differentially require BUBR1's GLEBS domain to suppress lethal consequences of altered KT function by promoting attachment of MTs to KTs[60]. Removal of BUBR1 from KTs of GSCs or genetically transformed fibroblasts results in lethality due to a lack of KT-MT attachments, while non-transformed cells are unaffected[60,75]. Oncogenic signaling alters KT regulation, resulting in short sisters' IKDs and KT-MT instability[60]. This causes BUBR1's GLEBS domain activity to become essential in order to suppress lethal KT-MT attachment defects and promote KT-MT attachments[60]. Thus, GBM isolates appear to be more sensitive to perturbation of certain activities of SAC proteins than non-transformed cells. This added sensitivity in GSCs has led us to isolate a facilitator of BUB3 function, *ZNF207*, an uncharacterized $Cysteine_2$ $Histidine_2$ (C2H2) zinc-finger domain containing gene[42,98]. Since we

implicated ZNF207 below as a key effector of BUB3 function, we renamed the gene *BuGZ* (Bub3 interacting GLEBS and Zinc finger domain containing protein).

ZNF207 and Zfp207, the *Mus musculus* equivalent, contain two C2H2 zinc finger motifs close to the N-terminal region[98,99]. 3% of all genes in the human genome encode for C2H2 zinc finger proteins (ZFP), making them the second most prevalent protein motif[100]. There are 20 different types of zinc finger (ZF) domains, each categorized by the structure of their zinc stabilizing amino acids[100]. The classical C2H2 finger is a self-contained domain stabilized by a zinc ion ligated to a pair of cysteines and a pair of histidines, and by an inner hydrophobic core[101]. ZFPs may contain between 1 and 40 ZF domains that are frequently arranged in groups of clusters of tandem repeats[100]. It was initially believed that ZFs could only recognize DNA by one-to-one interaction between the individual amino acids from the recognition helix of the ZF to individual DNA bases[100-102]. However, it is now known that ZFs can also bind to RNA and interact with proteins[100,103]. In addition, ZFPs can act as multi-functional regulators by binding to DNA and RNA through their ZF domains; thus, connecting transcriptional and post-transcriptional regulatory networks that often utilize feedback mechanisms[103]. Moreover, ZFPs can bind to proteins through their ZF domains or other domains[103].

ZNF207, an uncharacterized gene, is genetically altered at a very low frequency in GBM, as only 2 of 281 (0.7%) GBM patient isolates examined contained a missense mutation[23,104,105]. Nonetheless, ZNF207 is expressed in almost all human tissues, including the brain[106]. Interestingly, Zfp207 is strongly expressed in the embryonic and neonatal brains, and has been shown to reside in the nucleus[99]. In the mouse adult brain, strong expression of ZNF207 is restricted to the cerebellum and the olfactory bulb, with moderate expression detected in the hippocampus and the cortex[99]. Here, we report that the human *BuGZ/ZNF207* gene encodes a

GLEBS domain-containing and KT binding protein that is required for BUB3 stability, BUB1 KT function, and chromosome alignment.

Results

BuGZ was isolated from an RNAi screen targeting putative human transcription factors to identify key regulators of GSC's expansion and survival. As with our previous studies [42,60], we compared GSCs screen results with those from non-transformed human neural stem cells (NSCs), a candidate cell of origin for GBM, to identify GBM-specific lethality hits (Figure 2.1A). We found *BuGZ* shRNAs in this category. Thus, we set out to validate *BuGZ* as a candidate cancer lethal gene and then attempted to ascertain its cellular function.

Figures 2.1A-D show that, consistent with the screen data, *BuGZ* knockdown results in differential growth inhibition of GSCs when compared to proliferating human NSCs. Multiple shRNAs provided robust GSC-specific growth inhibition and penetrant knockdown in both GSCs and NSCs (see also Figure 2.2A). Knockdown of *KIF11/Eg5* was used as a positive proliferation control. Its inhibition blocks growth of cultured cells regardless of transformation status (Figures 2.1B and 2.1F)[42,60].

BuGZ knockdown also inhibited the growth of SSEA1+ GSC subpopulations, which are enriched for tumor initiating cell activity [11] (Figure 2.1E), and inhibited tumor sphere formation, a surrogate assay for stem cell self-renewal [107,108] (Figure 2.2B). However, *BuGZ* knockdown did not alter expression of SSEA1 or other progenitor markers, including SOX2 and NESTIN, or neural lineage markers, including GFAP and TUJ1 (data not shown). In addition, *BuGZ*-knockdown-insensitive-NSCs could be converted to sensitive by genetic transformation with *hTERT*, dominant-negative $TP53^{DD}$, *CyclinD1*, $CDK4^{R24C}$, $H\text{-}RAS^{V12}$, and MYC^{T58A} [42,46] (Figure

2.1F). Interestingly, the addition of *CyclinD1* and $CDK4^{R24C}$ alone in the *BuGZ*-knockdown-insensitive-NSCs significantly sensitize the NSCs to *BuGZ* depletion, indicating that disruption of the RB-axis can lead to the requirement of *BuGZ* in mammalian cells (Figure 2.3). Other GSC patient isolates also showed sensitivity to *BuGZ* knockdown, demonstrating that the effect is not patient-specific (Figure 2.1F). Finally, we performed an *in vivo* competition experiment to directly test the effects of *BuGZ* suppression in an orthotropic xenograft model of GBM by mixing GSCs containing GFP-expressing *shBuGZ* or shControl with non-shRNA control GSCs at an approximate 9:1 ratio respectively [42]. Following 17 days post injection, non-shRNA control GSCs drastically outcompeted *shBuGZ* GSCs, while shControl GSCs comprised the bulk tumor mass (Figures 2.1G and 2.2C). Thus, *BuGZ* expression is required for GBM tumor formation *in vivo.* Taken together, these results suggest that GSCs have a differential requirement for *BuGZ*, which is likely driven by oncogenic activity.

To gain insight into the molecular function of BuGZ, we next performed affinity purification mass spectrometry to identify candidate protein binding partners (see Methods for details). This analysis revealed BUB3 as the top-scoring hit (Figure 2.4A). We confirmed this interaction in reciprocal co-immunoprecipitation experiments. BuGZ was able to pull down BUB3 and vice versa in GSCs (Figure 2.4B) and 293T cells (Figure 2.5), demonstrating the proteins interact in cells.

Since SAC signaling is an essential and highly conserved process, we performed phylogenetic analysis to identify *BuGZ* orthologs and examine available data on their function in model genetic systems. *BuGZ* shows strong conservation among eukaryotes with the exception of budding and fission yeasts, where no orthologs could be identified (Figure 2.4C) [109]. This is in contrast to *BUB3*, which is highly conserved in all eukaryotes, including budding and fission

yeasts, where it was first identified [110]. Additionally, examination of protein-protein interaction databases available for humans, worms, flies, and plants revealed additional evidence for BuGZ ortholog interaction with BUB3 from genome-scale yeast two-hybrid screens or mass spectrometry analysis (Table 2.1). However, other candidate proteins identified in our mass-spectrometry analysis were not found. This suggests that BuGZ-BUB3 interactions are highly conserved among higher eukaryotes.

We next examined whether BuGZ interacts with BUB3 through a GLEBS domain, similar to BUB1 and BUBR1. We observed that *BuGZ* orthologs also harbor a single conserved GLEBS domain motif (AA 344-376 for human), which contains the characteristic two glutamate residues found in all GLEBS domains (AA 358 and 359 for human *BuGZ*) (Figure 2.4D). Furthermore, mutational analysis of human *BuGZ* followed by immunoprecipitations revealed that BuGZ's GLEBS domain is required for interaction with BUB3, while its zinc finger domains are dispensable (Figures 2.4E and 2.4F). Thus, similar to BUB1 and BUBR1, BuGZ interacts with BUB3 through a GLEBS domain.

To further explore the role of BuGZ-BUB3 binding, we evaluated the protein levels of each binding partner after RNAi depletion. We found that depletion of *BuGZ* led to ~2-fold depletion of BUB3 protein in GSCs, NSCs, and HeLa cells, while other SAC and KT proteins (including BUB1, BUBR1, MAD2L1, HEC1, and CDC20) were unaffected (Figures 2.6A, 2.6B, and 2.7A-C). However, mRNA levels of *BUB3* remain unchanged with *BuGZ* knockdown (Figure 2.6C), suggesting the effects are not due to transcriptional regulation or to off-target RNAi. In addition, BUB3 loss due to *BuGZ* depletion can be rescued by overexpressing a *BuGZ* allele that is resistant to the *shBuGZ* (Figure 2.6D). Moreover, mutational analysis revealed that the glutamic acid residues E358 and E359 of BuGZ's GLEBS domain are critical for BUB3

stability (Figure 2.6D). These two glutamic acid residues are invariant among consensus residues for BUB1, BUBR1 and NUP98 GLEBS domains (Figure 2.4D) and are essential for their binding to BUB3 or RAE1 [79,90,96,97,111,112]. These results suggest that the BuGZ-BUB3 GLEBS-mediated interaction decreases protein turnover of BUB3.

We next addressed whether BuGZ and BUB3 have overlapping localization patterns in cells. Similar to reports for BUB3 [90], a BuGZ-GFP fusion localized primarily to the nucleus in interphase, concentrated at KTs prior to nuclear envelope breakdown and during early prometaphase, and disappeared from KTs upon MT binding (Figure 2.6E). Immunostaining of BuGZ revealed a similar localization pattern (Figure 2.8A). We next determined co-localization patterns of BuGZ and BUB3 in HeLa cells. BUB3, just like BuGZ, maximally localized to KTs prior to nuclear envelope breakdown and remained bound throughout prometaphase as previously described [113] (Figure 2.9A). However, unlike BuGZ, low levels of BUB3 persisted at metaphase KTs.

In contrast to BuGZ and BUB3 KT localization, BUB1 and BUBR1, which also associate with BUB3 via GLEBS domains, concentrate at KTs after nuclear envelope breakdown (Figure 2.8B), consistent with previously published results [114,115]. Similar to these proteins, BuGZ's GLEBS domain is required for KT localization (Figure 2.9B), while its zinc finger motifs are dispensable (Figure 2.9B). In addition, depletion of *BUB3* using RNAi prevented BuGZ localization to the KT (Figure 2.9C). Previous reports demonstrated that BUB3, BUB1, and BUBR1 all require KNL-1 in order to bind KTs [84,87,116,117]. We found that *KNL-1* depletion also resulted in a loss of BuGZ from KTs (Figure 2.9D). Moreover, when cells were treated with nocodazole, causing spindle MTs to depolymerize, unattached KTs re-accumulated BuGZ (Figure 2.9E). Conversely, treating cells with taxol, which stabilizes KT-MTs attachments, did

not recruit BuGZ to MT-attached KTs (Figure 2.9E). This behavior is similar to BUB3 and other SAC proteins [118]. Together, these results indicate that BuGZ localizes to KTs by binding to BUB3 through its GLEBS domain and BuGZ's KT localization is regulated by attachment of MTs.

Previous studies report that BUB3 and its binding partners BUB1 and BUBR1 exhibit interdependencies for KT localization [67,70]. We therefore analyzed KT localization of BUB3, BUB1, and BUBR1 in *BuGZ*-depleted HeLa cells. After *BuGZ* depletion, BUB3 levels are reduced at KTs, which is not unexpected due to the decrease in total protein (Figure 2.9F). BUB1 KT localization is also significantly decreased (Figure 2.10A), which is likely due to loss of its obligate KT recruitment factor BUB3 [90,114,119]. Intriguingly, BUBR1 KT association is not affected after *BuGZ* depletion (Figure 2.10A), though previous studies have demonstrated that BUBR1 KT recruitment relies on BUB3 [83,120]. It is possible that BUBR1 out-competes BUB1 for limiting BUB3 binding sites that remain post-*BuGZ* depletion, or alternatively, that BuGZ plays a more direct role in BUB1 KT recruitment.

In addition to their well-known roles in SAC signaling, BUB1, BUBR1, and BUB3 have also been implicated in facilitating chromosome alignment during mitosis [81-83]. We therefore examined chromosome alignment in *BuGZ*-depleted HeLa cells treated with the proteasome inhibitor MG132 (to prevent precocious anaphase entry), and found that this process was significantly compromised (Figure 2.10B). In control populations, >95% of cells were able to fully align chromosomes, whereas proper chromosome alignment was observed in less than 55% of *BuGZ*-depleted cells (Figure 2.10B). We also detected similar chromosome alignment defects in GSC-0131 and transformed NSC-CB660 upon *BuGZ* depletion and MG132 treatment (Figure 2.10C). However, non-transformed NSC-CB660 cells were able to fully align chromosomes

following *BuGZ* depletion (Figure 2.10C). In addition, co-depleting both *BuGZ* and *BUB3* in GSC-0131 resulted in partial to severe chromosome alignment defects similar to *BuGZ* and *BUB3* depletion alone (Figure 2.10D). The chromosome alignment defects in GSC-131 following depletion of endogenous *BuGZ* could be rescued by ectopic expression of the *BuGZ* ORF (Figure 2.10E), which further demonstrates that the chromosome alignment defects are due to *BuGZ* depletion and not due to off-target RNAi. However, *BuGZ* GLEBS domain mutations (E358K and E359K) failed to rescue the chromosome alignment defects (Figure 2.10E). The alignment defects were also observed in live *BuGZ*-depleted cells, which exhibited significantly extended mitotic transit times (120 min compared to 60 min in control cells) (Figures 2.10F and 2.11). Together, these results suggest oncogenic stress alters KT function, which leads to a differential requirement for BuGZ's GLEBS domain in cancer cells for chromosome congression.

To understand the source of these attachment errors, we assayed BUB1 kinase activity, which is implicated in mediating proper chromosome alignment through localization and activation of ABK [91,121,122]. BUB1 kinase activity was measured in cells by immunostaining its substrate, histone H2A-T120. Consistent with loss of BUB1 at KTs, pH2A levels were significantly lower after *BuGZ* depletion (Figure 2.12A). Consistent with loss of ABK activity at KTs after *BuGZ* depletion, we also observed significant loss of phosphorylation of HEC1-S44, a critical downstream KT substrate of ABK involved in the regulation of KT-MT attachments (Figure 2.12A) [94]. Thus, BuGZ affects chromosome alignment by ensuring BUB3 mediated recruitment of BUB1, which in turn ensures appropriate ABK-mediated phospho-regulation of KT-MT attachments.

However, unlike BUB1 and BUBR1, *BuGZ* depleted cells retained a functional SAC response and elicited a significant mitotic delay in response to MT poisons, albeit at diminished levels (Figures 2.12B and 2.13). *BuGZ* and *BUB3* co-depleted cells did not sustain a checkpoint arrest under these same conditions, which was similar to the behavior of cells depleted of *BUB3* alone (Figure 2.12C). These results suggest that *BuGZ* depleted cells have enough residual BUB1 and BUB3 to activate the SAC.

BUB1, *BUB3*, and *BUBR1* are all essential for mouse development, as null mutations of these genes cause early embryo lethality [75,123-125]. However, the heterozygous state is permissive for normal development, albeit with increases in mitotic abnormalities. Our knockdown studies suggest that the hypomorphic *BuGZ* state is permissive for viability of non-transformed cells, where BUB3 expression is probably equivalent to BUB3 heterozygous cells (Figures 2.6A, 2.6B, and 2.9F). Therefore, we set out to determine whether *BuGZ* is essential in non-transformed NSCs. To this end, we employed clustered regularly interspaced short palindromic repeats (CRISPR)-Cas9 technology (see Chapter 3 for methodology details) using an all-in-one LV-single guide RNA (sgRNA):Cas9 platform system to target and knockout the *BuGZ* gene[126,127]. Briefly, CRISPR-Cas9 is a dual RNA-guided DNA endonuclease that makes two cuts in the genomic DNA at the targeted site[80,128]. Nonhomologous end joining then typically repairs this double-stranded break, which results in an insertion/deletion (indel) that causes a premature stop codon and the initiation of nonsense-mediated decay of the transcript[80,129]. *BuGZ* knockout using multiple single guide RNAs (sgRNA) resulted in a significant and robust growth inhibition in both the GSCs and NSCs (Figure 2.14). These results were comparable to the positive proliferation control, *HEATR1*, which is involved in transcription of ribosomal genes (rDNA) by

RNA polymerase I and pre-rRNA processing (see Chapter 3 for further details on HEATR1)[130]. Thus, like *BUB1*, *BUBR1*, and *BUB3*, *BuGZ* is also essential in both NSCs and GSCs.

Discussion

Here, we report that the human *BuGZ/ZNF207* gene encodes a GLEBS domain-containing and KT binding protein that is required for BUB3 stability, BUB1 KT function, and chromosome alignment. A model for BuGZ function is presented in Figure 2.12D. We propose that BuGZ activity is required for BUB3 stability during interphase and mitosis. *BuGZ* depletion, therefore, results in a reduction of BUB3 protein levels during interphase and decreased binding to KTs during mitosis. As a consequence, BUB3-dependent BUB1 recruitment to KTs is compromised. This, in turn, compromises BUB1-dependent recruitment of ABK, which causes lethal chromosome congression defects in cancer cells. Importantly, viability defects and chromosome alignment defects resulting from *BuGZ* depletion were recreated in non-sensitive cells through oncogenic transformation. This suggests that oncogenic stress can drive an added requirement for BuGZ function in our GBM isolates and other cancer lines.

We previously established that GSCs differentially require BUBR1's GLEBS domain to suppress lethal consequences of altered KT function by promoting attachment of MTs to KTs [60]. Similar to BuGZ, BUBR1-GLEBS viability requirement can be reproduced in non-sensitive cells through genetic transformation with RAS^{G12V}. However, the phenotypes associated with BUBR1-GLEBS domain requirement appear to be distinct from those observed for BuGZ. For example, *BUBR1* knockdown results in severe defects in KT-MT attachment in GBM isolates with short inter-KT distances at metaphase, while *BuGZ* knockdown results in alignment defects similar to those produced by BUB3 depletion in all GSC isolates (Figure 2.10D). We postulate that GBM

isolates and transformed NSCs have an added requirement for *BuGZ* due to oncogenic signaling that leads to changes in either KT protein activity (e.g., through changes in stoichiometry) or feedback regulation of genes involved in chromosome congression (e.g., *ABK*). Based upon these studies, the RTK/RAS pathway is a likely candidate for triggering a *BuGZ* requirement. The RTK/RAS pathway is over activated in many cancers, including GBM, and there is evidence that RAS-down stream effectors ERK1/2 can directly phosphorylate the C-terminal domain of CENP-E, a key KT protein, which is predicted to decrease its MT binding ability [131]. Though RAS is not commonly mutated in GBM, the RTK/MAP kinase signaling cascade is a necessary feature of GBM tumors[22] and our GSCs (See Figures 3.2A and 3.3 in Chapter 3). Future studies are warranted to determine if expression of commonly altered genes in GBM that are involved in the MAP kinase and PI3K-AKT kinase signaling pathways, such as *EGFR*, *PTEN*, *PI3K*, and *NF1*[22], generate the requirement for *BuGZ*.

One possible KT protein that may play a pivotal role in GSCs' requirement for BuGZ is MPS1. The SAC kinase MPS1 is recruited to unattached and tensionless KTs, and phosphorylates multiple MELT motifs on the KT scaffold KNL-1[84-87]. Interestingly, members of the MAP kinase signaling pathway, MEK and ERK, can stabilize MPS1, and overexpression of the *B-RAF*^{V660E} mutant can increase MPS1 expression through MEK and ERK[132,133]. In addition, *HRAS*^{G12V} and *MEK*^{DD} oncogenic altered cells exhibit increased ABK activity and weaken KT-MT attachments[76]. Taken together, the activation of the MAP kinase pathway in GSCs could lead to an increase in MPS1 at the KT, which would likely result in an increase of phosphorylation on KNL-1's MELT motifs[87]. This in turn could lead to a higher expression of BuGZ at the KT compared to non-transformed cells, followed by an amplification of BUB1 activity and then ABK activity.

It was also recently found that BUB3 KT recruitment is driven by MPS1/TTK-dependent phosphorylation of KNL-1's MELT motifs [84,86,87,116,117]. Consistent with this result, we find that BuGZ KT localization is KNL-1-dependent (Figure 2.9D). Interestingly, BUB3 binding of phosphorylated MELT motifs is ~10-fold greater when BUB1 is present [86]. Future work will be required to determine whether BuGZ, BUB1, and BUBR1 have similar effects on KNL-1-dependent BUB3 KT localization.

Moreover, MPS1 has been shown to be required in breast tumor cells deficient for *PTEN*, which is commonly lost in GBM[22,134,135]. These cells could be sensitive to *BuGZ* depletion since MPS1 is potentially responsible for recruiting BuGZ to the KT. Thus, it is likely that other oncogenic alterations, such as alterations in *PTEN*, can also sensitize cancer cells to *BuGZ* depletion.

In addition to potential *PTEN* loss, our data suggest that disruption of the RB-axis by expressing *Cyclin D1* and $CDK4^{R24C}$ in *BuGZ*-knockdown-insensitive-NSCs can sensitize NSCs to *BuGZ* depletion (Figure 2.3). *BuGZ* depletion in these oncogenic altered cells leads to an inhibition of cell growth (Figure 2.3). Interestingly, depletion of *RB* leads to an increase in HEC1 expression, which could then require an increase in ABK activity[136]. HEC1 is a critical downstream KT substrate of ABK that is involved in the regulation of KT-MT attachments[94], and phosphorylation of HEC1 is decreased upon *BuGZ* depletion (Figure 2.12A). In addition, ABK can also phosphorylate S780 on RB, which stabilizes the E2F1: phosphorylated-RB interaction[137,138]. This interaction is believed to serve as an additional post-mitotic cell checkpoint after an aberrant mitosis in order to prevent endoreduplication and subsequent polyploidy cell formation[137,138]. Therefore, the increase in HEC1 expression, which may lead to an increase in ABK activity, following *RB* depletion could be due to the cell's attempt to counter

the disruption in the potential ABK-RB feedback loop in order to activate the post-mitotic checkpoint. Notably, we observed a subpopulation of *BuGZ*-depleted cells that were able to successfully complete mitosis or exit from an aberrant mitosis, but the majority of these cells experienced cell death during the ensuing mitosis (data not shown). Taken together, disruption of the RB-axis may lead to an increase in BuGZ's localization to the KT, which then leads to an increase in ABK activity. Thus, cells that have an alteration in the RB-axis may require higher expression of BuGZ at the KT than non-transformed cells, which sensitizes them to *BuGZ* depletion. Future experimentation is necessary to determine how the KT localization of BuGZ and other KT proteins are altered following common GBM oncogenic alterations.

The functional dichotomy between BuGZ and BUBR1 is also observed in the SAC. BUBR1's essential function is to maintain an intact mitotic checkpoint until all chromosomes are properly aligned and KTs are under proper tension. We observe a significant mitotic delay in cancer cells following depletion of *BuGZ* despite a significant loss of both BUB1 and BUB3 at the KT (Figures 2.12B and 2.13). This mitotic delay is checkpoint dependent as co-depletion of *BuGZ* and *BUB3* prevents mitotic arrest (Figure 2.12C). Thus, it is likely that unattached KTs present in *BuGZ* depleted cells are able to generate a functional SAC signal. It is known that BUB1 must be depleted >95% to cause checkpoint abrogation [81]. Therefore, the >40% of BUB3 and BUB1 present in *BuGZ* depleted cells is likely sufficient for SAC activation. However, we cannot preclude the possibility that BuGZ is also involved in SAC silencing, which contributes to the mitotic delay observed. In addition, BuGZ may have additional roles during mitosis that contribute to the mitotic delay observed following its depletion. For example, BUB3 was recently shown to promote the metaphase to anaphase transition by enhancing the binding of APC/C and CDC20 through its interaction with CDC20 at the KT[139,140]. Thus, loss of BUB3 at

the KT following *BuGZ* depletion may impair binding of APC/C with its activator CDC20, which would lead to a mitotic delay.

Our studies raise a key question: Is *BuGZ* essential during development? *BUB1*, *BUB3*, and *BUBR1* are all essential for mouse development, as null mutations of these genes cause early embryo lethality [75,123-125]. Our results suggest that *BuGZ* is essential for development, as knocking out *BuGZ* by CRISPR-Cas9 technology in non-transformed NSCs leads to a significant decrease in viability (Figure 2.14). However, consistent with being non-essential, BUBR1's GLEBS domain is not required for mouse embryo fibroblast proliferation or KT-MT attachment [60,75]. It will be interesting to see if GLEBS domains are essential for mammalian development, given that our findings suggest targeting GLEBS domain interactions with BUB3 may represent a precision therapy for GBM. In addition, future investigation is warranted to determine if the complete removal of *BuGZ* would reduce BUB3 levels at the KT to less than 60%, which is the residual expression of BUB3 at the KT following *BuGZ* depletion (Figure 2.9F).

Although *BuGZ* is essential in non-transformed NSCs (Figure 2.14), we found minimal inhibition in cell growth following depletion of *BuGZ* (Figures 2.1B-D and 2.7C). Our data suggest that non-transformed cells, such as NSCs, can tolerate reduced levels of BUB3 at the KT. However, we can not preclude the possibility that other GLEBS domain-containing proteins that bind to BUB3, such as BUB1, BUBR1, and PKM2[79,97,141], may be able to partially compensate for the reduction of BuGZ in non-transformed cells. For example, tumor-specific pyruvate kinase M2 (PKM2), which has important roles in glycolysis and gene transcription, binds to BUB3 during mitosis and phosphorylates residue Y207, a regulatory event required for BUB3-BUB1 complex recruitment to KTs in GBM cells[66,141]. These BUB3-BUB1 complexes then interact with KNL-1, which is essential for proper KT-MT attachments, chromosome

congression, and chromosome segregation in GBM cells[141]. It will be interesting to determine whether the double depletion of BuGZ and another GLEBS domain-containing protein, such as PKM2, would substantially reduce BUB3 levels at the KT compared to depletion of *BuGZ* alone, and whether this treatment results in synthetic lethality in non-transformed NSCs. Nonetheless, BuGZ and BUB3 may also have additional essential cellular functions that were not revealed by our studies. Thus, other GLEBS domain-containing proteins may only be able to compensate for *BuGZ* depletion during mitosis by stabilizing and localizing BUB3 to the KT, but may not be able to compensate for other BuGZ's cellular activities.

Zinc finger proteins, like BuGZ, can have multiple cellular functions, as they can bind to DNA and RNA through their zinc finger domains and can bind to proteins by their zinc finger domains or other domains[100,103]. Interestingly, proteomic analysis of affinity purified spliceosomal complexes have found BuGZ and BUB3 to be associated with the prespliceosome A complex as non-core proteins, but not with any downstream spliceosome complexes[142-148]. It was recently shown that *BuGZ* and *BUB3* are required for pre-messenger RNA splicing in cancer cells, as depletion of *BuGZ* or *BUB3* leads to exon skipping in many transcripts[148]. Moreover, the deficiency in RNA splicing due to *BuGZ* or *BUB3* depletion leads to an increase in the formation of RNA-DNA hybrids (R-loops), which leads to DNA damage, TP53 activation, and cell death[148]. Previously, we have shown that *PHF5A* is differentially required in GSCs, but not NSCs, for proper 3' pre-messenger splice site recognition; and thus, GSCs are vulnerable to splicing perturbations[42]. Nonetheless, BuGZ's specific function in the spliceosome and processing of pre-messenger RNA is unknown. In addition, it remains to be determined whether BuGZ's zinc finger domains or GLEBS domain contribute to its splicing function, and whether BuGZ's splicing function is essential in GSCs.

Our findings also raise a critical question regarding BuGZ's role to facilitate BUB3's function: How does BuGZ regulate BUB3's stability? One possibility is that upon BUB3 binding, BuGZ's GLEBS domain masks post-translational modifications of BUB3, such as phosphorylation, ubiquitination, or sumoylation, which prevents it degradation. However, we were unable to detect increases in BUB3 expression from *BuGZ* depleted cells treated with the proteasome inhibitor MG132 (Figure 2.6B) or the sumoylation inhibitor ginkgolic acid (data not shown). Another possibility is that BuGZ acts as a molecular chaperone for BUB3 by converting an unfolded or partially folded BUB3 to its final compact and stable confirmation [97], which, for example, may prevent specific proteases from recognizing and degrading unfolded BUB3. Over expression of *BuGZ* increases the steady-state levels of ectopically expressed and also endogenous BUB3 (Figures 2.4F and 2.6D), suggesting that *BuGZ* expression is rate-limiting for BUB3 stability. Thus, further experimentation is warranted to determine the nature of the change in BUB3 turnover following *BuGZ* depletion.

Another question is how BuGZ-dependent BUB3 regulation affects BUB1 and BUBR1 function at KTs? BUB3 and its binding partners BUB1 and BUBR1 exhibit interdependencies for kinetochore localization [67,70]. Our results suggest that *BuGZ* inhibition preferentially depletes BUB1 recruitment to the KT, leaving BUBR1 levels unchanged (Figure 2.10A). This appears to contradict previous studies that have established roles for BUB1 and BUB3 in recruiting BUBR1 to kinetochores [83,90,117,123,149,150]. However, these studies produce knockdowns of >90% of BUB1 or BUB3. Our studies produce more modest changes in BUB3 levels after *BuGZ* knock down (Figure 2.9F) and only partial loss of recruitment of BUB1 to KTs (Figure 2.10A). This suggests that BUBR1 may outcompete BUB1 at KTs for residual BUB3 (e.g., BUBR1 could have higher

affinity for BUB3 than BUB1). Alternatively, BuGZ could act as an exchange factor facilitating BUB3-BUB1 interactions.

In summary, we find that BuGZ is a novel GLEBS domain-containing and KT binding protein required for BUB3 stability and KT function. In transformed cells, *BuGZ* knockdown results in defects in KT-MT attachments and chromosome congression. For cancer biology, these results raise the possibility that inhibiting GLEBS domain interactions with BUB3 may be a therapeutic strategy for refractory cancers like GBM, which suffer from lethal KT-MT instability brought about by oncogenic stress [60]. For evolutionary biology, these results suggest that BuGZ function may have arisen in higher eukaryotes to facilitate BUB3 function and chromosome congression.

Figures

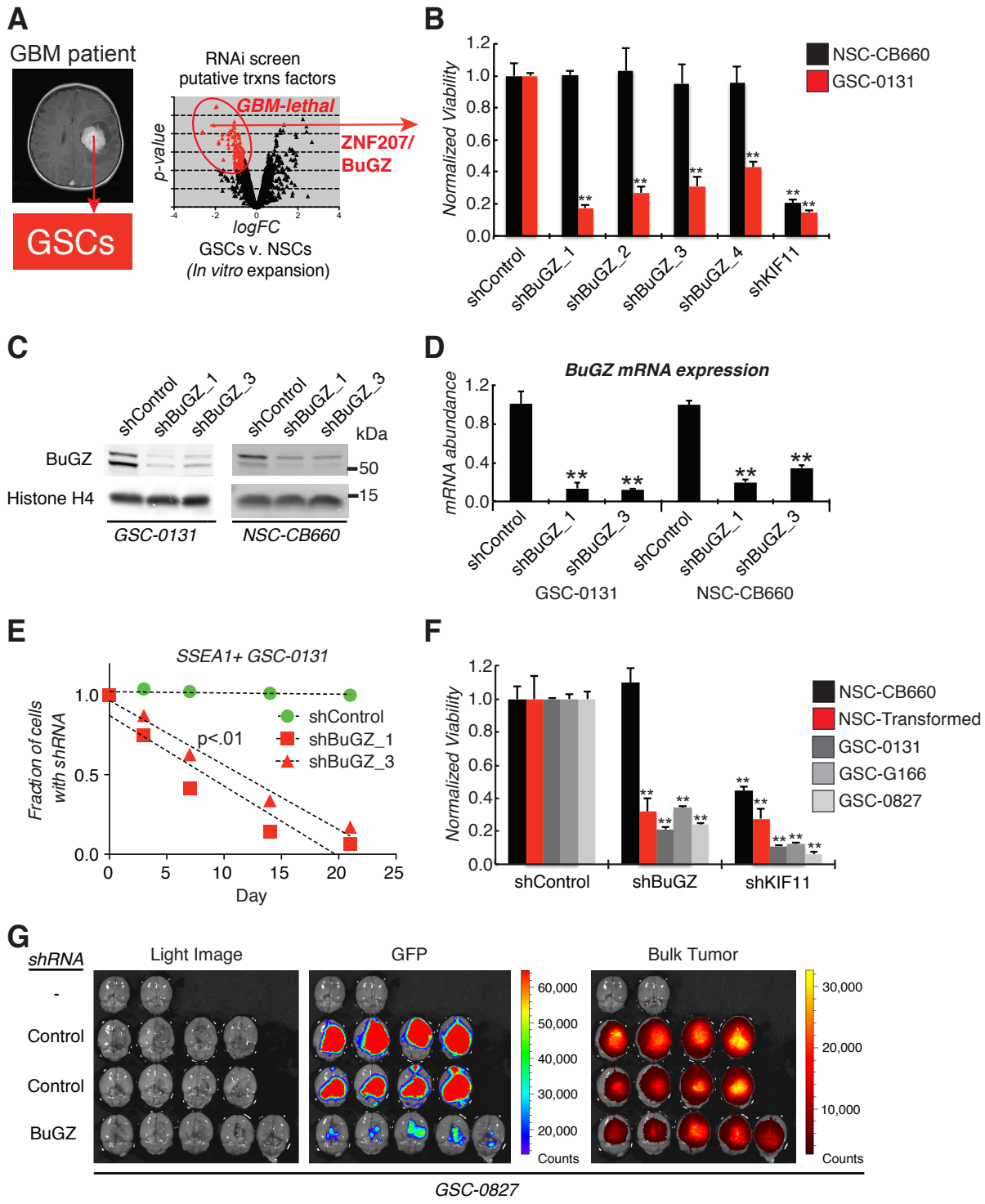

Figure 2.1. *BuGZ* is a candidate GBM-lethal gene.
(A) An RNAi screen of putative transcription factors revealed *ZNF207/BuGZ* as differentially required for GSC expansion as compared to NSCs.

(B) *BuGZ* knockdown causes loss of viability in GSCs, but not NSCs. Cells were infected with lentiviruses expressing *BuGZ*, *KIF11* or control shRNAs, outgrown for 7 days, and assayed for growth. Knockdown of *KIF11* was used as a positive control for both RNAi knockdown and cell proliferation. All viral clones were normalized to their respective shControl. (**Student t test, $p<0.01$, +SD).
(C and D) Western blot analysis and quantitative real time PCR (qRT-PCR) for BuGZ protein and mRNA expression, respectively, of whole cell extracts from GSC-0131 and NSC-CB660 following shRNA knockdown. (**Student t test, $p<0.01$, +SD).
(E) *BuGZ* knockdown compromises growth of SSEA1+ GSC subpopulations. Flow cytometry analysis of SSEA1+ GSC-0131 cells infected with *shBuGZ*-GFP+ or shControl-GFP+, mixed with untreated cells, and followed for 21 days *in vitro* under self-renewing conditions.
(F) *BuGZ* knockdown compromises growth of transformed NSCs and multiple GSC isolates, but not NSCs (assay same as (**B**)). (**Student t test, $p<0.01$, +SD).
(G) Suppression of *BuGZ* expression compromises GBM tumor formation *in vivo*. Images of *in vivo* competition mouse brains 17 days post orthotopic xenograft of GSC-0827 cells expressing GFP-shControl or GFP-*shBuGZ* mixed with non-shRNA GSC-0827 cells. Right, light images of brains. Middle, GFP+ fluorescence marking shRNA-containing cells. Left, fluorescent signal from Tumor paint (Chlorotoxin: indocyanine green) to identify total tumor mass. First mouse brain of top row did not receive GSC-0827 cells or Tumor Paint, while the second mouse brain of top row did not receive GSC-0827 cells but received Tumor paint. Quantification of GFP fluorescence is shown in Figure 2.2C. (**Student t test, $p<0.01$).

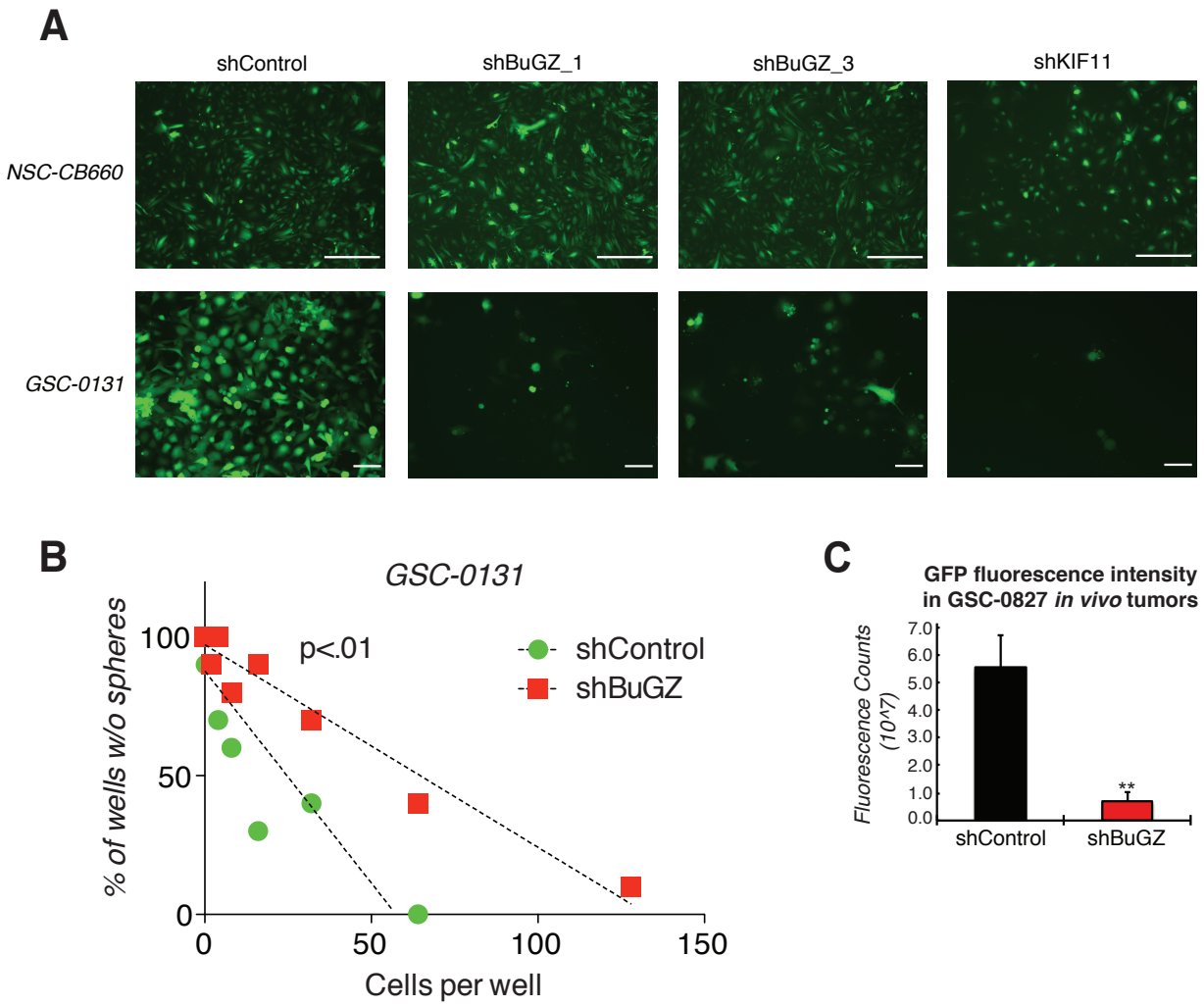

Figure 2.2. *BuGZ* knockdown differentially inhibits growth of GSCs in monolayer culture, in a tumor sphere formation assay, and an *in vivo* mouse orthotopic xenograft competition experiment.

(A) Images of NSC-CB660 and GSC-0131 isolates' viability after 7 days of infection with shControl or two independent shRNA clones targeting *BuGZ*. Visualization of the cells using pGIPZ-shRNA-green fluorescent protein (GFP). An shRNA targeting *KIF11*, a microtubule motor protein critical for bipolar spindle formation during mitosis, was used as a positive control for both RNAi pathway activity and cell proliferation. Bar (NSC-CB660) 500μM; Bar (GSC-0131) 100μM.

(B) Limiting dilution sphere forming assay of GSC-0131 infected with two independent shRNA viral clones for in vitro tumor sphere formation and clonogenicity. Cells were plated into 96-well plates with various seeding densities (0.125-256 cells per well, 10 wells per condition).

(C) Quantification of GFP fluorescence from the in vivo mouse brain orthotopic xenograft GSC-0827 competition experiment. GFP-shControl expressing GSCs comprised the bulk of their respective tumors. However, GFP-*shBuGZ* expressing GSCs were unable to contribute to the formation of their tumors and yielded tumor masses dominated by non-shRNA GSCs with no detectable GFP expression. (**, Student t test, unequal variance, 2 tails; P<0.01; +SD).

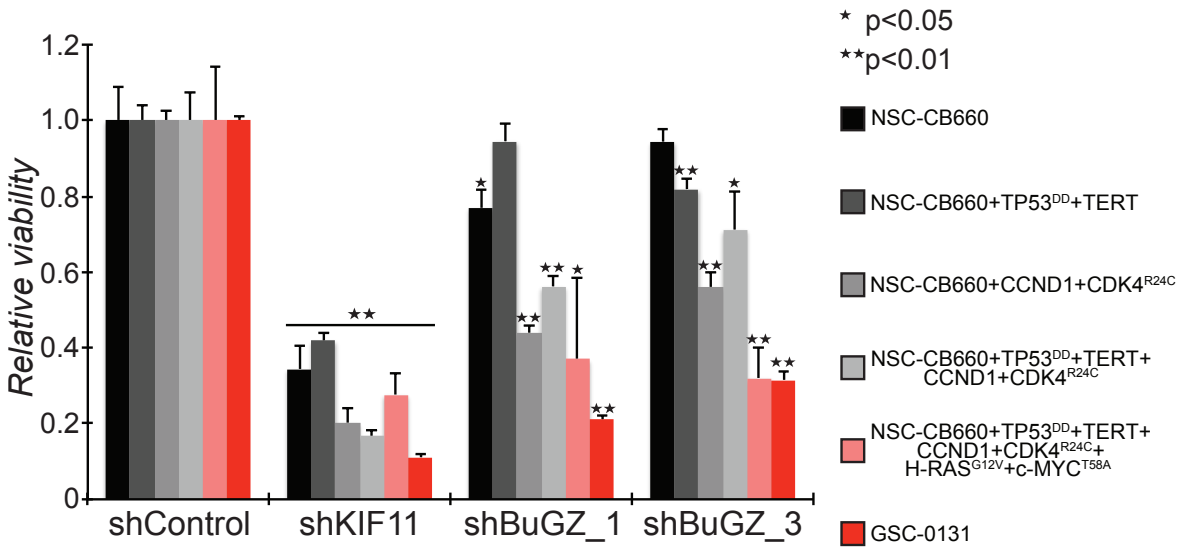

Figure 2.3. Disruption of the TP53 and RB pathways in conjunction with activation of RTK/RAS pathway sensitizes NSCs to *BuGZ* depletion.

Inactivation of RB leads to a loss of viability in NSCs upon *BuGZ* knockdown. In addition, *BuGZ* knockdown causes a decrease in viability in genetically transformed NSCs (disruption of the TP53 and RB axis and activation of the RTK/RAS pathway) and GSCs. Cells were infected with lentiviruses expressing *BuGZ*, *KIF11* or control shRNAs, selected with puromycin, outgrown for 7 days, and assayed for growth using alamar blue. Cells were maintained under puromycin selection during the outgrowth assay. Knockdown of *KIF11* was used as a positive control for both RNAi knockdown and cell proliferation. All viral clones were normalized to their respective shControl. (**Student t test, +SD).

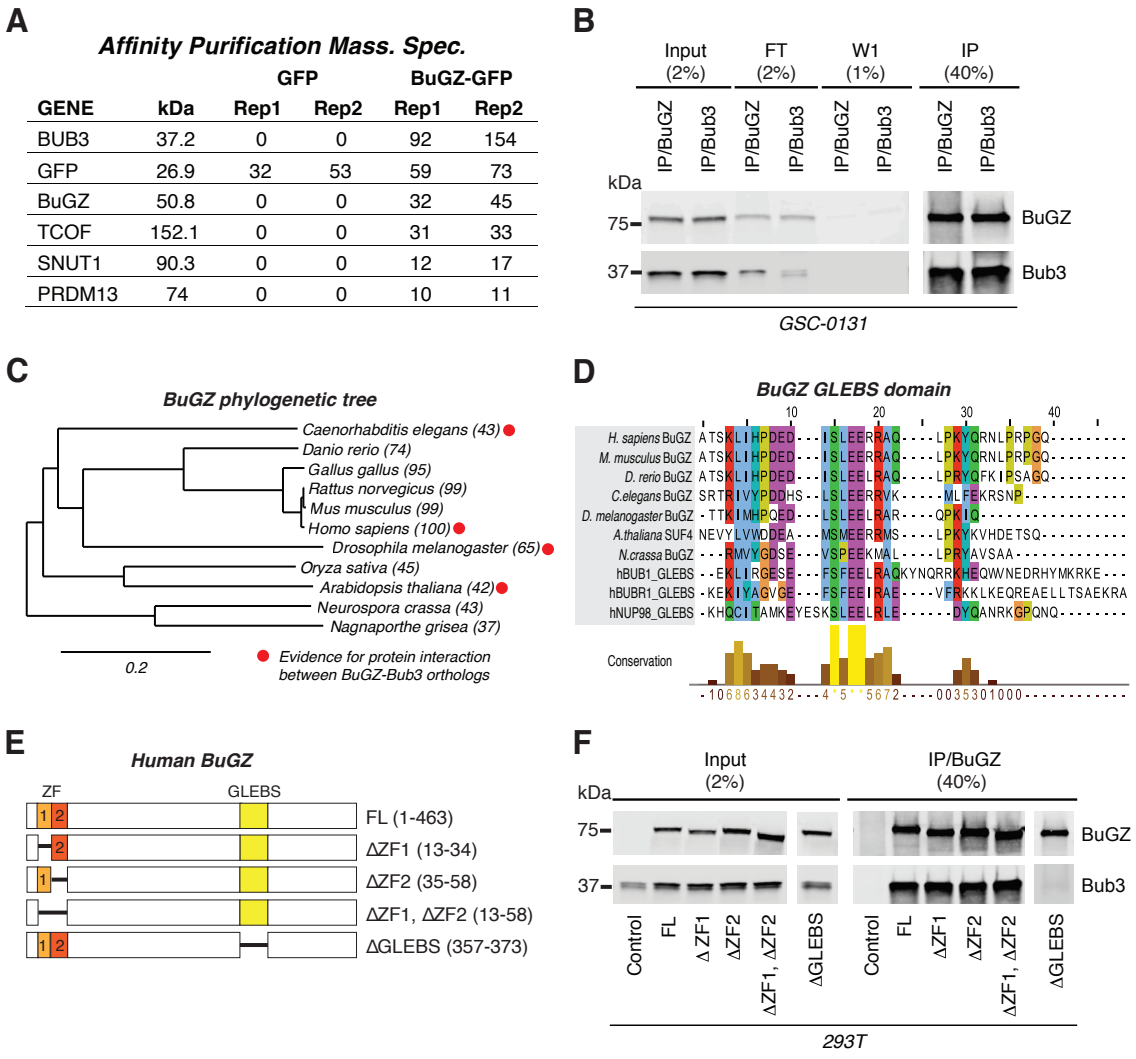

Figure 2.4. BuGZ binds to BUB3 through a highly conserved GLEBS domain.

(A) Results of affinity purification mass spectrometry of 293T cell extracts transfected with GFP-tagged ZNF207 open reading frame (ORF). BUB3 was identified as the top candidate protein to interact with BuGZ. GFP control ORF was used to identify non-specific protein interactions.

(B) BuGZ binds to BUB3 and vice versa. Western blot analysis with anti-turboGFP (BuGZ) and anti-BUB3 of immunoprecipitates with the turboGFP antibody (BuGZ) or V5 antibody (BUB3) from GSC-0131 cells infected with V5-*BUB3* and turboGFP-*BuGZ* constructs. FT= flow through; W1=wash 1; IP= immunoprecipitation.

(C) Evolutionary distance between orthologs of *ZNF207/BuGZ* sampled from major phyla. Percent protein identify to human BuGZ from pair-wise protein alignments is indicated in parentheses (NCBI, HomoloGene data base). Red dot indicates evidence for BuGZ-BUB3 interactions from protein-protein interaction databases (Table 2.1).

(D) *BuGZ* orthologs contain a highly conserved GLEBS domain. GLEBS domains from hBUB1 (AA240-280), hBUBR1 (AA400-440), and hNUP98 (157-213) (Larsen et al., 2007[97]; Wang et al., 2001[79]) were used to create pair-wise alignments of indicated *BuGZ* orthologs using CLUSTW.

(E) Human *BuGZ* alleles generated and used in these studies. FL= Full length *BuGZ* open reading frame (ORF); ΔZF1= deletion of first zinc finger motif; ΔZF2= deletion of second zinc finger motif, ΔZF1, ΔZF2= deletion of the two zinc finger motifs; ΔGLEBS= deletion of a portion of the GLEBS motif.

(F) BuGZ binds to BUB3 through its GLEBS domain. Western blot analysis with anti-turboGFP and anti-BUB3 of immunoprecipitates with the turboGFP antibody (BuGZ) from 293T cells transfected with the mutant alleles in (**E**) or the control (V5-*BUB3*).

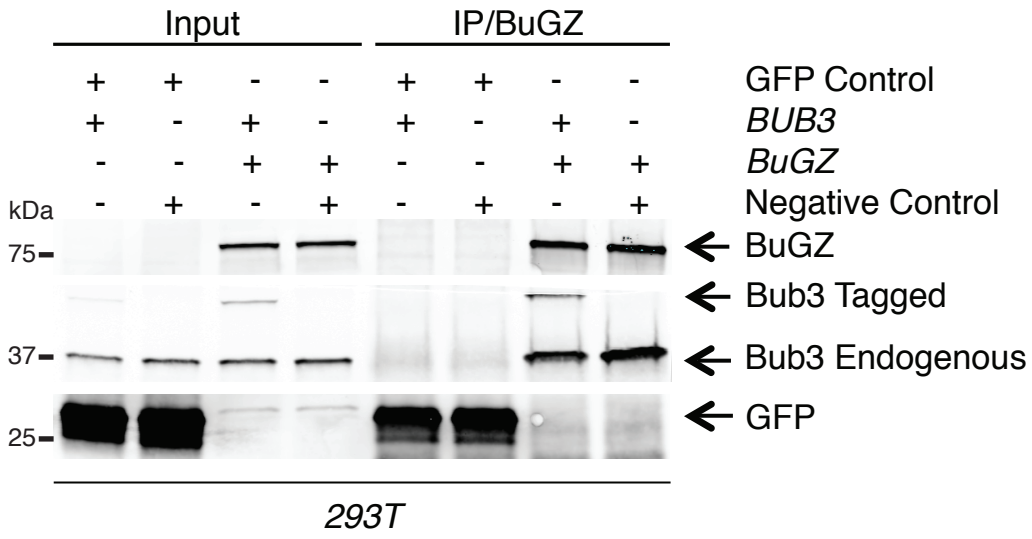

Figure 2.5. Co-immunoprecipitation of BuGZ and BUB3 in 293T cells.
Western blot analysis with anti-turboGFP (BuGZ) and anti-BUB3 of immunoprecipitates with the turboGFP antibody (BuGZ) from 293T cells infected with mCherry-*BUB3* and turboGFP-*BuGZ* constructs. IP= immunoprecipitation.

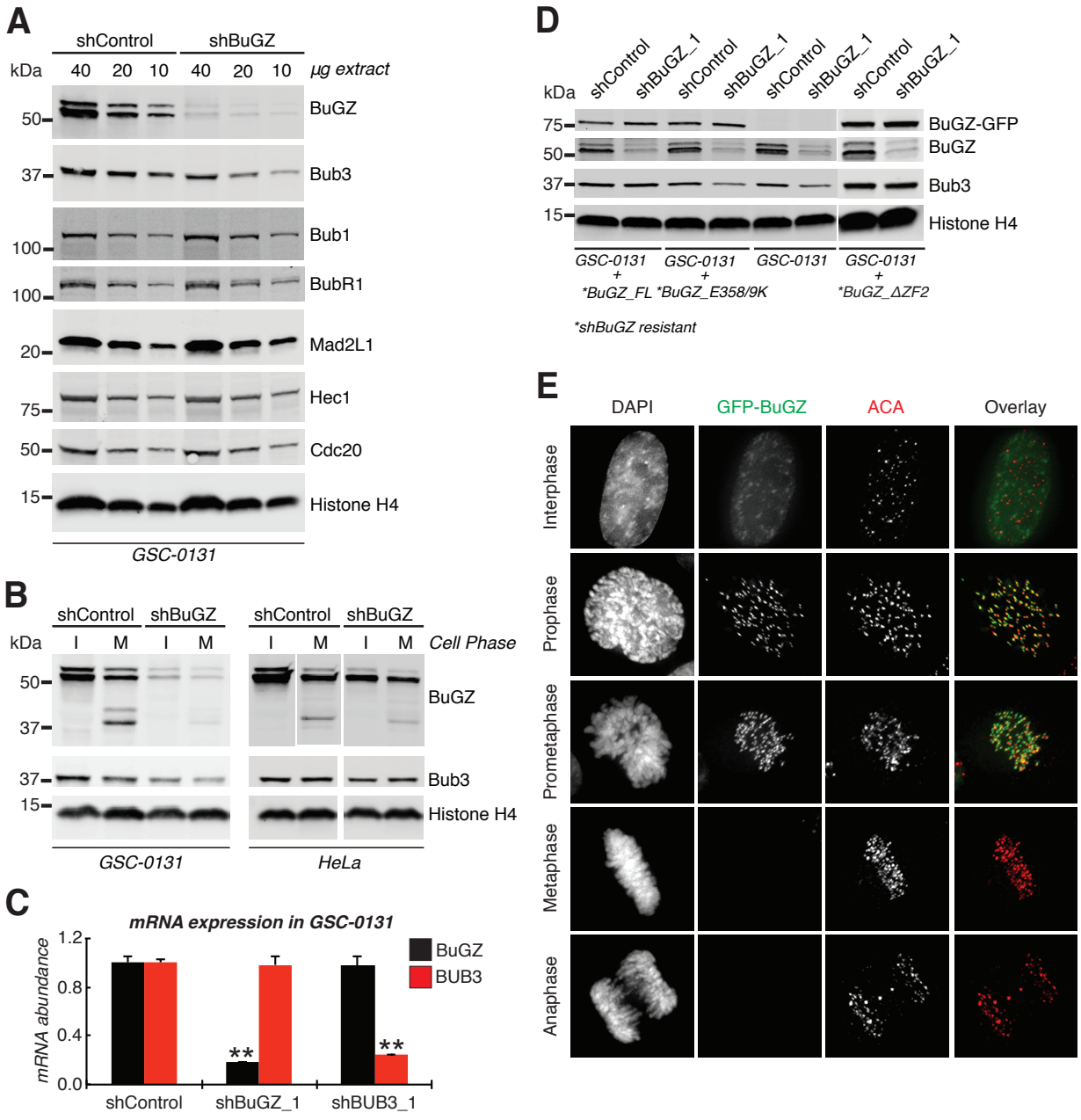

Figure 2.6. BuGZ stabilizes BUB3 expression and localizes to the kinetochore.

(A) BuGZ stabilizes BUB3 expression. Western blot analysis of GSC-0131 whole cell extracts infected with shControl or *shBuGZ* virus for antibodies to multiple KT-associated proteins and to the loading control anti-Histone H4.

(B) BuGZ stabilizes BUB3 expression in interphase and mitotic cells. Western blot analysis of GSC-0131 and HeLa interphase or mitotic cell extracts for anti-BuGZ, anti-BUB3, and loading control anti-Histone H4 antibodies. GSC-0131 cells were infected with shControl or *shBuGZ* virus and treated with the proteasome inhibitor MG-132 for 18.5 hours. HeLa cells were not treated with MG-132. Interphase and mitotic cells were collected by shake-off for both GSC-0131 and HeLa cells. *Mitotic extracts contain additional lower molecular weight species of BuGZ, which could represent a cleavage or degradation product.

(C) Knockdown of *BuGZ* does not alter *BUB3* mRNA levels and vice versa. Quantitative real time PCR was used to access *BuGZ* and *BUB3* mRNA expression after shRNA viral infection with shControl, *shBuGZ*, and *shBUB3*. (**Student t test, $p<0.01$, +SD).
(D) Expression of *BuGZ* in *BuGZ*-depleted GSCs rescues BUB3 expression, but *BuGZ*-GLEBS domain mutants (E358K E359K) do not. Western blot analysis of GSC-0131 cell extracts for anti-turboGFP, anti-BuGZ, anti-BUB3, and loading control anti-Histone H4 antibodies. GSC-0131 cells were first infected with *BuGZ* ΔZF2 (*shBuGZ*_1 targets the second zinc finger motif), *shBuGZ* resistant (denoted by *) full length (FL) *BuGZ*, or *shBuGZ* resistant *BuGZ* E358K E359K. Following selection, these cells were virally transduced with shControl or *shBuGZ*.
(E) BuGZ localizes to KTs in prophase and prometaphase but diminishes during metaphase. HeLa cells were transfected with GFP-*BuGZ* fusions and imaged for DAPI, GFP, and KTs (ACA). Representative images are shown.

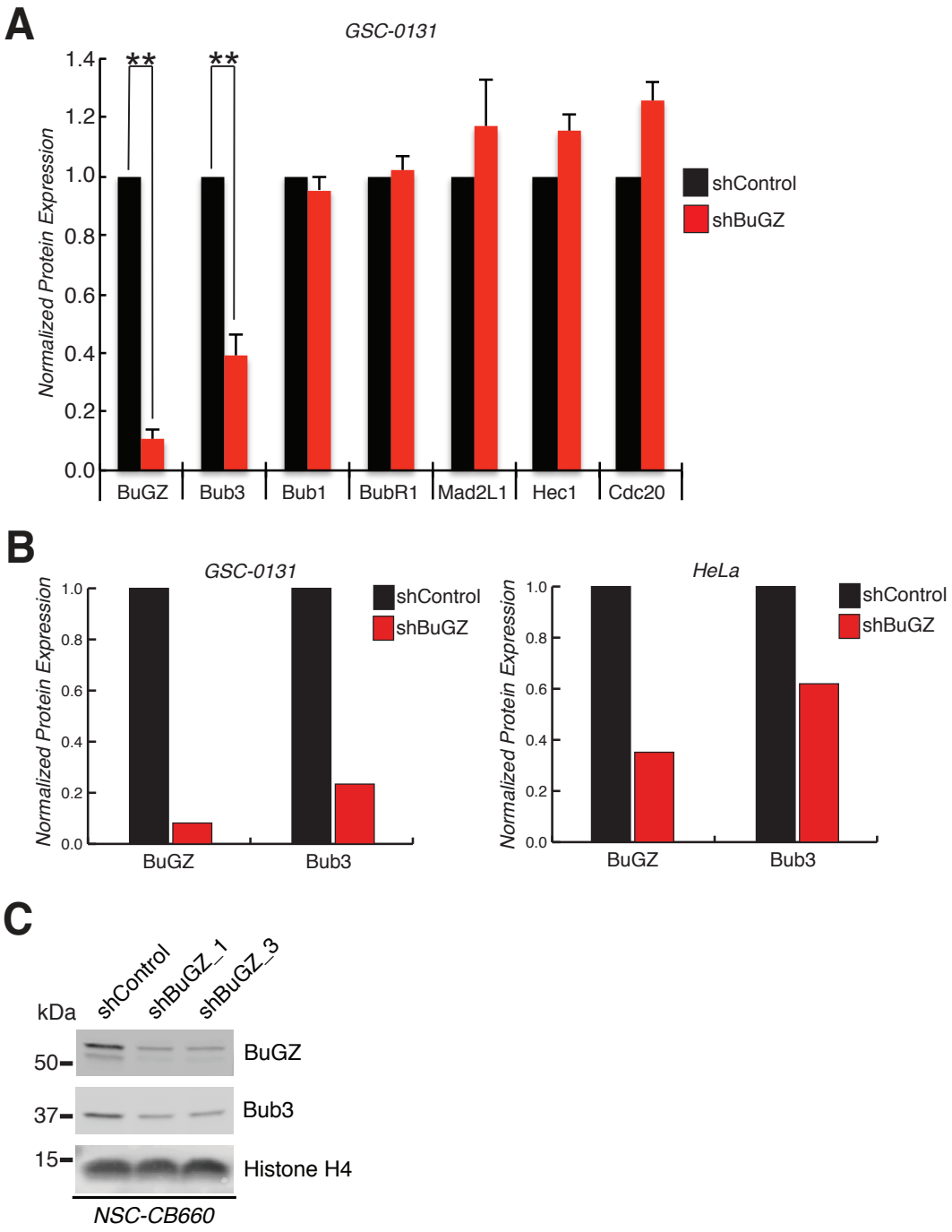

Figure 2.7. BuGZ stabilizes BUB3 expression in multiple cell types.
(A) Quantification of protein levels from Western blot shown in Figure 2.6A. Each lane was first normalized to its respective loading control anti-Histone H4 followed by normalization to its respective shControl. Average of the three protein extract dilutions for each shRNA were then calculated. (**Student t test, $p<0.01$, +SD).
(B) Quantification of protein levels from Western blot shown in Figure 2.6B.
(C) *BuGZ* knockdown in NSCs shows similar reduction in BUB3 protein levels. Western blot analysis of NSC-CB660 whole cell extracts 6 days after viral transduction with two independent *shBuGZ* viral clones to deplete *BuGZ* or shControl.

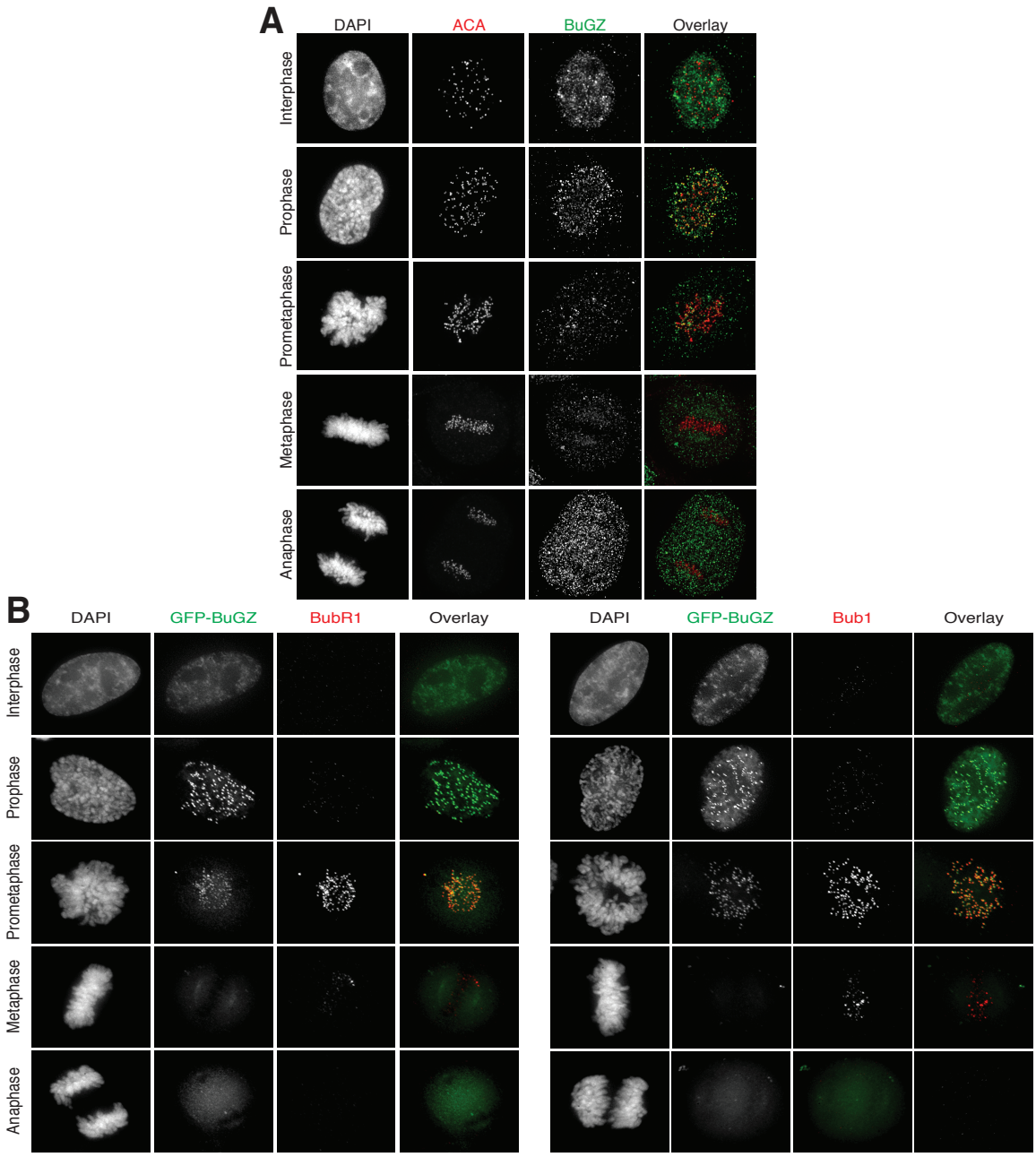

Figure 2.8. BuGZ localizes to the nucleus in interphase and to kinetochores prior to nuclear envelope breakdown, while BUBR1 and BUB1 localize to the kinetochore after BuGZ kinetochore localization in early mitosis.

(A) Immunofluorescent staining of BuGZ in HeLa cells. Consistent with observations using GFP-*BuGZ* fusion protein, BuGZ is primarily nuclear in interphase and localizes to kinetochores in prophase before nuclear envelope breakdown. Upon microtubule attachment at metaphase, BuGZ kinetochore levels drastically reduce.
(B) Immunofluorescent co-staining of BUB1 or BUBR1 with GFP-*BuGZ* through mitotic phases in HeLa cells. BuGZ concentrates at kinetochores prior to nuclear envelope breakdown and before significant levels of BUBR1 or BUB1 kinetochore localization. BuGZ is undetectable at metaphase and anaphase, while BUBR1 and BUB1 levels are low, but detectable. Figure by Jake Herman.

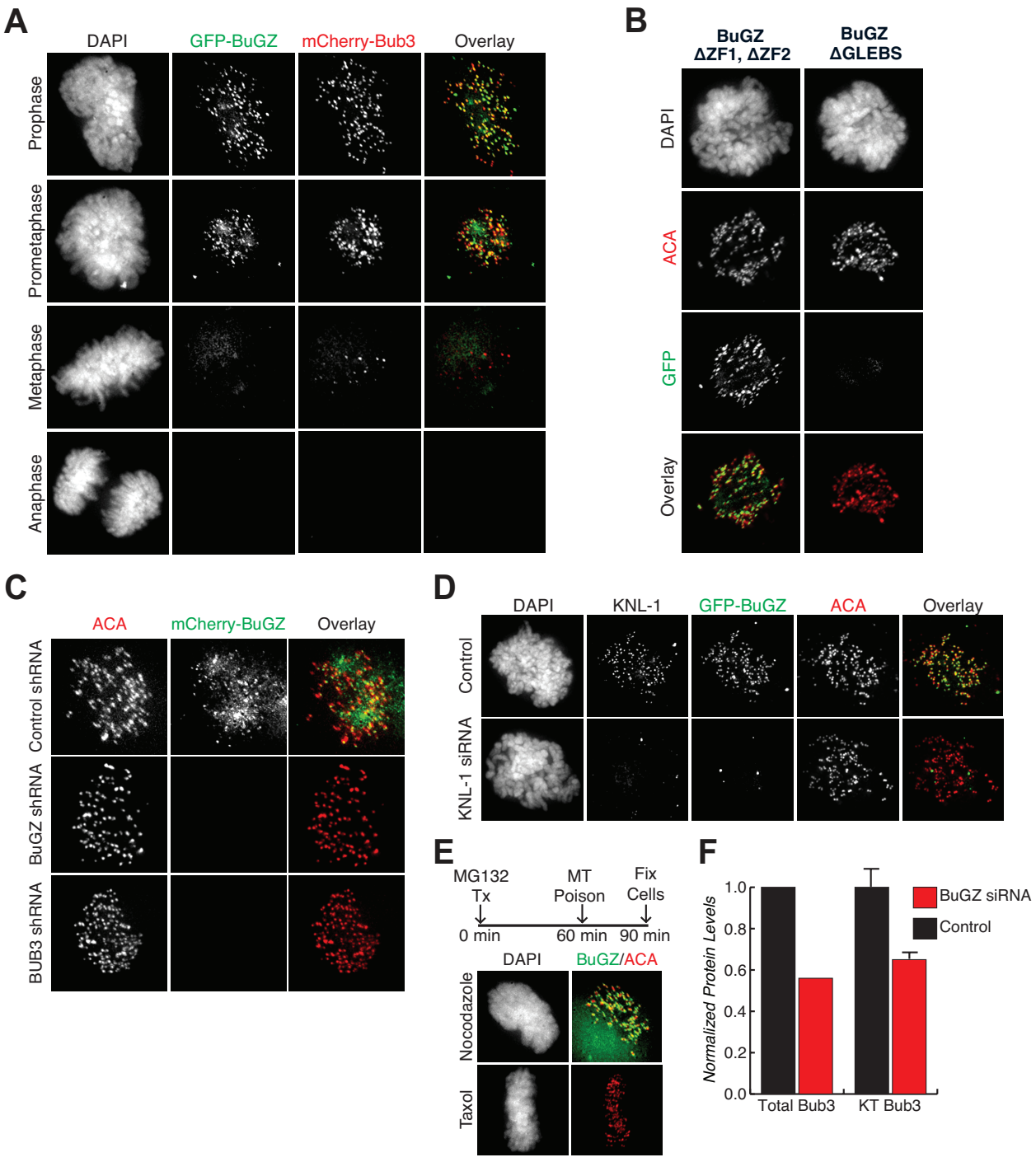

Figure 2.9. BuGZ co-localizes with BUB3 at KTs during early mitosis by virtue of its GLEBS domain and reduces BUB3 levels at KTs when inhibited.

(A) BuGZ and BUB3 co-localization in HeLa cells transfected with GFP-*BuGZ* and mCherry-*BUB3* expression constructs. BuGZ and BUB3 co-localize during prophase and prometaphase. Representative images shown.

(B) BuGZ localization in HeLa cells transfected with GFP-*BuGZ* ΔZF1, ΔZF2 or *BuGZ* ΔGLEBS mutants. BuGZ ΔZF1, ΔZF2 localizes to the KTs, while BuGZ ΔGLEBS does not. KTs are stained with anti-centromere antibody (ACA).

(C) BuGZ localization is BUB3-dependent. HeLa cells stably expressing *BuGZ*-mCherry were infected with shControl, *shBuGZ*, or *shBUB3*, selected, and stained with ACA.
(D) BuGZ KT localization requires KNL-1. HeLa cells stably expressing *BuGZ*-GFP were transfected with siControl or *siKNL-1* and stained with ACA.
(E) BuGZ KT binding is regulated by KT-MT attachment. GFP-*BuGZ* stable Hela cells were treated as shown with Nocodazole or Taxol and imaged.
(F) BUB3 total and KT associated protein decreases after *BuGZ* depletion. Normalized protein levels determined by western blot (left) and immunofluorescence (right). (N=2; error bars represent cellular deviation [control] and experimental deviation [*BuGZ* siRNA]). Figure by Jake Herman.

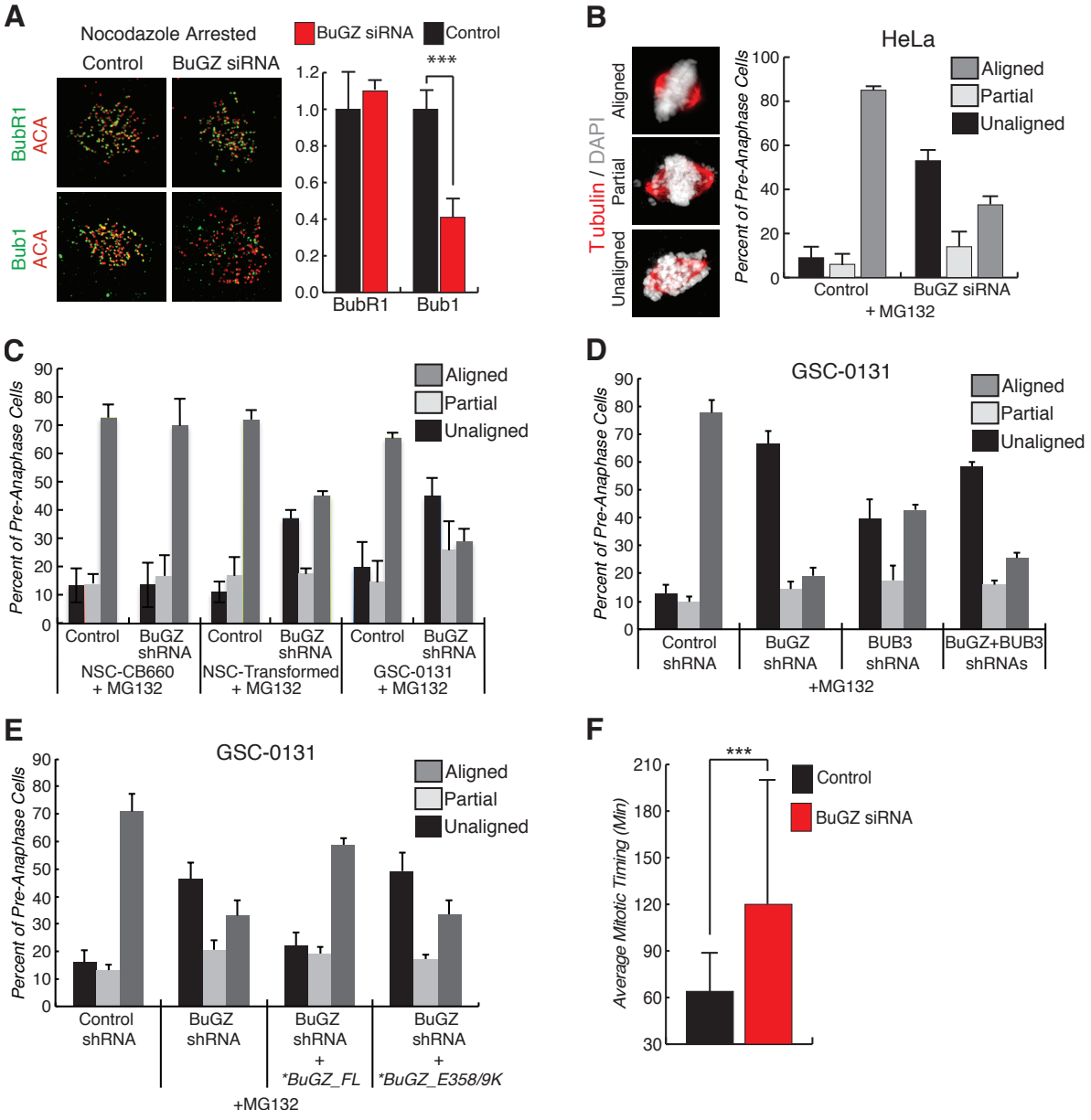

Figure 2.10. BuGZ activity is required for proper chromosome alignment.

(A) Immunofluorescence analysis of BUBR1 and BUB1 KT association. Representative images (left) and quantitative analysis (right) show *BuGZ* depletion does not alter BUBR1 levels, but BUB1 localization significantly reduces (student t test $p<0.001$). Both BUBR1 and BUB1 total protein levels are unaltered (Figure 2.6). (N=2; error bars represent cellular deviation [control] and experimental deviation [*BuGZ* siRNA]).

(B) *BuGZ* depletion causes chromosome alignment defects in HeLa cells. After MG132 treatment, 35% of *BuGZ* depleted cells align chromosomes compared to 85% of control cells. (>800 cells counted/condition, +SD).

(C) *BuGZ* depletion causes chromosome alignment defects in transformed NSC-CB660 and GSC-0131 cells, but not in non-transformed NSC-CB660 cells. After 2 hours of MG132 treatment, 70% of *BuGZ* depleted NSC-CB660 cells align chromosomes compared to 45% of *BuGZ* depleted transformed NSC-CB660 cells. (>395 cells counted/condition, +SD).

(D) In GSC-0131 cells, *BuGZ* and *BUB3* co-depletion causes chromosome alignment defects similar to *BuGZ* and *BUB3* depletion alone. After 2 hours of MG132 treatment, 26% of *BuGZ*/*BUB3* co-depleted GSC-0131 cells align

chromosomes compared to 19% of *BuGZ* depleted cells and 43% of *BUB3* depleted cells. (>535 cells counted/condition, +SD).

(E) Ectopic expression of wild type *BuGZ*, but not *BuGZ* GLEBS domain mutants (E358K E359K), rescues chromosome alignment defects in GSCs depleted for endogenous *BuGZ*. After two hours of MG132 treatment, 59% of *BuGZ* depleted GSCs expressing *shBuGZ* resistant (denoted by *) full length *BuGZ* display align chromosomes compared to 34% for the *BuGZ* allele containing mutations in the GLEBS domain. (>445 cells counted/condition; +SD).

(F) *BuGZ* depletion delays mitotic timing. HeLa cells expressing H2B-GFP fusion protein were imaged at five minutes intervals to determine time from nuclear envelope breakdown until anaphase onset. *BuGZ* depleted cells average mitotic timing was 120 minutes compared to 60 minutes in control cells. (***Mann-Whitney test $p<0.001$; $n>60$ cells/condition; +SD).

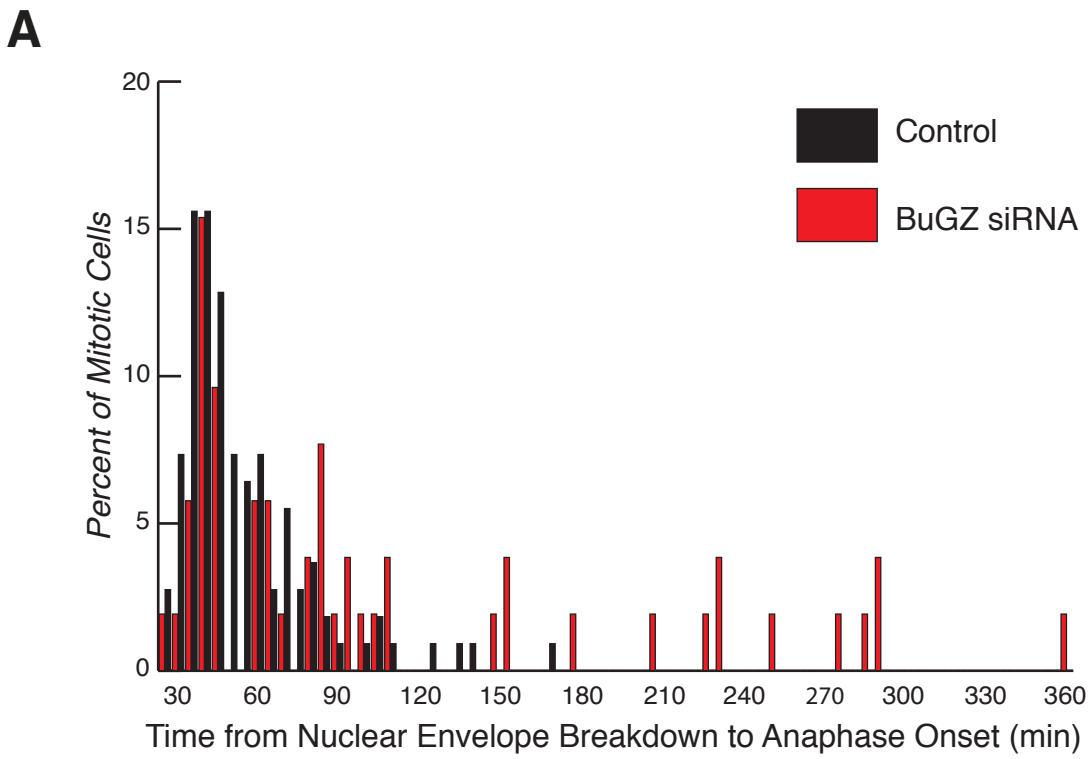

Figure 2.11. *BuGZ* depletion delays mitotic timing.
(A) HeLa cells expressing H2B-GFP fusion protein were imaged at five-minute intervals to determine time from nuclear envelope breakdown until anaphase onset. Control cells (black) transited mitosis within 60 minutes on average. *BuGZ* depletion causes a significant delay in most cells, resulting in a 120 minutes mitosis (Mann-Whitney test $p<0.001$). Averages summarized on right ($n>60$ cells/condition). Figure by Jake Herman.

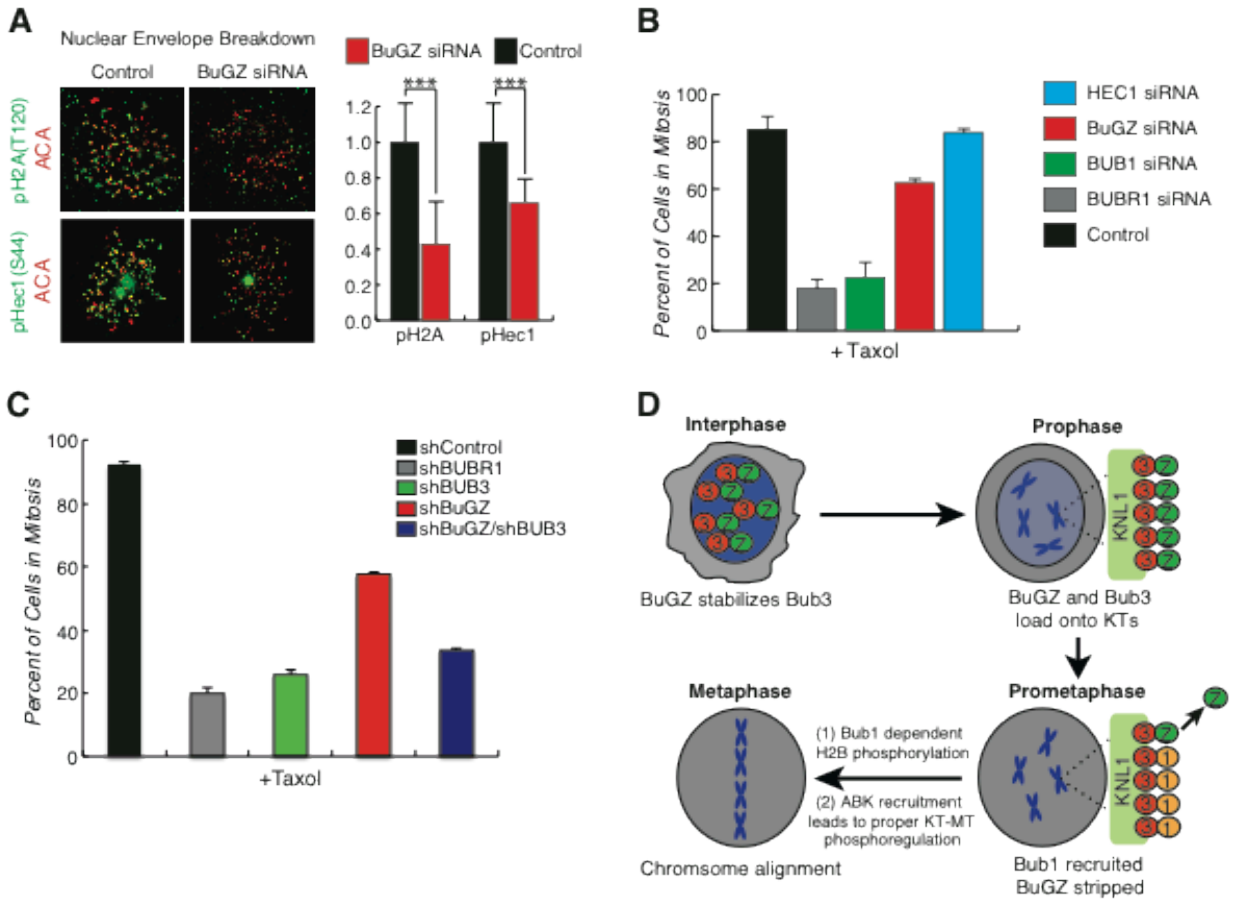

Figure 2.12. BuGZ activity is required for localization and activation of ABK, and possibly the spindle assembly checkpoint.

(A) Immunofluorescence analysis for kinase activity of BUB1 and Aurora B. Representative images (left) and quantitative analysis (right) show *BuGZ* depletion decreases phosphorylation of BUB1 and Aurora B substrates, H2A and HEC1 respectively. (***student t test $p<0.001$; N=2; error bars represent cellular deviation [control] and experimental deviation [*BuGZ* siRNA]).

(B) *BuGZ* depleted cells sustain a moderate mitotic arrest in microtubule poisons. A majority of control (black) and attachment factor *HEC1* (blue) depleted cells are mitotic after 24 hours in taxol. Depleting SAC proteins *BUBR1* (gray) and *BUB1* (green) causes premature mitotic exit. *BuGZ* depletion (red) causes an intermediate phenotype, suggesting cells establish a SAC response but cannot maintain it. (N=2; >1000 cells counted/condition; +SD).

(C) *BuGZ* and *BUB3* (blue) co-depleted cells do not sustain a checkpoint arrest. A majority of control (black) depleted cells are mitotic after 24 hours in taxol. Depleting SAC proteins *BUBR1* (gray) and *BUB3* (green) causes a premature mitotic exit, while *BuGZ* depletion (red) causes an intermediate phenotype. Thus, BuGZ induced arrests require checkpoint signaling. (N=3; >1000 cells counted/condition; +SD).

(D) Model of BuGZ function.

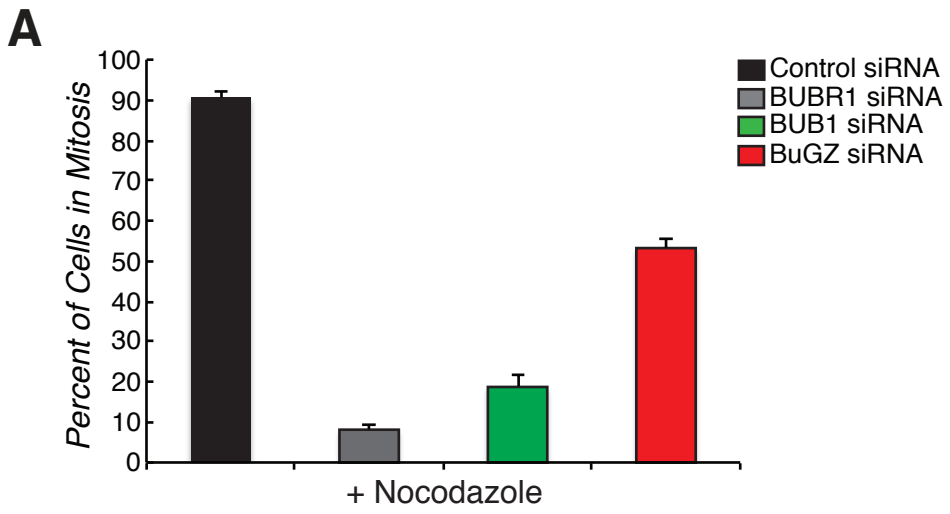

Figure 2.13. *BuGZ* depletion causes a weakened checkpoint arrest in response to MT poisons.

(A) Control cells (black) robustly arrest in mitosis after 24 hours in the microtubule depolymerizing drug, nocodazole. Depletion of checkpoint proteins *BUBR1* (gray) or *BUB1* (green) drastically decreases the number of cells arrested in mitosis. *BuGZ* depletion (red) results in a moderate phenotype suggesting functional, yet less robust SAC function. (N=1; >2,400 cells counted/condition; +SD). Figure by Jake Herman.

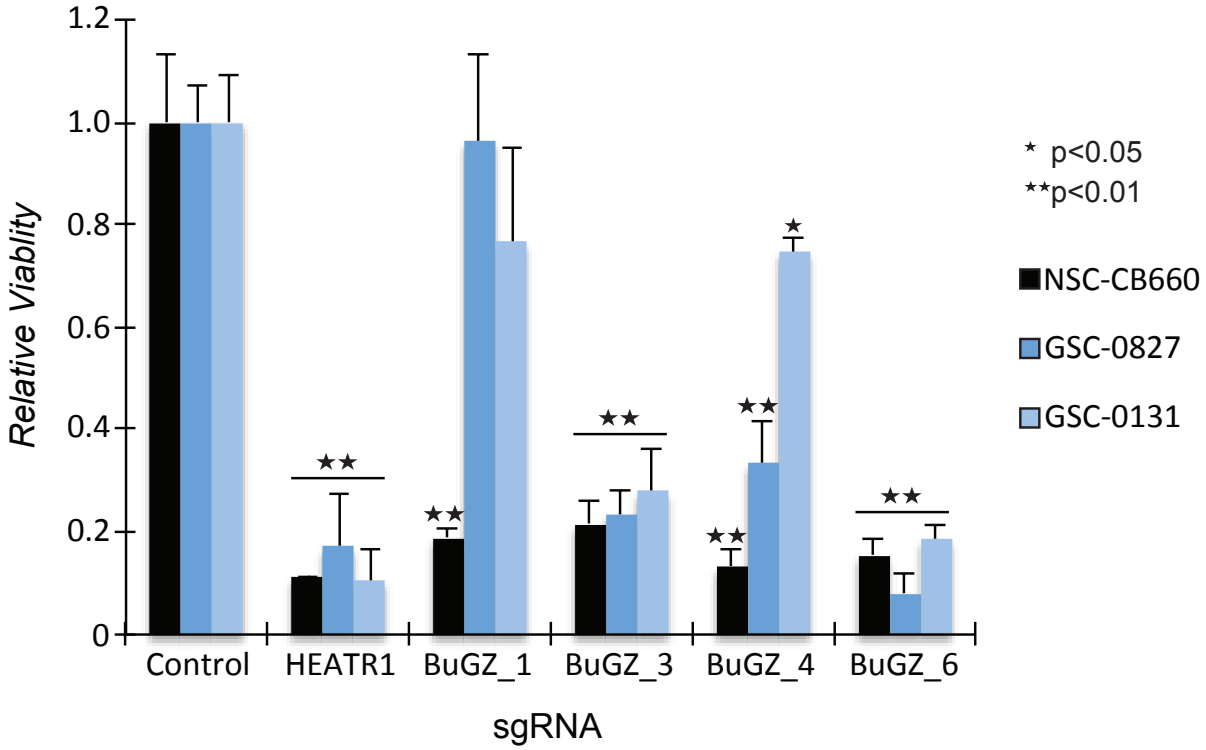

Figure 2.14. *BuGZ* is essential in both the human non-transformed NSCs and transformed GSCs.

Knockout of *BuGZ* using CRISPR-Cas9 technology causes a loss of viability. Cells were infected with lentiviruses expressing *BuGZ*, *HEATR1* or control sgRNAs, selected with puromycin, and plated into 96-well plates for outgrowth following 2 (NSC-CB660 and GSC-0131) or 3 (GSC-0827) days post-selection. After 12 days (NSC-CB660 and GSC-0131) or 13 days (GSC-0827) of outgrowth, cells were assayed for viability using CellTiter-Glo (Promega) or alamar blue. Knockout of *HEATR1* was used as a positive control for cell proliferation. . All viral clones were normalized to their respective shControl. (**Student t test, +SD).

Tables

BuGZ ortholog	Gene ID	Method	Reference
Homo Sapiens	7756	Co-fractionation, Y2H	(Havugimana et al., 2012[151]; Hegele et al., 2012[144]; Wang et al., 2011[152])
Drosophila melanogaster	35004	Y2B	(Giot et al., 2003[153])
Caenorhabditis elegans	178042	Y2H	(Li et al., 2004[154])
Arabidopsis thaliana	839984	Affinity capture-MS	(Van Leene et al., 2010[155])

Table 2.1. Evidence of BuGZ ortholog interaction with BUB3 from protein-protein interaction databases.
Multiple methods have detected the highly conserved BuGZ-BUB3 interaction. Y2H=Yeast-two-hybrid screen. MS=Mass spectrometry

Methods

Cell culture and drug treatment

GSC and NSC lines were grown in N2B27 neural basal media (StemCell Technologies) supplemented with EGF and FGF-2 (20ng/mL each) (Peprotech) on laminin (Sigma) coated polystyrene plates and passaged as described previously [42,60]. Specifically, cells were detached from their plates using Accutase (Millipore), centrifuged, and resuspended with the appropriate media every 3 to 4 days. 293T and HeLa cells (ATCC) were grown in 10% FBS/DMEM (Invitrogen). Cells were treated with 800nM or 10μM nocodazole (Sigma) for 24 hours and 1 hour incubations respectively. Taxol (Sigma) was used at 10μM for 24 hours, and MG132 (Tocris) was also used at a final concentration of 10μM. Live cell imaging was performed in Leibovitz's L-15 media (Invitrogen) supplemented with 10% FBS, 7 mM HEPES, pH 7.0 and 4.5 g/l glucose.

RNAi and lentiviral production

shRNAs were obtained from Open Biosystems (Huntsville, AL) in the pGIPZ lentiviral vector. For virus production, pGIPZ-shRNA plasmids were transfected with lipofectamine 2000 (Invitrogen) into 293T cells along with psPAX and pMD2.G packing plasmids to produce lentivirus. Following approximately 24 hours after transfection, neural stem cell expansion medium was added to replace the original 293T growth medium. Virus was harvested and filtered approximately 24 hours after media change and stored at -80˚C. GSCs and NSCs were infected at MOI <1 for all cell lines except for GSC-G166 and GSC-0827 (MOI >1). HeLa cells were infected at MOI<1 and MOI>1 with respect to the experiment in the presence of 8μg/mL of

polybrene. Cells were infected for 48 hours followed by selection with 1-4μg (depending on the target cell type) of puromycin for 2-4 days [42,156].

HeLa cells were transfected with *BuGZ, BUBR1, BUB1, and HEC1* siRNA (Qiagen) at a final concentration of 135mM using Oligofectamine (Invitrogen). *BuGZ* depleted cells were fixed 30 hours after siRNA treatment to determine phenotype and kinetochore localization. To determine escape from drug induced arrest, all cells were fixed 48 hours after siRNA treatment. Target sequences of siRNA are as follow: *BuGZ* (CAGTATGGTGGTCATCATCAA); *BUBR1* (ACGAGAATACCTAATATGTGA); *BUB1* (CAGCTTGTGATAAAGAGTCAA); *HEC1* (AACCCTGGGTCGTGTCAGGAA).

Growth assays

For short-term single clone validation assays, cells were infected with lentivirus containing a single shRNA or single sgRNA to the respective gene. Following selection, cells were harvested, counted (NucleoCounter, NBS) and plated in triplicate onto 96-well plates coated with laminin [42,60]. After 7 days under standard growth conditions with 0.5μg/mL of puromycin to maintain selection and prevent outgrowth of residual uninfected cells, cell proliferative rates were measured using Alamar blue reagent (Invitrogen) or CellTiter-Glo (Promega) according to manufacture instructions. Cells containing sgRNAs were not maintained under puromycin selection during the outgrowth assay. For analysis, shRNA and sgRNA containing samples were normalized to their respective shControl samples.

Western blotting

Cells were harvested following infection with their respective shRNA and selection, washed with PBS, and lysed with the modified RIPA buffer. Western blots were carried out using standard laboratory practices (www.cshprotocols.org), except cells were lysed in a modified RIPA buffer (150mM NaCl, 50mM Tris, pH 7.5, 2mM $MgCl_2$, 0.1% SDS, 2mM DDT, 0.4% deoxycholate, 0.4% Triton X-100, 1X complete protease inhibitor cocktail (complete Mini EDTA-free, Roche), and 1U/μL benzonase nuclease (Novagen)) at RT for 15 minutes [42,60,157]. Additionally, some cells were subjected to treatment with the protease inhibitor MG-132 (EMD Millipore) at 10μM for 18.5 hours following the infection/selection process. The shake-off method was also performed for HeLa cells to generate interphase and mitotic cells. However, HeLa cells were not treated with MG-132 due to the high mitotic index. After a shake-off, cells in suspension (mitotic cells) were harvested. Cells remaining attached to the culture plate were washed with PBS to remove the remaining mitotic cells in culture and detached (interphase/asynchronous cells). Attached cells were then washed with PBS and lysed using the modified RIPA buffer. Cell lysates were quantified using Perce 660nm protein assay reagent and identical amounts of proteins were loaded onto SDS-PAGE for western blot. Trans-Blot Turbo transfer system was used according to the manufacture instructions. Antibodies against ZNF207 (Novus, # NBP1-89550, 1:1000), ZNF207 (Thermo Scientific, # PA5-30641, 1:1,000), BUB3 (BD Transduction Laboratories, # 611730, 1:1,000), turboGFP (d) (Evrogen, # AB513), histone 4 (Abcam, # 17036-100, 1:2,000), BUB1 (Abcam, #548931:1,000), BUB1B (Cell Signaling, # 4116S, 1:500), MAD2L1 (D8A7) (Cell Signaling, # 4636, 1:1,000), HEC1 (Thermo Scientific, # MA1-23308, 1:500), and CDC20 (Cell Signaling, # 4823, 1:1,000) were used for these experiments. An Odyssey infrared imaging system was used to visualize blots (LI-COR) following the manufacturer instructions. For quantification, an ROI using the Odyssey software for each

shRNA cell lysate sample was acquired, normalized to a loading control (histone 4 or beta-actin (not shown)), and then normalized to the respective shControl.

Immunofluorescence

Cells were grown on sterile, acid washed coverslips in 35mm cell culture dishes. Cells were rinsed with PHEM (60mM PIPES, 25nM HEPES, 10mM EGTA, 4mM $MgSO_4$) and either immediately treated with 4% paraformaldehyde for 20 minutes at room temperature, or for phosphorylation specific antibodies, treated with lysis buffer (PHEM+1.0%Triton X-100) for 5 minutes at 37°C and then PFA fixed for 20 minutes at room temperature. Fixed cells were washed, blocked for 1 hour at room temperature in PHEM+10% boiled donkey serum (BDS). Primary antibodies were diluted in PHEM+5% BDS and incubated for 16 hours at 4°C. Coverslips were washed, then incubated with secondary antibodies conjugated to fluorescent dyes (Jackson ImmunoReserach Laboratories) again diluted in PHEM+5% BDS for 45 minutes at room temperature. Coverslips were washed, stained with 2 ng/mL 4',6-diamidino-2-phenylindole (DAPI) diluted in PHEM, and then mounted onto microscope slides in an anti-fade solution containing 90% glycerol and 0.5%*N*-propyl gallate.

Commercial antibodies used: Tubulin-DM1α (Sigma, #T9026, 1:300); CREST (Antibodies, Inc., #15-234-0001, 1:500); ZNF207/BuGZ (Thermo Scientific, #PA5-30641, 1:600); BUB1 (Abcam, #548931, 1:300); BUB3 (BD Transduction Laboratories, #611730, 1:1000); BUBR1 (Millipore, #3612, 1:1000); pH2A-T120 (Active Motif, #39391, 1:2000). HEC1-S44 phosphorylation specific antibody was generated and affinity purified by 21st Century Biochemicals as previously described [94].

Image acquisition and analysis

Fixed-cell images were acquired using a DeltaVision PersonalDV Imaging System (Applied Precision/GE) on a Photometrics CoolSnap HQ2 camera (Roper Scientific) and a 60x/1.42NA Planapochromat DIC oil immersion lens (Olympus). All immunofluorescence images were collected as z-stacks at 0.2 μm intervals. Kinetochore integrated pixel intensity values were measured on deconvolved images with SoftWorx software (Applied Precision) applying background correction.

Live cell imaging of control and *BuGZ* depleted cells was performed on the same microscope using an environmental chamber to maintain the stage at 37°C. Cells expressing a GFP-H2B fusion were imaged every 5 minutes for 12 hours on a single plane. Imaging of *BuGZ* depleted cells began 24 hours post siRNA treatment.

Transformed neural stem cells

Normal CB660 neural stems were simultaneously infected with retrovirus containing pbabe-*hTERT* + $TP53^{DD}$ (Addgene, Plasmid 11128), pbabe-*CyclinD1* + $CDK4^{R24C}$ (Addgene, Plasmid 11129), and pbabe-$c\text{-}MYC^{T58A}$ + $HRAS^{G12V}$ (Addgene, Plasmid 11130) for three consecutive rounds of infection [42]. After recovery, cells were selected with both neomycin for RAS and blasticidin for c-MYC respectively.

Generation of tagged *BuGZ* and *BUB3* ORFs and mutant *BuGZ* alleles

Human *ZNF207* (*BuGZ*) cDNA (full length) (# MHS1011-202826090) and *BUB3* open reading frame (ORF) was obtained from Open Biosystems (Thermo Scientific). pGIPZ vector containing

a non-silencing control hairpin (shControl) was cut with XbaI and NotI to remove the CMV promoter and turboGFP. The UCOE SFFV enhancer promoter complex, fluorescent proteins (mCherry and turboGFP), and ORFs were PCR amplified using Platinum Taq HI FI (Invitrogen) and primers designed to introduce 15bp overlap homology with adjoining components. PCR products were gel purified using the Zymoclean Gel DNA Recovery Kit (Zymo Research). Constructs were assembled using the In-Fusion cloning Kit and transformed into Stellar Competent Cells (Clontech). Clones were screen by restriction digest, capillary sequencing, and antibody staining of the respective protein. Mutant alleles of *BuGZ* were generated using the turboGFP *BuGZ* fusion construct and cutting with restriction enzymes BlpI and NotI to remove the *BuGZ* ORF. Two-part ORFs were generated by PCR with deletions engineered to occur at the overlap and cloned into the parental vector.

SSEA1+ outgrowth assays

Cells were infected with shControl and *shBuGZ* virus for 48 hours followed by selection with puromycin for 72 hours. Cells were detached from their respective plate, counted with a nucleocounter, and mixed with untreated cells. After mixing, cells were seeded to a 6-well tissue culture dish coated with laminin for further growth. After three days in culture, cells were harvested, counted, and seeded to a 6-well tissue culture dish coated with laminin for further growth. Cells used for flow analysis were then blocked with cold PBS containing 0.5% BSA for 15 minutes at 4˚C, followed by an one hour incubation with APC mouse anti human CD15 (SSEA1, BD Pharmingen, # 551376) or APC Mouse IgM, kappa Isotype control (BD Pharmingen, # 555585) at 4˚C on a shaker in the dark. Following two washes with cold PBS containing 0.5% BSA, cells were suspended with PBS containing 0.5% BSA and analyzed using

a FACS Canto flow cytometer (Becton Dickinson). Cells were analyzed at days 0, 3, 7, 14, and 21. Data analysis was performed using FlowJo (Three Star).

Limiting dilution assay

Cells were infected with shControl or *shBuGZ* virus for 48 hours followed by selection with puromycin for 72 hours (Day 0). Cells were detached from their respective plate, dissociated into single-cell suspensions, counted with a nucleocounter, and then plated into non-tissue culture treated 96-well plates not coated with laminin with various seeding densities (0.125-256 cells per well, 10 wells per seeding density). Cells were incubated at 37˚C for 3 weeks and fed with 10X EGF and FGF-2 neural stem cell expansion media every 3 to 4 days. At the time of quantification, each well was examined for the formation of tumor spheres.

Affinity purification

The human *ZNF207* ORF was acquired from the DNA Resource Core at Harvard Medical School (Boston, MA) and cloned into pcDNA5/FRT/TO-eGFP plasmid (a kind gift from AC Gingras) via Gateway® Cloning. Flp-In T-Rex cell lines harboring the GFP-*ZNF207* construct as previously described [158]. Expression was induced using 2μl/ml doxycycline (Sigma), and cells from 2x15cm plates were collected in duplicate. Cells were resuspended in 1X High Salt AFC buffer with protease inhibitors and phosphatase inhibitors and lysed using 3 consecutive freeze-thaw cycles and sonication (1 cycle; 8 times, 0.3s on, 0.7s off, amplitude 30%), followed by ultracentrifugation. An anti-GFP rabbit polyclonal antibody (Invitrogen, G10362) and Protein G magnetic beads (Invitrogen) were used for immunoprecipitation. Purified protein was eluted from beads using ammonium hydroxide, reduced using iodoacetamide (Sigma), alkylated using TCEP (Pierce), and then digested in-solution using Proteomics Grade Trypsin Singles (Sigma).

Peptide mixtures were then lyophilized by SpeedVac centrifugation and re-suspended using 1% FA (formic acid; Fluka).

Mass spectrometry

Mass spectrometry experiments were performed using an online EasyLC nanopump (Thermo) fitted to a hybrid LTQ-Velos-Orbitrap instrument (Thermo), a C18 pre-column (75um i.d. x 2.5 cm length), and an uLC analytical column (75um i.d. x 10 cm length). The mass spectrometer was run in data-dependent acquisition mode (16 MS/MS scans per MS scan at 60,000 resolution). Reverse phase chromatography was performed using a 95min gradient from water to acetonitrile, each containing 0.1% FA at a flow rate of 0.3 ul/min. The acquired spectra were searched by SEQUEST using the UniProt reference human proteome, and matched peptides were filtered using a 20ppm precursor ion threshold.

Immunoprecipitations

GSCs and NSCs were lysed following the infection/selection process. 293Ts were transfected using Lipofectamine 2000 (Invitrogen) and lysed 48 hours later. Cell lysates were extracted using the modified RIPA buffer supplemented with PhosStop phosphatase inhibitor cocktail (Roche), 10μM sodium fluoride (anti-phosphatase inhibitor), and 10μM sodium metavanadate. After 10 minutes of incubation on ice, cell lysates were harvested and rotated at 4˚C for 20 minutes. The extract was then spun and down and the supernatant was harvested. Antibodies used for immunoprecipitations were anti-turboGFP (Evrogen, 1:25) and anti-V5 (Sigma, #V8012, 1;25). Binding was performed for 3 hours at 4˚C on a rotator. Immunoprecipitates were captured on Protein A/G Plus Agarose beads (Santa Cruz, #2003) and incubated at 4˚C for 2.5 hours on a rotator. After a brief spin, the beads were washed three times with the supplemented

modified RIPA buffer. Following the washes, 3X SDS sample buffer (New England BioLabs, #B7709S) was added, gently mixed, boiled, and analyzed by SDS-PAGE followed by Western blotting.

qRT-PCR

Cells containing shRNAs were harvested following infection/selection process and total RNA from cells was extracted using TRIzol (Invitrogen) according to manufacture instructions. QuantiTect quantitative real-time PCR (qRT-PCR) primer sets and SYBR Green PCR Master Mix (Applied Biosystems) were used according to manufacture instructions with the ABI PRISM 7900 Sequence detection System (Genomics Resource, FHCRC). Ct values of the samples were normalized to beta-actin followed by the respective shControl. Relative transcript abundance was analyzed using the $2^{-\Delta\Delta Ct}$ method [156].

Xenotransplantation

0827 GSCs were infected with pGIPZ shRNA virus and selected for 3 days in puromycin (1μg/mL). Cells were then harvested using Accutase (Sigma), counted, resuspended in an appropriate volume of culture media, mixed 90% GIPZ plus 10% untreated cells (non-infected cells), and kept on ice prior to immediate transplantation (Hubert et al., 2013). NOD-scid IL2Rgammanull mice (Jackson Labs #005557) were sedated by inhalation of isoflourane. A small bore hole was made in the skull using a hand drill with a Meisinger #009 steel burr bit (Hager and Meisinger GmbH). $1x10^5$ cells were slowly injected by pipet into the right frontal cortex approximately 2mm rostral to Bregma, 2mm lateral and 3mm deep through a 0.2-10μL disposable sterile aerosol barrier tip (Fisher Scientific #02-707-30). The burr hole was closed using SURGIFOAM (Johnson & Johnson) and the skin rejoined using TISSUMEND II

(Veterinary Product Laboratories, Phoenix, AZ). 17 days after initial transplantation, mice were injected intravenously through the tail with 100μL of 10μM Chlorotoxin: indocyanine green (Blaze Bioscience, Seattle, WA) 4 hours prior to sacrifice by carbon dioxide inhalation. The brain and tumor were removed from the skull and imaged for GFP and indocyanine green fluorescence using the Xenogen IVIS Spectrum imaging system (Caliper Life Sciences).

Chapter 3-Comprehensive identification of glioblastoma multiforme therapeutic targets and growth suppressor genes using gene editing

Note: This work is currently under review.

Chad M. Toledo[1,2]*, Yu Ding[1]*, Pia Hoellerbauer[1,2], Ryan J. Davis[2,3], Ryan Basom[4], Emily J. Girard[3], Eunjee Lee[5], Philip Corrin[1], Traver Hart[6], Hamid Bolouri[1], Jerry Davison[4], Qing Zhang[4], Justin Hardcastle[1], Bruce J. Aronow[7], Jason Moffat[6], Ronald S. Cheung[1], Qi Lin[8], Xiao-Nan Li[8], Do-Hyun Nam[9], Jeongwu Lee[10], Steven M. Pollard[11], Jun Zhu[5], Jeffery J. Delrow[4], Bruce E. Clurman[1,3], James M. Olson[3#], and Patrick J. Paddison[1,2#]

[1]Human Biology Division, Fred Hutchinson Cancer Research Center, Seattle, WA 98109, USA; [2]Molecular and Cellular Biology Program, University of Washington, Seattle, WA 98195, USA; [3]Clinical Research Division, Fred Hutchinson Cancer Research Center, Seattle, WA 98109, USA; [4]Genomics Shared Resource, Fred Hutchinson Cancer Research Center, Seattle, WA 98109, USA; [5]Department of Genetics and Genomic Sciences, Icahn Institute of Genomics and Multiscale Biology, Icahn School of Medicine at Mount Sinai, New York, NY 10029, USA; [6]Donnelly Centre and Banting and Best Department of Medical Research, University of Toronto, Toronto, ON, Canada M5S 1A8; [7]Division of Biomedical Informatics, Cincinnati Children's Hospital Medical Center, Cincinnati, OH 45229; [8]Brain Tumor Program, Texas Children's Cancer Center, Department of Pediatrics, Baylor College of Medicine, Houston, TX 77030, USA; [9]Institute for Refractory Cancer Research, Samsung Medical Center, Seoul, Korea 135-710; [10]Department of Stem Cell Biology and Regenerative Medicine, Lerner Research Institute, Cleveland Clinic, Cleveland, OH 44192, USA; [11]Edinburgh CRUK Cancer Research Centre and MRC Centre for Regenerative Medicine, The University of Edinburgh, Edinburgh, UK EH16 4UU.

*These authors contributed equally.

[#] To whom correspondence should be addressed: paddison@fredhutch.org or jolson@fredhutch.org.

Key words: CRISPR-Cas9, gene editing, Glioblastoma multiforme, *PKMYT1*, Myt1, *CREBBP*, cancer therapeutics, tumor suppressor genes, functional genomics

Abstract

Glioblastoma multiforme (GBM) is the most aggressive and common form of brain cancer in adults[3,159]. Currently, effective treatment options do not exist for GBM patients [3-7]. To identify new therapeutic targets for GBM, we performed genome-wide CRISPR-Cas9 "knockout" (KO) screens in patient-derived GBM stem-like cells (GSCs)[10,12] and human neural stem cells (NSCs)[160], non-neoplastic tissue of origin controls. These screens revealed thousands of gene candidates acting to promote or limit expansion of GSCs and NSCs. *In vitro* and *in vivo* validation studies revealed several novel therapeutic targets, including the wee1-like kinase, *PKMYT1/Myt1*[161,162]. Mechanistic studies revealed that PKMYT1 acts redundantly with WEE1 to promote timely completion of mitosis in NSCs, but that this redundancy is lost in most GBM isolates and in NSCs harboring activated alleles of *EGFR* and *AKT1*. In addition to lethal genes, KOs promoting *in vitro* expansion of NSCs were also examined. For this category, we validated multiple genes, including: *ARID1A*, *ARID1B*, *CREBBP*, *EP300*, *NF2*, *PDCD10*, *PTPN14*, *TAOK1*, *TGFBR2*, and *TP53*, whose inhibition shortens NSC cell cycle transit times, causing dramatic growth advantages, and, in the case of *CREBBP* KO, dramatic deregulation of cell

cycle gene expression and precocious S-phase entry. Taken together, these results demonstrate the use of CRISPR-Cas9 gene editing to identify novel cancer therapeutic targets and growth suppressor genes in human GBM isolates and NSCs.

Introduction

One common concept in cancer research is the notion that genomic and molecular profiling of patient samples will enable the discovery of patient-tailored therapeutic strategies. However, it remains unclear whether analytic or computational approaches based solely on descriptive data sets are powerful enough to predict successful therapies. Alternative approaches are to directly identify molecular vulnerabilities in patient samples using functional genetic experimentation alone or in conjunction with analytical/computational approaches. The former has recently been achieved for GBM, where RNAi screens have been performed directly in patient-derived GSCs[42,43,57-60,163]. GSCs retain tumor-initiating potential and tumor-specific genetic and epigenetic signatures *in vitro*[10,12], under culture conditions that mimic the neural progenitor perivascular niche[164,165]. By performing control screens in fetal NSCs, which have similar expression profiles and developmental potential but are not transformed[10,12], candidate GSC-specific therapeutic targets can be identified[42,43,60]. However, because most targets identified by gene knockdown screens have essential activities even in non-transformed cells (see for example[166]), it remains unclear whether inhibitors of these targets would ultimately have better therapeutic windows than conventional cytotoxic chemotherapies.

With the emergence of CRISPR-Cas9 gene editing technology, functional genetic single-guide RNA (sgRNA) libraries now exist that are in theory capable of triggering biallelic insertion-deletion (indel) mutations in most genes in the human genome[126,167]. In 1987,

CRISPRs, clustered regularly interspaced short palindromic repeats, were first discovered in the genome of *Escherichia coli*[80]. It was later found that CRISPR and *cas* (CRISPR-associated) genes constitute the microbial adaptive immune system against foreign genetic elements, such as viruses and plasmids[80,128,168]. Three types of CRISPR systems have been identified across a wide range of bacterial and archaeal hosts[80,128,169]. Each system contains a CRISPR RNA array (crRNA), which consists of *cas* genes, noncoding RNAs, and a distinctive array or repetitive elements (direct repeats)[128]. The repetitive elements are interspaced by short variable sequences of 20 base pairs derived from exogenous DNA targets known as protospacers[80,128]. Each protospacer in CRISPR system II is always accompanied by a 3-basepair (5'-NGG) protospacer adjacent motif, which is also known as the PAM sequence[127,128].

CRISPR system II, which is derived from *Streptococcus pyogenes*, is typically utilized for genomic engineering in eukaryotic cells[80,128,129]. This CRISPR system requires a single gene, *Cas9,* to encode a dual, RNA-guided DNA endonuclease that uses a guide RNA to recognize its targeted DNA, and binds the targeted DNA through Watson-Crick base-pairing[80,127-129]. In addition, it requires the tracrRNA, trans-activating CRISPR RNA, which is comprised of bacterial trans-encoded small RNA with 24 nucleotides complementary to the repeat regions of precursor crRNA transcripts[80,170]. The tracrRNA directs the maturation of the precursor crRNA into discrete crRNA subunits by the activities of the widely conserved endogenous RNase III and Cas9[80,170]. Recently, the crRNA and the tracrRNA were engineered as a single guide (sgRNA) chimeric, which permitted the use of the CRISPR-Cas9 technology in mammalian cells[127,171].

Following successful lentiviral transduction and expression of CRISPR-Cas9, Cas9 binds to the guide RNA and undergoes a large conformational rearrangement[80]. Cas9 and the tracrRNA:crRNA duplex then seeks its targeted DNA, and Cas9 goes through another

conformation change upon association with the targeted double-stranded DNA (dsDNA)[80]. The PAM site is critical for Cas9 recognition and binding to its DNA target[80,127]. The interaction between the Cas9 complex and the dsDNA results in a formation of a R-loop, which permits RNA strand invasion and RNA-DNA hybrid formation[80,127]. Cas9 then mediates a double-stranded break 3 base pairs upstream from the PAM sequence by using its conserved HNH and RuvC nuclease domains[127,128]. The HNH nuclease domain of Cas9 cleaves the DNA strand that is complementary to the 20-nucelotide sequence of the crRNA, while the RuvC-like nuclease domain of Cas9 cleaves the DNA strand opposite of the complementary strand, resulting in a double-stranded break[80,127]. This double-stranded break can be repaired by one of the two major pathways for DNA repair: the error-prone nonhomologous end joining (NHEJ) or the high-fidelity homology-directed repair in mammalian cells[80,128,129]. In the absence of a repair template, the double stranded break is re-ligated by NHEJ, which results in indel mutations at the repair site[128,129]. The indel repair typically causes a coding frameshift, which can lead to a premature stop codon and the initiation of nonsense-mediated decay of the transcript; thus, the indel creates a homozygous "knockout" of the targeted gene and complete loss of protein function[128,129].

CRISPR-Cas9 technology has not been widely used for the identification of essential genes in mammals. Here, we applied a genome-wide CRISPR-Cas9 library screen to GSCs and NSCs in an attempt to identify GBM candidate therapeutic targets with large therapeutic windows, essential genes to both the GSCs and NSCs, and growth-limiting genes in NSCs. These screens revealed multiple GSC-sensitive hits, including the WEE1 homologous kinase *PKMYT1*[161,162,172]. *PKMYT1* was validated as a GSC-sensitive candidate therapeutic target in multiple studies, and *PKMYT1* is required in 80% of GSC patient isolates examined.

In mammalian cells, the decision to enter mitosis is regulated by the master regulator cyclin-dependent kinase 1 (CDK1), which is the only member of the CDK subfamily that is essential for driving cell cycle progression in human cells[64,173-175]. CDK1 does not exhibit kinase activity on its own, but becomes partially active once bound to a cyclin[176]. CDK1 predominantly binds to cyclin B, which begins to be transcribed during S-phase and reaches peak expression during late G2[173,176,177]. CDK1-cyclin B complexes are phosphorylated on residue T161 of CDK1's T-loop by CDK-activating kinase, which stabilizes the CDK1-cyclin B complex and induces conformational rearrangements that result in the activation of CDK1's kinase activity[176-178]. However, before the onset of mitosis, PKMYT1 and WEE1 kinases rapidly inactivate the CDK1-cyclin B complexes by phosphorylating residues T14 and Y15 of CDK1, which blocks ATP binding and hydrolysis[176-178]. The dephosphorylation of these inhibitory phosphorylation residues through positive and double negative feedback loops leads to the abrupt activation of the CDK1-cyclin B complexes at centrosomes, which initiates the onset of mitosis[173,176-178].

PKMYT1, WEE1, and cell division cycle 25 (CDC25) are key regulators of the DNA-damage checkpoint response that halt entry into mitosis in response to DNA damage or incomplete replication[176,178,179]. *PKMYT1 (aka Myt1)* encodes a dual specificity protein kinase homologous to the WEE1 kinase that localizes to the endoplasmic reticulum-Golgi complex and the cytoplasm[161,162,180,181]. PKMYT1 inhibits cytoplasmic cyclin B-CDK1 activity before the onset of mitosis by phosphorylating CDK1's amino-terminal ATP binding domain at T14 and to a lesser extent Y15[161,162,172]. WEE1, by contrast, is a nuclear protein that phosphorylates Y15 of both CDK1 and CDK2, but is incapable of phosphorylating T14[182,183].

During G2, CDK1 abruptly activates its kinase activity once cyclin B exceeds a threshold[176]. Activated CDK1-cyclin B complexes then phosphorylate and activate CDC25 dual-

specificity phosphatases, which can remove the inhibitory phosphorylations at T14 and Y15 of CDK1[176-178,184]. There are three isoforms of CDC25 in human cells: CDC25A, CDC25B, and CDC25C. CDC25A appears to be mainly nuclear, while CDC25C appears to be mainly cytoplasmic[177,184]. In HeLa cells, the dephosphorylation of Y15 of CDK1 is gradual and starts before nuclear envelope breakdown and continues through prometaphase, which involves a series of cellular changes that requires active CDK1-cyclin B complexes[176,185]. Active CDK1-cyclin B complexes also phosphorylate and negatively regulate PKMYT1 and WEE1 kinase activity[162,176,177]. The CDK1-dependent phosphorylation begins a cascade of events that promote WEE1 degradation and inhibition of PKMYT1 kinase activity[176,177,186]. The interplay between these feedback loops promotes mitotic entry and proper mitotic progression by timely regulating CDK1's inactivity and activity.

Drosophila homologs of *PKMYT1* and *WEE1* have been shown to act redundantly during fly development,[180] and loss of both proteins results in synthetic lethality[180]. Expression of mutant *Drosophila* homologs of *PKMYT1* or *WEE1* alone increases the number of mitotic cells in the imaginal wing discs, and expression of both *PKMYT1* and *WEE1* double mutants further increase the incidence of mitosis in imaginal wing discs[180]. In addition, *Drosophila* type I larval brain neuroblasts, which are well-characterized large neural stem cells, display extended mitotic transit times when CDK1-T14A-Y15F double mutants are express[187]. Together, these studies demonstrate that PKMYT1 and WEE1 can act redundantly to prevent mitosis and to regulate CDK1's activity, which is important for proper mitotic entry and progression in non-transformed cells.

On the contrary, *PKMYT1* and *WEE1* loss of function studies have shown functional differences between the two kinases during the cell cycle, which suggests that PKMYT1 and

WEE1 are not functionally redundant. For example, previous work in HeLa cells has demonstrated sole reliance on WEE1 for CDK1-Y15 inhibitory phosphorylation[188]. In addition, loss or depletion of *WEE1* in HeLa cells, mouse embryonic fibroblast, yeast, and *Drosophila* leads to premature mitotic entry before completion of DNA replication (i.e., mitotic catastrophe), which is not observed in *PKMYT1*-depleted HeLa cells or *Drosophila* expressing CDK1-T14A mutant that cannot be phosphorylated by PKMYT1[181,187-189]. Mitotic catastrophe due to the loss or depletion of *WEE1* then causes an increase in DNA damage and cell death[188,189]. On the other hand, *PKMYT1* knockdown fails to affect the timing of mitotic entry of HeLa cells despite dramatically reducing CDK1-T14 phosphorylation[181,188]. In addition, PKMYT1 phosphorylation of CDK1-T14 promotes the activating T161 phosphorylation of CDK1-cyclin B complexes by constitutively active CDK-activating kinase (CAK) in the nucleus; thus, the activating phosphorylation at CDK1-T161 is tightly coupled to the phosphorylation of T14 on CDK1, which is dependent on PKMYT1 expression, but not between CDK1-T161 and -Y15 phosphorylations[188]. This activity by PKMYT1 protects CDK1-cyclin B complexes from premature activation and ensures that it is only activated by dephosphorylation of CDC25[188]. Taken together, these results suggest that PKMYT1 and WEE1 do not act redundantly to phosphorylate CDK1-Y15 and to promote timely completion of mitosis by properly regulating CDK1's activity. However, many of these studies were conducted in transformed HeLa cells, and it is possible that PKMYT1 and WEE1 can act redundantly, in addition to their protein-specific functions, in non-transformed mammalian cells.

The abruptness of CDK1 activation is critical for mitotic initiation, mitotic progression, and synchronicity of subsequent events[185,190]. Equally as important is the inactivation of CDK1, which is important for proper mitotic exit and the establishment of G1[177,191-193]. Following

mitotic initiation, the activity of CDK1 continues to rise until prometaphase[185]. During the rise to CDK1's peak activity in prometaphase, CDK1's activity passes a necessary threshold that allows for the proper activation of the APC, which is required for the metaphase-anaphase transition and mitotic exit[185]. Interfering with the timing of CDK1's activation and/or inactivation during mitosis by expressing an uninhabitable CDK1 (CDK1-T14A-Y15F) or by loss or depletion of *WEE1*, which also promotes precious entry into mitosis, can result in elongated mitotic transit time (from nuclear envelope breakdown to cytokinesis), polyploidy, and cell death[187,189,190,193,194]. The elongated mitotic transit time is likely due to the activation of the spindle assembly checkpoint and/or the extended time the cells need in order to activate the anaphase-promoting complex (APC)-CDC20[190,193,195].

The inactivating counterpart to CDK1 is the APC, an E3 ubiquitin ligase that targets cyclin B and other mitotic proteins to promote entry into anaphase[64,177,193]. APC-induced proteolysis can also contribute to SAC inactivation[64]. APC activation is coupled to the dynamics of CDK1 activation, as amplification of active CDK1-cyclin B complexes is critical to ensure that APC is stimulated properly[192,193]. During early mitosis, CDK1-cyclin B complexes activate the first active APC complex, APC-CDC20, which degrades substrates such as cyclin B and securin; and thus, APC inactivates its activator, CDK1[193,195]. As CDK1 activity diminishes in late mitosis, CDH1 then replaces CDC20[193]. Upon dephosphorylation, CDH1 associates with APC, and APC-CDH1 ubiquitylates substrates that include: CDC20, Polo-like kinase 1 (PLK1), Aurora A kinase, and Aurora B kinase (ABK)[193]. Interestingly, expression of the uninhibitable CDK1 (CDK1-T14A-Y15F) in HeLa cells, which activates the SAC, prevents the complete degradation of these mitotic proteins at the end of mitosis due to incomplete activation of APC-CDH1[193,195]. This yields G1 daughter cells that undergo premature S-phase and early mitotic

events[193,195]. In somatic cells, APC-CDH1 complexes remain active until CDH1 is degraded in late G1[193]. Taken together, APC-CDH1 activity completely resets new G1 cells from their prior mitotic state and prevents mitotic catastrophe in subsequent cell cycles[193].

In addition, the normal degradation of WEE1 during mitosis depends on proper activation and function of APC, which then leads to the degradation of mitotic regulators and full restoration of cells to an interphase state[177,193]. Interestingly, WEE1 also interacts with the co-activators of the activated APC complex, CDC20 and CDH1, but *WEE1* loss does not affect formation of the APC complex[194]. However, *WEE1* loss does increase the degradation of key mitotic proteins, such as cyclin B, ABK, PLK1, and securin in both asynchronous and mitotic synchronized MEFs[194]. The degradation of these mitotic proteins can be attributed to an increase in APC activity[194]. Therefore, the untimely expression or depletion of WEE1 prior to mitosis can disrupt the relationship between the dynamics of CDK1's activation, APC's activation, and CDK1's inactivation[193,194]. As cells exit mitosis and transition to G1, the down regulation of CDK1's activity activates PKMTY1 kinase and inhibits CDC25 phosphatase[191]. This returns CDK1 to an inactive state by the addition of inhibitory phosphorylations[191].

Collectively, PKMYT1 and WEE1 prevent mitosis by regulating CDK1's activity[176-178], and loss or depletion of *WEE1*, but not *PKMYT1*, causes precious entry into mitosis[181,187-189], which likely then contributes to the disruption of subsequent mitotic events and the timely completion of mitosis[190,193,194]. Interestingly, loss or depletion of *WEE1*, and presumably *PKMYT1*, leads to extended mitotic transit times[187,189,190,194]. In addition to entering mitosis prematurely, these observed elongated mitotic transit times are also likely due to alterations in the abruptness of CDK1's activation and continual increase in activity through prometaphase, which then disrupts the activation of APC and subsequent inactivation of CDK1[177,185,190-195].

Nonetheless, WEE1 and/or PKMYT1 may also have an additional functional role(s) during mitosis that is required for timely completion of mitosis. For example, PKMYT1 has been shown to be essential for Golgi and endoplasmic reticulum assembly during mitotic exit[181].

Validation studies of CRISPR screens results revealed that *PKMYT1* is essential in transformed human GSCs, but dispensable in non-transformed human NSCs. Here, I investigated whether PKMYT1 and WEE1 have redundant functions in human non-transformed NSCs and transformed GSCs, and determined the oncogenic alterations in GSCs that can lead to the requirement for *PKMYT1*. I demonstrated that PKMYT1 acts redundantly with WEE1 in order to phosphorylate CDK1-Y15 in NSCs and to promote timely completion of mitosis. However, the redundancy between PKMYT1 and WEE1 is lost in GSCs and genetically altered NSCs expressing constitutively active *EGFR* and *AKT1*. I also examined and identified multiple growth-limiting genes that promote the expansion of NSCs upon knockout that include: *CREBBP*, *EP300*, *ARID1A*, *ARID1B*, and *TP53*. For this gene category, I illustrated that inhibition of these growth-limiting genes shortens NSCs' cell cycle transit time, and in the case of *CREBBP*, results in precocious entry into S-phase.

Results

Genome-wide CRISPR-Cas9 screens in human GSCs and NSCs

We first examined the efficacy of delivering a CRISPR-Cas9 targeting system by lentiviral (LV) transduction. Consistent with previous reports[16], an all-in-one LV-sgRNA:Cas9 platform system was highly effective at targeting reporter and endogenous genes in human GSCs and NSC isolates (Figure 3.1), including: randomly integrated copies of *EGFP* (>85%), a non-essential endogenous gene, *TP53*, assayed by western blot, and an essential gene, *MCM2*[196],

assayed by viability of *in vitro* expanded cells. In each case, we were able to observe profound reduction in target gene activity in GSCs and NSCs. Importantly, peak suppression occurred 10-14 days post-infection and non-targeting sgRNA controls had no effect on cell viability.

Given these successful demonstrations of gene editing, we next performed genome-wide screens using two adult GSC isolates, 0131 and 0827[11], and two control NSC lines, CB660[20] and U5 (Figure 3.2A). These GSC isolates best resemble mesenchymal and proneural GBM subtypes, respectively (Figure 3.3), two subtypes accounting for over half of adult GBM cases[28]. These isolates also harbor characteristic gene and pathway alterations commonly observed in GBM tumors[23], including alterations in: *EGFR*, *NF1*, *MDM2/4*, *PI3KCA*, *PTEN*, *RB1*, *TERT*, and/or *TP53* (Figures 3.2A and 3.3).

The screens were performed using a "shot gun" approach where GSCs and NSCs were transduced with a LV pool containing a human CRISPR-Cas9 library composed of 64,751 unique sgRNAs targeting 18,080 genes[16] and out grown in self-renewal conditions for ~3 weeks (see Methods for details). The pool library was maintained at 500-fold representation during the outgrowth for each biological screen replicate (n=2 per isolate). For the primary screen readout, we deep sequenced library sgRNAs from transduced cell populations before and after outgrowth, and then used edgeR (empirical analysis of digital gene expression in R)[197] to assess changes in individual sgRNA representation (see Methods for details), which identified 99.8% of all sgRNAs in the pool. Based on normalized read counts, each screen replicate tightly clustered at Day 0 and displayed cell type-specific differences after expansion (Figure 3.2B). EdgeR analysis revealed thousands of significantly scoring sgRNAs for each screen, representing both candidate essential and growth limiting genes (Figure 3.2C).

To assess screen performance, we employed a Bayesian classifier that uses predetermined essential and non-essential gene training sets to help determine functional genetic screen quality[198](Figure 3.4). This analysis allowed independent scoring of essential genes in each isolate, supporting observations reported below for edgeR analysis, including total number of essential genes predicted for each screen and GSC-sensitive screen hits (Figures 3.4 and 3.5). Importantly, using hypergeometric testing, we did not observe enrichment of GSC screen hits at specific genome addresses; nor did we observe enrichment for genes contained within sites of GSC-specific CNV (copy number variation) among screen hits (data not shown). This suggests that CNV differences in GSCs were not a major factor affecting screen outcomes.

Gene set enrichment analysis (GSEA) for each screen identified core cellular processes, including: translation, ribonucleoprotein complex biogenesis and assembly, RNA splicing, RNA processing, mRNA processing, and DNA replication (Figures 3.2D and 3.6). This indicated that the screens were effective at revealing essential gene targets, which is consistent with previous use of this library[16]. Interestingly, each screen was enriched for genes involved in cerebrum and central nervous system development, suggesting that each of the isolates retains the function of brain-specific gene networks (Figure 3.2E). Closer examination of these hits revealed genes with critical roles in regulating asymmetric and symmetric divisions of neural progenitors during cortical development (Figure 3.2F)[199], indicating that brain tumor cells likely require their function to maintain symmetrical self-renewal divisions during *in vitro* expansion. Interestingly, among hits specifically enriched in NSCs screens, but not GSCs, were sgRNAs belonging to a network of citric acid cycle and respiratory electron transport genes (Figure 3.7), and also the Fanconi anemia pathway gene network (Figures 3.2F and 3.7), which is required to suppress apoptosis in mouse neural progenitors[199]. The former is consistent with the notion that GBM

cells experience the Warburg effect where metabolism shifts from oxidative phosphorylation to lactate production[200]. Follow-up studies revealed that the NSCs and GSCs are not deficient in any Fanconi anemia proteins upstream of FANCI/D2 ubiquitination (data not shown).

We also observed GSC-specific differences in how sgRNAs affecting TP53 function and NF2/Merlin scored. NSCs and GSC-0827s harbor *TP53*^{wt}, while GSC-0131 cells have a homozygous *TP53*^{V147D} mutation of unknown function. In each *TP53*^{wt} isolate, sgRNAs targeting *MDM2* and *MDM4*, which destabilize TP53 and prevent inappropriate TP53 activation[201], were lost during the screening procedure. However, in GSC-0131 *TP53*^{V147D} cells, these sgRNAs had no effect, consistent with the bypass of MDM2 and MDM4 function for viability (Figure 3.2G). By contrast, sgRNAs targeting *TP53* were enriched in *TP53*^{wt} isolates, indicating a growth advantage, but lost in GSC-0131 cells, possibly indicating a reliance on mutant TP53 function (Figure 3.2G).

The tumor suppressor NF2/Merlin inhibits multiple signaling cascades, including membrane receptor, PI3K, and Hippo pathways[202]. Previous work has established that NF2 function is either inhibited or bypassed in GBM[202]. Consistent with both notions, *NF2* sgRNAs were dramatically enriched in outgrown NSCs (characterized below), but not in either GSC isolate, which interestingly includes loss of *NF2* sgRNAs in the *NF1* mutant GSC-0131 cells (Figure 3.2H). This suggests that NF2 function does not limit the growth of these GSCs.

Validation of essential and GSC-sensitive genes *in vitro* and *in vivo*

To validate lethal screen hits, we created a retest pool consisting of 7 essential genes and 51 GSC-sensitive genes picked essentially at random from edgeR analysis (3-4 sgRNAs per gene) comparing GSCs to NSCs sgRNAs with logFC<-1 (Figure 3.8A and Table 3.1). We first

examined performance of individual sgRNAs from the pool in *in vitro* growth assays in NSC-CB660, GSC-0131, and GSC-0827 cells, testing 47 individual sgRNAs (~2 sgRNAs per gene) (Figures 3.8B, 3.9, & Table 3.2). Of the 47 sgRNAs tested, 27 (57%) scored in a manner consistent with the initial screen, which included *PKMYT1*, a candidate GSC-sensitive gene, and *HEATR1*, a candidate top scoring essential gene that is involved in transcription of ribosomal genes (rDNA) by RNA polymerase I and pre-rRNA processing[130] (Figures 3.8B and 3.9).

Next, we performed parallel screens with the full retest pool both *in vitro* in GSCs and NSCs and *in vivo* in brain tumors derived from GSC-0131 and GSC-0827 cells (Figure 3.8B). These approaches again used sgRNA-seq of a day 0 population versus populations after 3 weeks of outgrowth *in vitro* or post-tumor formation *in vivo* as the readout. These approaches yielded 17 genes (7 essential and 10 GSC-sensitive) that retested prominently both *in vitro* and *in vivo* (Figure 3.8C and Table 3.2). However, GSC-0827 cells had very few of the original hits retest *in vivo* (Table 3.2), possibly indicating how differently or variably GSC-derived tumor cells can behave *in vivo*. Nonetheless, both *in vitro* and *in vivo* retests yielded *PKMYT1* as the top GSC-sensitive gene. Other hits consistent with original screen results included: *FBXO42* (GSC 0827-sensitive), *HDAC2* (GSC 0827-sensitive), and *TFAP2C* (GSC 0131-sensitive), among others (Figure 3.8C).

Since the CRISPR-Cas9 screens produced results consistent with identification of GSC-sensitive genes, we also compared the results to previously performed genome-wide shRNA screens conducted in NSC-CB660, GSC-0131, and GSC-0827 cells in identical outgrowth conditions, which also produced GSC-specific sensitive hits. The overlap between the screens was relatively low for the total number of lethal genes (only 928) and also GSCs-sensitive hits (65 total) (Figure 3.10). Nevertheless, there was a greater number of total "essential hits" in

sgRNA screens predicted to be lethal to all isolates compared to shRNA screens (769 versus 95) (Figure 3.10), which is consistent with CRISPR-Cas9 screens preferentially identifying essential genes. Interestingly, there was convergence of GSC-sensitive hits from both sgRNA and shRNA screens on several networks and pathways, including: pre-mRNA processing/splicing processes, which includes genes previously reported as GSC-sensitive involved in 3' splice-site recognition[42]; control of the G2/M transition, including two key negative regulators of cyclin B-CDK1 activity, *PKMYT1*[161,162] and *WEE1*[182]; DNA damage checkpoint, including *ATRIP*, *MDC1*, and *CLSPN*; the *PAF1* transcriptional regulatory complex[203]; members of the *COP9* signalosome complex[204]; and the *LKB1/STRADA/MO25* kinase complex, with one down stream substrate, *SIK3*[205] (Figures 3.8D and 3.10.). Importantly, several nodes among these complexes, including *PKMYT1* and *CAB39*, were validated in the course of the sgRNA retests (Figure 3.8C). Taken together, the results suggest that these pathways and complexes cross validate between the two technology platforms as GBM-sensitive. Figure 3.8D also shows networks only arising from sgRNA screens for *SREBF2/SREBP* dependent regulation of cholesterol biosynthesis, and two genes that participate in bidirectional membrane trafficking between the ER and Golgi (Uniprot), all of which are candidate GSC-0131 sensitive hits with at least one node retesting.

To further evaluate retesting sgRNA screen hits, we next examined targeting of *PKMYT1*, *FBXO42, HDAC2, TFAP2C* and *HEATR1*, as well as two control sgRNAs, in 10 different GSC isolates along with the non-transformed control NSCs using *in vitro* viability assays (Figure 3.8E and Table 3.3). The results revealed that *PKMYT1* was required for viability in 8 of the 10 isolates examined, while *HDAC2* and *TFAP2C* requirement appeared more specific to GSC-0827 and GSC-0131 cells, respectively. However, targeting of *FBXO42*, which can promote ubiquitination and degradation of TP53[206], showed profound sensitivity in both the GSC-0827

and GSC-G166 isolates (Figure 3.8E and Table 3.3). This likely indicates that patient-specific genetic or epigenetic alterations drive differential requirement for these genes. In contrast, *HEATR1* sgRNAs were lethal to all isolates examined (Figure 3.8E and Table 3.3), demonstrating that the differences in GSC-specific requirement for the other genes are not technical artifacts.

Molecular and phenotypic analysis of *PKMYT1* depletion

Since *PKMYT1* emerged as a robust GSC-sensitive hit both *in vivo* and *in vitro* among our retests, we wished to further validate it as a candidate therapeutic target for GBM. *PKMYT1 (aka Myt1)* encodes a dual specificity protein kinase homologous to WEE1 that localizes to the endoplasmic reticulum-Golgi complex, and inhibits cytoplasmic cyclin B-CDK1 activity before the onset of mitosis by phosphorylating CDK1's ATP binding domain at T14 and to a lesser extent Y15[161,162]. WEE1, by contrast, phosphorylates Y15 of both CDK1 and CDK2, but is incapable of phosphorylating T14[182]. *Drosophila* homologs of *PKMYT1* and *WEE1* have been shown to act redundantly during fly development[180]. However, loss of function experiments in human cells, which have been performed mainly in HeLa cells, suggest that human PKMYT1 and WEE1 are not functionally redundant. For example, knockdown of *WEE1* in HeLa cells induces loss of Y15 phosphorylation, premature entry into mitosis before completion of DNA replication (i.e., mitotic catastrophe), and apoptosis[181,187-189]. By contrast, *PKMYT1* knockdown fails to affect the timing of mitotic entry and exit of HeLa cells despite dramatically reducing CDK1-T14 phosphorylation[181,188]. Nonetheless, *WEE1* did score as a GSC-sensitive hit in both GSC-0131 and GSC-0827 cells in our shRNA screens (Figure 3.8D). Given these results, we

were interested to determine how PKMYT1 and WEE1 might specifically sustain the viability of GSCs and whether they have redundant functions in NSCs.

We began by examining the effects of *PKMYT1* and *WEE1* inhibition on CDK1/2-T14 and -Y15 phosphorylation in our NSC isolates (Figure 3.11A), which permit KO of *PKMYT1* without significant loss of viability (Figure 3.8C and E). In NSC-CB660 cells, we observed that *PKMYT1* KO results in dramatic reduction of PKMYT1 protein and CDK1-T14 phosphorylation with little or no effect on CDK1/2-Y15, consistent with previous studies. However, we find that PKMYT1 does in fact act redundantly with WEE1 to phosphorylate CDK1-Y15 in our NSCs. Western blot analysis (Figures 3.11A and 3.11B) clearly shows that PKMYT1 activity sustains CDK1-Y15, but not CDK2-Y15, phosphorylation in the presence of a potent and specific WEE1 inhibitor (MK1775) (Figures 3.11A and 3.11B). Intriguingly, in GSC-0131 cells, a similar trend is observed; albeit, there was a partial reduction of CDK1-Y15 phosphorylation after *PKMYT1* KO or WEE1 inhibition alone (Figure 3.12). Moreover, western blot analysis of GSC-0131s indicates that WEE1 may be the dominant CDK1-Y15 kinase in GSCs, as there was a larger decrease in CDK1-Y15 inhibitory phosphorylation after WEE1 inhibition alone compared to *PKMYT1* KO alone (Figure 3.12). Taken together, these results suggest some loss of redundancy in the GSCs.

To investigate these effects phenotypically, we used time-lapse microscopy to measure mitotic transit times (MTT) (from nuclear envelop break down to successful completion of cytokinesis). In *Drosophila*, loss of *myt1* and *wee1* dramatically increases the mitotic index of imaginal wing disc cells[180] and a similar phenotype is observed in HeLa cells overexpressing CDK1-T14A-Y15F, which cannot be inhibited by PKMYT1 or WEE1 activity[207]. We reasoned that this is likely due to the activation of the spindle assembly checkpoint (SAC), which blocks

anaphase until end-on attachment of kinetochores and microtubules has occurred, and chromosomes are properly aligned and stable[67]; thus, we would expect MTT to be similarly delayed in our cells. First examining NSCs, we find that KO of *PKMYT1* or WEE1 inhibition alone led to modest but significant increases in MTT (Figure 3.11C), where the average MTT in control cells was 37 minutes compared to 47-51 minutes in *PKMYT1* KO or WEE1 inhibited cells. However, loss of *PKMYT1* and WEE1 activity together resulted in synergistic increases in MTTs to over 100 minutes on average, with many cells having a MTT well over 150 minutes (Figure 3.11C). Importantly, concomitant synergistic increases in cell death during mitosis and cytokinesis failure were also observed (Figures 3.11D and 3.13). Collectively, these data again suggest that PKMYT1 and WEE1 can act redundantly. In addition, visual inspection of double inhibited cells with extended MTTs revealed that they spend most of their time arrested at metaphase, consistent with a SAC-induced arrest (data not shown).

We next repeated the same set of experiments in parallel in NSC-CB660 and GSC-0827 cells, this time using an siRNA pool to inhibit *PKMYT1*, which allowed for better control of timing of *PKMYT1* inhibition in GSCs. Importantly, the siRNA pool resulted in dramatic loss of PKMYT1 protein expression (Figure 3.14). In NSC-CB660 cells, the *siPKMYT1* pool precisely phenocopied the effects of *PKMYT1* KO, showing the same increase in MTTs for *PKMYT1* inhibition alone and together with WEE1 inhibition (Figure 3.11E). By contrast and strikingly, in GSC-0827 cells, inhibition of *PKMYT1* or WEE1 alone was sufficient to cause dramatic increases in MTTs similar to those observed for double inhibition in NSCs (Figure 3.11F). The MTT in GSCs increased from 55 minutes in controls to 153 minutes in *siPKMYT1* treatment, 206 minutes after WEE1 inhibition, and 177 minutes with double treatment, which was not significantly different from either treatment alone (Figure 3.11F). As before, extended MTTs

were associated with cell death during mitosis and also cytokinesis failure (Figure 3.11G). However, unlike NSCs, *PKMYT1* depletion or WEE1 inhibition alone in GSCs resulted in cell death during mitosis and also cytokinesis failure, and double treatment resulted in the majority of the cells experiencing cell death during mitosis (Figure 3.11G). Importantly, these data demonstrate that PKMYT1 and WEE1 act redundantly to promote timely completion of mitosis in human NSCs, and that this redundancy is lost in GBM cells, giving rise to the differential requirement for *PKMYT1* (and, incidentally, *WEE1*).

Oncogenic activation of *EGFR* and *AKT1* sensitize NSCs to loss of PKMYT1 function

We next wondered what could cause the loss of PKMYT1 and WEE1 redundancy in GSCs. Previous studies have established that the AKT and MAP kinase pathways can negatively impact PKMYT1 or WEE1 activity during meiosis/oocyte maturation[208,209] and the somatic cell cycle[210,211]. In human cells, AKT has been shown to directly phosphorylate WEE1 at S642, which causes its retention in the cytoplasm and loss of WEE1 activity[210]. In addition, MEK1 activity has been implicated in down regulation of PKMYT1 during mitosis[211]. Since activation of PI-3 kinase and RTK/MAP kinase signaling cascades are necessary features of GBM tumors[22] and our GSCs (Figures 3.2A and 3.3), we next asked whether altering these pathways would be sufficient to trigger *PKMYT1* KO sensitivity in our NSCs.

To this end, we used constitutively active alleles of *EGFR**[212] and *AKT1**[213] in combination with *TERT*, dominant-negative $TP53^{DD}$, and $CCND1{+}CDK4^{R24C}$ (p16 resistant)[46] in NSC-CB660 cells. To note, manipulation of the TP53 and RB-axis is required in order to bypass *EGFR** induced senescence or apoptosis in our NSCs. Figures 3.15A and 3.15B demonstrates the effects of various combinations of these human oncogenes on CDK1-T14 and CDK1/2-Y15

phosphorylation levels. The results were interesting, if somewhat complicated. NSCs with *TERT+TP53*^{DD}*+CCND1+CDK4*^{R24C} showed ~50% increase in T14 and Y15 phosphorylation over their respective NSCs controls. However, adding *EGFR** and then *AKT1** to these cells dramatically suppressed T14 and Y15 phosphorylation to ~2-fold below the base line found in NSCs and >3-fold from levels found in *TERT+TP53*^{DD}*+ CCND1+CDK4*^{R24C} cells. Interestingly *AKT1** did not produced this affect alone; rather, it potentiated the effect of *EGFR** (Figures 3.15A and 3.15B). These results demonstrate that EGFR and AKT pathways can suppress the steady state levels of CDK1-T14 and CDK1/2-Y15 phosphorylation in NSCs.

To determine whether *EGFR** and *AKT1** affected the requirement for *PKMYT1*, we again performed MTT assays using *siPKMYT1* pools. In these assays, we found that NSC-CB660s with *TERT+TP53*^{DD}*+CCND1+CDK4*^{R24C} behaved exactly like unmanipulated NSCs, showing small increases in MTT when *PKMYT1* or WEE1 were inhibited alone, but synergistic increases when combined (Figure 3.15C). Importantly, though, the addition of *EGFR** and *AKT1** to these cells in the presence of *siPKMYT1* produced similar effects on MTTs that were observed for GSCs (Figure 3.15D), as *PKMYT1* depletion almost doubled the MTTs. This pattern also extended to increases in the frequency of unsuccessful mitoses (Figure 3.15E), which, again, were similar to GSCs. It is also interesting to note that *EGFR** and *AKT** expression in control experiments increased NSC MTTs from 40 to 69 minutes. GSC-0827 cells showed a similar trend with MTTs of 55 minutes. This suggests that EGFR and/or AKT induce changes in feed-back regulation of mitosis for which cells are required to compensate (e.g., via SAC activity[66]). Taken together, these results suggest that overactive EGFR and PI-3 kinase signaling is sufficient to cause the loss of redundancy between PKMYT1 and WEE1, and differential sensitivity to loss of *PKMYT1*.

Validation and characterization of genes limiting the expansion of human NSCs

In addition to lethal genes, our gene editing screens also revealed genes predicted to limit the expansion of NSCs (Table 3.4). Hits from this group (logFC>1, FDR<0.05; a) ≥1 sgRNA scored in both NSC-CB660 and NSC-U5 screens or b) >2 sgRNAs scored in NSC-CB660 or NSC-U5) included many genes found altered in adult and pediatric gliomas/GBM (42 of 272 hits)[104,105,214-216] (Provisional GBM data set from TCGA) or other cancers; 31 genes implicated in promoting neural development or brain function; 16 genes with causal roles in human syndromes affecting brain function; 11 genes involved in TP53 signaling; and 8 genes that antagonize Hippo signaling (Table 3.4). We retested 18 of these hits using competitive outgrowth assays mimicking screen conditions, and found 12 of the 18 hits to retest in multiple assays (Figure 3.16A and Table 3.5). We confirmed loss of protein expression for several hits: *CREBBP*, *NF2*, and *TP53* (Figures 3.16B and 3.1C), which indicates proper indel formation at the targeted gene sites. We next asked whether these differences could be due to an increase in cell cycle transit times. Consistent with this notion, time-lapse microscopy for 72 hours (~1.5 cell cycles) for 10 positively scoring hits, including: *ARID1A*, *ARID1B*, *CREBBP*, *EP300*, *NF2*, *PDCD10*, *PTPN14*, *TAOK1*, *TGFBR2*, and *TP53,* revealed that each gene KO triggered significantly faster cell cycle transit times, without observable effects on viability (Figure 3.16C) (not shown). Moreover, 8 of the confirmed growth-limiting genes that we examined (*ARID1A*, *ARID1B*, *CREBBP*, *NF2*, *PTPTN14*, *TAOK1*, *TGFBR2*, and *TP53*) contained lower total protein compared to the control (Figure 3.17), which is likely due to the cells not having an ample amount of time to synthesize proteins in the G1 phase of the cell cycle.

Since NSCs spend the majority of their 45-60 hour cell cycle in G1, we wondered whether decreased cell cycle transit times resulted from an increase entry into S-phase. As a test case, we further examined the histone acetyltransferase and transcriptional coactivator CREBBP, which possess hematologic and solid tumor suppressor activity[217-219]. We first determined whether shRNA technology, which allowed for better control of timing of *CREBBP* inhibition in NSCs, would produce a similar decrease in cell cycle transit time compared to CRISPR technology in both competitive outgrowth assays mimicking screen conditions and time-lapse microscopy. In both assays, *CREBBP* depletion using 3xmiR30-based shRNAs cassette, which increases knockdown efficiency of the targeted gene, in NSCs revealed a growth advantage compared to control NSCs (Figure 3.18). Next, we found that *CREBBP* inhibition significantly increased BrdU incorporation in NSC expansion cultures, which is consistent with the notion that inhibition or loss of growth-limiting genes increase S-phase entry (Figure 3.16D). Further, *CREBBP* inhibition caused dramatic increases in steady-state levels of mRNAs for cell cycle genes up regulated during the G1/S transition, along with predicted CREB pathway genes (Figure 3.16E and Tables 3.6). This suggests that CREBBP limits NSC growth through transcriptional repression of genes involved in feed-forward loops controlling G1/S transition. Taken together, these results indicate that sgRNA-enriched screen hits, such as *CREBBP*, limit expansion of NSCs by affecting entry into S-phase.

Examining CRISPR-Cas9-triggered insertion-deletion mutation formation

Lastly, we confirmed sgRNA:Cas9 on-target activity by deep sequencing target sites for multiple sgRNAs used above (Figure 3.19A and Table 3.7). As expected, we observed high frequencies of on-target indel formation (Figure 3.19 and Table 3.7). However, we surprisingly

found unexpected biases in mutation spectra. For example, in many cases, single nucleotide insertions were dramatically overrepresented (Figure 3.19B), biasing indels toward reading frame shifts (Figure 3.19D). In addition, deletion lengths around the targeted site varied greatly (Figure 3.19C), which again biased indels toward reading frame shifts (Figure 3.19D). In fact, of the seven target sites shown in Figure 3.19D, only one target site showed nearly unbiased reading frame shifts after indel formation, which we would expect to occur 1/3 of the time. This is an important point for identifying essential genes using CRISPR-Cas9 screens, since without bias, small indels and/or in-frame indels could have little affect on gene function; and, thus, nearly a third of the time would lead to little or no phenotypic difference. Thereby, frame shift bias helps explain the highly penetrant phenotypic effects produced by this technology in human cells.

Discussion

Here, we report the successful application of gene editing technology to identify and characterize genes promoting and limiting growth of human GSCs and NSCs. Our results contribute to a growing body of work demonstrating the power of CRISPR-Cas9 based functional genetic approaches in mammals[126,167,220-222], and in our case, in patient-derived GBM isolates and tissue of origin control cells, NSCs. In particular, our approach illustrates the utility of performing screens in patient samples, as many of the candidate therapeutic targets arising are not found using thorough computational analysis of patient tumor genomic data sets, including Bayesian network analysis of GBM TCGA data sets (data not show). By comparing GSCs and NSCs, our screens revealed hundreds of GSC-sensitive genes, which may represent GBM therapeutic targets with large therapeutic windows, as their KO suppresses GSC expansion, but

have little effect on NSCs. In addition, previous CRISPR screens were performed either *in vitro*[126,167,220,221] or *in vivo* (screen for metastasis genes)[222] alone, but failed to perform parallel *in vivo* and *in vitro* studies. Here, we performed the first parallel *in vivo* and *in vitro* CRISPR-Cas9 validation studies to candidate sensitive genes by choosing 58 genes that significantly scored as candidate essential, GBM-sensitive, or patient-specific sensitive. In this class of hits, validation and follow up studies, in particular, shed new light on PKMYT1 function.

Human *PKMYT1/Myt1* is a WEE1-like dual specificity kinase that acts to inhibit cytoplasmic cyclin B-bound CDK1 activity by preferentially phosphorylating T14 in CDK1's ATP binding pocket, and to a lesser extent Y15 of CDK1[161,162]. Our results help redefine PKMYT1 function in human cells. We find that in human NSCs, PKMYT1 acts redundantly with WEE1 to both maintain CDK1-Y15 phosphorylation and to promote timely completion of mitosis. Previous work in HeLa cells, in particular, has demonstrated sole reliance on WEE1 for CDK1-Y15 inhibitory phosphorylation, preventing premature entry into mitosis and mitotic catastrophe, and timely completion of mitosis[181,187-190,194]. Our data, however, clearly demonstrate that PKMYT1 activity can compensate for both Y15 phosphorylation and the prevention of extended MTTs in WEE1 inhibited non-transformed NSCs (Figure 3.11). This is consistent with the observation that *Drosophila* wee1 and myt1 have redundant and overlapping roles during fly development[180]; and also the original biochemical assays used to examine Myt1 activity from *Xenopus*[172], which demonstrated that Myt1 can independently phosphorylate CDK1-T14 or Y15 and that each phosphorylation can contribute to inhibition of CDK1 activity. We predict that the same redundancy will be observed in other *non-transformed* vertebrate cell types. This is critical, since our results suggest that PKMYT1 and WEE1 redundancy in human

somatic cells and tissues will help avoid dose-limiting toxicities for PKMYT1 targeted cancer therapies. The question of general redundancy awaits further experimentation.

We also find that patient-derived GSCs show loss of redundancy between PKMYT1 and WEE1 both *in vitro* and *in vivo*. In GSCs, *PKMYT1* loss alone leads to dramatic increases in MTTs, as well as cell death during mitosis and cytokinesis failures (Figure 3.11). This is consistent with the notion that PKMYT1 and WEE1 activity in GSCs has diminished capacity to sustain CDK1-Y15 inhibitory phosphorylation when one or the other is inhibited compared to NSCs (Figure 3.12).

Conspicuously, *PKMYT1* is not commonly altered in GBM, as it's amplified in only 0.4% of GBM[104,105] (Provisional GBM data set from TCGA), and expression levels vary between GBM isolates examined (data not shown). Thus, why does GBM isolates require *PKMYT1* while NSCs do not? Here, we identified a plausible mechanism for why GSCs are sensitive to loss of *PKMYT1*. We show that activation of EGFR and AKT pathways suppress CDK1/2-Y15 and CDK1-T14 phosphorylation in NSCs (Figure 3.15). This strongly suggests that activation of these pathways together results in net loss of inhibition of CDK1 and CDK2 during the G2/M transition. Importantly, although previous work has found that the AKT and MEK1 kinases negatively regulate WEE1 or PKMYT1 activity[210,211], respectively, other mechanisms are possible. This includes changes in the activity of CDC25 phosphatase, which is responsible for removing inhibitory phosphorylations at T14 and Y15 of CDK1 and which has been shown to be a target of EGFR signaling in a *Drosophila* model of glioma[34]. It should be noted that future experiments will be required to address whether EGFR and AKT signaling acts through direct or indirect regulation of WEE1 and PKMYT1 activity in GBM cells.

Further, although EGFR and AKT1 activation are common features of glioma tumors, our results demonstrate that *PKMYT1* requirement does not specifically arise from specific alterations in *EGFR* and *AKT1,* but rather in the AKT and MAP kinase pathways, as *PKMYT1* sensitive GSCs (e.g., 0131 and 0827) have varying lesions in these pathways (e.g., *NF1* loss vs. *EGFR* amplification, *PTEN* loss vs. *PI3KCA* mutation). Thus, importantly, the requirement for *PKMYT1* could arise in most GBM tumors where these pathways are affected. However, we did find that 2 of 10 GSC isolates were resistant to *PKMYT1* KO (Figure 3.8E). Examination of *CDC25* gene expression revealed that expression of *CDC25A* and *CDC25C* are 5-10-fold and 2-4-fold higher, respectively, in GSC isolates sensitive to *PKMYT1* KO, compared to resistant GSC isolates and NSCs (data not shown). In addition, GSC-G179, which is resistant to *PKMYT1* KO, contains an alteration in *CDC25C,* which appears to be mainly cytoplasmic just like PKMYT1[177]. Interestingly, both CDC25C and PKMYT1 are phosphorylated by polo-like kinase one (PLK1)[186]. Thus, additional work is required to determine whether alterations in CDC25, PKMYT1, or WEE1 activity or other regulatory factors could play key roles in *PKMYT1* sensitivity in GBM.

One possible kinase that may play a key role in sensitizing GSCs to *PKMYT1* KO is PLK1. PLK1 is part of the regulatory circuit that controls entry into mitosis[178]. Activated CDK1-cyclin B complexes phosphorylate many targets, including PKMYT1, WEE1, and CDC25, which creates a docking site for PLK1[177,178]. PLK1 can then find and bind its substrates, such as PKMYT1, WEE1, and CDC25C, and phosphorylate them[177,178,186]. Phosphorylation of PKMYT1 by PLK1 inactivates PKMYT1's kinase activity, while phosphorylation of WEE1 by PLK1 leads to its degradation[177,186,223]. Interestingly, PLK1's catalytic activity is stimulated by phosphorylation on S99 via AKT, and inhibition of PI3K or

AKT1 delays the metaphase to anaphase transition in HeLa cells, which is likely due to the activation of the SAC[224]. Thus, an active PI3K-AKT pathway in GSCs could indirectly disrupt the dual regulatory feedback loops involving PKMYT1/WEE1 and CDC25 that regulates CDK1-cyclin B dynamics by altering PLK1's kinase activity. An increase of PLK1's kinase activity could then lead to an increase in WEE1's degradation; and thus, GSCs could become dependent on PKMTY1 activity to regulate CDK1-cyclin B dynamics during mitotic progression and exit since PKMYT1 is not degraded like WEE1.

Another regulatory factor that might play a pivotal role in sensitizing GSCs to *PKMYT1* KO is cyclin A. Cyclin A can bind both CDK1 1 and CDK2[176]. In addition, cyclin A has been shown to promote WEE1 phosphorylation and inhibit its activity, which decreases inhibitory phosphorylation of Y15 on CDK1 and weakens the negative feedback loop that regulates CDK1-cyclin B dynamics[176]. Thus, cyclin A primes mitotic entry through cyclin B by enhancing CDK1-cyclin B activity[176]. Interestingly, AKT activity phosphorylates CDK2 and enhances cyclin A binding[225], and CDK2-cyclin A activated complexes can phosphorylate AKT to promote its activation[226]. Taken together, AKT can enhance cyclin A activity, which leads to a decrease in WEE1's kinase activity, and possibly an increase in WEE1's degradation due to an increase in PLK1's activity (see above paragraph). Once again, GSCs could become dependent on PKMTY1's activity to regulate CDK1-cyclin B dynamics during mitotic progression and exit since PKMYT1 is not degraded like WEE1.

In GBM cells, active PI3K-AKT and MAP kinase pathways may regulate CDK1-cyclin B dynamics by directly phosphorylating and inactivating WEE1 and/or PKMYT1[208-211] and/or indirectly through other regulatory substrates like PLK1 and/or cyclin A[176-178,186,223-226]. Therefore, active PI3K-AKT and MAP kinase pathways likely disrupt the timing of the

activation and inactivation of CDK1-cyclin B complexes, which is critical for proper mitotic entry, progression, and exit[177,185,190-193]. The requirement for *PKMYT1* in GBM cells could arise from alterations in the dynamics of CDK1's activation and inactivation. Our data demonstrates that CDK1 expression remains relatively constant among all manipulated NSC-CB660 lines, suggesting that the addition of constitutively active *EGFR* and *AKT* may lead to an increase in activated CDK1-cyclin B complexes (Figure 3.15B). An increase in CDK1-cyclin B activity in GSCs compared to non-transformed cells could lead to the requirement for *PKMYT1* in cancer cells in order to counteract and inhibit the activity of CDK1 and to maintain its inactivity during mitotic exit, which allows for proper mitotic exit and establishment of G1[177,191-193]. Although PKMYT1 and WEE1 may have independent activities, our data suggest that PKMYT1 and WEE1 also act redundantly in non-transformed cells to phosphorylate Y15 of CDK1 and to promote timely completion of mitosis. In addition, our data suggest that this redundancy is loss in cancer cells due to oncogenic alterations, which may disrupt the relationship between the dynamics of CDK1's activation, APC's activation, and CDK1's inactivation[193].

Our findings lead to a key question: how does neural stem cells and other non-transformed cells compensate for the loss of inhibitory phosphorylation at T14 of CDK1 following *PKMYT1* loss? One possibility is that another kinase can phosphorylate T14 and/or Y15 of CDK1 to inhibit its activity, such as WEE1b[227]. Even with complete loss of *PKMYT1* and WEE1 inhibition in NSCs, residual inhibitory phosphorylation remained on CDK1 (Figure 3.11A). Another possibility is that the relationship between the dynamics of CDK1's activation, APC's activation, and CDK1's inactivation is more robust in NSCs, but not GSCs due to the oncogenic alterations that GSCs have acquired. For example, non-transformed somatic cells, such as NSCs, may be able to tolerate dampen oscillations from inactive to active CDK1, and

then back to inactive CDK1 following activation of APC[192,193,195]. In addition, unlike cancer cells, abrupt activation of CDK1 may not be necessary in order to properly stimulate APC activity in non-transformed somatic cells[190,195]. Although NSCs experience a modest, but significant, increase in mitotic transit time following *PKMYT1* KO or depletion (~37 minutes to ~47 minutes), these manipulated NSCs were able to successfully complete mitosis (Figure 3.11C and D). A third possibility is that the doubly phosphorylated CDK1 isoform (CDK1-T14-Y15) that remains upon *PKMYT1* KO in NSCs (Figure 3.11A and B) may be able to antagonize CDC25 function more effectively than the residual doubly phosphorylated CDK1 isoform (CDK1-T14-Y15) that remains upon *PKMYT1* KO in GSCs (Figure 3.12)[180,228], as NSCs have a higher ratio of doubly phosphorylated CDK1 isoform to total CDK1 and a lower expression of *CDC25A* and *CDC25C* compared to GSCs that are sensitive to *PKMYT1* KO. Thus, NSCs may have more inactive CDK1 compared to GSCs upon *PKMYT1* KO, which could be due to other kinases or mechanisms that can inhibit the activity of CDK1 in NSCs. Moreover, the total amount of doubly phosphorylated CDK1 isoform that remains in NSCs upon *PKMYT1* KO may be sufficient to cause an abrupt change in oscillation from inactive to active CDK1, which allows for the proper stimulation of APC. Further investigation is warranted to determine how the relationship between the dynamics of CDK1's activation, APC's activation, and CDK1's inactivation is altered upon *PKMYT1* KO, and whether altering these dynamics by the reduction of both PKMYT1 and WEE1 expression in NSCs and GSCs can create a larger therapeutic window compared to PKMYT1 and WEE1 inhibition alone. These studies could lead to a new therapeutic approach for GBM.

While *PKMYT1* function has not previously been studied in GBM or other cancers, there has been great interest in *WEE1* as a potential therapeutic target[229]. Preclinical studies

demonstrated that *WEE1* might be a novel cytotoxic chemotherapy and/or radiation sensitizer since it is required for radiation-induced arrest and repair[229]. In GBM, for example, GSCs appear more resistant to radiation through increased repair proficiency[230,231]. Thus, WEE1 inhibition may enhance radiation treatment. By contrast, our results suggest that inhibiting PKMYT1's kinase activity alone may be a GBM-therapeutic target. However, it is currently unclear whether PKMYT1 inhibition would synergize with cytotoxic therapies that engage WEE1 or whether cytotoxic therapies that engage WEE1 could suppress the requirement for PKMYT1. Nonetheless, the combination of the standard of care for GBM patients (surgery followed by temozolomide and radiation) with the inhibition of PKMYT1's kinase activity may provide a better therapeutic response since it would activate both the G2/M checkpoint from temozolomide treatment and an extended SAC response and cell death during mitosis from PKMYT1's kinase inhibition[7,232,233]. Though the WEE1 inhibitor, MK1775, and temozolomide preclinical combinational studies in mouse flank GBM models were highly effective, the combinational treatment in mouse brain orthotopic xenograft models were ineffective due to the limited heterogeneous distribution of MK1775 across the blood-brain barrier[234]. Because the current WEE1 inhibitor in clinical trials is not effective in penetrating the blood-brain barrier, future studies are warranted in order to identify PKMYT1-specific inhibitors, as *PKMYT1* depletion is specifically lethal to GSCs, but not NSCs. To our knowledge, PKMYT1 inhibitors have not been successfully developed thus far[235,236]. Future studies will also have to address whether combinational therapies using PKMYT1's kinase inhibitors and another therapeutic and/or the standard of care treatment for GBM patients will be more effective than the respective stand alone treatments.

In addition to lethal genes, our screens identified hundreds of growth limiting genes for expansion of NSCs (Figure 3.16 and Table 3.4). Many of these genes have functions implicated in central nervous system development and other developmental pathways, such as *Hippo* signaling (Table 3.4). In addition, many of these genes are mutated at intermediate and low frequencies in glioma/GBM and other cancers, suggesting that they might act as tumor suppressors. Follow up experiments examining cell cycle transit time were consistent with this notion, as all 10 growth-limiting hits examined sped up the cell cycle of NSCs (Figure 3.16C). Focused experiments on the transcription regulator *CREBBP*[49,50] demonstrated that its activity blocks entry into S-phase and negatively regulates a network of G1/S and cell cycle genes, further consistent with this notion. One possibility from these results is that many of these hits have epistatic relationships such that KO of one is equivalent to KO of another (e.g. *CREBBP* and *EP300; ARID1A* and *ARID1B)*. This might explain their low penetrance in glioma/GBM and other cancers. It also raises interesting questions about the convergence of multiple pathways to regulate exit from G0/G1 or entry into S-phase for NSCs.

Our studies raise another key question: How does CRISPR technology compare to shRNA technology for screen-based approaches? Here, we identify 7 essential and 10 GBM sensitive genes (29% retest rate) (Figure 3.8) that scored in both *in vivo* and *in vitro* studies, demonstrating the power of CRISPR technology combined with primary tumor patient isolates and human NSCs to discover new cancer therapeutic targets and mammalian essential genes. Individual *in vitro* sgRNA retest of 23 of the 58 genes in the retest pool to candidate sensitive genes yielded a higher retest rate of 57% for individual sgRNAs (27/47) (Figures 3.8B and 3.9). From these individual *in vitro* sgRNA retest, 43% of the genes (10/23) had both sgRNAs score correctly. We found a higher retest rate of 67% for candidate growth-limiting genes (12/18)

(Figure 3.16A), but these studies were performed in *in vitro* conditions only. Previously, we have seen a retest rate of 25-40% for whole-genome and focused shRNA screens that were conducted under *in vitro* conditions only[42,60]; and thus, CRISPR technology seems to be more effective for viability screens. In addition, CRISPR technology was more effective than shRNA technology in identifying total essential genes [769 (CRISPR technology) versus 95 genes (shRNA technology)], but less effective in identifying GBM-specific genes [946 genes (CRISPR technology) versus 1355 genes (shRNA technology)]. However, the therapeutic targets identified by CRISPR technology may have larger therapeutic windows than the therapeutic targets identified by shRNA technology, as the therapeutic targets identified by shRNA technology likely have essential activities in non-transformed cells (see for example *BuGZ* KO studies in Figure 2.14).

Like shRNA screen-based approaches, there are limitations and screen biases associated with CRISPR technology. First, we found it took a minimal of 4 days to see a loss of protein expression (Figure 3.12B), but found this can vary depending on the gene targeted and cell line used for experimentation. Generally, the technology has the greatest penetrant effect, both at the genomic and phenotypic states, between days 10-13, as reported before[126,129,167], which is 7-10 days longer than shRNA technology. This could be due the following: 1) levels of Cas9 and/or sgRNAs need to reach a certain threshold; 2) CRISPR-Cas9 accessibly to the gDNA; and/or 3) CRISPR-Cas9 finding both of its targets (one target per allele) is rate limiting. Further investigation is warranted to determine why CRISPR-Cas9 technology requires an extended period of time for genomic editing and whether this correlates with the doubling time of cells. Another limitation of CRISPR-Cas9 technology is the efficiency of the sgRNA to make the targeted cut that results in a reading frame shift (Figure 3.19). In addition, the number of

sgRNAs per gene that cause a penetrant phenotypic effect can vary, which could be due to the location of the targeted site within the gene or the accessibility of the gDNA of the targeted gene. However, we observed sgRNAs targeting early exons or exon-intron boundaries to be more effective (data not shown). It will be interesting to determine if a CRISPR-Cas9 plasmid containing multiple sgRNAs per gene that target early exons and exon-intron boundaries would create a more efficient library for screening and decrease the time for penetrant phenotypic effects in cell culture.

In summary, we employed CRISPR technology to identify novel therapeutic targets in GBM, but which are dispensable in non-transformed cells, and tumor genetic drivers in NSCs. These studies show that GBM tumor cells harbor cancer-specific essential genes, such as *PKMYT1*, which in non-transformed cells have redundant and non-essential activities, a concept originally proposed by Hartwell *et al.*[51] for cancer cells. The results also demonstrate the power of using gene KO screens to assign functions to genes found altered at intermediate or low frequencies in cancers, but that play important roles in regulating cell growth and cell cycle progression, such as *CREBBP*. Collectively, our results illustrate that CRISPR-Cas9 gene editing technology can be used to assemble a catalogue of validated and characterized key genetic drivers and therapeutic targets in primary tumors, which one day may assist clinicians in prescribing an effective treatment regimen based upon a patient-specific tumor genetic profile.

Figures

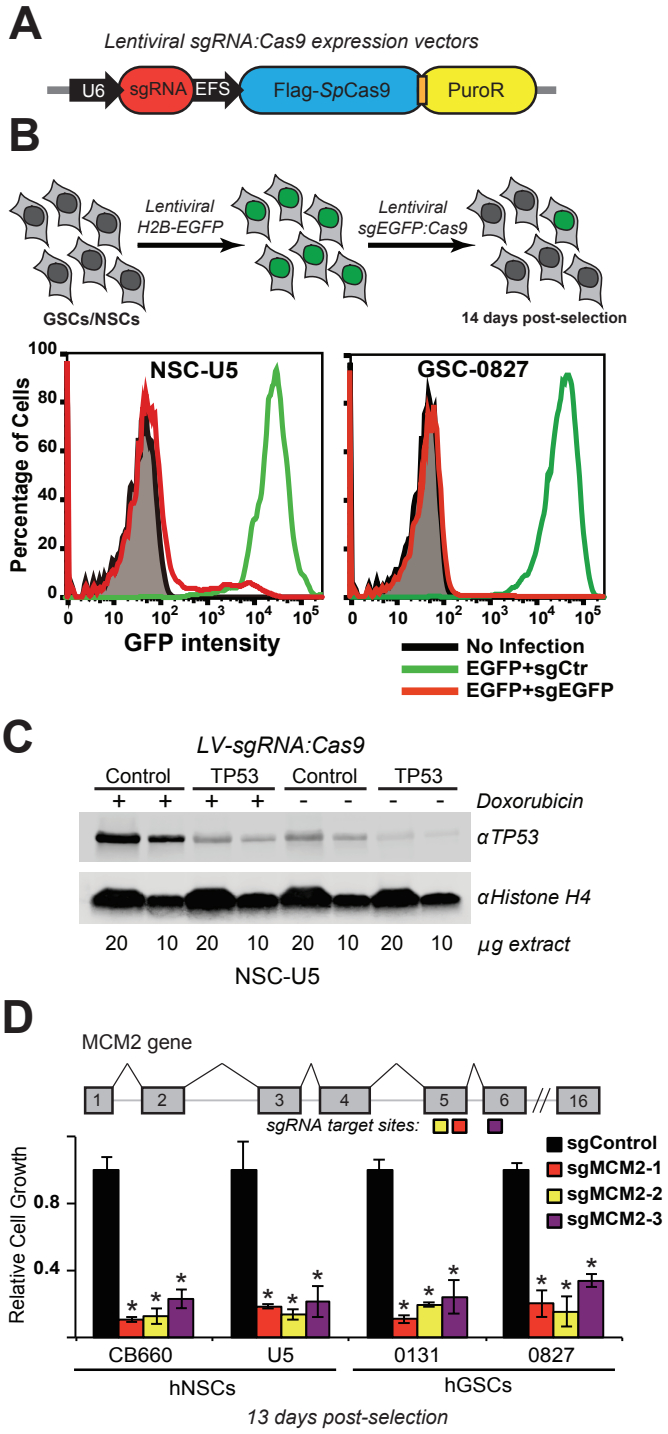

Figure 3.1. Validation of CRISPR-Cas9-based gene targeting in human GSCs and NSCs.
(A) Cartoon of lentiviral construct used for sgRNA:Cas9 expression.
(B) *sgEGFP*:Cas9 was used to target stably expressed *H2B-EGFP* in GSCs and NSCs. Cells were first infected with LV-EGFP-H2B at MOI>2 and passaged for 1 week, and then infected with sgControl or *sgEGFP* at MOI<1, selected, outgrown for 14 days, and flow analyzed.

(C) Western blot confirmation of TP53 protein expression after targeting *TP53* gene with sgRNA:Cas9 in NSC-U5 cells. Cells were outgrown for >21 days following selection. Doxorubicin treatment (0.75 μg/ml for 6 hrs) was used to stabilize TP53 in response to DNA damage.
(D) CRISPR-Cas9-based targeting of an essential gene, *MCM2*. Cells were infected with sgRNAs and seeded 3 days post-selection for a ten-day culture in triplicate. After ten days, cell viability was measured using alamar blue reagent. *$p<0.01$, student's t-test (unpaired, unequal variance).

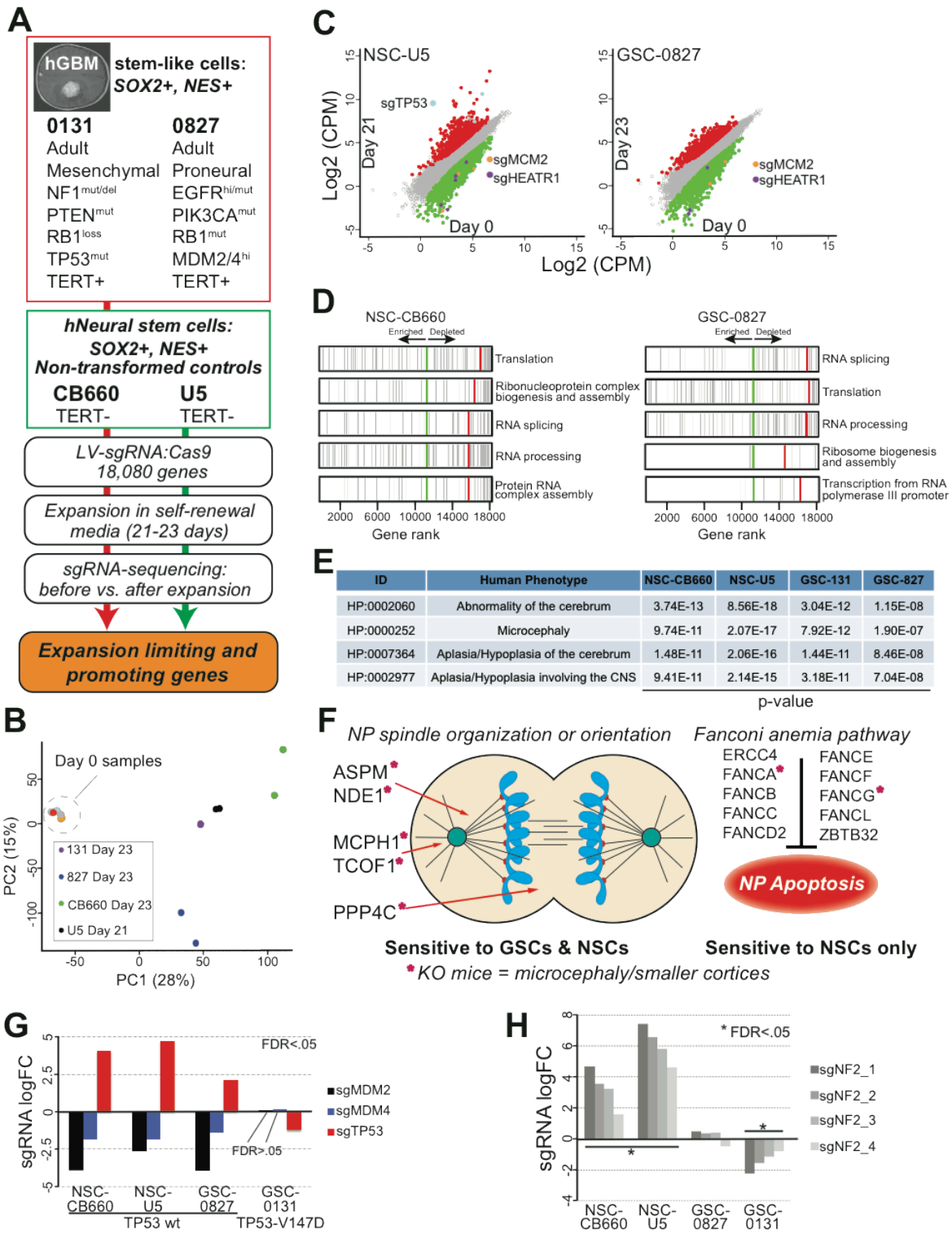

Figure 3.2. Genome-wide CRISPR-Cas9 KO screens in GSCs and NSCs.
(A) Overview of GSC and NSC isolates used and screen procedure.
(B) Principal component analysis of sgRNA-sequencing results of biological screen replicates (n=2).

(C) Scatter plots showing log2 normalized library sgRNA read counts comparing Day 21 or 23 to Day 0. Each dot represents a specific sgRNAs. Red dots indicate significantly overrepresented sgRNAs (LogFC>1, FDR<0.05), while green dots indicate significantly underrepresented sgRNAs (LogFC<-1, FDR<0.05) after outgrowth. *HEATR1* and *MCM2* were top scoring essential gene hits, while *TP53* showed strong enrichment in NSC screens.
(D) GSEA for gene ontology biological processes terms was conducted on all sgRNAs from screen results. Top 5 depleted gene sets in NSC-CB660 (FDR-q<0.0001) and GSC-0827 (FDR- q<0.011, 0.010, 0.012, 0.057, and 0.070 respectively) are displayed. Green line represents the point where the ratios (end point of screen/day 0) change from positive (left) to negative (right). Red line represents the point where the running sum statistic has its maximum deviation from 0 (enrichment score).
(E) Overlapping human phenotype ontology gene sets enriched among candidate sensitive hits (logFC<-1.0, FDR<0.05). Each set shown was among top ten gene sets enriched.
(F) Significant screen hits (logFC<-1, FDR<0.05) were overlapped with genes involved in cortical neural progenitor (NP) organization or orientation during symmetrical-asymmetrical division and the Fanconi anemia pathway. A gene was scored if one or more sgRNA(s) per gene met the criterion.
(G) Changes in representation of sgRNAs targeting *MDM2*, *MDM4*, and *TP53* during the screening procedure (see Results for further details).
(H) Changes in representation of sgRNAs targeting the tumor suppressor *NF2/Merlin* during the screening procedure (see Results for further details).

A

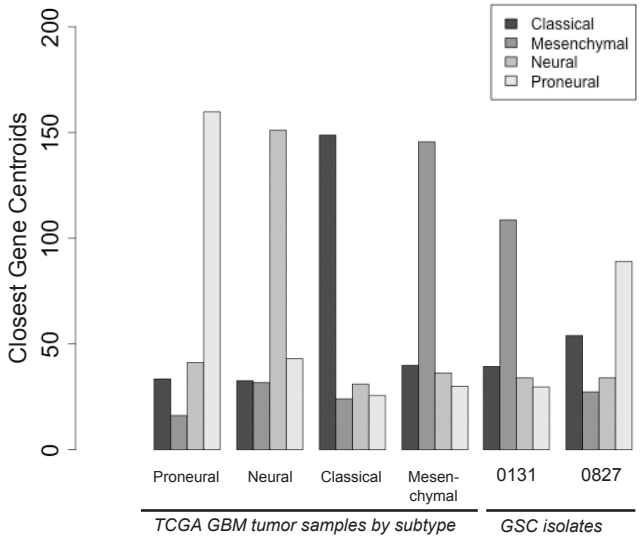

B

Subtype	Gene	GSC-131	GSC-0827
Proneural	CHD7	3.2 (0.2)	22.3 (2.1)
	EPHB1	0.3 (0.2)	7.6 (0.4)
	HDAC2	18.5 (1.8)	30.5 (2.0)
	KLRC4	0	2.0 (0.3)
	OLIG2	0	66.0 (4.6)
	RHOT2	18.4 (0.2)	30.3 (3.3)
	SOX11	0	18.8 (0.8)
	SOX4	3.9 (1.0)	58.2 (4.1)
Mesenchymal	CD44	252.9 (48.7)	60.4 (27.4)
	COL1A2	38.7 (9.1)	0
	DKK3	100.7 (25.5)	5.6 (1.3)
	FHL2	48.2 (1.3)	12.2 (0.3)
	ITGB1	170.8 (6.7)	68.1 (6.3)
	ITGB5	51.5 (9.5)	2.6 (0.6)
	LAMB1	145.0 (20.5)	25.2 (2.7)
	MET	13.0 (3.0)	0.7 (0.1)
	SERPINE1	341.9 (120.6)	5.9 (1.3)

C

Gene	GSC-131	GSC-827
CDKN2C	n.o.c.	CNV:loss / reduced expression
EGFR	n.o.c.	E396Q / High expression
MDM4	n.o.c.	CNV:gain / higher expression
NF1	Frame shift / CNV:loss	CNV:loss? / n.o.c.
PI3KCA	n.o.c.	H1047Y*
PTEN	L70P	n.o.c.
RB1	CNV:loss / No expression	D458H / frame shift
TERT	Expressed	Expressed
TP53	V146D / CNV:loss	Higher expression

n.o.c. = no observed change
*H1047 is a hotspot for activating mutations in PI3KCA

D

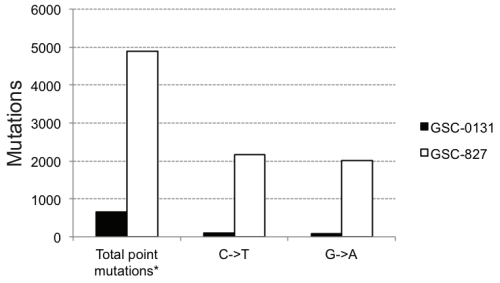

Figure 3.3. Molecular characterization of GSC-0131 and GSC-0827 isolates.
(A) GBM subtype assignment for GSC-0131 and GSC-0827. Associations of GSCs with specific GBM subtypes were determined by minimum Manhattan distance to expression centroids (see Methods for details). The y-axis represents the sum of subtype-associated gene centroids. TCGA tumor data were used to validate our classification approach and shows appropriate subtyping. GSC-0131 and GSC-0827 are most consistent with mesenchymal and proneural subtypes, respectively.
(B) Relative expression values of examples of genes in mesenchymal and proneural classifications from Verhaak *et al*[28] and Beier et al[237]. Average FPKM normalized RNA-sequencing values (n=3) are shown with standard deviations (SDs). The data reveal characteristic differences in expression of mesenchymal and proneural subtype-specific genes.
(C) Genomic alterations observed in oncogenes and tumor suppressors, which are frequently altered in GBM, for GSCs used for CRISPR-Cas9 screens (Figure 3.2).
(D) Analysis of point mutation frequency suggests that GSC-0827 cells are mutators, showing >7-folder more mutations than GSC-0131 and other GSC isolates (not shown). The majority of the GSC-0827 point mutations are consistent with C to T transition mutations in forward or reverse strands of exons. Elevation in C->T mutations could result from CpG island methylator phenotype (CIMP)[238], where cells have higher than normal 5-methyl-cytosine content in their DNA. 5-methyl-cytosine spontaneously deaminates in dsDNA resulting in conversion of C to T[239]. While glioma CIMP tumors characteristically contain *IDH1* mutations and GSC-0827 does not, a small number have been observed with wild type *IDH1*[240]. Further study will be required to determine if GSC-0827 cells fit into this category.

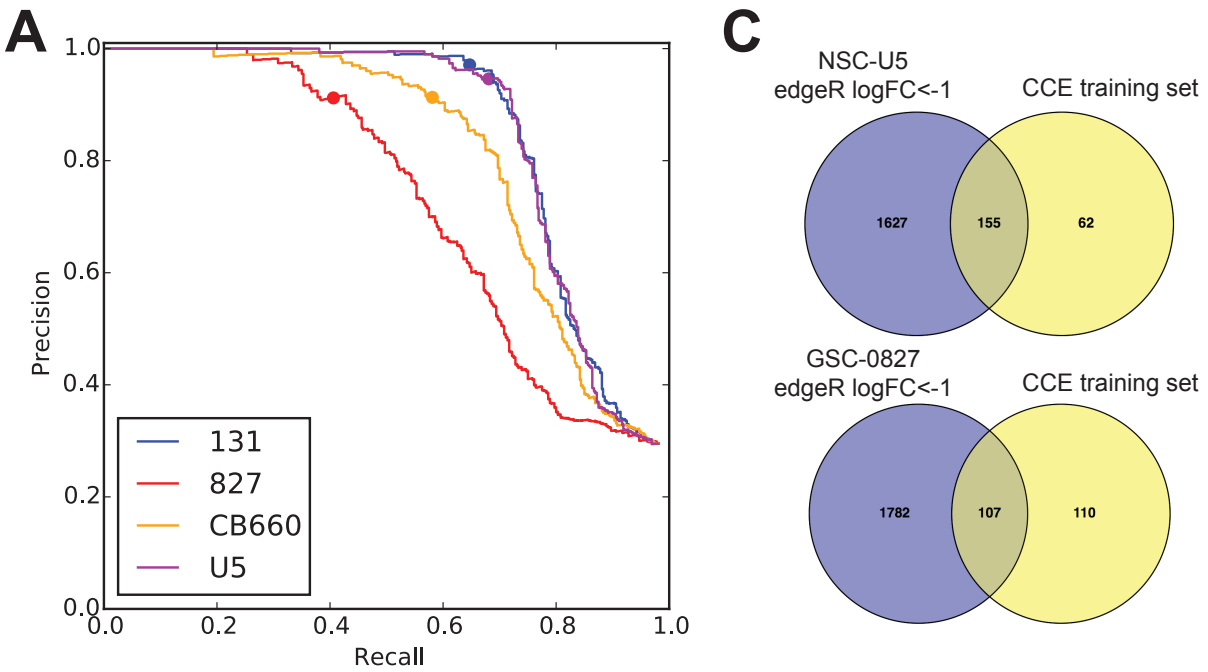

B

Screen	BF_threshold	Recall	Precision	FDR	Fmeasure	#Hits
GSC-131	3.00	0.647	0.971	2.9%	0.777	1820
NSC-U5	3.00	0.681	0.946	5.4%	0.792	1934
NSC-660	3.00	0.581	0.913	8.7%	0.710	1673
NSC-827	3.00	0.406	0.912	8.8%	0.562	1243

Figure 3.4. GSC and NSC CRISPR-Cas9 screen quality assessment using Bayesian classifier of gene essentiality.

(A) Precision versus recall graphs to assess screen performance. Screens were evaluated using predetermined "constitutive core essential" gene and "non-essential" gene reference training sets, as described in Hart *et al.* 2014[198], to train a Bayesian classifier to identify essential genes in each screen. For each screen, genes are ranked by their "Bayesian Factor (BF)" (i.e., the log likelihood that a gene's sgRNAs were drawn from either essential or reference distribution) and compared to withheld reference sets to evaluate the cumulative precision [TP/(TP+FP)] and recall [TP/(TP+FN)][198]. TP= true positives, the number of genes in the essentials test set with BF scores greater than current gene. FP = false positives, the number of genes in the nonessentials test set with BF score greater than the current gene. The filled dot represents the point on the precision-recall curve where the BF crosses zero.
(B) Summary statistics for CRISPR-Cas9 screens using Bayes classifier analysis from **(A)**. F-measure represents the "harmonic mean of precision & recall" and can be used as a measure of quality. Hart *et al.*[198] judged that screens with F-measures ≥ 0.75 to be high performing. The results suggest that GSC-0827 screen under performed relative to other screens.
(C) Comparison of overlaps of "constitutive core essential" genes used for deriving BFs and edgeR-scoring essential genes for NSC-U5 and GSC-0827 isolates. Data shows less overlap of constitutive core essential (CCE) genes with GSC-0827 edgeR data, possibly suggesting why the GSC-0827 screen under performed using BF analysis. Figure by Jason Moffat.

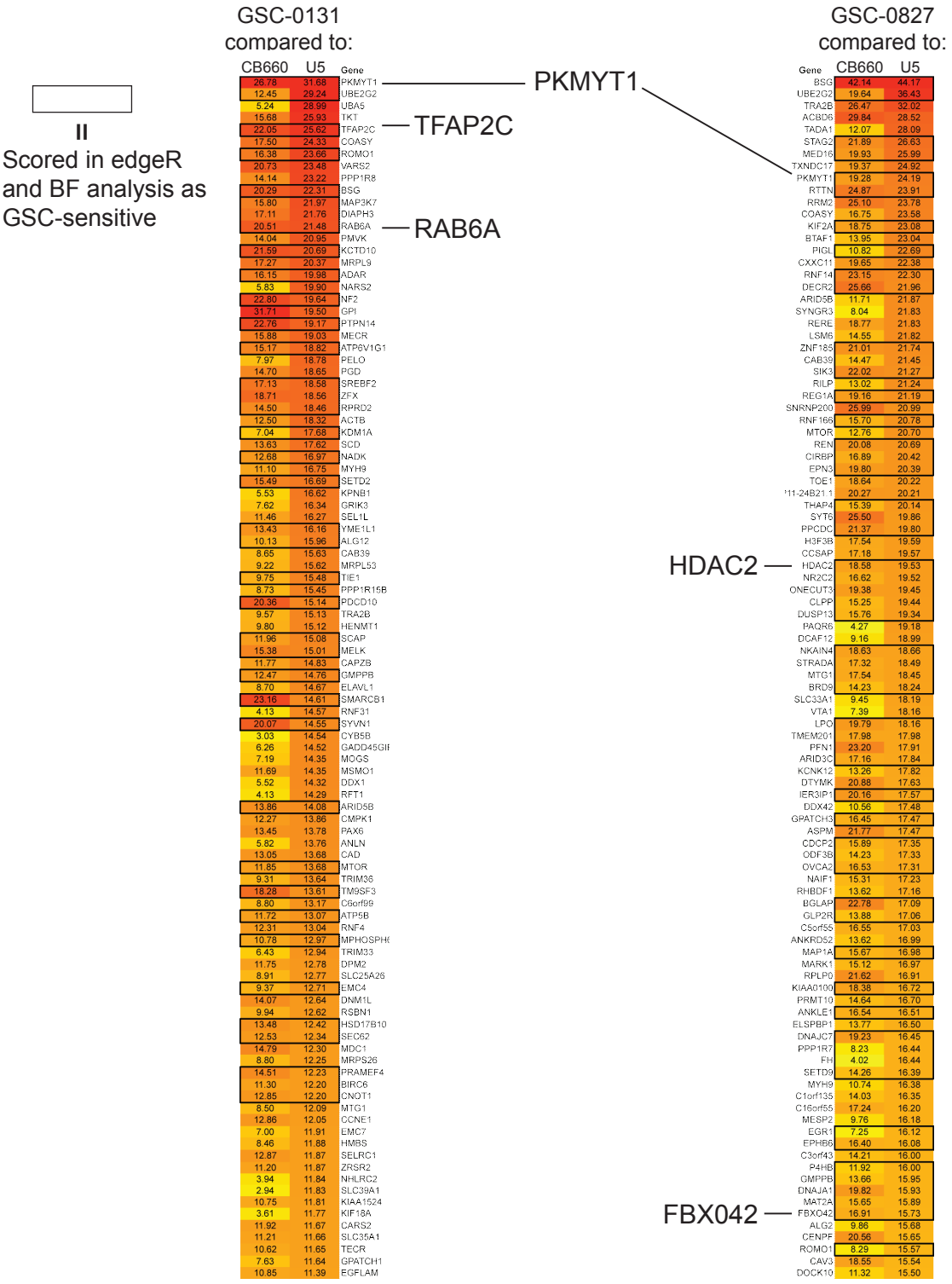

Figure 3.5. Identification of GSC sensitive genes using a Bayesian classifier of gene essentiality.

Heatmaps of the top 100 genes shows added sensitivity for GSC-0131 (left) and GSC-0827 (right) compared to NSC-CB660 and NSC-U5. The heatmaps represent comparisons of "Bayesian Factors (BF)" (i.e., the log likelihood

that a gene's sgRNAs were drawn from either essential or non-essential gene distribution[198]) for 0131 versus CB660 or U5 and 0827 versus CB660 or U5 by subtracting BF_{GSC} from BF_{NSC} for each scoring gene. Highly positive BF_{GSC} -BF_{NSC} values suggest GSC sensitivity. Heatmaps are rank ordered by BF_{GSC} -BF_{NSC}-U5 values. Boxed values and genes indicate hits that also scored as GSC sensitive by edgeR analysis. Importantly, BF analysis independently calls *PKMYT1* as a top scoring GBM-sensitive hit and also reveals GBM isolate-specific genes that were validated in Figure 3.8 including: *HDAC2*, *FBX042*, *RAB6A*, and *TFAP2C*.

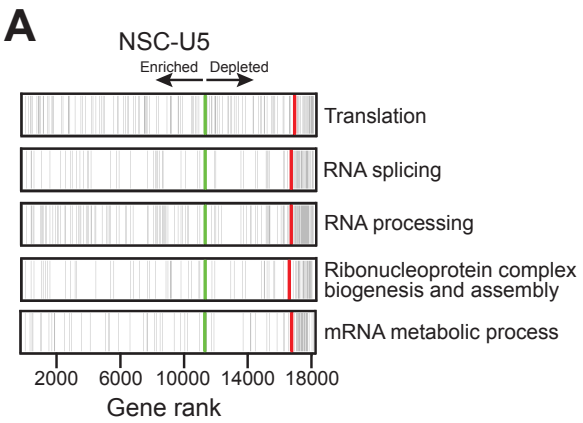

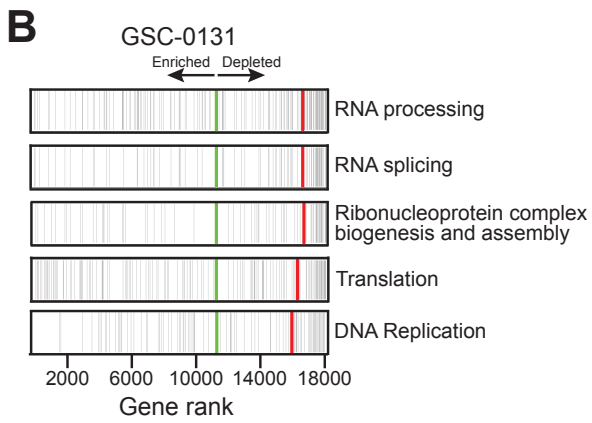

C

Shared GO biological processes in NSCs and GSCs

Gene set name
Translation
Ribonucleoprotein complex biogenesis and assembly
RNA splicing
RNA processing
Protein RNA complex assembly
Macromolecule biosynthetic process
mRNA processing _GO 0006397
mRNA metabolic process
RNA splicing via transesterification reactions
DNA replication
Ribosome biogenesis and assembly
Transcription from RNA polymerase III promoter

Figure 3.6. Enrichment for Gene Ontology (GO) biological terms for CRISPR-Cas9 screen hits in NSCs and GSCs.

Gene set enrichment analysis (GSEA) from the Broad Institute of MIT was conducted on all sgRNAs from the genome-wide CRISPR screen results (see Methods for details).

(A) and **(B)** GSEA revealed that most depleted sgRNAs targeted essential genes in biological processes such as translation. The top 5 most significantly depleted gene sets (false discovery rate (FDR-q<0.0001) in NSC-U5 **(A)** and GSC-0131 **(B)** by GSEA are displayed here. The green line represents the point where the ratios (end point of screen/day 0) change from positive (on the left) to negative (on the right). The red line represents the point where the running sum statistic has its maximum deviation from 0, which is the enrichment score for the gene set.

(C) In common GO biological processes for all of NSCs and GSCs isolates used in the screen. The top 20 scoring gene sets in NSC-CB660, NSC-U5, GSC-0827, and GSC-0131 were analyzed for common gene sets shared among all of the lines and displayed here.

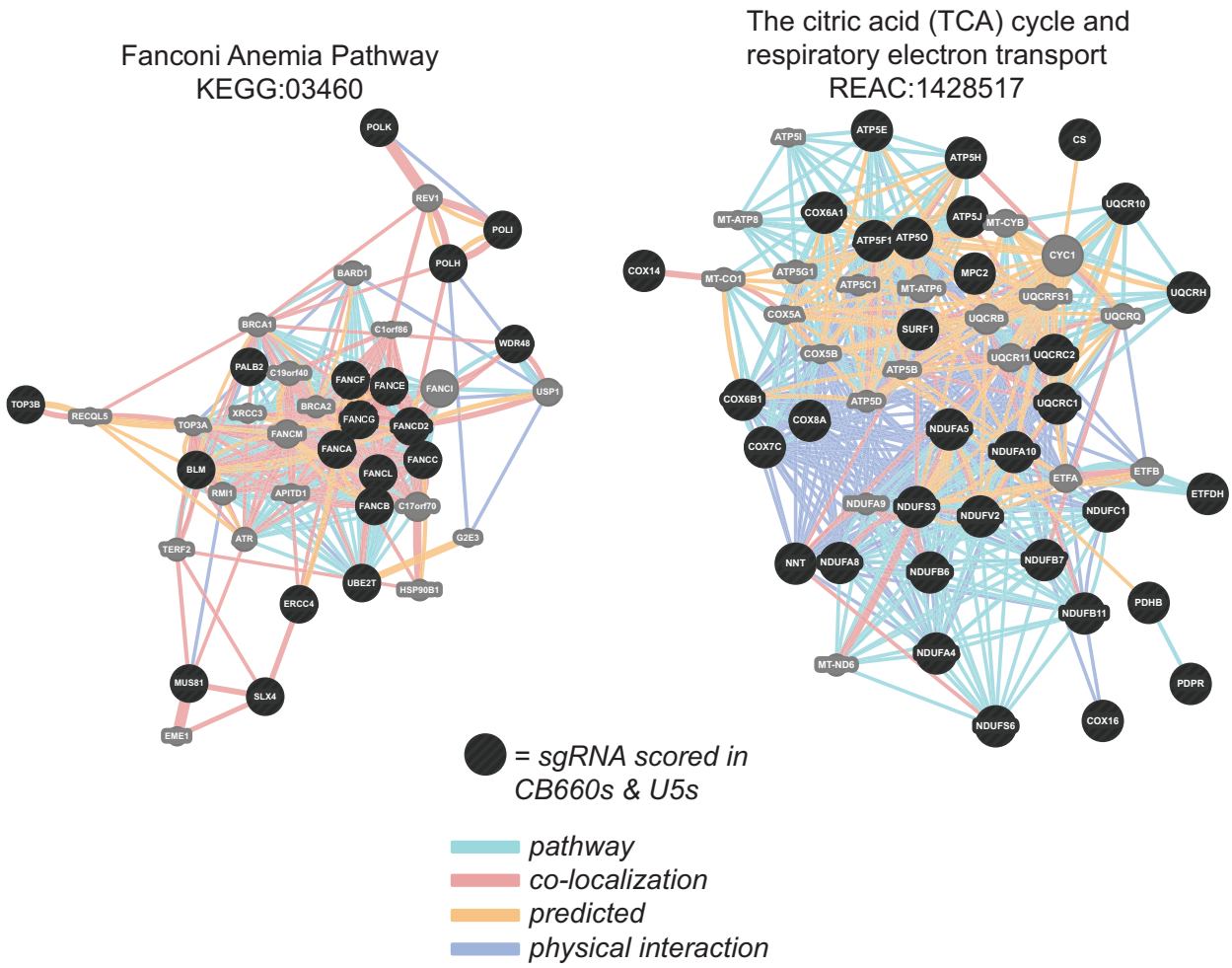

Figure 3.7. Pathway enrichment analysis using NSC-specific screen hits.
Shared NSC-U5 and NSC-CB660-specific hits (logFC<-1.0, FDR<0.05) were analyzed using ToppGene tool suite (toppgene.cchmc.org) for pathway enrichment. The Fanconi anemia pathway (p=7.843E-8) and The Citric Acid (TCA) cycle and respiratory electron transport (p=3.467E-7) were the top scoring pathways with 19 hits scoring among 53 total genes possible for the former and 32 screen hits among 136 total genes for the latter. The screen hits in these pathways were then inputted into GeneMANIA network viewer (www.genemania.org) to obtain the above networks.

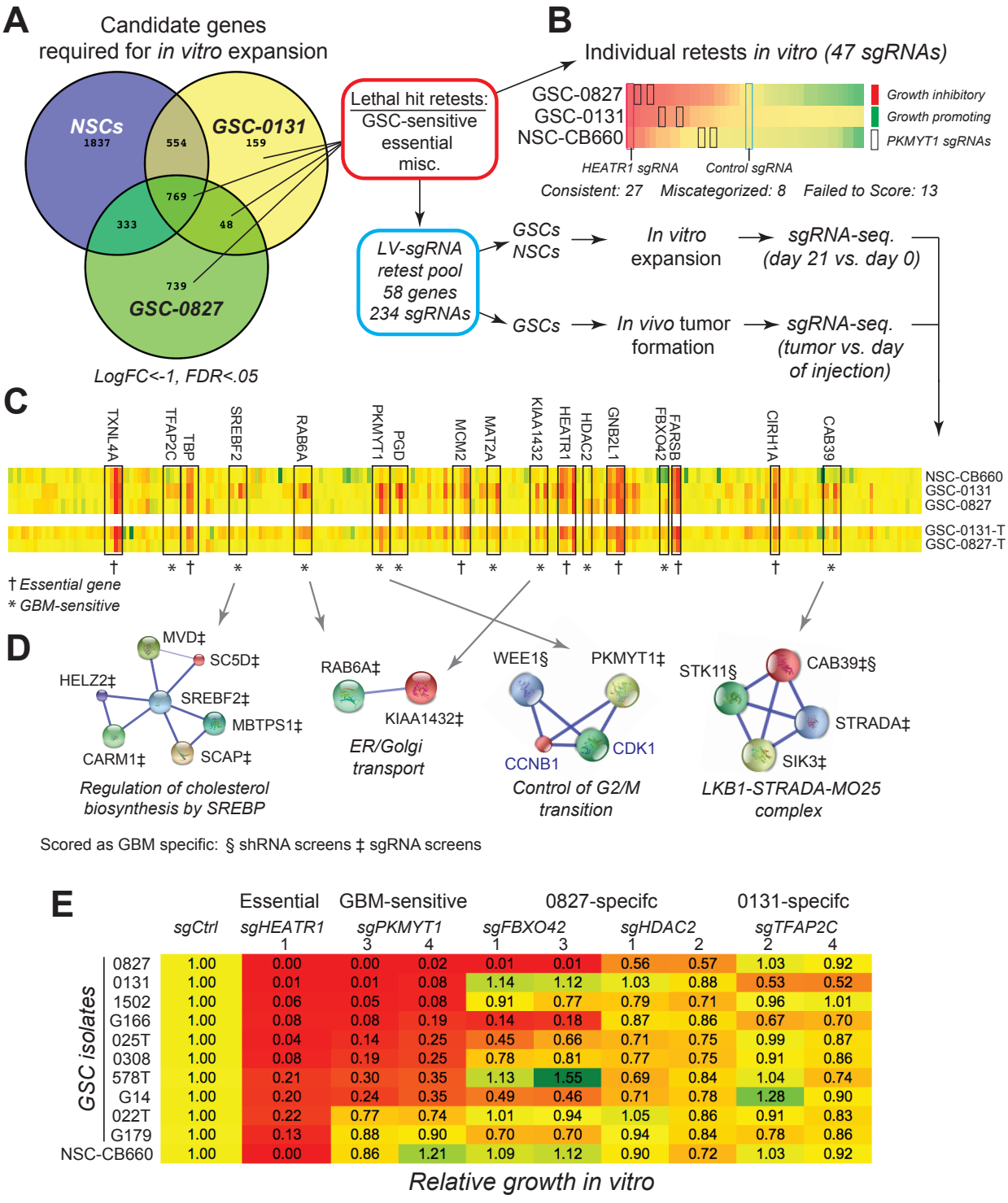

Figure 3.8. Validation of CRISPR-Cas9 screen hits required for GSC expansion *in vitro* and *in vivo*.

(A) Venn diagram showing overlap among candidate genes. sgRNAs with logFC<-1.0 (FDR<0.05) were considered candidate sensitive genes. For simplicity, NSC-U5 and NSC-CB660 were combined.

(B) Heat map of retested candidate sensitive individual sgRNAs (2 sgRNAs/gene; 23 genes). Cells were infected with lentivirus containing individual sgRNAs, and cultured (15-22 days) in triplicate. Overall growth of each sgRNA was calculated and normalized to sgControl. Each sgRNA was categorized as essential, GBM sensitive, or patient-specific according to screen results, and then compared. Figure 3.9 contains sgRNAs scores and Table 3.2 contains source data.
(C) Heat map of retested *in vivo* and *in vitro* pools (58 genes; 3-4 sgRNAs/gene). For *in vivo* studies, GSCs were injected into mice (n=5) following selection (see Methods for details). Tumors were cut into two, sequenced, and scored using limma. -T denotes tumor. See Table 3.1 for pool information and Table 3.2 for source data.
(D) STRING network[241] representations of GSC-specific hits scoring in pooled retest assays, along with other GSC-specific hits either scoring in CRISPR-Cas9 or shRNA genome wide screens (see Results and also Figure 3.10 for details of sgRNA and shRNA screen comparisons).
(E) *In vitro* viability assays retesting individual sgRNAs in multiple GSC isolates for genes indicated. Samples were outgrown for 12 days following selection and assayed by alamar blue or cultured for 18 days following selection and counted with each split every 5-7 days to determine total cell number. All samples were normalized to sgControl. See Table 3.3 for student's t-tests. Figure by Yu Ding and Patrick Paddison.

	Cell growth relative to non-targeting sgRNA control								
sgRNA construct	NSC-CB660 Day 15	NSC-CB660 Day 20	GSC-0131 Day 17	GSC-0131 Day 22	GSC-0827 Day 17	GSC-0827 Day 22	Screen Category	Retest result	Total retests: 47
HEATR1-1	0.09	0.07	0.00	0.00	0.02	0.03	Essential	Confirmed	Confirmed: 27
MAT2A-1	0.10	0.06	0.00	0.00	0.02	0.02	GBM-sensitive	Essential (miscategorized)	Miscategorized: 8
GMPPB-2	0.23	0.18	0.11	0.08	0.09	0.09	GBM-sensitive	Essential (miscategorized)	Failed to Score: 13
GMPPB-1	0.24	0.10	0.10	0.05	0.12	0.13	GBM-sensitive	Essential (miscategorized)	
HEATR1-2	0.37	0.39	0.27	0.20	0.20	0.16	Essential	Confirmed	
GNB2L1-2	0.48	0.42	0.05	0.03	0.00	0.00	Essential	Confirmed	
MAT2A-2	0.59	0.55	0.40	0.33	0.31	0.35	GBM-sensitive	Essential (miscategorized)	
GNB2L1-1	0.60	0.57	0.16	0.15	0.02	0.01	Essential	Confirmed	
NAA15-1	0.60	0.62	0.33	0.24	0.25	0.19	Essential	Confirmed	
KIAA1704-2	0.70	0.90	0.87	1.00	1.25	1.51	0827-Specific	Failed to score	
KIAA1432-1	0.71	0.71	0.12	0.06	0.30	0.35	0131-sensitive	Confirmed	
UNG-1	0.84	0.98	0.92	0.92	0.67	0.80	0827-Specific	Confirmed	
ZBTB33-2	0.85	0.95	0.89	0.94	0.26	0.20	0827-Specific	Confirmed	
LAMB3-1	0.86	0.95	0.87	0.97	0.15	0.16	0827-Specific	Confirmed	
PKMYT1-1	0.87	0.91	0.59	0.64	0.20	0.22	GBM-sensitive	Confirmed	
PAX6-2	0.88	1.10	0.81	0.83	1.17	1.42	0131-Specific	Confirmed	
PTK2B-2	0.91	1.14	0.86	0.93	1.95	2.14	0827-Specific	Failed to score	
PKMYT1-2	0.92	1.03	0.44	0.44	0.09	0.11	GBM-sensitive	Confirmed	
RAB10-1	0.96	1.02	0.88	0.89	1.29	1.41	0827-Specific	Failed to score	
EGFP	0.99	1.19	0.89	0.94	0.92	0.93	Control	Confirmed	
PYGO2-2	1.00	0.98	0.85	0.87	1.37	1.61	GBM-sensitive	Failed to score	
NTC	1.00	1.00	1.00	1.00	1.00	1.00	Control	Confirmed	
CARM1-1	1.02	1.16	0.93	0.93	0.34	0.21	GBM-sensitive	0827-specific (miscategorized)	
KIAA1432-2	1.03	0.98	0.91	0.92	1.83	1.93	0131-sensitive	Failed to score	
UNG-2	1.04	1.27	0.88	0.93	0.70	0.88	0827-Specific	Confirmed	
PYGO2-1	1.05	1.11	0.83	0.94	0.82	1.13	GBM-sensitive	Failed to score	
RAB10-2	1.05	1.04	0.84	0.82	1.96	2.00	0827-Specific	Failed to score	
LAMB3-2	1.05	1.01	0.84	0.89	1.70	1.82	0827-Specific	Failed to score	
TYRO3-2	1.06	1.16	0.90	0.95	0.99	1.08	0131-Specific	Failed to score	
CARM1-2	1.06	1.14	0.96	1.03	0.46	0.28	GBM-sensitive	0827-specific (miscategorized)	
ZBTB33-1	1.09	1.17	0.90	0.93	1.00	1.12	0827-Specific	Failed to score	
PAX6-1	1.10	1.22	0.80	0.89	1.22	1.30	0131-Specific	Confirmed	
NAA15-2	1.12	1.15	0.75	0.77	2.07	2.10	Essential	Failed to score	
PTK2B-1	1.12	1.23	0.86	0.92	1.40	1.52	0827-Specific	Failed to score	
FBXO42-2	1.14	1.33	0.81	0.86	0.49	0.61	0827-Specific	Confirmed	
KIAA1704-1	1.17	1.23	0.89	1.01	1.73	1.82	0827-Specific	Failed to score	
TYRO3-1	1.20	1.35	0.78	0.86	2.16	2.23	0131-Specific	Confirmed	
PTPN14-2	1.25	1.49	0.94	1.08	0.57	0.51	0131-Specific	0827-specific (miscategorized)	
FBXO42-1	1.25	1.36	0.81	0.88	0.10	0.12	0827-Specific	Confirmed	
HDAC2-2	1.26	1.39	0.86	0.96	0.21	0.21	0827-Specific	Confirmed	
HDAC2-1	1.26	1.35	0.88	1.03	0.10	0.06	0827-Specific	Confirmed	
TFAP2C-1	1.36	1.49	0.33	0.23	1.31	1.46	0131-Specific	Confirmed	
TFAP2C-2	1.37	1.58	0.34	0.26	2.27	2.24	0131-Specific	Confirmed	
PTPN14-1	1.52	1.67	0.86	0.98	1.46	1.57	0131-Specific	Failed to score	
CAND1-1	1.88	2.18	0.58	0.56	1.87	1.73	0131-Specific	Confirmed	
CAND1-2	1.92	2.22	0.64	0.59	1.71	1.67	0131-Specific	Confirmed	
NF2-4	2.33	2.81	0.68	0.75	2.42	2.64	0131-Specific	Confirmed	
NF2-3	2.38	2.82	0.64	0.77	2.40	2.58	0131-Specific	Confirmed	

Figure 3.9. Heat map depicting the results of the *in vitro* individual sgRNA retest of the lethal pool in NSCs and GSCs.

NSCs and GSCs were infected with lentivirus containing individual sgRNAs to the respective gene or to control. Following selection, cells were harvested, counted, and plated in triplicate. Cells were routinely cultured for 15-22 days (split every 3-4 days), and counted at each split. The overall growth of each well containing an individual sgRNA was calculated and compared to the sgControl well. The growth defects were graphed using the ratio between the individual sgRNAs to sgControl. Following the screen results, each sgRNA was categorized as essential, GBM sensitive, or patient specific. Following the individual retest, each sgRNA was compared to its assigned category from the screen results to determine whether the sgRNA was scored correctly. Source data can be found in Table 3.2. Figure by Yu Ding and Patrick Paddison.

A

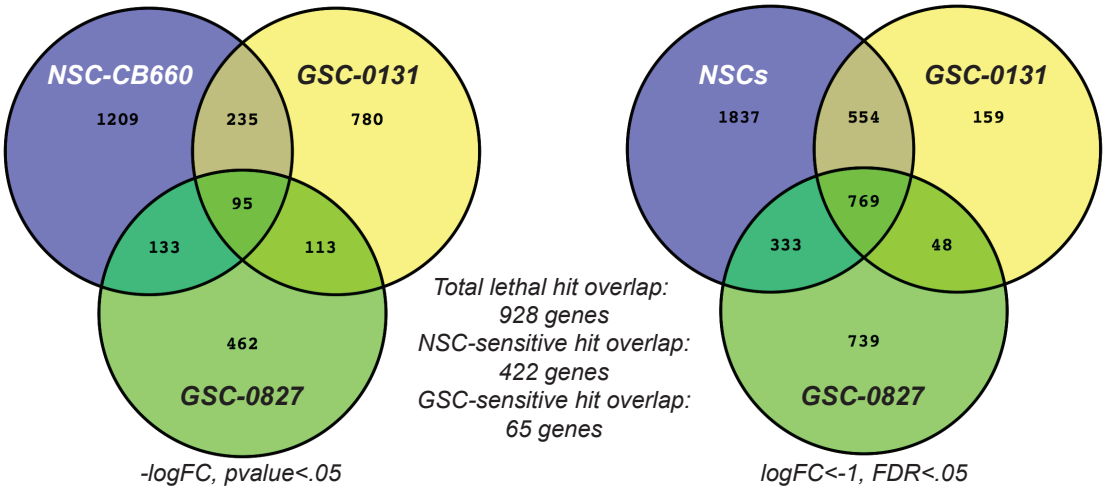

B

ID	Name	pValue	Total hits	shRNA hits	sgRNA hits	Genes in Annotation
160950	Processing of Capped Intron-Containing Pre-mRNA	8.33E-08	40	30	10	143
105765	Cell Cycle, Mitotic	2.06E-06	81	56	25	416
530733	Cell Cycle	2.93E-06	95	64	31	514
105951	mRNA Splicing	2.99E-06	31	25	6	112
83056	Ubiquitin mediated proteolysis	5.23E-06	35	26	9	137
MAP00240	MAP00240 Pyrimidine metabolism	8.35E-05	15	14	1	44

C

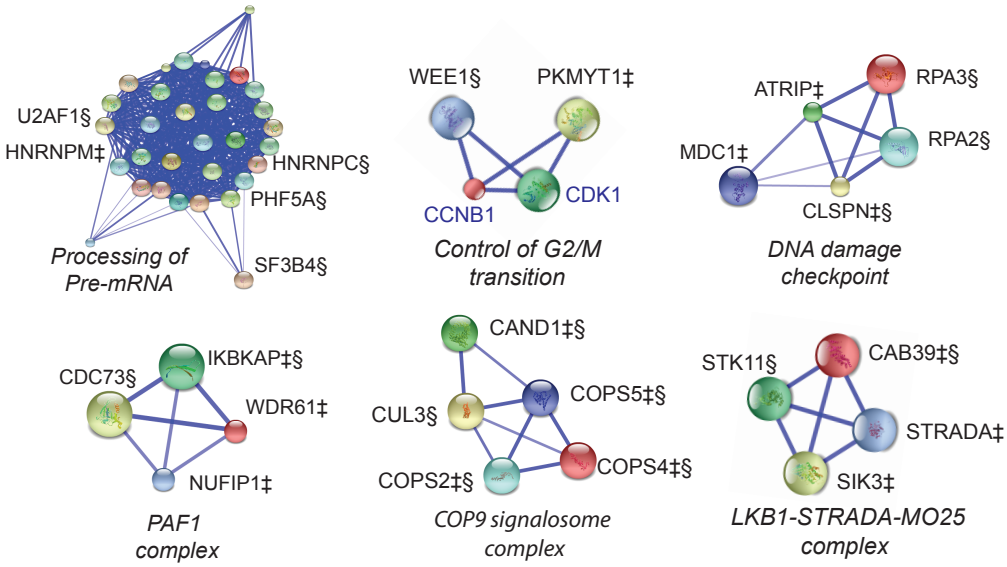

Scored as GBM specific in: § shRNA screens ‡ sgRNA screens

Figure 3.10. Comparison of genome-wide shRNA and sgRNA screen hits required for *in vitro* expansion of NSCs and GSC-0131 and GSC-0827 isolates.

(A) Venn diagrams showing overlap of lethal screen hits from previously published genome-wide shRNA screens[42] (left) and CRISPR-Cas9 screens from the current studies (right) in NSC-CB660, GSC-0131, and GSC-0827 cells. **(B)** Pathway enrichment for combined candidate GBM-specific lethals for both shRNA and sgRNA screens, primary showing enrichment for processing of pre-mRNA/mRNA splicing and cell cycle related genes among shared hits. Analysis was performed using ToppGene gene enrichment analysis[242].

(C) Combined shRNA and sgRNA GBM-specific hits were evaluated using STRING network analysis[241]. Those shown are networks with 4 or more nodes. Note that *CCNB1* and *CDK1* were added to illustrate WEE1 and PKMYT1 interactions with cyclin B-CDK1 complex and did not score as GBM-specific. Thus, although there was little overlap among GBM-specific screen hits, the results suggest that screens nonetheless converged on these networks/pathways, which implies cross validation.

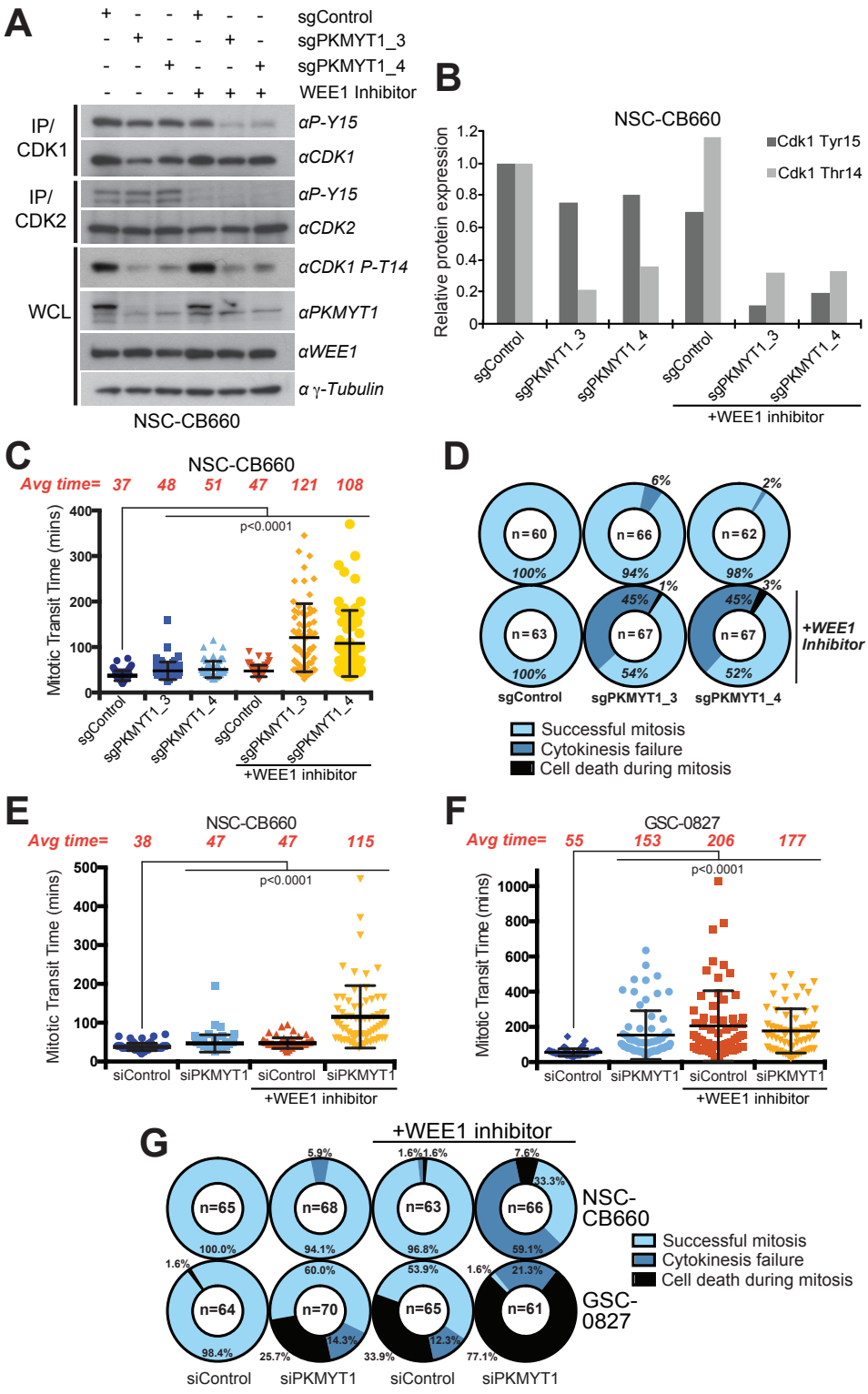

Figure 3.11. Molecular and phenotypic characterization of PKMYT1 function in GSCs and NSCs.

(A) PKMYT1 and WEE1 act redundantly to phosphorylate CDK1-Y15 in NSC-CB660 cells. Western blot analysis on whole cell lysates (WCL) or following immunoprecipitation (IP) of CDK1 or CDK2. NSC-CB660s were

outgrown for 14 following selection, and then treated with 300nM of MK1775 (WEE1 inhibitor) for 6 hours or mock-treated. PKMYT1 antibody recognizes a non-specific protein that appears below PKMYT1 predicted molecular weight.
(B) Semi-quantification of western blot in (**A**) using ImageJ software. Each band was normalized to their respective sgControl (-MK1775) sample.
(C) and **(D)** PKMYT1 and WEE1 act redundantly in NSC-CB660 cells to promote timely completion of mitosis.
(C) Mitotic transit times (MTTs) of individual NSC-CB660 cells after *PKMYT1* KO, -/+ WEE1 inhibition (minimum of 6 hours). NSC-CB660s were outgrown for 15 days following selection, treated with MK1775 (300nM) or mock-treated, and subjected to time-lapse microscopy for 72 hours. Mann-Whitney test; $n \geq 60$ cells/condition; $\pm$SD.
(D) Phenotypic outcome of mitotic cells observed in (C). See Methods for details. A cell was considered to enter mitosis when nuclear envelope breakdown was visible or when a morphology change was observed (from flat to rounded-up).
(E-G) PKMYT1 and WEE1 redundancy is lost in GSC-0827**.**
(E) and **(F)** Mitotic transit time of individual NSC-CB660 (E) and GSC-0827 (F) cells after *PKMYT1* depletion, -/+ WEE1 inhibition (minimum of 6 hours). Cells were transfected, treated with MK1775 (300nM) or mock-treated (48 hours after initial transfection), and subjected to time-lapse microscopy for 48 hours. Mann-Whitney test; $n \geq 60$ cells/condition; $\pm$SD.
(G) Phenotypic outcome of mitotic cells observed in (E) and (F).

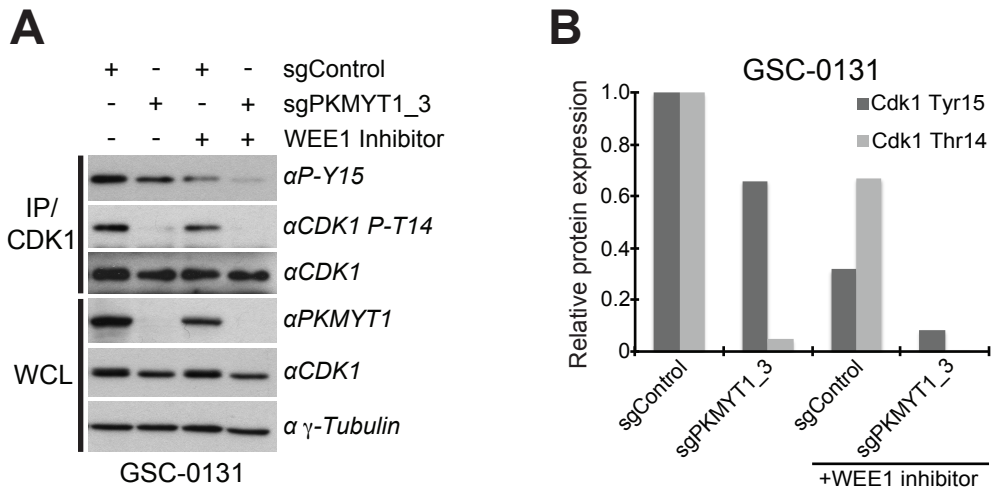

Figure 3.12. *In vitro* molecular function of PKMYT1 in GSCs.

PKMYT1 and WEE1 act redundantly to phosphorylate CDK1-Y15 in GSC-0131. However, there is a slight reduction in phosphorylation of CDK1-Y15 upon KO of *PKMYT1* or WEE1 inhibition, which suggest some loss of redundancy in GSCs.

(A) Western blot analysis on whole cell lysates (WCL) or following immunoprecipitation (IP) of CDK1. GSC-0131s were outgrown for 4 days following selection, and then treated with 300nM of MK1775 (WEE1 inhibitor) for 6 hours or mock-treated.

(B) Semi-quantification of western blot in **(A)** using ImageJ software. Each band was semi-quantified and then normalized to their respective sgControl (-MK1775) sample.

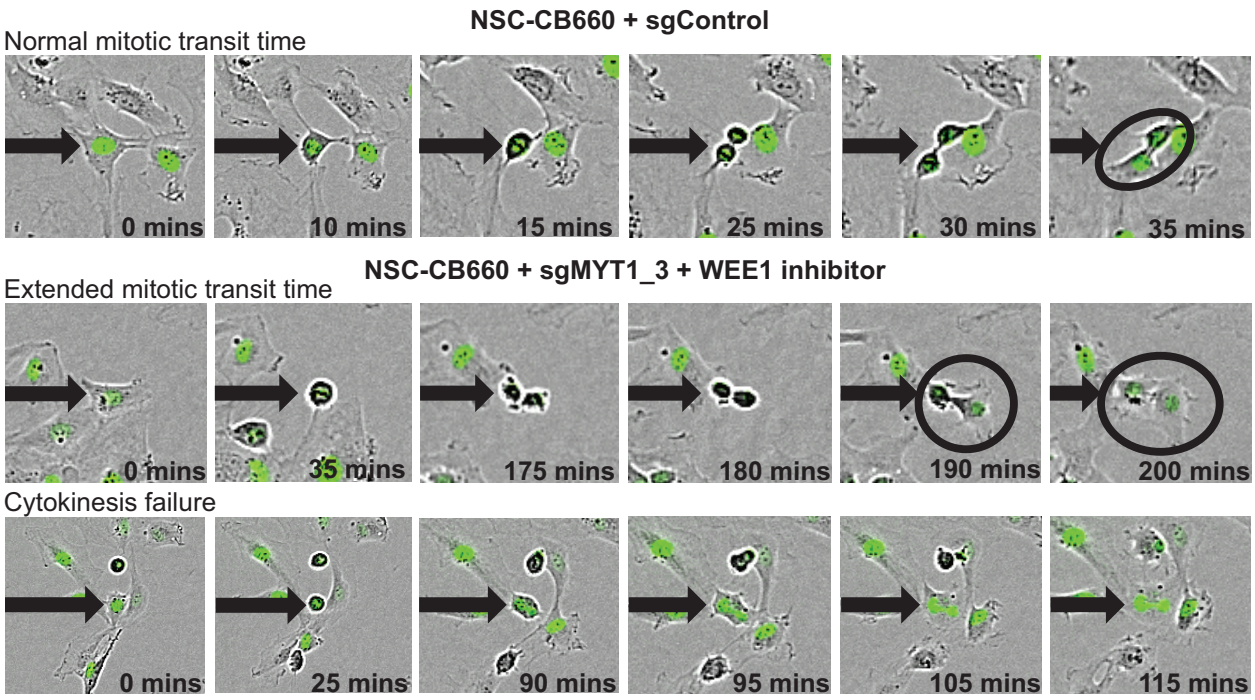

Figure 3.13. *PKMYT1* loss with or without WEE1 inhibition in NSCs results in extended mitotic transit time, cytokinesis failure, and cell death during mitosis.
Images of time-lapse microscopy from Figures 3.11C and 3.11D. NSC-CB660s were transduced with individual sgRNA constructs to *PKMYT1* and control, selected for 4 days, and outgrown for 15 days. Cells were then treated with 300nM of the WEE1 inhibitor MK1775 or mock-treated, followed by time-lapse microscopy for 72 hours. Images were acquired at 5-minute intervals. Mitotic transit time was analyzed for individual cells following 6 hours of WEE1 inhibition.

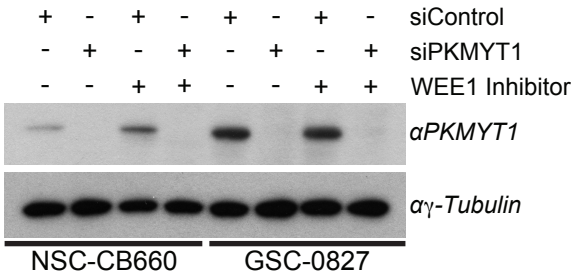

Figure 3.14. Protein expression levels following *PKMYT1* depletion by RNAi with or without WEE1 inhibition in NSCs and GSCs.

PKMYT1 depletion with siRNAs in NSC-CB660 and GSC-0827 -/+ MK1775 (WEE1 inhibitor). Western blot analysis on whole cell extracts that were transfected with siControl or *siPKMYT1* (see Methods for details) for 24 hours. Following 48 hours from the initial transfection, cells were treated with 300nM of MK1775 (WEE1 inhibitor) for 6 hours or mock-treated, and harvested for protein extraction.

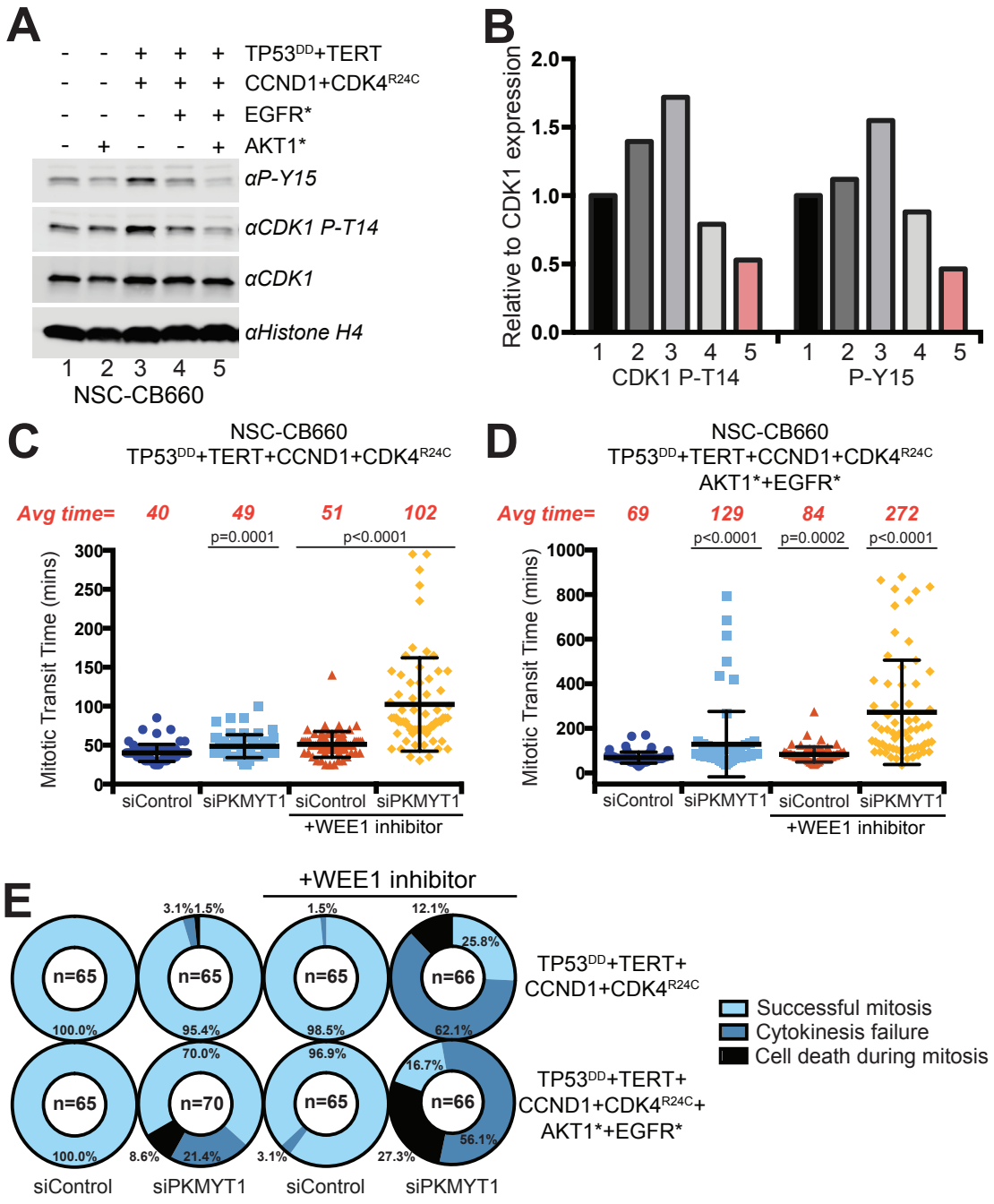

Figure 3.15. Constitutively active alleles of *EGFR* and *AKT* sensitize NSCs to *PKMYT1* depletion.

(A) and **(B)** *EGFR** and *AKT** cause a depletion of steady-state levels of CDK1/2-Y15 and CDK1-T14 phosphorylation in NSC-CB660 cells.

(A) Western blot analysis of total CDK1/2-Y15 phosphorylation and CDK1-T14 phosphorylation using whole cell lysates (WCL). Histone H4 was used as a loading control. Lane number corresponds to its respective number in (B). Note that TP53 and RB-axis pathway perturbations are required to bypass *EGFR**-induced senescence and apoptosis in NSCs. Thus, *EGFR** experiments could not be carried out alone.

(B) Semi-quantitative analysis of western blot from (A). Samples were first normalized to their respective loading control followed by their respective CDK1 expression.

(C-E) *EGFR** and *AKT1** induce the requirement for *PKMYT1* in NSC-CB660 cells.
(C) and **(D)** Mitotic transit time of individual genetically altered NSCs after *PKMYT1* depletion, -/+ WEE1 inhibition (minimum of 6 hours). Cells were transfected, treated with MK1775 (300nM) or mock-treated (48 hours after initial transfection), and subjected to time-lapse microscopy for 48 hours. Mann-Whitney test; $n \geq 65$ cells/condition; $\pm$SD.
(E) Phenotypic outcome of mitotic cells observed in (C) and (D). Analysis was conducted as in Figure 3.11.

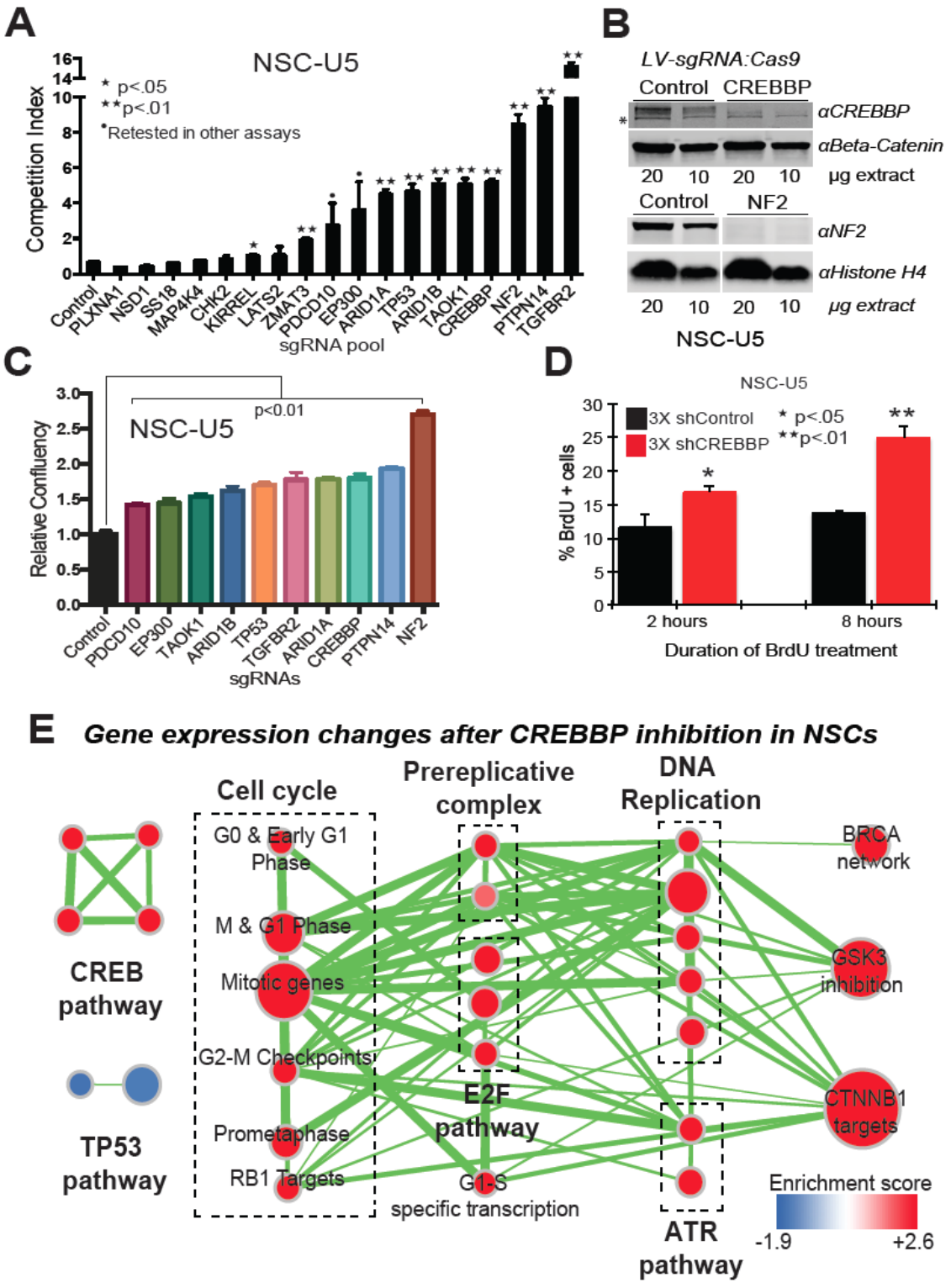

Figure 3.16. Validation and characterization of growth limiting screen hits for NSCs.
(A) *In vitro* competition assays retesting sgRNAs overrepresented in NSC outgrowth screens. Cells were infected with lentiviral gene pools containing 3-4 sgRNAs per gene, and mixed with GFP+ NSCs at an approximate 1:9 ratio, respectively. Cultures were outgrown for 23-31 days, and flow analyzed every 7-8 days for GFP. Competition index

is the percent of GFP- cells at each time point divided by the percent of GFP- cells at the start of the experiment. n=3, Student's t-test (unpaired, unequal variance), +SD.
(B) Western blot of CREBBP and NF2 expression after sgRNA:Cas9 KO. *Indicates non-specific protein band.
(C) Time-lapse microscopy results examining confluency of NSC-U5s manipulated as in Figure 3.16A and outgrown for 13 days. Cells were imaged at 60 min intervals for 72 hours. Samples were first normalized to their respective time 0 point and then to the sgControl. n=3, Student's t-test (unpaired, unequal variance), +SD.
(D) *CREBBP* inhibition increases NSCs proliferation. NSCs were infected with lentivirus containing 3xmiR30-based shRNAs, and outgrown for 14 days. Cells were treated with 10μM of bromodeoxyuridine (BrdU), and analyzed for BrdU incorporation (see Methods for details). Student's t-test (unpaired, unequal variance), n>1,085 cells/condition; +SD.
(E) GSEA network of RNA-Seq data from NSC-CB660s infected with lentiviruses containing 3xmiR30-based shRNAs, and outgrown for 6 days (see Methods for details). Node size represents the number of genes in each gene-set, and edge thickness is proportional to the overlap between gene sets.

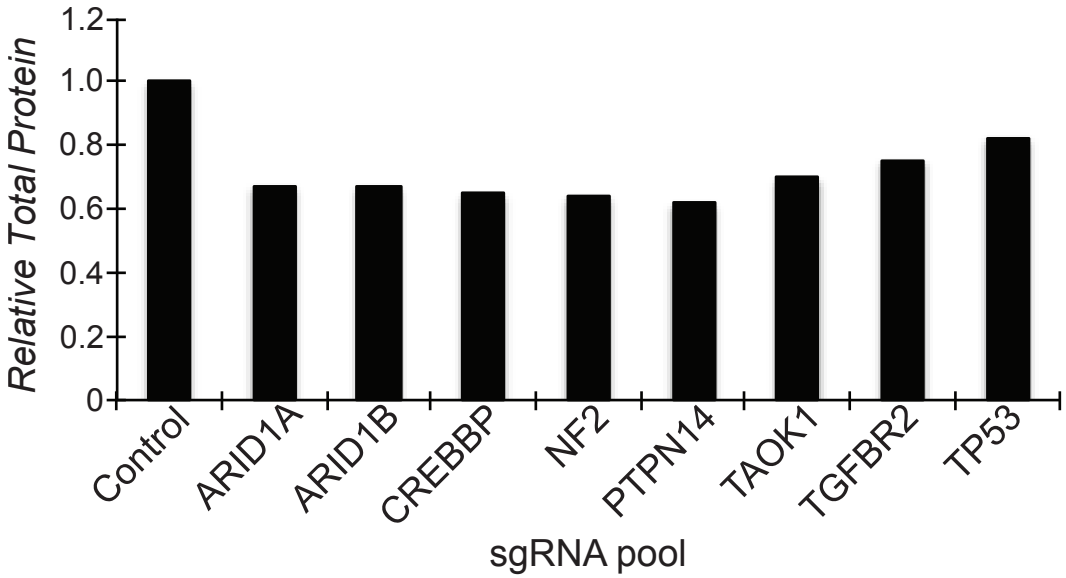

Figure 3.17. Knockout of growth-limiting genes in NSCs leads to a decrease in total protein.

Deletion of growth-limiting genes in NSCs causes a decrease in cell cycle transit times, which then leads to a decrease in total protein, presumably due to a shorter G1 phase. Cells were infected with lentiviral gene pools containing 3-4 sgRNAs per gene, puromycin selected, and outgrown. Cells were maintained under puromycin selection for an additional 3 days following the initial selection. Following 19 days (*ARID1A*, *NF2*, and *TGFβR2* samples), 20 days (*PTPN14*), 21 days (*ARID1B*), 22 days (*CREBBP*, *TAOK1*, and *TP53*), and 38 days (control), 3 million cells were from each samples were harvested and lysed in a modified RIPA buffer (see Methods). Total protein was then quantified using Perce 660nm protein assay reagent.

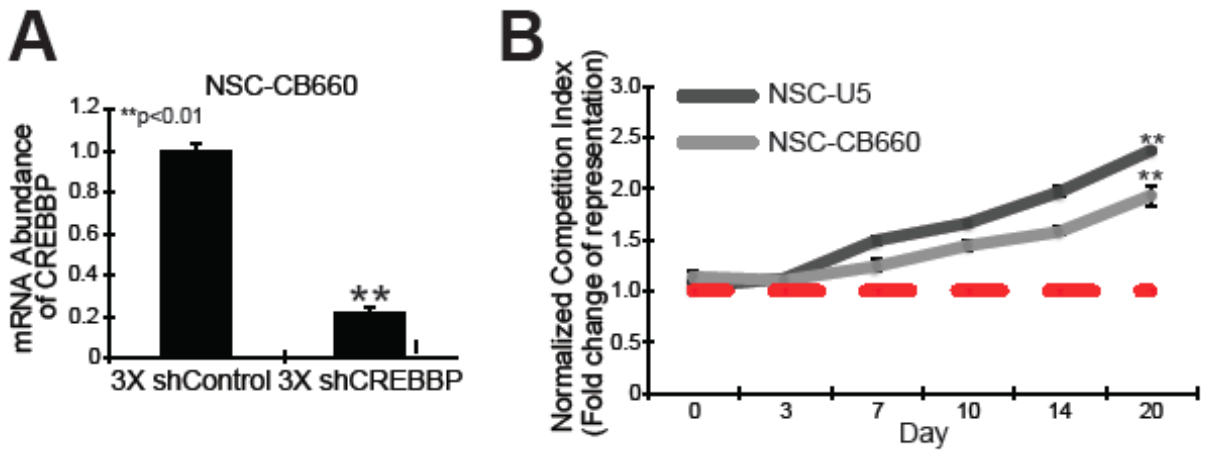

Figure 3.18. *CREBBP* inhibition increases proliferation in NSCs.
(A) Quantitative RT-PCR (qRT-PCR) for *CREBBP* mRNA expression of whole cell extracts from NSC-CB660 following shRNA knockdown of *CREBBP*. n=4 technical replicates, Student's t-test (unpaired, unequal variance), **p<0.01, +SD.
(B) NSCs with *CREBBP* inhibition outgrew wild type NSCs in *in vitro* competition assays. Cells were infected with lentiviruses containing 3xmiR30-based shRNAs to *CREBBP* or control, selected for 4 days, and mixed with wild type NSCs at an approximate 1:4 ratio, respectively in triplicate. Cultures were outgrown for 20 days and flow analyzed every 3-6 days for GFP expression. Competition index is the percent of GFP+ cells at each time point divided by the percent of GFP+ cells at the start of the experiment. Normalized competition index is the competition index for the 3xmiR30-based *shCREBBP* sample normalized to the competition index for the 3xmiR30-based shControl sample. Student's t-test (unpaired, unequal variance), **p<0.01, +SD.

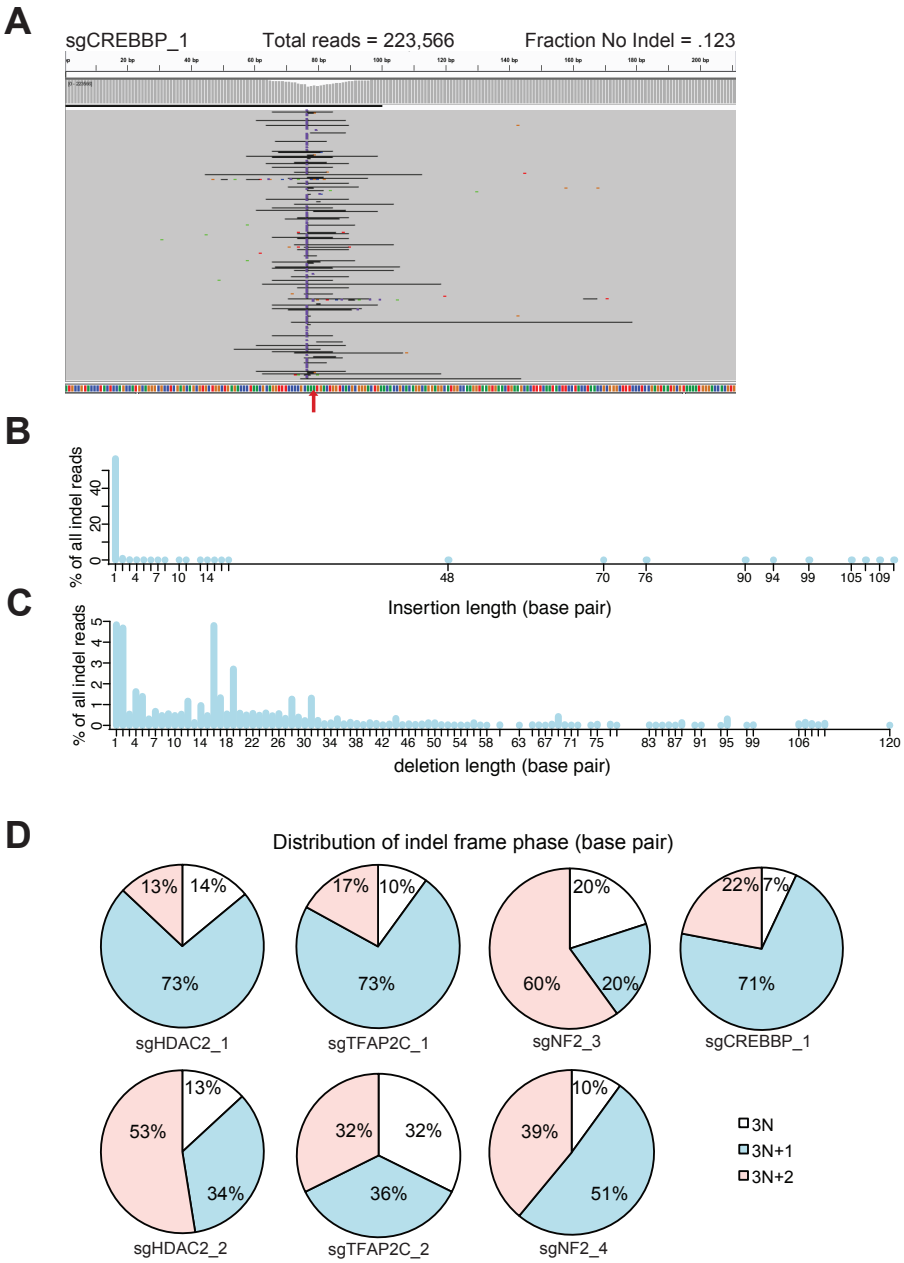

Figure 3.19. Analysis of alteration induction by sgRNAs for multiple validating screen hits in NSC-CB660 cells.

Cells were transduced with individual sgRNAs to *CREBBP*, *NF2*, *TFAP2C*, or *HDAC2* at MOI<1, selected, and outgrown for 12 days (*sgCREBBP*) or 21 days (remaining sgRNAs). The ~250bp genomic region around the target locus was then PCR amplified and deep-sequenced.

(A) Integrative Genomics Viewer (IGV) image of 220 representative deep sequencing reads for *sgCREBBP_1*. Red arrow denotes predicted Cas9 cutting site. 4-colored line above the red arrow shows the reference sequence. Black or purple bars in grey sequencing reads indicate deletions or insertions, respectively. Other colors within grey sequencing reads indicate SNPs, possibly due to PCR or sequencing error.

(B) Frequency and distribution of insertion length for the sample *sgCREBBP_1*.

(C) Frequency and distribution of deletion length for the sample *sgCREBBP_1*.

(D) Frame phase of all indels for each of the 7 sgRNA samples, calculated as the length of indels modulus 3. Note that 3N equals in-frame. Figure by Pia Hoellerbauer and Hamid Bolouri.

Tables

Controls:
RNA name
Control
EGFP

Sensitive pool (includes GBM-sensitive and essential genes):			
AC114947.1	FARSB	METTL14	TAF5L
ACBD6	FBXO42	NAA15	TBP
ANKFY1	GABRR2	PAX6	TFAP2C
ATP6V1G1	GMPPB	PGD	TRMT1L
BBX	GNB2L1	PKMYT1	TRNAU1AP
CAB39	H2AFX	PTK2B	TSC2
CAND1	HDAC2	PTPN14	TXNL4A
CARM1	HEATR1	PYGO2	TYRO3
CCNC	KCTD10	RAB10	UBASH3B
CIRH1A	KIAA1432	RAB6A	UNG
CNEP1R1	KIAA1704	RASA2	YTHDF2
CNOT1	LAMB3	RBM43	ZBTB33
CYB5B	MAT2A	RMND1	ZNF425
EMC7	MBTPS1	SREBF2	
FAM126A	MCM2	STX12	
Growth-limiting genes:			
ARID1A	KIRREL	PDCD10	TGFBR2
ARID1B	LATS2	PLXNA1	TP53
CHEK2	MAP4K4	PTPN14	ZMAT3
CREBBP	NF2	SS18	
EP300	NSD1	TAOK1	

Table 3.1. Genes examined and sgRNA sequences used for validation studies.

Table 3.2. CRISPR-Cas9 *in vitro* and *in vivo* retests analyses for candidate sensitive genes (see attached Excel file).

The average ratios of candidate sgRNAs compared to their respective controls with standard deviation (STDEV) for individual sgRNA retests in NSC-CB660, GSC-0827, and GSC-0131 (Figure 3.8B) can be found in this table. In addition, GSC-0827 and GSC-0131 log fold change (FC) values for each sgRNA from the *in vitro* pool retests are compared to the NSC-CB660 logFC values for each sgRNA from the *in vitro* pool retests. Moreover, the GSC-0827 and GSC-0131 logFC values for each sgRNA from the *in vivo* pool retests are listed here. Lastly, each gene is categorized as essential, cancer-lethal, patient-specific lethal, or other based upon the retest analyses. Table by Yu Ding and Patrick Paddison.

TTEST	CB660	131	827	G166	1502	308	G179	025T	022T	G14	578T
sgControl	na	na	na	na	na	na	na	na	na	na	na
sgHEATR1-1	0.0002	0.0001	0.0001	0.0006	0.0025	0.0002	0.0022	0.0082	0.0054	0.0175	0.0051
sgPKMYT1-3	0.0017	0.0001	0.0001	0.0003	0.0021	0.0001	0.2780	0.0102	0.0748	0.0168	0.0065
sgPKMYT1-4	0.0353	0.0001	0.0001	0.0000	0.0022	0.0004	0.2360	0.0127	0.0419	0.0240	0.0083
sgTFAP2C-2	0.5865	0.0259	0.3136	0.0018	0.5025	0.0449	0.0535	0.9573	0.3166	0.1162	0.7871
sgTFAP2C-4	0.3739	0.0298	0.1197	0.0011	0.8414	0.0105	0.2303	0.2729	0.1330	0.5102	0.0368
sgFBXO42-1	0.2708	0.3058	0.0001	0.0004	0.2001	0.0110	0.0208	0.0097	0.9006	0.0252	0.5223
sgFBXO42-3	0.2909	0.5489	0.0002	0.0001	0.0251	0.0040	0.0171	0.0470	0.4749	0.0326	0.0496
sgHDAC2-1	0.2111	0.7905	0.0001	0.1308	0.0338	0.0479	0.4462	0.0701	0.5164	0.1059	0.0224
sgHDAC2-2	0.0134	0.3402	0.0035	0.0329	0.0163	0.0252	0.2180	0.1315	0.1344	0.2836	0.2335
										p<0.01	p<0.05

Table 3.3. P-values of each individual sgRNA retested in Figure 3.8E.

Student's t-test (unpaired, unequal variance) was performed for each individual sgRNA in comparison to its respective sgControl. Red filled boxes corresponds to sgRNAs that have a P-value of less than 0.01 and yellow filled boxes corresponds to sgRNAs that have P-value of less than 0.05.

Table 3.4 Candidate growth-limiting genes from the genome-wide CRISPR screen results in NSCs (see attached Excel file).

Screen results from the initial genome-wide CRISPR screens in NSC-CB660 and NSC-U5 isolates were compared and analyzed. sgRNAs with a log fold change greater than 1 and a false-discovery rate of less than 0.05 were considered to be significant scoring sgRNAs and were used for further analyses. Genes that had more than 1 or more significantly scoring sgRNAs in both the NSC-CB660 and NSC-U5 screens or that had more than 2 significantly scoring sgRNAs in NSC-CB660 or NSC-U5 screens were considered candidate growth-limiting genes. Each gene was then examined to determine if the gene is commonly mutated in pediatric and/or adult glioma/GBM. Interestingly, many candidate growth-limiting genes have been implicated in promoting neural development or brain function, causal roles in human syndromes affecting brain function, TP53 signaling, or antagonizing Hippo signaling. These genes are highlighted in this table.

Gene Name*	# sgRNAs scored NSC-CB660 NSC-U5	Log2FC of each sgRNA	Retest in competition assay (Figure 3.16A)?	Retest in individual growth assay (Figure 3.16C)?	Mutation/loss frequency in adult glioma/GBM and pediatric glioma/GBM	Highest mutation/loss frequency in non-glioma cancers (TCGA) [www.cbioportal.org]	Function (Reference)
NF2	4 of 4 4 of 4	3.24, 4.68, 3.57, 1.56 5.81, 6.61, 7.44, 4.64	**Yes**	**Yes**	1.03% -	7% - Kidney Renal Papillary Cell Carcinoma 6% - Pancreatic Adenocarcinoma	Hippo signaling antagonist (PMID:20643348)
PTPN14	4 of 4 4 of 4	2.37, 2.47, 2.07, 1.85 6.03, 6.65, 5.89, 4.38	**Yes**	**Yes**	1.20% 1.47%	14% - Pancreatic Adenocarcinoma 7.8% - Uterine Corpus Endometrial Carcinoma	Hippo signaling antagonist (PMID:22948661)
CREBBP	4 of 4 4 of 4	1.74, 1.40, 1.61, 1.74 3.58, 3.72, 3.29, 3.36	**Yes**	**Yes**	2.06% 0.74%	16.5% - Bladder Urothelial Carcinoma 10.9% - Stomach Adenocarcinoma	chromatin remodeling; tumor suppression (PMID:22941188)
TAOK1	3 of 3 3 of 3	2.57, 1.89, 1.28 4.42, 4.27, 3.20	**Yes**	**Yes**	0.86% -	4.1% - Stomach Adenocarcinoma 3.7% - Uterine Corpus Endometrial Carcinoma	Hippo signaling antagonist (PMID:22075148)
TP53	3 of 4 3 of 4	4.05, 1.60, 2.62 4.72, 2.30, 3.28	**Yes**	**Yes**	39.97% 16.91%	94.9% - Ovarian Serous Cystadenocarcinoma 91.1% - Uterine Carcinosarcoma	p53 signaling pathway (KEGG:04115)
KIRREL	5 of 6 4 of 6	2.13, 2.50, 1.46, 1.96, 1.21 1.63, 1.82, 1.49, 1.56	**Yes**	**n/d**	1.03% -	5.4% - Uterine Corpus Endometrial Carcinoma 4.5% - Stomach Adenocarcinoma	kidney glomerular podocytes (PMID:11416156)
PDCD10	4 of 5 3 of 5	1.28, 2.28, 1.59, 1.51 1.24, 1.10, 1.31	**Tendency**	**Yes**	1.03% 0.74%	<1% for TCGA cancers	cell proliferation/apoptotic pathways (Uniprot)
TGFBR2	1 of 5 5 of 5	0.84 3.47, 3.44, 3.70, 3.13, 0.92	**Yes**	**Yes**	1.20% -	12% - Kidney Renal Papillary Cell Carcinoma 10.4% - Colorectal Adenocarcinoma	TGF-beta signaling (Uniprot)
ZMAT3	3 of 5 3 of 5	1, 0.98, 0.82 1.92, 1.27, 1.33	**Yes**	**n/d**	1.72% 1.47%	3.7% - Uterine Corpus Endometrial Carcinoma 3.6% - Uterine Carcinosarcoma	p53 pathway signaling (PMID:12135743)
MAP4K4	1 of 3 2 of 3	1.17 1.17, 1.31	**No**	**n/d**	0.69% -	4.5% - Lung Squamous Cell Carcinoma 4.1% - Stomach Adenocarcinoma	response to environmental stress and cytokines (Uniprot)
EP300	1 of 4 3 of 4	1.09 1.91, 1.77, 1.20	**Tendency**	**Yes**	1.03% 1.47%	18.1% Bladder Urothelial Carcinoma 12.1% - Cervical Squamous Cell Carcinoma	chromatin remodeling; tumor suppression (PMID:24390348)
CHEK2	2 of 2 0 of 2	1.85, 2.01	**No**	**n/d**	3.09% -	15.6% - Pancreatic Adenocarcinoma 8% - Adrenocortical Carcinoma	DNA damage checkpoint; p53 signaling pathway (KEGG:04115)
SS18	1 of 4 2 of 4	2.23 1.21, 1.58	**No**	**n/d**	0.86% -	6.6% - Pancreatic Adenocarcinoma 3.6% - Stomach Adenocarcinoma	transcriptional coactivator (Uniprot)
ARID1B	1 of 4 2 of 4	1.1 1.7, 1.32	**Yes**	**Yes**	2.57% 0.74%	10.8% - Stomach Adenocarcinoma 10.8% - Skin Cutaneous Melanoma	chromatin remodeling & tumor suppression (PMID:23355908)
ARID1A	0 of 4 3 of 4	 3.16, 2.40, 0.85	**Yes**	**Yes**	2.74% -	33.3% - Uterine Corpus Endometrial Carcinoma 33.1% - Stomach Adenocarcinoma	chromatin remodeling & tumor suppression (PMID:23208470)
LATS2	1 of 3 1 of 3	2.66 1.12	**No**	**n/d**	1.54% -	5.8% - Lung Adenocarcinoma 5.4% - Uterine Corpus Endometrial Carcinoma	Hippo signaling antagonist (PMID:22153608)
PLXNA1	3 of 6 1 of 6	1.66, 2.57, 1.21 0.75	**No**	**n/d**	0.69% -	8.6% - Stomach Adenocarcinoma 7.4% - Uterine Corpus Endometrial Carcinoma	axon guidance, invasive growth and cell migration (Uniprot)
NSD1	2 of 7 2 of 7	1.57, 0.97 1.55, 1.35	**No**	**n/d**	1.20% -	12.3% - Head and Neck Squamous Cell Carcinoma 9.5% - Uterine Corpus Endometrial Carcinoma	Transcriptional regulation; Sotos syndrome (PMID:25345081)

Table 3.5. Summary of the candidate growth-limiting genes retests.

Each candidate growth-limiting gene was retested in multiple assays, including competitive outgrowth assays (Figure 3.16A) and individual growth assays using time-lapse microscopy (Figure 3.16C). The number of sgRNAs and the log fold change of each significantly scored sgRNA from the genome-wide screen is listed in the table. In addition, the alteration frequencies in pediatric and adult glioma/GBM for each candidate growth-limiting gene retested were examined[104,105,214-216](Provisional GBM data set from TCGA). Moreover, the alteration frequencies for each candidate gene retested was examined in non-glioma/GBM cancers. For each gene, the top two genetically altered non-glioma/GBM cancers are listed. Lastly, common function(s) of each gene are displayed.

Human Phenotype or Biological Function	Gene Set Name	SIZE	ES	NES	NOM p-val	FDR q-val
CREB Pathway	REACTOME_PKA_MEDIATED_PHOSPHORYLATION_OF_CREB	14	0.72032523	1.9852656	0	0.02006591
	REACTOME_DAG_AND_IP3_SIGNALING	26	0.55570626	1.7874722	0	0.07384427
	PID_LPA4_PATHWAY	12	0.7144361	1.8338121	0.002583979	0.056256704
	REACTOME_CA_DEPENDENT_EVENTS	24	0.5838532	1.8533871	0.003115265	0.055383377
TP53 Pathway	AMUNDSON_DNA_DAMAGE_RESPONSE_TP53	14	-0.75545466	-1.8269696	0.001533742	0.02243323
	PID_P53DOWNSTREAMPATHWAY	113	-0.44860703	-1.6176153	0.00239521	0.09588908
Cell Cycle	REACTOME_G0_AND_EARLY_G1	18	0.74943703	2.1813414	0	0.002690234
	REACTOME_MITOTIC_M_M_G1_PHASES	144	0.41318044	1.8364108	0	0.056667585
	REACTOME_CELL_CYCLE_MITOTIC	268	0.3772994	1.8305975	0	0.057118535
	REACTOME_G2_M_CHECKPOINTS	32	0.6561292	2.2004907	0	0.002161323
	REACTOME_MITOTIC_PROMETAPHASE	72	0.52455175	2.0817733	0	0.008306677
	EGUCHI_CELL_CYCLE_RB1_TARGETS	22	0.7796253	2.4594524	0	0
Prereplicative Complex	REACTOME_ACTIVATION_OF_THE_PRE_REPLICATIVE_COMPLEX	21	0.71682006	2.1870937	0	0.002493005
	BIOCARTA_MCM_PATHWAY	12	0.7177169	1.8624969	0.005025126	0.052845754
E2F Pathway	REN_BOUND_BY_E2F	54	0.6017078	2.2955894	0	3.96E-04
	PID_E2F_PATHWAY	64	0.4555329	1.8509524	0	0.05601548
	REACTOME_E2F_MEDIATED_REGULATION_OF_DNA_REPLICATION	22	0.6756676	2.0941455	0	0.007485894
DNA Replication	REACTOME_UNWINDING_OF_DNA	10	0.82120436	2.0444944	0	0.012127125
	REACTOME_DNA_REPLICATION	162	0.409212	1.8658171	0	0.05224017
	KEGG_DNA_REPLICATION	33	0.5763363	1.9269397	0	0.031138595
	REACTOME_DNA_STRAND_ELONGATION	27	0.6476592	2.067108	0	0.008978351
	DNA_DEPENDENT_DNA_REPLICATION	44	0.51375	1.8705465	0	0.05097429
ATR Pathway	REACTOME_ACTIVATION_OF_ATR_IN_RESPONSE_TO_REPLICATION_STRESS	27	0.6781672	2.1764739	0	0.002773625
	PID_ATR_PATHWAY	38	0.5738074	2.0352676	0	0.012710674
Miscellaneous	REACTOME_G1_S_SPECIFIC_TRANSCRIPTION	13	0.79846394	2.1084502	0	0.005995398
	PUJANA_BRCA_CENTERED_NETWORK	108	0.599061	2.5332928	0	0
	WANG_RESPONSE_TO_GSK3_INHIBITOR_SB216763_DN	279	0.37392455	1.8282794	0	0.057408463
	FEVR_CTNNB1_TARGETS_DN	425	0.37013334	1.9070765	0	0.03703524

Table 3.6 Gene sets displayed in the GSEA network map from Figure 3.16E.

The gene sets displayed in Figure 3.16E have a nominal p-value (correction for gene set size and multiple hypothesis testing[243,244]) of less than 0.01 and false discovery rate (FDR q-value) of less than 0.1. Size refers to the number of genes within the gene set. ES refers to the enrichment score and NES refers to the normalized enrichment score. The NES accounts for differences in gene set size and in correlations between gene sets and the expression dataset[243,244].

Sample	Target Sequence	Locus	Reads	Percentage of Total			
				del.	insert.	compl.	wt
sgCREBBP_1	CCCGCGTGACCAGTCATTTGCGG	chr16:-3900331	223,566	35.10	50.90	1.77	12.23
Off target-1	CaCGCGcGAgCAGTCATTTGAAG	chr17:-17258417	227,176	0.05	0.00	0.00	99.95
Off target-2	tCtGtGTGAtCAGTCATTTGTAG	chr18:+73917823	302,698	0.02	0.00	0.01	99.97
Off target-3	CtCagtTGACCAGTCATTTGAGG	chr4:+129177685	259,840	0.04	0.00	0.00	99.96
Off target-4	CCCtCGTtttCAGTCATTTGCAG	chr7:+105321025	214,380	0.06	0.00	0.03	99.91
sgHDAC2_1	TACAACAGATCGTGTAATGACGG	chr6:+114274490	299,800	42.40	56.00	0.50	1.10
Off target-1	TggAAgAcATCGTGTAATGATGG	chr3:+18312338	258,215	0.02	0.00	0.85	99.13
Off target-2	aACtACAGcaCGTGTAATGAGAG	chr15:-97275690	64,511	0.04	0.00	0.04	99.91
Off target-3	TACAACAGAgaaTGTAATGgTGG	chr6:-138734665	275,727	0.02	0.00	0.00	99.98
sgCTRL	GTAGCGAACGTGTCCGGCGT	N/A					
Off-target-1	GTtaaGAAgGTGTCCGGCGTGGG	chr22:+20132871	227,557	0.06	0.00	0.12	99.83
Off-target-2	GTAcCGgcCGgGTCCGGCGTGAG	chr13:+112727861	204,560	0.49	0.03	0.02	99.46

Table 3.7 Analysis of on- and off-target alterations induced by sgRNAs in NSC-CB660 cells.

Cells were manipulated as in Figure 3.19 with individual sgRNAs to *CREBBP*, *HDAC2*, or non-targeting sgControl (CTRL), except that 3-4 sequences with very close identity to primary target sequence were also sequenced. Percentage breakdown of reads with deletions, insertions, complex alterations, or no alteration (wild-type) are shown. Bases within off-target sites that differ from the on-target sgRNA sequence are shown in lower-case. sgCTRL does not have an on-target site, but the sequence is shown for comparison. Genomic PAM sequences are underlined. Table by Pia Hoellerbauer and Hamid Bolouri.

Methods

GSC classifications

In order to classify GSC isolates by tumor subtypes according to gene expression signatures produced by The Cancer Genome Atlas (i.e., classical, mesenchymal, neural, and proneural)[27,28], we first performed RNA-seq (n=3) using an Illumina HiSeq 2000 according to the manufacturer's instructions (FHCRC Genomics Shared Resource). RNA-Seq reads were aligned to the GRCh37/hg19 assembly using Tophat[245] and counted for gene associations against the UCSC genes database with HTSeq, a python package for analysis of high-throughput sequencing data[246]. All data was combined and normalized using a trimmed mean of M-values (TMM) method from the R package, edgeR[197,247,248]. Normalized counts were then log transformed, and the means across all the cell lines were used to calculate relative gene expression levels. The GSC data was clustered using a Manhattan distance complete-linkage method to establish leaflets. Previously, 173 GBM tumors were subtyped using the expression of 840 signature genes[28]. Our samples were clustered using 790 of these genes. Associations of GSCs with specific GBM subtypes were determined by minimum Manhattan distance to expression centroids produced by ClaNC. If a gene was expressed consistently in a particular subtype by absolute distance than that was counted as a 1 and the number of associated genes in each category were summed. As a validation, the four subtypes are clearly distinguished when the method is applied to the 173 glioma tumors described previously[28].

Cell culture and drug treatment

GSC and NSC lines were grown in N2B27 neural basal media (StemCell Technologies) supplemented with EGF and FGF-2 (20ng/mL each) (Peprotech) on laminin (Sigma) coated

polystyrene plates and passaged according to Ding[43,60]. Cells were detached from their plates using Accutase (Millipore). 293T (ATCC) cells were grown in 10% FBS/DMEM (Invitrogen). Cells were treated with 0.75μg/mL Doxorubicin (Seattle's Children Hospital) for 6 hours or treated with 300nM of the WEE1 inhibitor MK1775 (Supplier: Fisher Scientific; Part Number: 508890; Manufacturer Name: Selleck Chemical Llc; Manufacturer Part Number: S1525-5MG) for 6 hours (IP/WBs) or 48-72 hours (time-lapse microscopy).

Library acquisition and Individual sgRNA assembly

The genome wide CRISPR library was provided by the lab of Zhang Feng at MIT[10]. sgRNA sequences were obtained from Shalem *et al*[126] and Addgene, and cloned into lentiCRISPR v2 plasmid. Briefly, DNA oligonucleotides were synthesized with sgRNA sequence flanked by the following:

5': tatatcttGTGGAAAGGACGAAACACCg

3': gttttagagctaGAAAtagcaagttaa

PCR was then performed with the following primers[126]:

ArrayF: TAACTTGAAAGTATTTCGATTTCTTGGCTTTATATATCTTGTGGAAAGGAC GAAACACCG

ArrayR: ACTTTTTCAAGTTGATAACGGACTAGCCTTATTTTAACTTGCTATTTCT AGCTCTAAAAC

The PCR product was then ran on a 2% TAE gel, and purified using the ZymoClean Gel DNA recovery kit (Zymo Research). Gibson Assembly Master Mix (NEB) was used to ligate the cut lentiCRISPR v2 plasmid with the purified PCR product (sgRNA). The ligated plasmid was then transformed into Stellar Competent cells (Clontech), and streaked onto LB agar plates.

3xmiR30-based shRNA assembly

The parental vector pGIPZ (Open Biosystems) was cut with XhoI and MluI. Selected *CREBBP* hairpins (Human GIPZ lentiviral shRNAmir library, Open Biosystems) were PCR amplified to add flanking homology for assembly, restored to the native miR30 sequence by eliminating 3' EcoRI (improving hairpin function), and unique restriction sites were added for subsequent hairpin reconfiguration. The construct was assembled via In-Fusion Cloning Kit (Clontech). Primer sequences:

H1 Xho for: CAACAGAAGGCTCGAGgatccAAGAAGGTATATTGCTGTTGACAGTGAG

H1 Nhe rev: AAGATAATTGCTAGCatcgtagCCCTTGAAGTCCGAGGCAGTAGGC

H2 Nhe for: GCTAGCAATTATCTTgatccAAGAAGGTATATTGCTGTTGACAGTGAG

H2 Spe rev: GATAGCAAGACTAGTatcgtagCCCTTGAAGTCCGAGGCAGTAGGC

H3 Spe for: ACTAGTCTTGCTATCgatccAAGAAGGTATATTGCTGTTGACAGTGAG

H3 Mlu rev: ATTGTTCCAGACGCGTatcgtagCCCTTGAAGTCCGAGGCAGTAGGC

siRNA

Reverse transfections were performed with RNAiMAX reagent (Life Technologies) according to manufacture instructions on siControl (AllStars Negative control siRNA; Qiagen) and *siPKMYT1* (ON-TARGETplus Human *PKMYT1* (9088) siRNA – SMARTpool; GE Dharmacon). Plates were coated with laminin for 3 hours, aspirated, and then coated with the respective siRNA/RNAiMAX/Opti-MEM (Life Technologies) mixture. Following 1-hour incubation, cells resuspended in media without antibiotics were then added to the siRNAs. After 24 hours, media was changed. Following 48 hours from the initial transfection, cells were treated

with MK1775 (WEE1 inhibitor) or mock-treated, and harvested for protein or used for other experiments (i.e. time-lapse microscopy).

shRNA and lentiviral production

shRNAs were obtained from Open Biosystems (Huntsville, AL) in the pGIPZ lentiviral vector. For virus production, pGIPZ-shRNA and lentiCRISPR v2 plasmids were transfected with Lipofectamine 2000 (Life Technologies) into 293T cells along with psPAX and pMD2.G packing plasmids (Addgene) to produce lentivirus. Approximately 24 hours after transfection, neural stem cell expansion medium was added to replace the original 293T growth medium. Virus was harvested and filtered approximately 24 hours after media change and stored at -80˚C. GSCs and NSCs were infected at MOI <1 for all cell lines. Cells were infected for 48 hours followed by selection with 1-4μg/mL (depending on the target cell type) of puromycin for 2-4 days[43,60]. For the growth-promoting genes, cells were maintained under selection with 0.5μg/mL of puromycin in order to prevent outgrowth of residual uninfected cells. To produce lentivirus for the whole-genome wide CRISPR library, 25x150mm plates of 293T cells were seeded at ~15 million cells per plate.

Cell transduction and titering for CRISPR whole-genome library

Cells were transduced with the GeCKO library using the regular infection method. To determine optimal viral volumes for MOI <1 (~30% infection efficiency), each cell line was tested individually. In brief, $1x10^6$ cells were plated onto 12 well plates. The next day, each well received viral supernatant in a dilution format. A non-transduction control was also included. Following 48 hours of infection, cells were split into duplicate wells, and selected with

puromycin 24 hours later. After 3 days, cells were counted to calculate the percentage of transduction. The ratio is calculated as cell count from the replicate with puromycin versus the replicate without puromycin. The amount of virus that produced an MOI <1 and close to ~30% infection efficiency was chosen for the genome wide screen.

CRISPR-Cas9 screening

A human genome-wide CRISPR-Cas9 library[126] was used in pooled format for large-scale virus production and transduction of GSCs and NSCs. For large-scale transduction, ~ 220 million GSC or NSC cells were plated into T225 flasks at an appropriate density and such that each replicate had ~500 fold representation. 2 days after transduction, puromycin was added (1-4μg/ml) and maintained for 3 days. A portion of cells were harvested as Day 0 time point. The remaining cells were then passaged into T225 flasks maintaining 500-fold representation and cultured for an additional 21-23 days or ~8-10 cell doublings. Genomic DNA was extracted using QiaAmp blood purification Midi kit (Qiagen). Two-step PCR procedure was then performed to amplify sgRNA sequence: For the first PCR, the amount of genomic DNA for each sample was calculated in order to achieve 500-fold coverage over the library (~6.6 μg of gDNA for 10^6 cells), which resulted in ~213 μg DNA per sample. For each sample, ~100 separate PCR reactions were performed with 2 μg genomic DNA in each reaction using Herculase II Fusion DNA Polymerase (Agilent). Afterwards, a second PCR was performed to add on Illumina adaptors and to barcode samples, using 5ul of the product from the first PCR. We used a primer set to include both a variable 1-6 bp sequence to increase library complexity and 6 bp Illumina barcodes for multiplexing of different biological samples. Resulting amplicons from the second PCR were column purified using the combination of PureLink PCR purification kit (Life

Technologies) and MinElute PCR purification kit (Qiagen) to remove genomic DNA and first round PCR product. Purified products were quantified, mixed, and sequenced using HiSeq 2500 (Illumina). The whole amplification was carried out with 12 cycles for the first PCR and 21 cycles for the second PCR to maintain the linear amplification. The resulting reads were mapped onto a reference library containing library sgRNA sequences and filtered (phred score= 37). Mapped reads were tallied and compared using R/Bioconductor package, edgeR, developed for RNA-seq analysis, which subtracts control from experimental replicates to calculate logFC and uses the Benjamini-Hochberg FDR calculation to adjust p-values for multiple comparisons. PCA was performed in R, using the log2 normalized CPM (counts per million) values generated by the Bioconductor package edgeR. Raw and mapped data files are available through NIH's Gene Expression Ominibus:
www.ncbi.nlm.nih.gov/geo/query/acc.cgi?token=mtgtecymtxejzwr&acc=GSE70038.

H2B Flow analysis

NSCs were infected with *EGFP-H2B* (Addgene) at MOI>2 and passaged for 1 week. Cells were then infected with sgControl and *sgEGFP* at MOI<1 and selected by puromycin for 3 days. The cells were then plated onto 12-well plates and kept in culture for 14 days with regular passaging and media changing. Images were taken on day 14 using a fluorescent microscope (Nikon TI) to determine the knock out effect. Flow analysis (FACS Canto flow cytometer from Becton Dickinson) was then performed to analyze the percentage of eGFP in both sgControl and *sgEGFP* cells.

Growth assays

For short-term single clone validation assays, cells were infected with lentiviral gene pools containing 3-4 sgRNAs per gene (growth-limiting genes only) or with lentivirus containing a single sgRNA to the respective gene. Following selection, cells were harvested, counted (NucleoCounter, NBS) and plated in triplicate onto 96-well plates coated with laminin[43,60] in dilution format starting at 1,000 cells to 3,750 cells per well (cell density depended on cell line and duration of assay). Cells were fed with fresh medium every 3-4 days. After 7-12 days under standard growth conditions, cell proliferative rates were measured using Alamar blue reagent according to manufacturer's instructions (Invitrogen). For analysis, sgRNA-containing samples were normalized to their respective sgControl samples. For long-term growth assays (21 days or greater), cells infected with individual sgRNAs or sgControl were plated in triplicate. Cells were routinely cultured for 21 days (split every 3-4 days), and counted at each split. The overall growth of each well containing an individual sgRNA was calculated and compared to the sgControl well. The growth defects were graphed using the ratio between the individual sgRNAs to sgControl.

Competition experiment

NSCs were infected with lentiviral gene pools containing 3-4 sgRNAs per gene, puromycin selected, and mixed with NSCs infected with lentiviruses containing turboGFP at an approximate 1:9 ratio, respectively. Cultures were outgrown for 23 to 31 days and flow analysis (FACS Canto flow cytometer from Becton Dickinson) was conducted every 7-8 days for GFP expression. Flow analysis data was analyzed using FlowJo software. For each sample, the GFP- population for each time point was normalized to its respective Day 0 GFP- population (competition index).

Western blotting

Cells were harvested following infection with their respective shRNA and selection, washed with PBS, and lysed with modified RIPA buffer or snap-frozen and stored at -80˚C until lysis. Western blots were carried out using standard laboratory practices (www.cshprotocols.org), except cells were lysed in a modified RIPA buffer (150mM NaCl, 50mM Tris, pH 7.5, 2mM $MgCl_2$, 0.1% SDS, 2mM DDT, 0.4% deoxycholate, 0.4% Triton X-100, 1X complete protease inhibitor cocktail (complete Mini EDTA-free, Roche), and 1U/μL benzonase nuclease (Novagen)) at RT for 15 minutes[43,60]. Cell lysates were quantified using Pierce 660nm protein assay reagent and identical amounts of proteins were loaded onto SDS-PAGE for western blot. Trans-Blot Turbo transfer system was used according to the manufacturer's instructions. The following commercial antibodies were used: histone H4 (Abcam, # 17036-100, 1:2,000), Beta-actin (Cell Signaling, #3700, 1:1,000), CREBBP (Cell Signaling, #7389, 1:500), NF2 (Santa Cruz, SC-332, 1:200), and TP53 (Calbiochem, # OP03, 1:1,000). An Odyssey infrared imaging system was used to visualize blots (LI-COR) following the manufacturer's instructions. The Odyssey software was used to semi-quantify the blots.

Immunoprecipitation-Western blotting

Frozen cell pellets were lysed in NP-40 lysis buffer (50 mM Tris pH 8.0, 150 mM NaCl, and 0.5% Nonidet P-40, 1mM DTT; supplemented with protease and phosphatase inhibitors), cleared by centrifugation, and quantified by Bio-Rad Protein Assay. For western blots, samples were normalized for total protein, separated on polyacrylamide gels, transferred to PVDF membranes, blocked in 5% milk/TBST, and incubated with primary antibodies overnight. For immunoprecipitations, lysates were normalized for total protein and rotated with specific

antibodies at 4 degrees for two hours, followed by an additional one hour of rotation after addition of Protein G agarose. All IPs were washed three times with lysis buffer and eluted with Laemmli sample buffer and boiling. The following commercial antibodies were used: CDK1 (BD, #610037, 2 ul/IP, 1:500 WB), CDK1 (Santa Cruz, clone p34 (17), Cat # SC-54, 1:750 dilution), CDC2 (Cell Signaling Technology, #POH1, Cat #9116), CDK2 (Santa Cruz, #Clone D12, 2 ul/IP), CDK2 (Santa Cruz, #Clone M2, 1:1000), p-Y15 CDK1/CDK2 (Millipore, #219440, 1:1000), p-T14 CDK1 (Abcam, # Ab58509, 1:750), WEE1 (Cell Signaling Technologies, # D10D2, 1:1000), PKMYT1 (Abcam, #114022, 1:1500), and γ-tubulin (Santa Cruz, #C-20, 1:1000).

RNA sequencing expression analysis

NSC-CB660s were infected with 3xmiR30-based shRNAs to control or *CREBBP* for 48 hours, puromycin selected for 72 hours, and outgrown for 5-6 days. Cells were lysed with Trizol reagent (Life Technologies), and RNA was extracted according to manufacture instructions (Life Technologies). Total RNA integrity was checked using an Agilent 2200 TapeStation (Agilent Technologies, Inc., Santa Clara, CA) and quantified using a Trinean DropSense96 spectrophotometer (Caliper Life Sciences, Hopkinton, MA). RNA-seq libraries were prepared from total RNA using the TruSeq RNA Sample Prep Kit (Illumina, Inc., San Diego, CA, USA) and libraries size distributions were validated using an Agilent 2200 TapeStation (Agilent Technologies, Santa Clara, CA, USA). Additional library QC, blending of pooled indexed libraries, and cluster optimization was performed using Life Technologies' Invitrogen Qubit® 2.0 Fluorometer (Life Technologies-Invitrogen, Carlsbad, CA, USA). RNA-seq libraries were pooled and clustered onto a flow cell lane using an Illumina cBot. Sequencing was performed

using an Illumina HiSeq 2500 in Rapid Run mode and employed a paired-end, 50 base read length (PE50) sequencing strategy.

RNA sequencing data analysis

Reads of low quality were discarded prior to alignment to the reference genome (UCSC hg19 assembly) using TopHat v2.0.12[249]. Counts were generated from TopHat alignments for each gene using the Python package HTSeq v0.6.1[250]. Genes with counts above threshold equal to at least the number of samples in the smallest group were retained, prior to identification of differentially expressed genes using the Bioconductor package edgeR v3.6.8[197]. A false discovery rate (FDR) method was employed to correct for multiple testing[251]. Differential expression was defined as $|\log2 (\text{ratio})| \geq 0.585$ (± 1.5-fold) with the FDR set to 5%.

Exome Sequencing and Preprocessing

Exome sequencing and preprocessing were performed at the Genome Core Facility of Mount Sinai School of Medicine. Whole genome amplified was used for exome sequencing. Whole-exome capture libraries were constructed using ligation of Illumina adaptors. Each captured library was then loaded onto the HiSeq 2500 sequencing platform. Exome sequence preprocessing and analysis were performed using standard pipelines recommended by the Genome Analysis Toolkit (GATK)[252]. Three GSC cell lines were aligned independently. For each sample, the reads were aligned to NCBI build 37 (hg19) human reference sequence using BWA[253] (http://bio-bwa.sourceforge.net), and duplicated were marked using Picard (http://picard.sourceforge.net). Local realignment around indels and the base recalibration process were performed, ending in an analysis-ready BAM file for each cell line.

Mutation detection and annotation

Mutation detection and annotation were performed at the Genome Core Facility of Mount Sinai School of Medicine as follows. For each sample, GATK was used to detect all variants that differ from a reference genome. Variants identified were annotated using the snpEff software[254].

Variant Filtration

The variants were filtered in four steps following the previous study[255]. First, the variants with low allelic fraction were excluded. The allelic fraction was calculated for each detected variant per cell line as a fraction of reads that supported an alternative allele (e.g., different from the reference) among reads overlapping the position. Only reads with allelic fractions above 0.25 were used in the downstream analysis. Additionally, the variants that were detected as common germline variants were excluded. Variants for which the global allele frequency (GAF) in dbSNP138 or allele frequency in the NHLBI Exome Sequencing Project (http://evs.gs.washington.edu/EVS, data release ESP2500) was higher than 0.1% were excluded from further analysis. Furthermore, variants detected in a panel of 278 whole exomes sequenced at the Broad as part of the 1000 Genomes Project were excluded from further analysis. Finally, the variants with low quality (e.g. insufficient read depth and insufficient genotype quality) were filtered with the variant quality score tools.

Obtaining high-confidence mutations

We selected high-confident mutations by their annotation obtained from snpEff[17]. We filtered silent mutations and extract high and moderate impact of mutations including non-synonymous,

nonsense, frame shift, codon insertion/deletion mutations.

Transcript assembly and abundance estimation

The resulting aligned reads were analyzed further by Cufflinks[256] with the reference genome. Cufflinks assembled the aligned reads into transcripts with reference genome and reported the expression of those transcripts in Fragments Per Kilobase of exon per Million fragments mapped (FPKM). FPKM is an expression of the relative abundance of transcripts. We set an FPKM value of 0.05 as the lower bound and FPKM value were log-transformed in our subsequent analyses. We determined the expression status of our cell lines for the genes within the frequently altered genomic regions in glioblastoma patients[23]. For the set of genes located in each altered genomic region, we clustered all available 67 GSC samples based on their expression levels using K-means clustering. For each sample and gene, we determined the expression status as overexpressed/ non-variable for the gene in amplified regions, and depleted/non-variable for the gene in deleted regions.

Time-lapse microscopy

NSCs were infected with lentiviral gene pools containing 3-4 sgRNAs per gene or with individual sgRNAs, puromycin selected, outgrown for 13-15 days, and plated onto 96-well plates or 24-well plates. Also NSCs and GSCs were transfected with siRNAs (see siRNA). Plates were then inserted into the IncuCyte ZOOM (Essen BioScience), which was in an incubator set to normal culturing conditions, and analyzed with its respective software for processing videos or determining the confluency of each well. For the growth-limiting assay, phase images were taken

every hour for 72 hours. For the mitotic transit time, phase and fluorescence (GFP) images were taken every 5 minutes for 48-72 hours.

Mitotic transit time

NSC-CB660s were transduced with individual sgRNA constructs to *PKMYT1* and control for 48 hours, and puromycin selected for 96 hours. Cells were outgrown for 15 days, treated with 300nM of the WEE1 inhibitor MK1775, and followed by time-lapse microscopy for 72 hours using the IncuCyte ZOOM. Mitotic transit time was analyzed for individual cells following 6 hours of WEE1 inhibition. In addition, NSC-CB660s and GSC-0827s were transfected with siRNAs for 24 hours, and treated with 300nM of the WEE1 inhibitor MK1775 following 48 hours from the initial transfection. Plates were then placed into the IncuCyte ZOOM for time-lapse microscopy for 48-72 hours. Videos were compiled and $n \geq 60$ cells were analyzed to determine the mitotic transit time, and whether each cell successfully completed mitosis or experience cytokinesis failure or cell death in mitosis. A cell was considered to enter mitosis when nuclear envelope breakdown was visible or when a visible morphology change was observed (cell begins to go from flat to rounded-up). Following successful cytokinesis (proper cell division resulting in two daughter cells), a cell was categorized as successfully completing mitosis. A cell was classified as cytokinesis failure if the cell failed to divide following mitotic entry due to an abrupt mitotic exit while in metaphase or anaphase, or failure to complete cytokinesis. If a cell experienced cytokinesis failure, the cell was followed for additional amount of time to ensure that the cell indeed experienced cytokinesis failure and was categorized as such. A cell was categorized as cell death in mitosis if a cell erupted and died during mitosis (from nuclear envelop break through cytokinesis).

Immunofluorescence

NSCs were infected with lentiviruses containing 3xmiR30-based shRNAs to *CREBBP* or control, puromycin selected for 72 hours, and outgrown for 14 days. Cells were then treated with 10μM of bromodeoxyuridine (BrdU) for 2 and 8 hours. Cells were fixed with 4% formaldehyde for 1 hour in 37˚C, washed with PBS, incubated with 2M HCl (in water) for 2 hours at 37˚C, washed with Borate buffer (0.1M Borate, pH 8.5), blocked in block for 30 minutes (PBST (0.25% Triton X-100 in PBS), 0.3M Glycine, 3% BSA, 5% goat serum), stained with anti-BrdU (FHCRC core) diluted in block overnight, washed with PBS, stained with secondary antibody (Alexa Fluor 568 Goat anti-mouse IgG (H+L), Life Technologies, # A11004, 1:200), washed with PBS, stained with 2 ng/mL 4',6-diamidino-2-phenylindole (DAPI) diluted in PBS, and washed with PBS. 10X images were acquired for each replicate using the Nikon TI, and analyzed for BrdU+ cells, n>1,085 cells.

Gene set enrichment analysis (GSEA)

The gene set enrichment analysis software from the Broad Institute[243,244] was used for analysis of the NSC-CB660 3X shControl and *3X shCREBBP* RNA-Seq data. Briefly, normalized RNA-Seq expression was used for the analysis, and uploaded into a gct file (expression dataset). The following gene sets were curated in MSigDB and used for analysis:

Collection: Curated, Gene Ontology, Oncogenic Signatures

Organism: Homo sapiens

CHIP: EntrezGeneIds, Human_GENE_SYMBOL, UniProtIds

Contributor: All

A total of 3566 gene sets were used for analysis.

The following parameters were used for the analysis run: Number of permutations: 1,000; phenotype labels: *3X shCREBBP* vs. 3X shControl; Collapse dataset to gene symbols: false; permutation type: gene set; Chip platform: GENE_SYMBOL; Enrichment statistic: Weighted; Metric for ranking genes: Log2_Ratio_of_Classes; Gene list sorting mode: Real; Gene list ordering mode: descending; Max size (exclude larger sets) 650; Min size (exclude smaller sets): 8. For the advance field, all settings were default except: Omit features with no symbol match, which was changed to false. The enrichment map was initiated from the GSEA software, and created in Cytoscape v3.1.1 (Enrichment map plug-in) as described[257]. The p-value cutoff was 0.01 and the FDR Q-value cutoff was 0.1. The enrichment map was then curated.

For GSEA of the whole-genome CRISPR screen results for both NSCs and GSCs (Figure 3.2D and Figure 3.6), all sgRNAs from the screen results were used for the analysis. GSEA was performed as previously described[243,244] on each of the four cell lines, using the Gene Ontology Biological Process gene sets with 10,000 permutations.

In vivo validation with lentiviral sgRNA retest pool

0827 and 0131 GSCs were infected with the LV-retest-pool retest virus for 48 hours and selected for 4 days in puromycin (1 and 2μg/mL respectively). Cells were then harvested using Accutase (Sigma), counted, resuspended in an appropriate volume of culture media, washed with PBS, resuspended in a final concentration of 5 million cells/100μL of PBS, and kept on ice prior to immediate transplantation. Each mouse received 100μL of resuspended cells (5 million cells). All *in vivo* experiments were conducted in accordance with the NIH Guide for the Care and Use

of Experimental Animals, and with approval from the Fred Hutchinson Cancer Research Center Institutional Animal Care and Use Committee (IR#1457). Cells were implanted subcutaneously into the right flank of female 6-week-old athymic nude mice (Harlan). Tumors were monitored three times weekly and allowed to grow to ~1500mm3 before harvesting the tumors. The DNeasy Blood and Tissue Kit (Qiagen) was used to dissociate the tumor and extract gDNA. Lethal-pool retest was also conducted in vitro as previously described (see CRISPR-Cas9 screening). Library pools for both the *in vivo* and *in vitro* samples were prepared as described earlier (see CRISPR-Cas9 screening). Raw counts from each sgRNA were transformed to log2 CPM (counts per million) using the Bioconductor package edgeR[197], followed by normalization within each sample to a common control sgRNA. Differentially expressed sgRNAs were identified using the Bioconductor package limma[258], where a false discovery rate (FDR) method was employed to correct for multiple testing[251]. Differential expression was defined as $|\log2(\text{ratio})| \geq 0.585$ (± 1.5-fold) with the FDR set to 5%.

qRT-PCR

Cells containing shRNAs were harvested following infection/selection process and total RNA from cells was extracted using TRIzol (Invitrogen) according to manufacturer's instructions. QuantiTect quantitative real-time PCR (qRT-PCR) primer sets and SYBR Green PCR Master Mix (Applied Biosystems) were used according to manufacturer's instructions with the ABI PRISM 7900 Sequence detection System (Genomics Resource, FHCRC). Ct values of the samples were normalized to beta-actin followed by the respective shControl. Relative transcript abundance was analyzed using the $2^{-\Delta\Delta Ct}$ method[43].

Deep sequencing of CRISPR modified loci

The genomic regions surrounding the CRISPR target loci of several different sgRNAs were PCR amplified from corresponding CRISPR-transduced NSC-CB660 DNA samples and prepared for deep sequencing using a two-step PCR procedure. In the primary PCR, the genomic region of interest was amplified for 14 cycles using Herculase II Fusion Polymerase (Agilent Technologies) and the genomic primers listed below (preceded by an additional 24 or 28 bp sequence corresponding to the secondary PCR primers).

	Primer 1 (5'->3')	*Primer 2 (5'->3')*
sgCREBBP_1	…ATGCCGTACCCTACTCCAG	…CACGTGGTCCCATTTTACGC
sgNF2_4	…TGGTTTGTTATTGCAGATGAAGTG	…GCTAGGCGCCTGCTCA
sgTFAP2C_1	…AAAATGGAGGCCGGTCCTTG	…CATCTCTACTTGCAACCAAGTTTTA
sgHDAC2_2	…TATTTTTCGAACTGTTGCAGTATG	…GTAATGAGAACACTTACCATTGGG

5 µl of the primary PCR reaction was then used as the template for the secondary PCR reaction, which again used Herculase II Fusion Polymerase and was carried out for 23 cycles. Secondary PCR primers matched the additional sequence added on by the primary PCR primers ("…" in the chart above) and also added Illumina adapters and sample-specific barcodes. Final amplicons were then electrophoresed on a 1.5% agarose gel, and bands with expected fragment sizes +/- 100 bp (to capture larger indels) were excised and purified using the Zymoclean Gel DNA Recovery Kit (Zymo Research). Amplicon concentration was measured using Life Technologies' Invitrogen Qubit® 2.0 Fluorometer (Life Technologies-Invitrogen, Carlsbad, CA, USA). The various products were then pooled in equal proportions and sequenced on an Illumina MiSeq machine (250 bp paired-end reads). Data were processed according to standard Illumina

sequencing analysis procedures, and reads were mapped to the PCR amplicons as reference sequences. An R script was used to assess length and prevalence of insertions and deletions by analyzing cigar sequences found in sam/bam alignment files. Indel phase was calculated as the length of insertions or deletions modulus 3.

Genetically transformation of human neural stem cells

NSC-CB660 cells were simultaneously infected with retrovirus pBabe-*TP53*^{DD} + human *TERT* and pBabe-*CyclinD1* + *CDK4*^{R24C} (Addgene) over three consecutive rounds of infection as previously described[42]. After recovery, cells containing the two constructs were infected with lentivirus pCDF1-MCS2-EF1-copGFP [CMV-ΔII-VIII *EGFR*] (kindly provided by Robert Bachoo, UT Southwestern). After recovery and expansion, cells were sorted for GFP+ population and expanded. Following expansion, these cells and normal CB660 neural stem cells were infected with retrovirus pBabe-Puro-Myr-Flag-*AKT1* (Addgene) over three consecutive rounds of infection. After recovery, cells were selected with puromycin and expanded.

Statistics

All student's t-tests were conducted using unpaired and unequal variance.

Chapter 4-Conclusion

~90% of adult GBM patients receiving standard of care therapies die within 2 years of diagnosis due to ineffective therapies[3]. New treatment options are limited because of the many challenges in treating GBM, such as the blood-brain barrier, highly invasive proliferative cells, and the heterogeneity of the disease[259]. Thus, it's necessary to explore new technologies in order to identify novel therapeutic targets for refractory cancers like GBM. Here, I employed shRNA and CRISPR-Cas9 technologies to identify novel gene targets that are differentially required by GSCs, but are dispensable in non-transformed NSCs, a non-neoplastic tissue of origin control. I identified a novel kinetochore protein, BuGZ, by shRNA technology (Chapter 2) and a WEE1-like dual specificity kinase, PKMYT1, by CRISPR-Cas9 technology (Chapter 3) that are required by GSCs, but not NSCs. In addition, I identified multiple genes that limit the expansion of NSCs by preventing precious entry into S-phase; and thus, these growth-limiting genes negatively regulate cell proliferation in order to prevent cells from becoming highly proliferative cancer cells. More importantly, these studies identified multiple molecular vulnerabilities specific to GSCs in processes that include mitotic entry and progression and kinetochore regulation.

BuGZ and GLEBS-BUB3 interactions are candidate GBM therapeutic targets

Previously, our lab has shown that the KT protein BUBR1, specifically its GLEBS domain, is required by GSCs in order to suppress lethal consequences of altered KT function by promoting attachment of MTs to KTs [60]. Here, I tested the hypothesis that *BuGZ* is required in GSCs due to its functional role in the KT. Others[260] and we found that BuGZ acts as a molecular chaperone for the KT protein BUB3, which is essential for the establishment of correct KT-MT

attachments and crucial for the recruitment of BUBR1 and BUB1 to unattached kinetochores[83,97]. Like BUBR1[97], BuGZ contains a GLEBS domain that allows it to bind to BUB3 (Figure 2.4). Depletion of *BuGZ* or deletion of the GLEBS domain results in the reduction of BUB3 in both interphase and mitosis (Figures 2.6 and 2.9). More importantly, for KT biology, the depletion of *BuGZ* or deletion of the GLEBS domain decreases BUB3 binding to the KT in mitosis, which causes a reduction in BUB1 localization and activity at the KT (Figures 2.9 and 2.10A). This leads to a decrease in ABK activity, and causes lethal chromosome congression defects in cancer cells followed by cell death (Figures 2.10 and 2.12A). I also found that *BuGZ*-knockdown-insensitive NSCs can be sensitize to *BuGZ* depletion by genetically disrupting the RB-axis pathway, and can resemble GSCs' sensitivity to *BuGZ* depletion by genetic alterations in the TP53 and RB pathways in conjunction with the activation of the RTK/RAS pathway (Figures 2.1F and 2.3). Moreover, *BuGZ* expression is required for GBM tumor formation *in vivo* (Figures 2.1G and 2.2C). Taken together, BuGZ is a key GLEBS domain-containing KT protein that is required for BUB3 stability, and inhibiting GLEBS domain interactions with BUB3 may be a therapeutic strategy for refractory cancers like GBM.

A common theme arising from analysis of mitotic defects in GBM patient isolates is the GSC-specific requirement for GLEBS domain activity of BUBR1 and BuGZ[43,60,66]. GLEBS domains are highly conserved, and consist of short disordered regions of about 40 amino acids that form a series of salt bridges between the WD40 domains of BUB3 or RAE1 and two glutamate residues in the GLEBS domain[79,90,96,97]. We have shown that the activation of the RTK/RAS signaling pathway alters KT function and dynamics, which results in the requirement for BUBR1's and BuGZ's GLEBS domains in GSCs, but not NSCs[60,76]. Thus, targeting these BUB3-GLEBS domains interaction is an ideal therapeutic approach[43,66]. One method to target

these interactions is to use a small-molecule mimetic capable of binding BUB3 at its WD40–GLEBS interface and blocking one or both of BUBR1 and BuGZ GLEBS domain interactions[66]. Another method is to create an allosteric interaction with a molecule that distorts the GLEBS domain interface[66]. However, both approaches will require the therapeutic to be highly specific since BUB1 and NUP98 also contain a GLEBS domain[43,66,96,97]. NUP98 though, appears to only bind to RAE1's WD40 repeat domain, but not BUB3[66,97,111]. While our data suggest that non-transformed cells can tolerate low expression of BUB3, complete inhibition of BUB3 would likely cause massive cell death in all cells. Therefore, like all cancer drugs, the establishment of a therapeutic window will be crucial for the success of this potential therapeutic.

In addition to the GLEBS domain, BuGZ also contains two zinc finger domains[98,99], which may participate in other cellular functions. Recently, it was shown that *BuGZ* and *BUB3* are required for pre-messenger RNA splicing in cancer cells, as depletion of *BuGZ* or *BUB3* leads to exon skipping in many transcripts[148]. Our lab has previously shown that GBM patient isolates are vulnerable to splicing perturbations, and GSCs, but not NSCs, differentially require *PHF5A* for proper 3' pre-messenger splice site recognition[42]. Future experimentation is warranted to determine if BuGZ's zinc finger domains participate in its splicing function and whether its splicing function is essential in GSCs. Moreover, it will be interesting to determine whether targeting BuGZ's zinc finger domain would distort its GLEBS domain interface, and vice versa; and thus, a therapeutic to either domain could disrupt both cellular functions of BuGZ. These experiments would demonstrate that *BuGZ* is the ideal GBM therapeutic target since it may be involved in two cellular functions that are specifically required by GBM patient isolates.

PKMYT1 is a candidate GBM therapeutic target

One concern with the potential GBM therapeutic targets identified by shRNA technology is whether inhibitors to these targets will ultimately have better therapeutic windows than current cytotoxic chemotherapies. To identify candidate GBM therapeutic targets with potentially large therapeutic windows, we performed CRISPR-Cas9 screens to determine genes that are differentially required by GSCs, but not NSCs, upon knockout. We found that the WEE1-like dual specificity kinase, *PKMYT1*[161,162,172], is required in GSCs, but not NSCs, in order to maintain inhibitory phosphorylations at T14 and Y15 of CDK1 and to promote timely completion of mitosis (Figures 3.11 and 3.12). Knockout of *PKMYT1* in GSCs leads to extended mitotic transit times, which are associated with cytokinesis failures and cell death during mitosis (Figure 3.11). In addition, our results help redefine PKMYT1 function in non-transformed human cells, as we found that PKMYT1 and WEE1 can act redundantly to maintain CDK1-Y15 phosphorylation and to promote timely completion of mitosis (Figure 3.11). These results are imperative for PKMYT1 targeted cancer therapies, as it suggest that PKMYT1 and WEE1 redundancy in human somatic cells and tissues will help avoid dose-limiting toxicities from therapeutics targeting PKMYT1. Moreover, I found that activation of EGFR and AKT pathways, which are commonly altered in GBM, suppress CDK1/2-Y15 and CDK1-T14 phosphorylations in NSCs (Figure 3.15). This strongly suggests that activation of these pathways together results in net loss of inhibition of CDK1 and CDK2 during the G2/M transition; and thus, alters the abrupt activation and inactivation of CDK1-cyclin B complexes, which is important for proper mitotic entry, progression, and exit[177,185,190-193]. More importantly, these data suggest that combinational therapies, such as targeting both PKMYT1 and EGFR, may not be beneficial for GBM patients since inhibiting the EGFR pathway might eliminate the

requirement for *PKMYT1* in GSCs (Figure 3.15). However, combining PKMYT1's kinase inhibitors with another therapeutic, such as paclitaxel, an FDA approved chemotherapeutic that stabilizes KT-MT attachments and induces mitotic arrest[261], or the standard of care treatment for GBM patients may be more effective than the respective stand alone treatments.

BuGZ and potentially *PKMYT1* depletion elicit a SAC response

The spindle assembly checkpoint prevents chromosome mis-segregation and aneuploidy by ensuring that proper KT-MT attachments have been formed, chromosomes are aligned, and KTs are under proper tension at the metaphase plate before cells enters anaphase[64,70]. *BuGZ* depleted cells and *PKMYT1* depleted or knockout cells spend most of their mitotic transit time arrested in metaphase, which is consistent with a SAC-induced arrest (Figure 2.12 and data now shown). Interestingly, it was shown that HeLa cells overexpressing CDK1-T14A-Y15F, which cannot be inhibited by PKMYT1 or WEE1 activity[207], were able to generate a SAC response that corresponded with active ABK and CDK1 regardless of their chromatin condensation state[193]. Further experimentation is necessary to determine if *PKMYT1* depletion or loss indirectly disrupts the timing of key mitotic events at the KT and elicit a SAC response in GSCs and NSCs. In addition, a subpopulation from *BuGZ* depleted cells and *PKMYT1* depleted or knockout cells can exit mitosis, but will undergo cell death during the sequential round of the cell cycle, particularly during the next round of mitosis (data not shown). Taken together, both BuGZ PKMYT1 functional activities are important for timely and successful completion of mitosis in GSCs.

Identifying GBM tumor suppressor genes using CRISPR-Cas9

In addition to GBM therapeutic targets, the CRISPR-Cas9 screens also revealed hundreds of candidate growth-limiting genes that promote the expansion of NSCs *in vitro* upon knockout (Table 3.4). Many of these observed growth-limiting genes are mutated at intermediate and low frequencies in glioma/GBM and other cancers (Table 3.5)[104,105,214-216](Provisional GBM data set from TCGA), suggesting that they might act as tumor suppressors. Consistent with this notion, I found that 10 confirmed growth-limiting genes reduced cell cycle transit times upon knockout in NSCs (Figure 3.16C). In addition, 7 of the 10 confirmed growth-limiting genes, which includes: *ARID1A*, *CREBBP*, *EP300*, *NF2*, *TAOK1*, *TFGβR2*, and *TP53*, have shown to act as tumor suppressors[218,219,262-267]. Focused experiments examining knockout of *CREBBP*, a known tumor suppressor in hematologic and non-GBM solid tumors[218,219], in NSCs revealed a significant increase entry into S-phase and caused dramatic increases in steady-state levels of mRNAs for cell cycle genes up regulated during the G1/S transition (Figure 3.16). Taken together, these studies suggest that the growth-limiting genes identified here may act as tumor suppressors in GBM. However, many of these growth-limiting genes are mutated at low or intermediate frequencies in pediatric and adult glioma/GBM (Table 3.5). One hypothesis from my results is that these hits may have epistatic relationships, such that knockout of one gene is equivalent to knockout of another gene (e.g. *CREBBP* and *EP300; ARID1A* and *ARID1B)*, which might explain their low penetrance in glioma/GBM and other cancers. The identification of these potential tumor suppressors here reveal new genetic drivers in glioma/GBM, which contributes to a growing body of work that will help redefine GBM gene signatures.

Interconnections between GBM-specific lethal genes

Tumor suppressor genes are part of a large network of genes that negatively regulates cell proliferation and helps prevent highly proliferative cancer cells[268]. Alterations in growth-limiting genes speeds up the cell cycle, and can create cellular stresses, particularly on mechanisms that participate in the cell's surveillance and survival. These stresses can lead to new alterations in tumor suppressors and/or oncogenes that further promote tumorigenesis[268]. In addition to tumor suppressors, alterations in other genes, such as oncogenes, can cause functional impairments and cellular stresses during the course of multistep tumorigenesis. Although these oncogenic alterations provide cancer cells with growth and survival advantages, they also lead to cancer-specific vulnerabilities and requirements on genes that are needed to overcome these cancer-specific stressors and permit survival[50]. One strategy to target cancer cells is to identify and therapeutically target these cancer-specific genes, which likely have redundant and non-essential activities in non-transformed cells [51]. Here, I identified multiple molecular vulnerabilities specific to GSCs in processes that include kinetochore regulation and mitotic entry and progression, which leads to the requirement for *BuGZ* and *PKMYT1,* respectively. Interestingly, *BuGZ* has also been shown to be required for pre-messenger RNA splicing in cancer cells[148], which we have previously shown is a source of vulnerability for GSCs, as GSCs require *PHF5A* for 3' pre-mRNA splice site recognition[42]. In addition, we have shown that *PHF5A* depletion triggers defective splicing of thousands of essential genes, including many important genes needed for mitotic progression (i.e., *CDC20*)[42]. Moreover, we have shown that *BUBR1* is required in a subset of GBM patient isolates for kinetochore regulation[60,76]. Thus, further experimentation is warranted to determine whether *BuGZ*, *PKMYT1*, *PHF5A*, and

BUBR1 are interconnected, and whether other genes within these networks and cellular processes are also candidate GBM therapeutic targets.

The candidate GBM therapeutic targets identified here, *BuGZ* and *PKMYT1*, and previously, *BUBR1*[60] and *PHF5A*[42], have begun to unveil altered sub-networks that are required in GSCs, but not in NSCs. Additional genes within these networks may also be required by GSCs, but not in NSCs. Intriguingly, previous focused RNAi kinome screens conducted in both GSCs and NSCs categorized *MPS1* and *PLK1* as lethal genes in GSCs[60]. MPS1/TTK-dependent phosphorylation of KNL-1's MELT motifs recruits BUB3 to the KT[84,86,87,116,117]. Consistent with this result, we found that BuGZ's localization to the KT is KNL-1-dependent (Figure 2.9D); and thus, BuGZ likely depends on MPS1/TTK-dependent phosphorylation of KNL-1's MELT motifs for its localization to the KT. PLK1, on the other hand, can phosphorylate PKMYT1, which inactivates PKMTY1's kinase activity[177,178,186,223]. Therefore, PLK1's kinase activity could regulate the dynamics of CDK1's activation and APC's activation during mitotic progression and exit through PKMYT1 (see Chapter 3 discussion for further details). Moreover, PLK1 phosphorylates the kinetochore attachment regulatory domain (KARD) in BUBR1, which leads to the recruitment of PP2A-B56A to KTs and promotes the direct interaction between BUBR1 and PP2A-B56A at KTs[78,269]. Activated CDK1-cyclin B complexes also phosphorylate BUBR1 at S670, which stimulates the binding between BUBR1 and PP2A-B56A[77]. PP2A then counteracts ABK phosphorylation of outer KT substrates, which allows for stable KT-MT attachments[60,66,76-78]. PP2A also promotes the recruitment of PP1 to KTs[85], which reverses MPS1 mediated phosphorylation of KNL-1 at KTs[85,87]. PP1's activity at the KT likely releases BUB3 from the KT, and turns off the SAC[85,87]. Moreover, PP2A can counteract CDK1's phosphorylation on APC and other substrates, which promotes proper mitotic progression and

exit[270-272]. Collectively, *PKMYT1* and *BuGZ* are members of a complex, interconnected network that regulates the kinetochore and mitotic entry, progression, and exit.

Current therapeutics in clinical trials that target the kinetochore and disrupt mitosis

Kinase inhibitors to MPS1 and PLK1 are currently in clinical trials[66,273,274]. MPS1 inhibitors may cause the same KT-MT attachment defects in GBM as BuGZ depletion since BuGZ localization to the KT is likely dependent on MPS1 phosphorylation of KNL-1's MELT motifs[66]. However, because MPS1 is essential for SAC signaling[64], it's unclear whether dose-limiting toxicities in non-transformed cells will limit the effectiveness of MPS1 inhibitors[66]. PLK1 inhibitors have also shown efficacy in preclinical trials using GBM models[275] and have had clinical success in acute myeloid leukemia[274]. The PLK1 inhibitor, BI-6727 (volasertib), was recently designated as a "breakthrough therapy" by the FDA for the treatment of acute myeloid leukemia after raising complete remission rates for AML patients enrolled in a phase II trial that were not considered suitable for intensive induction therapy (31% for volasertib + low dose cytarabine versus 13% for low dose cytarabine alone)[276]. It will be interesting to determine whether these inhibitors are tolerable and effective for the treatment of GBM patients compared to the standard of care treatment alone while therapeutics to BuGZ and PKMYT1 are being discovered and developed.

Treating GBM patients with new combinational therapies

GBM and many other solid tumors are composed of a heterogeneous cell population derived from cancer stem-like cells[4,10-12,268]. These tumors can evolve rapidly in order to overcome perturbations from cytotoxic therapies due in part to intratumoral heterogeneity[30]. For example, in GBM, therapeutically targeting one subtype of GBM may give rise to another

subtype within the tumor that is resistant to the treatment. Therefore, along with surgery and radiation, future GBM treatments should consist of multiple therapeutics or a "cocktail" of drugs, like in the treatment of HIV-1[277], targeting multiple GBM-specific lethal targets, such as BuGZ[43], PKMYT1, and PHF5A[42]. However, it remains to be determined whether targeting multiple GBM-specific lethal hits would result in synthetic lethality in non-transformed NSCs. Nonetheless, the combination of the standard of care for GBM patients (surgery followed by temozolomide and radiation[7]) with the inhibition of a GBM-specific lethal target may provide a better therapeutic response in patients since temozolomide would activate the G2/M checkpoint[232,233] and an inhibitor to BuGZ or PKMYT1 would target molecular vulnerabilities specific to GBM isolates. It will also be interesting to determine whether the GBM-specific lethal targets identified here are also required in other heterogeneous cancer types, but not their respective non-neoplastic tissue of origin controls, which would lead to new candidate therapeutic targets for those cancers.

Tumors are now recognized as multicellular organs that are comprised of specialized cell types in additional to cancer stem-like cells, such as tumor associated: endothelial cells, pericytes, immune cells, fibroblasts, and others[268]. Collectively, these specialized cell types comprise the tumor microenvironment[268]. One relatively new therapeutic approach is to target both the cancer cells and their microenvironment. Recently, in GBM, preclinical trials have shown that combination therapies targeting both the GBM cells with a PI3K inhibitor and the tumor-associated macrophages/microglia with the small molecular inhibitor BLZ945, an inhibitor to colony stimulating factor 1 receptor, prolongs overall survival in a GBM mouse model, as 90% of the mice survived to the trail end point (approximately 6 months)[278]. Thus, future preclinical trials are warranted to determine if targeting GBM-specific lethal hits *BuGZ*,

PKMYT1, *BUBR1*, and *PHF5A* in combination with inhibitors to the tumor microenvironment would provide a better therapeutic response than the respective stand-alone treatments.

The need to identify additional GBM-specific lethal genes

One strategy to target cancer cells is to identify genes that are required by cancer cells in order to overcome cancer-specific vulnerabilities[50], but have redundant and non-essential activities in non-transformed cells, a concept originally proposed by Hartwell *et al.* for cancer cells[51]. Although we have identified multiple GBM-specific lethal hits, it is likely that additional genes contributing to GBM vulnerabilities could yield similar or superior cancer-lethal effects; and hence, validation studies to additional candidate GBM-specific lethal hits are necessary. Because of the challenges of drug discovery, drug development, and clinical testing, multiple candidate GBM therapeutic targets are needed in order to find a successful GBM therapeutic. Many of these candidate therapeutics to these targets will likely fail due to: specificity of the therapeutic to its target, ability to cross the blood-brain barrier, drug penetration in solid tumors, efficiently knocking down expression of its target to therapeutic levels, and unforeseen and intolerable side-effects. Therefore, additional candidate GBM-specific lethal hits should be investigated upon validation studies. The ideal candidate GBM therapeutic target for drug discovery and development would be candidate GBM-specific lethal hits that scored in both the shRNA and sgRNA genome-wide screens. GBM-specific lethal hits that are not required by non-transformed cells upon knockout could have better therapeutic windows than conventional cytotoxic chemotherapies or candidate therapeutic hits identified by functional genetic knockdown technologies. However, it would be extremely challenging to develop a therapeutic that can both eliminate the expression of a protein in a solid tumor and have minimal side effects in the patient. Thus, a candidate GBM-lethal hit that scores in the shRNA screens in addition to

the sgRNA screens would be an ideal therapeutic target, since the therapeutic would only need to knockdown the protein expression in cells to therapeutic levels. Candidate GBM-lethal hits in this category would likely have large therapeutic windows.

Functional genetics and precision medicine

Today's strive for precision medicine, the prevention and treatment strategies that take individual variability into account, has been made possible because of the recent developments of large-scale biologic databases, powerful methods for characterizing patients, and computational tools for analyzing large data sets[279]. For precision oncology, the goal is to perform whole genome sequencing on a patient's tumor and non-neoplastic tissue of origin controls once a patient arrives into the clinic. The patient's genomic profile would then be compared to different oncogenic signatures for that respective cancer type, which would then lead to additional testing such as proteomics, metabolomics, or diverse cellular assays to further characterize the patient's tumor. This would then aid the oncologist in prescribing an effective treatment regimen based upon the patient's tumor genetic profile and tumor characteristics. However, over the last decade, genomics have overshadowed the importance for functional genetics in precision medicine. The candidate GBM therapeutic targets identified here, *BuGZ* and *PKMYT1*, and previously, *BUBR1*[60] and *PHF5A*[42], would have not been identified by genomics, as each target is not commonly altered in GBM isolates (less than 1%)[104,105](Provisional GBM data set from TCGA). The work presented here, as well as previous work, has demonstrated that functional genetics is equally as important as genomics, which will help the drive for precision medicine.

GBM genetic profiling has identified commonly altered genes and activated pathways[23-25]. However, it's unclear whether therapeutics to these altered genes and members of these

activated pathways will ultimately have better therapeutic windows than conventional cytotoxic chemotherapies. Nonetheless, these GBM drivers lead to cancer-specific vulnerabilities and cancer-specific lethal genes. Functional genetics can be used to reveal cancer-specific lethal genes, as well as tumor suppressor genes. Functional genetics is also an important tool for elucidating and understanding the biology of cancer-specific lethal genes in cancer cells, and understanding the biological differences between cancer cells and non-transformed cells.

An understanding of the GBM-specific lethal hits identified here and previously had lead to the discovery of novel candidate therapeutic approaches, such as targeting GLEBS-BUB3 interactions[66] or PKMYT1's kinase activity. In addition, elucidating the biology of the GBM-specific lethal hits by functional genetics has led to the development of cellular assays to look for candidate therapeutics to GBM-specific lethal genes, such as the synthetic RFP mis-splicing reporter that illuminates following PHF5A inhibition (data not shown), and assays that may predict sensitivity to candidate anticancer therapeutics, such as the length of inter-kinetochore distances at metaphase that may predict whether a GBM patient would respond to BUBR1 inhibition[60]. Moreover, combining genomics and functional genetics has led to the formation of gene signatures that may also predict sensitivity to candidate anticancer therapeutics, such as gene signatures associated with *BUBR1* sensitivity that can also predict inter-kinetochore distances at metaphase (data not shown). Future studies are necessary in order to develop cellular assays that can be use for the discovery of therapeutics to BuGZ and PKMYT1. For example, the development of fluorescence resonance energy transfer (FRET) assays that illuminate the GLEBS-BUB3 interaction or immunofluorescence assays to look at PKMYT1's kinase activity at CDK1-T14 can be used to discover candidate therapeutics. The candidate therapeutics would target and disrupt the FRET signal from GLEBS-BUB3's interactions or

decrease CDK1-T14 expression by inhibiting PKMYT1's kinase activity, respectively. Taken together, genomics and functional genetics are equally important for precision medicine, as it can identify genetically altered genes, cancer-specific lethal genes, and tumor suppressors, which then can be used to derive gene signatures that can help determine the appropriate treatment for each cancer patient based upon their tumor genetic profile and tumor characteristics. The work presented here is part of a rapidly growing body of work by the science community that will ultimately lead to new and improve therapeutics for patients fighting cancer.

References

1 Neer, E. J., Schmidt, C. J., Nambudripad, R. & Smith, T. F. The ancient regulatory-protein family of WD-repeat proteins. *Nature* **371**, 297-300, doi:10.1038/371297a0 (1994).

2 Huse, J. T. & Holland, E. C. Targeting brain cancer: advances in the molecular pathology of malignant glioma and medulloblastoma. *Nat Rev Cancer* **10**, 319-331, doi:10.1038/nrc2818 (2010).

3 Stupp, R. *et al.* Radiotherapy plus concomitant and adjuvant temozolomide for glioblastoma. *N Engl J Med* **352**, 987-996, doi:352/10/987 [pii] 10.1056/NEJMoa043330 (2005).

4 Chen, J., McKay, R. M. & Parada, L. F. Malignant glioma: lessons from genomics, mouse models, and stem cells. *Cell* **149**, 36-47, doi:10.1016/j.cell.2012.03.009 (2012).

5 Alcantara Llaguno, S. *et al.* Malignant astrocytomas originate from neural stem/progenitor cells in a somatic tumor suppressor mouse model. *Cancer Cell* **15**, 45-56, doi:10.1016/j.ccr.2008.12.006 (2009).

6 Dunn, G. P. *et al.* Emerging insights into the molecular and cellular basis of glioblastoma. *Genes Dev* **26**, 756-784, doi:10.1101/gad.187922.112 (2012).

7 Weller, M., Cloughesy, T., Perry, J. R. & Wick, W. Standards of care for treatment of recurrent glioblastoma--are we there yet? *Neuro Oncol* **15**, 4-27, doi:10.1093/neuonc/nos273 (2013).

8 Cuddapah, V. A., Robel, S., Watkins, S. & Sontheimer, H. A neurocentric perspective on glioma invasion. *Nat Rev Neurosci* **15**, 455-465, doi:10.1038/nrn3765 (2014).

9 Furnari, F. B. *et al.* Malignant astrocytic glioma: genetics, biology, and paths to treatment. *Genes Dev* **21**, 2683-2710, doi:10.1101/gad.1596707 (2007).

10 Lee, J. *et al.* Tumor stem cells derived from glioblastomas cultured in bFGF and EGF more closely mirror the phenotype and genotype of primary tumors than do serum-cultured cell lines. *Cancer Cell* **9**, 391-403, doi:S1535-6108(06)00117-6 [pii] 10.1016/j.ccr.2006.03.030 (2006).

11 Son, M. J., Woolard, K., Nam, D. H., Lee, J. & Fine, H. A. SSEA-1 is an enrichment marker for tumor-initiating cells in human glioblastoma. *Cell Stem Cell* **4**, 440-452, doi:S1934-5909(09)00104-0 [pii] 10.1016/j.stem.2009.03.003 (2009).

12 Pollard, S. M. *et al.* Glioma stem cell lines expanded in adherent culture have tumor-specific phenotypes and are suitable for chemical and genetic screens. *Cell Stem Cell* **4**, 568-580, doi:10.1016/j.stem.2009.03.014 (2009).

13 Chen, R. *et al.* A hierarchy of self-renewing tumor-initiating cell types in glioblastoma. *Cancer Cell* **17**, 362-375, doi:10.1016/j.ccr.2009.12.049 (2010).

14 Chen, J. *et al.* A restricted cell population propagates glioblastoma growth after chemotherapy. *Nature* **488**, 522-526, doi:10.1038/nature11287 (2012).

15 Lugert, S. *et al.* Quiescent and active hippocampal neural stem cells with distinct morphologies respond selectively to physiological and pathological stimuli and aging. *Cell Stem Cell* **6**, 445-456, doi:10.1016/j.stem.2010.03.017 (2010).

16 Ming, G. L. & Song, H. Adult neurogenesis in the mammalian brain: significant answers and significant questions. *Neuron* **70**, 687-702, doi:10.1016/j.neuron.2011.05.001 (2011).

17 Chow, L. M. *et al.* Cooperativity within and among Pten, p53, and Rb pathways induces high-grade astrocytoma in adult brain. *Cancer Cell* **19**, 305-316, doi:10.1016/j.ccr.2011.01.039 (2011).
18 Obermeier, B., Daneman, R. & Ransohoff, R. M. Development, maintenance and disruption of the blood-brain barrier. *Nat Med* **19**, 1584-1596, doi:10.1038/nm.3407 (2013).
19 Agarwal, S., Sane, R., Oberoi, R., Ohlfest, J. R. & Elmquist, W. F. Delivery of molecularly targeted therapy to malignant glioma, a disease of the whole brain. *Expert Rev Mol Med* **13**, e17, doi:10.1017/S1462399411001888 (2011).
20 Sun, Y. *et al.* Long-term tripotent differentiation capacity of human neural stem (NS) cells in adherent culture. *Mol Cell Neurosci* **38**, 245-258, doi:S1044-7431(08)00068-7 [pii] 10.1016/j.mcn.2008.02.014 (2008).
21 Holmberg, J. *et al.* Activation of neural and pluripotent stem cell signatures correlates with increased malignancy in human glioma. *PLoS One* **6**, e18454, doi:10.1371/journal.pone.0018454 (2011).
22 Cancer Genome Atlas Research Network. Comprehensive genomic characterization defines human glioblastoma genes and core pathways. *Nature* **455**, 1061-1068, doi:nature07385 [pii] 10.1038/nature07385 (2008).
23 Brennan, C. W. *et al.* The somatic genomic landscape of glioblastoma. *Cell* **155**, 462-477, doi:10.1016/j.cell.2013.09.034 (2013).
24 Parsons, D. W. *et al.* An integrated genomic analysis of human glioblastoma multiforme. *Science* **321**, 1807-1812, doi:1164382 [pii] 10.1126/science.1164382 (2008).
25 TCGA. Comprehensive genomic characterization defines human glioblastoma genes and core pathways. *Nature* **455**, 1061-1068 (2008).
26 Herbst, R. S. Review of epidermal growth factor receptor biology. *Int J Radiat Oncol Biol Phys* **59**, 21-26, doi:10.1016/j.ijrobp.2003.11.041 (2004).
27 Phillips, H. S. *et al.* Molecular subclasses of high-grade glioma predict prognosis, delineate a pattern of disease progression, and resemble stages in neurogenesis. *Cancer Cell* **9**, 157-173, doi:S1535-6108(06)00056-0 [pii] 10.1016/j.ccr.2006.02.019 (2006).
28 Verhaak, R. G. *et al.* Integrated genomic analysis identifies clinically relevant subtypes of glioblastoma characterized by abnormalities in PDGFRA, IDH1, EGFR, and NF1. *Cancer Cell* **17**, 98-110, doi:S1535-6108(09)00432-2 [pii] 10.1016/j.ccr.2009.12.020 (2010).
29 Sanchez-Ortiz, E. *et al.* NF1 regulation of RAS/ERK signaling is required for appropriate granule neuron progenitor expansion and migration in cerebellar development. *Genes Dev* **28**, 2407-2420, doi:10.1101/gad.246603.114 (2014).
30 Patel, A. P. *et al.* Single-cell RNA-seq highlights intratumoral heterogeneity in primary glioblastoma. *Science* **344**, 1396-1401, doi:10.1126/science.1254257 (2014).
31 Hambardzumyan, D., Parada, L. F., Holland, E. C. & Charest, A. Genetic modeling of gliomas in mice: new tools to tackle old problems. *Glia* **59**, 1155-1168, doi:10.1002/glia.21142 (2011).
32 Kwon, C. H. *et al.* Pten haploinsufficiency accelerates formation of high-grade astrocytomas. *Cancer Res* **68**, 3286-3294 (2008).
33 Uhrbom, L. *et al.* Ink4a-Arf loss cooperates with KRas activation in astrocytes and neural progenitors to generate glioblastomas of various morphologies depending on activated Akt. *Cancer Res* **62**, 5551-5558 (2002).

34 Read, R. D., Cavenee, W. K., Furnari, F. B. & Thomas, J. B. A drosophila model for EGFR-Ras and PI3K-dependent human glioma. *PLoS Genet* **5**, e1000374, doi:10.1371/journal.pgen.1000374 (2009).
35 Bier, E. Drosophila, the golden bug, emerges as a tool for human genetics. *Nat Rev Genet* **6**, 9-23, doi:10.1038/nrg1503 (2005).
36 Freeman, M. R. & Doherty, J. Glial cell biology in Drosophila and vertebrates. *Trends Neurosci* **29**, 82-90, doi:10.1016/j.tins.2005.12.002 (2006).
37 Holland, E. C., Hively, W. P., DePinho, R. A. & Varmus, H. E. A constitutively active epidermal growth factor receptor cooperates with disruption of G1 cell-cycle arrest pathways to induce glioma-like lesions in mice. *Genes Dev* **12**, 3675-3685 (1998).
38 Wei, Q. *et al.* High-grade glioma formation results from postnatal pten loss or mutant epidermal growth factor receptor expression in a transgenic mouse glioma model. *Cancer Res* **66**, 7429-7437, doi:10.1158/0008-5472.CAN-06-0712 (2006).
39 Holland, E. C. *et al.* Combined activation of Ras and Akt in neural progenitors induces glioblastoma formation in mice. *Nat Genet* **25**, 55-57, doi:10.1038/75596 (2000).
40 Marumoto, T. *et al.* Development of a novel mouse glioma model using lentiviral vectors. *Nat Med* **15**, 110-116 (2009).
41 Zhang, B., Rotelli, M., Dixon, M. & Calvi, B. R. The function of Drosophila p53 isoforms in apoptosis. *Cell Death Differ*, doi:10.1038/cdd.2015.40 (2015).
42 Hubert, C. G. *et al.* Genome-wide RNAi screens in human brain tumor isolates reveal a novel viability requirement for PHF5A. *Genes Dev* **27**, 1032-1045, doi:10.1101/gad.212548.112 (2013).
43 Toledo, C. M. *et al.* BuGZ is required for Bub3 stability, Bub1 kinetochore function, and chromosome alignment. *Dev Cell* **28**, 282-294, doi:10.1016/j.devcel.2013.12.014 (2014).
44 Gazdar, A. F., Butel, J. S. & Carbone, M. SV40 and human tumours: myth, association or causality? *Nat Rev Cancer* **2**, 957-964, doi:10.1038/nrc947 (2002).
45 Hahn, W. C. *et al.* Creation of human tumour cells with defined genetic elements. *Nature* **400**, 464-468, doi:10.1038/22780 (1999).
46 Kendall, S. D., Linardic, C. M., Adam, S. J. & Counter, C. M. A network of genetic events sufficient to convert normal human cells to a tumorigenic state. *Cancer Res* **65**, 9824-9828, doi:65/21/9824 [pii] 10.1158/0008-5472.CAN-05-1543 (2005).
47 Ali, S. H. & DeCaprio, J. A. Cellular transformation by SV40 large T antigen: interaction with host proteins. *Semin Cancer Biol* **11**, 15-23, doi:10.1006/scbi.2000.0342 (2001).
48 Serrano, M., Lin, A. W., McCurrach, M. E., Beach, D. & Lowe, S. W. Oncogenic ras provokes premature cell senescence associated with accumulation of p53 and p16INK4a. *Cell* **88**, 593-602 (1997).
49 Nakagawa, H. & Opitz, O. G. Inducing cellular senescence using defined genetic elements. *Methods Mol Biol* **371**, 167-178, doi:10.1007/978-1-59745-361-5_13 (2007).
50 Nijhawan, D. *et al.* Cancer vulnerabilities unveiled by genomic loss. *Cell* **150**, 842-854, doi:10.1016/j.cell.2012.07.023 (2012).
51 Hartwell, L. H., Szankasi, P., Roberts, C. J., Murray, A. W. & Friend, S. H. Integrating genetic approaches into the discovery of anticancer drugs. *Science* **278**, 1064-1068 (1997).
52 Whitehead, K. A., Langer, R. & Anderson, D. G. Knocking down barriers: advances in siRNA delivery. *Nat Rev Drug Discov* **8**, 129-138, doi:10.1038/nrd2742 (2009).

53 Paddison, P. J. *et al.* A resource for large-scale RNA-interference-based screens in mammals. *Nature* **428**, 427-431, doi:10.1038/nature02370 (2004).
54 Cowley, G. S. *et al.* Parallel genome-scale loss of function screens in 216 cancer cell lines for the identification of context-specific genetic dependencies. *Sci Data* **1**, 140035, doi:10.1038/sdata.2014.35 (2014).
55 Ngo, V. N. *et al.* A loss-of-function RNA interference screen for molecular targets in cancer. *Nature* **441**, 106-110, doi:10.1038/nature04687 (2006).
56 Cheng, P. *et al.* Kinome-wide shRNA Screen Identifies the Receptor Tyrosine Kinase AXL as a Key Regulator for Mesenchymal Glioblastoma Stem-like Cells. *Stem Cell Reports* **4**, 899-913, doi:10.1016/j.stemcr.2015.03.005 (2015).
57 Chudnovsky, Y. *et al.* ZFHX4 interacts with the NuRD core member CHD4 and regulates the glioblastoma tumor-initiating cell state. *Cell Rep* **6**, 313-324, doi:10.1016/j.celrep.2013.12.032 (2014).
58 Goidts, V. *et al.* RNAi screening in glioma stem-like cells identifies PFKFB4 as a key molecule important for cancer cell survival. *Oncogene* **31**, 3235-3243, doi:10.1038/onc.2011.490 (2012).
59 Wurdak, H. *et al.* An RNAi screen identifies TRRAP as a regulator of brain tumor-initiating cell differentiation. *Cell Stem Cell* **6**, 37-47, doi:10.1016/j.stem.2009.11.002 (2010).
60 Ding, Y. *et al.* Cancer-Specific requirement for BUB1B/BUBR1 in human brain tumor isolates and genetically transformed cells. *Cancer Discov* **3**, 198-211, doi:10.1158/2159-8290.CD-12-0353 (2013).
61 Strezoska, Z. *et al.* Optimized PCR conditions and increased shRNA fold representation improve reproducibility of pooled shRNA screens. *PLoS One* **7**, e42341, doi:10.1371/journal.pone.0042341 (2012).
62 Erlich, Y. *et al.* DNA Sudoku--harnessing high-throughput sequencing for multiplexed specimen analysis. *Genome Res* **19**, 1243-1253, doi:10.1101/gr.092957.109 (2009).
63 Foley, E. A. & Kapoor, T. M. Microtubule attachment and spindle assembly checkpoint signalling at the kinetochore. *Nat Rev Mol Cell Biol* **14**, 25-37, doi:10.1038/nrm3494 nrm3494 [pii] (2012).
64 Musacchio, A. & Salmon, E. D. The spindle-assembly checkpoint in space and time. *Nat Rev Mol Cell Biol* **8**, 379-393, doi:nrm2163 [pii] 10.1038/nrm2163 (2007).
65 McAinsh, A. D. & Meraldi, P. The CCAN complex: linking centromere specification to control of kinetochore-microtubule dynamics. *Semin Cell Dev Biol* **22**, 946-952, doi:10.1016/j.semcdb.2011.09.016 (2011).
66 Herman, J. A., Toledo, C. M., Olson, J. M., DeLuca, J. G. & Paddison, P. J. Molecular Pathways: Regulation and Targeting of Kinetochore-Microtubule Attachment in Cancer. *Clin Cancer Res*, doi:10.1158/1078-0432.CCR-13-0645 (2014).
67 Santaguida, S. & Musacchio, A. The life and miracles of kinetochores. *Embo J* **28**, 2511-2531, doi:emboj2009173 [pii] 10.1038/emboj.2009.173 (2009).
68 Cheeseman, I. M. & Desai, A. Molecular architecture of the kinetochore-microtubule interface. *Nat Rev Mol Cell Biol* **9**, 33-46, doi:nrm2310 [pii] 10.1038/nrm2310 (2008).
69 Kops, G. J., Weaver, B. A. & Cleveland, D. W. On the road to cancer: aneuploidy and the mitotic checkpoint. *Nat Rev Cancer* **5**, 773-785, doi:nrc1714 [pii] 10.1038/nrc1714 (2005).

70 Lara-Gonzalez, P., Westhorpe, F. G. & Taylor, S. S. The spindle assembly checkpoint. *Curr Biol* **22**, R966-980, doi:10.1016/j.cub.2012.10.006 S0960-9822(12)01189-X [pii] (2012).
71 Weaver, B. A. & Cleveland, D. W. Does aneuploidy cause cancer? *Curr Opin Cell Biol* **18**, 658-667, doi:10.1016/j.ceb.2006.10.002 (2006).
72 Suijkerbuijk, S. J. & Kops, G. J. Preventing aneuploidy: the contribution of mitotic checkpoint proteins. *Biochim Biophys Acta* **1786**, 24-31, doi:10.1016/j.bbcan.2008.04.001 (2008).
73 Malmanche, N., Maia, A. & Sunkel, C. E. The spindle assembly checkpoint: preventing chromosome mis-segregation during mitosis and meiosis. *FEBS Lett* **580**, 2888-2895, doi:10.1016/j.febslet.2006.03.081 (2006).
74 Bie, L. *et al.* The accuracy of survival time prediction for patients with glioma is improved by measuring mitotic spindle checkpoint gene expression. *PLoS One* **6**, e25631, doi:10.1371/journal.pone.0025631 PONE-D-11-09272 [pii] (2011).
75 Malureanu, L. A. *et al.* BubR1 N terminus acts as a soluble inhibitor of cyclin B degradation by APC/C(Cdc20) in interphase. *Dev Cell* **16**, 118-131, doi:S1534-5807(08)00478-4 [pii] 10.1016/j.devcel.2008.11.004 (2009).
76 Herman, J. A., DeLuca, K.F., Toledo, C.M., Paddison, P.J., & DeLuca, J.G. Oncogenic RAS/MAPK signaling 1 hyper-activates 2 Aurora B kinase and perturbs kinetochore3 microtubule attachments. *In review* (2015).
77 Kruse, T. *et al.* Direct binding between BubR1 and B56-PP2A phosphatase complexes regulate mitotic progression. *J Cell Sci* **126**, 1086-1092, doi:10.1242/jcs.122481 (2013).
78 Suijkerbuijk, S. J., Vleugel, M., Teixeira, A. & Kops, G. J. Integration of kinase and phosphatase activities by BUBR1 ensures formation of stable kinetochore-microtubule attachments. *Dev Cell* **23**, 745-755, doi:10.1016/j.devcel.2012.09.005 (2012).
79 Wang, X. *et al.* The mitotic checkpoint protein hBUB3 and the mRNA export factor hRAE1 interact with GLE2p-binding sequence (GLEBS)-containing proteins. *J Biol Chem* **276**, 26559-26567, doi:10.1074/jbc.M101083200 M101083200 [pii] (2001).
80 Doudna, J. A. & Charpentier, E. Genome editing. The new frontier of genome engineering with CRISPR-Cas9. *Science* **346**, 1258096, doi:10.1126/science.1258096 (2014).
81 Meraldi, P. & Sorger, P. K. A dual role for Bub1 in the spindle checkpoint and chromosome congression. *EMBO J* **24**, 1621-1633, doi:10.1038/sj.emboj.7600641 (2005).
82 Lampson, M. A. & Kapoor, T. M. The human mitotic checkpoint protein BubR1 regulates chromosome-spindle attachments. *Nat Cell Biol* **7**, 93-98, doi:ncb1208 [pii] 10.1038/ncb1208 (2005).
83 Logarinho, E., Resende, T., Torres, C. & Bousbaa, H. The human spindle assembly checkpoint protein Bub3 is required for the establishment of efficient kinetochore-microtubule attachments. *Mol Biol Cell* **19**, 1798-1813, doi:10.1091/mbc.E07-07-0633 (2008).
84 Yamagishi, Y., Yang, C. H., Tanno, Y. & Watanabe, Y. MPS1/Mph1 phosphorylates the kinetochore protein KNL1/Spc7 to recruit SAC components. *Nat Cell Biol* **14**, 746-752, doi:10.1038/ncb2515 (2012).

85 Nijenhuis, W., Vallardi, G., Teixeira, A., Kops, G. J. & Saurin, A. T. Negative feedback at kinetochores underlies a responsive spindle checkpoint signal. *Nat Cell Biol* **16**, 1257-1264, doi:10.1038/ncb3065 (2014).
86 Primorac, I. *et al.* Bub3 reads phosphorylated MELT repeats to promote spindle assembly checkpoint signaling. *Elife* **2**, e01030, doi:10.7554/eLife.01030 (2013).
87 London, N., Ceto, S., Ranish, J. A. & Biggins, S. Phosphoregulation of Spc105 by Mps1 and PP1 regulates Bub1 localization to kinetochores. *Curr Biol* **22**, 900-906, doi:10.1016/j.cub.2012.03.052 (2012).
88 Harris, L., Davenport, J., Neale, G. & Goorha, R. The mitotic checkpoint gene BubR1 has two distinct functions in mitosis. *Exp Cell Res* **308**, 85-100, doi:S0014-4827(05)00111-4 [pii] 10.1016/j.yexcr.2005.03.036 (2005).
89 Ricke, R. M., Jeganathan, K. B., Malureanu, L., Harrison, A. M. & van Deursen, J. M. Bub1 kinase activity drives error correction and mitotic checkpoint control but not tumor suppression. *J Cell Biol* **199**, 931-949, doi:10.1083/jcb.201205115 (2012).
90 Taylor, S. S., Ha, E. & McKeon, F. The human homologue of Bub3 is required for kinetochore localization of Bub1 and a Mad3/Bub1-related protein kinase. *J Cell Biol* **142**, 1-11 (1998).
91 Yamagishi, Y., Honda, T., Tanno, Y. & Watanabe, Y. Two histone marks establish the inner centromere and chromosome bi-orientation. *Science* **330**, 239-243, doi:10.1126/science.1194498 (2010).
92 Cheeseman, I. M., Chappie, J. S., Wilson-Kubalek, E. M. & Desai, A. The conserved KMN network constitutes the core microtubule-binding site of the kinetochore. *Cell* **127**, 983-997, doi:S0092-8674(06)01345-6 [pii] 10.1016/j.cell.2006.09.039 (2006).
93 DeLuca, J. G. *et al.* Kinetochore microtubule dynamics and attachment stability are regulated by Hec1. *Cell* **127**, 969-982, doi:S0092-8674(06)01408-5 [pii] 10.1016/j.cell.2006.09.047 (2006).
94 DeLuca, K. F., Lens, S. M. & DeLuca, J. G. Temporal changes in Hec1 phosphorylation control kinetochore-microtubule attachment stability during mitosis. *J Cell Sci* **124**, 622-634, doi:jcs.072629 [pii] 10.1242/jcs.072629 (2011).
95 Welburn, J. P. *et al.* Aurora B phosphorylates spatially distinct targets to differentially regulate the kinetochore-microtubule interface. *Mol Cell* **38**, 383-392, doi:10.1016/j.molcel.2010.02.034 (2010).
96 Bailer, S. M. *et al.* Nup116p and nup100p are interchangeable through a conserved motif which constitutes a docking site for the mRNA transport factor gle2p. *EMBO J* **17**, 1107-1119, doi:10.1093/emboj/17.4.1107 (1998).
97 Larsen, N. A., Al-Bassam, J., Wei, R. R. & Harrison, S. C. Structural analysis of Bub3 interactions in the mitotic spindle checkpoint. *Proc Natl Acad Sci U S A* **104**, 1201-1206, doi:10.1073/pnas.0610358104 (2007).
98 Pahl, P. M. *et al.* ZNF207, a ubiquitously expressed zinc finger gene on chromosome 6p21.3. *Genomics* **53**, 410-412, doi:10.1006/geno.1998.5442 (1998).
99 Taguchi, E. *et al.* Zep: A novel zinc finger protein containing a large proline-rich domain. *J Biochem* **124**, 1220-1228 (1998).
100 Brayer, K. J. & Segal, D. J. Keep your fingers off my DNA: protein-protein interactions mediated by C2H2 zinc finger domains. *Cell Biochem Biophys* **50**, 111-131, doi:10.1007/s12013-008-9008-5 (2008).

101 Klug, A. The discovery of zinc fingers and their applications in gene regulation and genome manipulation. *Annu Rev Biochem* **79**, 213-231, doi:10.1146/annurev-biochem-010909-095056 (2010).
102 Wolfe, S. A., Nekludova, L. & Pabo, C. O. DNA recognition by Cys2His2 zinc finger proteins. *Annu Rev Biophys Biomol Struct* **29**, 183-212, doi:10.1146/annurev.biophys.29.1.183 (2000).
103 Burdach, J., O'Connell, M. R., Mackay, J. P. & Crossley, M. Two-timing zinc finger transcription factors liaising with RNA. *Trends Biochem Sci* **37**, 199-205, doi:10.1016/j.tibs.2012.02.001 (2012).
104 Gao, J. *et al.* Integrative analysis of complex cancer genomics and clinical profiles using the cBioPortal. *Sci Signal* **6**, pl1, doi:10.1126/scisignal.2004088 (2013).
105 Cerami, E. *et al.* The cBio cancer genomics portal: an open platform for exploring multidimensional cancer genomics data. *Cancer Discov* **2**, 401-404, doi:10.1158/2159-8290.CD-12-0095 (2012).
106 Uhlen, M. *et al.* Proteomics. Tissue-based map of the human proteome. *Science* **347**, 1260419, doi:10.1126/science.1260419 (2015).
107 Singh, S. K. *et al.* Identification of human brain tumour initiating cells. *Nature* **432**, 396-401, doi:nature03128 [pii] 10.1038/nature03128 (2004).
108 Galli, R. *et al.* Isolation and characterization of tumorigenic, stem-like neural precursors from human glioblastoma. *Cancer Res* **64**, 7011-7021, doi:64/19/7011 [pii] 10.1158/0008-5472.CAN-04-1364 (2004).
109 Powell, S. *et al.* eggNOG v3.0: orthologous groups covering 1133 organisms at 41 different taxonomic ranges. *Nucleic Acids Res* **40**, D284-289, doi:10.1093/nar/gkr1060 (2012).
110 Hoyt, M. A., Totis, L. & Roberts, B. T. S. cerevisiae genes required for cell cycle arrest in response to loss of microtubule function. *Cell* **66**, 507-517, doi:0092-8674(81)90014-3 [pii] (1991).
111 Pritchard, C. E., Fornerod, M., Kasper, L. H. & van Deursen, J. M. RAE1 is a shuttling mRNA export factor that binds to a GLEBS-like NUP98 motif at the nuclear pore complex through multiple domains. *J Cell Biol* **145**, 237-254 (1999).
112 Ren, Y., Seo, H. S., Blobel, G. & Hoelz, A. Structural and functional analysis of the interaction between the nucleoporin Nup98 and the mRNA export factor Rae1. *Proc Natl Acad Sci U S A* **107**, 10406-10411, doi:10.1073/pnas.1005389107 (2010).
113 Howell, B. J. *et al.* Spindle checkpoint protein dynamics at kinetochores in living cells. *Curr Biol* **14**, 953-964, doi:10.1016/j.cub.2004.05.053 (2004).
114 Taylor, S. S. & McKeon, F. Kinetochore localization of murine Bub1 is required for normal mitotic timing and checkpoint response to spindle damage. *Cell* **89**, 727-735 (1997).
115 Jablonski, S. A., Chan, G. K., Cooke, C. A., Earnshaw, W. C. & Yen, T. J. The hBUB1 and hBUBR1 kinases sequentially assemble onto kinetochores during prophase with hBUBR1 concentrating at the kinetochore plates in mitosis. *Chromosoma* **107**, 386-396 (1998).
116 Kiyomitsu, T., Obuse, C. & Yanagida, M. Human Blinkin/AF15q14 is required for chromosome alignment and the mitotic checkpoint through direct interaction with Bub1 and BubR1. *Dev Cell* **13**, 663-676, doi:10.1016/j.devcel.2007.09.005 (2007).

117 Primorac, I. & Musacchio, A. Panta rhei: the APC/C at steady state. *J Cell Biol* **201**, 177-189, doi:10.1083/jcb.201301130 (2013).
118 Hoffman, D. B., Pearson, C. G., Yen, T. J., Howell, B. J. & Salmon, E. D. Microtubule-dependent changes in assembly of microtubule motor proteins and mitotic spindle checkpoint proteins at PtK1 kinetochores. *Mol Biol Cell* **12**, 1995-2009 (2001).
119 Vanoosthuyse, V., Valsdottir, R., Javerzat, J. P. & Hardwick, K. G. Kinetochore targeting of fission yeast Mad and Bub proteins is essential for spindle checkpoint function but not for all chromosome segregation roles of Bub1p. *Mol Cell Biol* **24**, 9786-9801, doi:10.1128/MCB.24.22.9786-9801.2004 (2004).
120 Meraldi, P., Draviam, V. M. & Sorger, P. K. Timing and checkpoints in the regulation of mitotic progression. *Dev Cell* **7**, 45-60, doi:10.1016/j.devcel.2004.06.006 (2004).
121 Kawashima, S. A. *et al.* Shugoshin enables tension-generating attachment of kinetochores by loading Aurora to centromeres. *Genes Dev* **21**, 420-435, doi:10.1101/gad.1497307 (2007).
122 Tsukahara, T., Tanno, Y. & Watanabe, Y. Phosphorylation of the CPC by Cdk1 promotes chromosome bi-orientation. *Nature* **467**, 719-723, doi:10.1038/nature09390 (2010).
123 Perera, D. *et al.* Bub1 maintains centromeric cohesion by activation of the spindle checkpoint. *Dev Cell* **13**, 566-579, doi:10.1016/j.devcel.2007.08.008 (2007).
124 Wang, Q. *et al.* BUBR1 deficiency results in abnormal megakaryopoiesis. *Blood* **103**, 1278-1285, doi:10.1182/blood-2003-06-2158 2003-06-2158 [pii] (2004).
125 Kalitsis, P., Earle, E., Fowler, K. J. & Choo, K. H. Bub3 gene disruption in mice reveals essential mitotic spindle checkpoint function during early embryogenesis. *Genes Dev* **14**, 2277-2282 (2000).
126 Shalem, O. *et al.* Genome-scale CRISPR-Cas9 knockout screening in human cells. *Science* **343**, 84-87, doi:10.1126/science.1247005 (2014).
127 Jinek, M. *et al.* A programmable dual-RNA-guided DNA endonuclease in adaptive bacterial immunity. *Science* **337**, 816-821, doi:10.1126/science.1225829 (2012).
128 Ran, F. A. *et al.* Genome engineering using the CRISPR-Cas9 system. *Nat Protoc* **8**, 2281-2308, doi:10.1038/nprot.2013.143 (2013).
129 Shalem, O., Sanjana, N. E. & Zhang, F. High-throughput functional genomics using CRISPR-Cas9. *Nat Rev Genet* **16**, 299-311, doi:10.1038/nrg3899 (2015).
130 Prieto, J. L. & McStay, B. Recruitment of factors linking transcription and processing of pre-rRNA to NOR chromatin is UBF-dependent and occurs independent of transcription in human cells. *Genes Dev* **21**, 2041-2054, doi:10.1101/gad.436707 (2007).
131 Benanti, J. A. & Galloway, D. A. The normal response to RAS: senescence or transformation? *Cell Cycle* **3**, 715-717 (2004).
132 Cui, Y. & Guadagno, T. M. B-Raf(V600E) signaling deregulates the mitotic spindle checkpoint through stabilizing Mps1 levels in melanoma cells. *Oncogene* **27**, 3122-3133, doi:10.1038/sj.onc.1210972 (2008).
133 Zhang, L. *et al.* [Study of negative feedback between wild-type BRAF or RAFV600E and Mps1 in melanoma]. *Zhonghua Bing Li Xue Za Zhi* **44**, 274-277 (2015).
134 Brough, R. *et al.* Functional viability profiles of breast cancer. *Cancer Discov* **1**, 260-273, doi:10.1158/2159-8290.CD-11-0107 (2011).
135 Naud, S. *et al.* Structure-based design of orally bioavailable 1H-pyrrolo[3,2-c]pyridine inhibitors of mitotic kinase monopolar spindle 1 (MPS1). *J Med Chem* **56**, 10045-10065, doi:10.1021/jm401395s (2013).

136 Ferretti, C. *et al.* Expression of the kinetochore protein Hec1 during the cell cycle in normal and cancer cells and its regulation by the pRb pathway. *Cell Cycle* **9**, 4174-4182 (2010).
137 Nair, J. S. *et al.* Aurora B kinase regulates the postmitotic endoreduplication checkpoint via phosphorylation of the retinoblastoma protein at serine 780. *Mol Biol Cell* **20**, 2218-2228, doi:10.1091/mbc.E08-08-0885 (2009).
138 Macdonald, J. I. & Dick, F. A. Posttranslational modifications of the retinoblastoma tumor suppressor protein as determinants of function. *Genes Cancer* **3**, 619-633, doi:10.1177/1947601912473305 (2012).
139 Yang, Y., Tsuchiya, D. & Lacefield, S. Bub3 promotes Cdc20-dependent activation of the APC/C in S. cerevisiae. *J Cell Biol* **209**, 519-527, doi:10.1083/jcb.201412036 (2015).
140 Kim, T. *et al.* Kinetochore-localized BUB-1/BUB-3 complex promotes anaphase onset in C. elegans. *J Cell Biol* **209**, 507-517, doi:10.1083/jcb.201412035 (2015).
141 Jiang, Y. *et al.* PKM2 regulates chromosome segregation and mitosis progression of tumor cells. *Mol Cell* **53**, 75-87, doi:10.1016/j.molcel.2013.11.001 (2014).
142 Behzadnia, N. *et al.* Composition and three-dimensional EM structure of double affinity-purified, human prespliceosomal A complexes. *EMBO J* **26**, 1737-1748, doi:10.1038/sj.emboj.7601631 (2007).
143 Zhou, Z., Licklider, L. J., Gygi, S. P. & Reed, R. Comprehensive proteomic analysis of the human spliceosome. *Nature* **419**, 182-185, doi:10.1038/nature01031 (2002).
144 Hegele, A. *et al.* Dynamic protein-protein interaction wiring of the human spliceosome. *Mol Cell* **45**, 567-580, doi:10.1016/j.molcel.2011.12.034 (2012).
145 Makarov, E. M. *et al.* Small nuclear ribonucleoprotein remodeling during catalytic activation of the spliceosome. *Science* **298**, 2205-2208, doi:10.1126/science.1077783 (2002).
146 Jurica, M. S., Licklider, L. J., Gygi, S. R., Grigorieff, N. & Moore, M. J. Purification and characterization of native spliceosomes suitable for three-dimensional structural analysis. *RNA* **8**, 426-439 (2002).
147 Deckert, J. *et al.* Protein composition and electron microscopy structure of affinity-purified human spliceosomal B complexes isolated under physiological conditions. *Mol Cell Biol* **26**, 5528-5543, doi:10.1128/MCB.00582-06 (2006).
148 Wan, Y. *et al.* Splicing function of mitotic regulators links R-loop-mediated DNA damage to tumor cell killing. *J Cell Biol* **209**, 235-246, doi:10.1083/jcb.201409073 (2015).
149 Klebig, C., Korinth, D. & Meraldi, P. Bub1 regulates chromosome segregation in a kinetochore-independent manner. *J Cell Biol* **185**, 841-858, doi:10.1083/jcb.200902128 (2009).
150 Liu, S. T., Rattner, J. B., Jablonski, S. A. & Yen, T. J. Mapping the assembly pathways that specify formation of the trilaminar kinetochore plates in human cells. *J Cell Biol* **175**, 41-53, doi:10.1083/jcb.200606020 (2006).
151 Havugimana, P. C. *et al.* A census of human soluble protein complexes. *Cell* **150**, 1068-1081, doi:10.1016/j.cell.2012.08.011 (2012).
152 Wang, J. *et al.* Toward an understanding of the protein interaction network of the human liver. *Mol Syst Biol* **7**, 536, doi:10.1038/msb.2011.67 (2011).
153 Giot, L. *et al.* A protein interaction map of Drosophila melanogaster. *Science* **302**, 1727-1736, doi:10.1126/science.1090289 (2003).

154 Li, S. *et al.* A map of the interactome network of the metazoan C. elegans. *Science* **303**, 540-543, doi:10.1126/science.1091403 (2004).
155 Van Leene, J. *et al.* Targeted interactomics reveals a complex core cell cycle machinery in Arabidopsis thaliana. *Mol Syst Biol* **6**, 397, doi:10.1038/msb.2010.53 (2010).
156 Ding, Y. *et al.* Cancer-specific requirement for BUB1B/BubR1 in human brain tumor isolates and genetically transformed cells. *Cancer discovery*, doi:2159-8290.CD-12-0353 [pii] 10.1158/2159-8290.CD-12-0353 (2012).
157 Chen, X. *et al.* G9a/GLP-dependent histone H3K9me2 patterning during human hematopoietic stem cell lineage commitment. *Genes Dev* **26**, 2499-2511, doi:10.1101/gad.200329.112 (2012).
158 Kean, M. J., Couzens, A. L. & Gingras, A. C. Mass spectrometry approaches to study mammalian kinase and phosphatase associated proteins. *Methods* **57**, 400-408, doi:10.1016/j.ymeth.2012.06.002 (2012).
159 American Cancer Society. *American Cancer Society: Cancer Facts and Figures 2010*.
160 Conti, L. *et al.* Niche-independent symmetrical self-renewal of a mammalian tissue stem cell. *PLoS Biol* **3**, e283, doi:04-PLBI-RA-0934R2 [pii] 10.1371/journal.pbio.0030283 (2005).
161 Liu, F., Stanton, J. J., Wu, Z. & Piwnica-Worms, H. The human Myt1 kinase preferentially phosphorylates Cdc2 on threonine 14 and localizes to the endoplasmic reticulum and Golgi complex. *Mol Cell Biol* **17**, 571-583 (1997).
162 Booher, R. N., Holman, P. S. & Fattaey, A. Human Myt1 is a cell cycle-regulated kinase that inhibits Cdc2 but not Cdk2 activity. *J Biol Chem* **272**, 22300-22306 (1997).
163 Gargiulo, G. *et al.* In vivo RNAi screen for BMI1 targets identifies TGF-beta/BMP-ER stress pathways as key regulators of neural- and malignant glioma-stem cell homeostasis. *Cancer Cell* **23**, 660-676, doi:10.1016/j.ccr.2013.03.030 (2013).
164 Kazanis, I. *et al.* Quiescence and activation of stem and precursor cell populations in the subependymal zone of the mammalian brain are associated with distinct cellular and extracellular matrix signals. *J Neurosci* **30**, 9771-9781, doi:10.1523/JNEUROSCI.0700-10.2010 (2010).
165 Lathia, J. D. *et al.* Laminin alpha 2 enables glioblastoma stem cell growth. *Ann Neurol* **72**, 766-778, doi:10.1002/ana.23674 (2012).
166 Luo, J. *et al.* A genome-wide RNAi screen identifies multiple synthetic lethal interactions with the Ras oncogene. *Cell* **137**, 835-848, doi:S0092-8674(09)00529-7 [pii] 10.1016/j.cell.2009.05.006 (2009).
167 Wang, T., Wei, J. J., Sabatini, D. M. & Lander, E. S. Genetic screens in human cells using the CRISPR-Cas9 system. *Science* **343**, 80-84, doi:10.1126/science.1246981 (2014).
168 Makarova, K. S., Grishin, N. V., Shabalina, S. A., Wolf, Y. I. & Koonin, E. V. A putative RNA-interference-based immune system in prokaryotes: computational analysis of the predicted enzymatic machinery, functional analogies with eukaryotic RNAi, and hypothetical mechanisms of action. *Biol Direct* **1**, 7, doi:10.1186/1745-6150-1-7 (2006).
169 Makarova, K. S. *et al.* Evolution and classification of the CRISPR-Cas systems. *Nat Rev Microbiol* **9**, 467-477, doi:10.1038/nrmicro2577 (2011).
170 Deltcheva, E. *et al.* CRISPR RNA maturation by trans-encoded small RNA and host factor RNase III. *Nature* **471**, 602-607, doi:10.1038/nature09886 (2011).

171 Mali, P. *et al.* RNA-guided human genome engineering via Cas9. *Science* **339**, 823-826, doi:10.1126/science.1232033 (2013).
172 Mueller, P. R., Coleman, T. R., Kumagai, A. & Dunphy, W. G. Myt1: a membrane-associated inhibitory kinase that phosphorylates Cdc2 on both threonine-14 and tyrosine-15. *Science* **270**, 86-90 (1995).
173 Brown, N. R. *et al.* CDK1 structures reveal conserved and unique features of the essential cell cycle CDK. *Nat Commun* **6**, 6769, doi:10.1038/ncomms7769 (2015).
174 Malumbres, M. & Barbacid, M. Cell cycle, CDKs and cancer: a changing paradigm. *Nat Rev Cancer* **9**, 153-166, doi:10.1038/nrc2602 (2009).
175 Bashir, T. & Pagano, M. Cdk1: the dominant sibling of Cdk2. *Nat Cell Biol* **7**, 779-781, doi:10.1038/ncb0805-779 (2005).
176 Deibler, R. W. & Kirschner, M. W. Quantitative reconstitution of mitotic CDK1 activation in somatic cell extracts. *Mol Cell* **37**, 753-767, doi:10.1016/j.molcel.2010.02.023 (2010).
177 Lindqvist, A., Rodriguez-Bravo, V. & Medema, R. H. The decision to enter mitosis: feedback and redundancy in the mitotic entry network. *J Cell Biol* **185**, 193-202, doi:10.1083/jcb.200812045 (2009).
178 Barr, F. A., Sillje, H. H. & Nigg, E. A. Polo-like kinases and the orchestration of cell division. *Nat Rev Mol Cell Biol* **5**, 429-440, doi:10.1038/nrm1401 (2004).
179 Poon, R. Y., Chau, M. S., Yamashita, K. & Hunter, T. The role of Cdc2 feedback loop control in the DNA damage checkpoint in mammalian cells. *Cancer Res* **57**, 5168-5178 (1997).
180 Jin, Z., Homola, E., Tiong, S. & Campbell, S. D. Drosophila myt1 is the major cdk1 inhibitory kinase for wing imaginal disc development. *Genetics* **180**, 2123-2133, doi:10.1534/genetics.108.093195 (2008).
181 Nakajima, H. *et al.* Myt1 protein kinase is essential for Golgi and ER assembly during mitotic exit. *J Cell Biol* **181**, 89-103, doi:10.1083/jcb.200708176 (2008).
182 Watanabe, N., Broome, M. & Hunter, T. Regulation of the human WEE1Hu CDK tyrosine 15-kinase during the cell cycle. *Embo J* **14**, 1878-1891 (1995).
183 Heald, R., McLoughlin, M. & McKeon, F. Human wee1 maintains mitotic timing by protecting the nucleus from cytoplasmically activated Cdc2 kinase. *Cell* **74**, 463-474 (1993).
184 Donzelli, M. & Draetta, G. F. Regulating mammalian checkpoints through Cdc25 inactivation. *EMBO Rep* **4**, 671-677, doi:10.1038/sj.embor.embor887 (2003).
185 Lindqvist, A., van Zon, W., Karlsson Rosenthal, C. & Wolthuis, R. M. Cyclin B1-Cdk1 activation continues after centrosome separation to control mitotic progression. *PLoS Biol* **5**, e123, doi:10.1371/journal.pbio.0050123 (2007).
186 Nakajima, H., Toyoshima-Morimoto, F., Taniguchi, E. & Nishida, E. Identification of a consensus motif for Plk (Polo-like kinase) phosphorylation reveals Myt1 as a Plk1 substrate. *J Biol Chem* **278**, 25277-25280, doi:10.1074/jbc.C300126200 (2003).
187 Ayeni, J. O. *et al.* Dual phosphorylation of cdk1 coordinates cell proliferation with key developmental processes in Drosophila. *Genetics* **196**, 197-210, doi:10.1534/genetics.113.156281 (2014).
188 Coulonval, K., Kooken, H. & Roger, P. P. Coupling of T161 and T14 phosphorylations protects cyclin B-CDK1 from premature activation. *Mol Biol Cell* **22**, 3971-3985, doi:10.1091/mbc.E11-02-0136 (2011).

189 Tominaga, Y., Li, C., Wang, R. H. & Deng, C. X. Murine Wee1 plays a critical role in cell cycle regulation and pre-implantation stages of embryonic development. *Int J Biol Sci* **2**, 161-170 (2006).
190 Santos, S. D., Wollman, R., Meyer, T. & Ferrell, J. E., Jr. Spatial positive feedback at the onset of mitosis. *Cell* **149**, 1500-1513, doi:10.1016/j.cell.2012.05.028 (2012).
191 Potapova, T. A., Daum, J. R., Byrd, K. S. & Gorbsky, G. J. Fine tuning the cell cycle: activation of the Cdk1 inhibitory phosphorylation pathway during mitotic exit. *Mol Biol Cell* **20**, 1737-1748, doi:10.1091/mbc.E08-07-0771 (2009).
192 Pomerening, J. R., Kim, S. Y. & Ferrell, J. E., Jr. Systems-level dissection of the cell-cycle oscillator: bypassing positive feedback produces damped oscillations. *Cell* **122**, 565-578, doi:10.1016/j.cell.2005.06.016 (2005).
193 Ma, Y., Yuan, X., Wyatt, W. R. & Pomerening, J. R. Expression of constitutively active CDK1 stabilizes APC-Cdh1 substrates and potentiates premature spindle assembly and checkpoint function in G1 cells. *PLoS One* **7**, e33835, doi:10.1371/journal.pone.0033835 (2012).
194 Vassilopoulos, A. *et al.* WEE1 murine deficiency induces hyper-activation of APC/C and results in genomic instability and carcinogenesis. *Oncogene* **34**, 3023-3035, doi:10.1038/onc.2014.239 (2015).
195 Pomerening, J. R., Ubersax, J. A. & Ferrell, J. E., Jr. Rapid cycling and precocious termination of G1 phase in cells expressing CDK1AF. *Mol Biol Cell* **19**, 3426-3441, doi:10.1091/mbc.E08-02-0172 (2008).
196 O'Donnell, M., Langston, L. & Stillman, B. Principles and concepts of DNA replication in bacteria, archaea, and eukarya. *Cold Spring Harb Perspect Biol* **5**, doi:10.1101/cshperspect.a010108 (2013).
197 Robinson, M. D., McCarthy, D. J. & Smyth, G. K. edgeR: a Bioconductor package for differential expression analysis of digital gene expression data. *Bioinformatics* **26**, 139-140, doi:btp616 [pii] 10.1093/bioinformatics/btp616 (2010).
198 Hart, T., Brown, K. R., Sircoulomb, F., Rottapel, R. & Moffat, J. Measuring error rates in genomic perturbation screens: gold standards for human functional genomics. *Mol Syst Biol* **10**, 733, doi:10.15252/msb.20145216 (2014).
199 Sun, T. & Hevner, R. F. Growth and folding of the mammalian cerebral cortex: from molecules to malformations. *Nat Rev Neurosci* **15**, 217-232, doi:10.1038/nrn3707 (2014).
200 Wu, S. H., Bi, J. F., Cloughesy, T., Cavenee, W. K. & Mischel, P. S. Emerging function of mTORC2 as a core regulator in glioblastoma: metabolic reprogramming and drug resistance. *Cancer Biol Med* **11**, 255-263, doi:10.7497/j.issn.2095-3941.2014.04.004 (2014).
201 Wade, M., Li, Y. C. & Wahl, G. M. MDM2, MDMX and p53 in oncogenesis and cancer therapy. *Nat Rev Cancer* **13**, 83-96, doi:10.1038/nrc3430 (2013).
202 Petrilli, A. M. & Fernandez-Valle, C. Role of Merlin/NF2 inactivation in tumor biology. *Oncogene*, doi:10.1038/onc.2015.125 (2015).
203 Jaehning, J. A. The Paf1 complex: platform or player in RNA polymerase II transcription? *Biochim Biophys Acta* **1799**, 379-388, doi:10.1016/j.bbagrm.2010.01.001 (2010).
204 Lee, M. H., Zhao, R., Phan, L. & Yeung, S. C. Roles of COP9 signalosome in cancer. *Cell cycle* **10**, 3057-3066 (2011).

205 Alessi, D. R., Sakamoto, K. & Bayascas, J. R. LKB1-dependent signaling pathways. *Annual review of biochemistry* **75**, 137-163, doi:10.1146/annurev.biochem.75.103004.142702 (2006).
206 Sun, L. *et al.* JFK, a Kelch domain-containing F-box protein, links the SCF complex to p53 regulation. *Proc Natl Acad Sci U S A* **106**, 10195-10200, doi:10.1073/pnas.0901864106 (2009).
207 Krek, W. & Nigg, E. A. Mutations of p34cdc2 phosphorylation sites induce premature mitotic events in HeLa cells: evidence for a double block to p34cdc2 kinase activation in vertebrates. *Embo J* **10**, 3331-3341 (1991).
208 Palmer, A., Gavin, A. C. & Nebreda, A. R. A link between MAP kinase and p34(cdc2)/cyclin B during oocyte maturation: p90(rsk) phosphorylates and inactivates the p34(cdc2) inhibitory kinase Myt1. *Embo J* **17**, 5037-5047, doi:10.1093/emboj/17.17.5037 (1998).
209 Okumura, E. *et al.* Akt inhibits Myt1 in the signalling pathway that leads to meiotic G2/M-phase transition. *Nat Cell Biol* **4**, 111-116, doi:10.1038/ncb741 (2002).
210 Katayama, K., Fujita, N. & Tsuruo, T. Akt/protein kinase B-dependent phosphorylation and inactivation of WEE1Hu promote cell cycle progression at G2/M transition. *Mol Cell Biol* **25**, 5725-5737, doi:10.1128/MCB.25.13.5725-5737.2005 (2005).
211 Villeneuve, J., Scarpa, M., Ortega-Bellido, M. & Malhotra, V. MEK1 inactivates Myt1 to regulate Golgi membrane fragmentation and mitotic entry in mammalian cells. *Embo J* **32**, 72-85, doi:10.1038/emboj.2012.329 (2013).
212 Bachoo, R. M. *et al.* Epidermal growth factor receptor and Ink4a/Arf: convergent mechanisms governing terminal differentiation and transformation along the neural stem cell to astrocyte axis. *Cancer Cell* **1**, 269-277 (2002).
213 Boehm, J. S. *et al.* Integrative genomic approaches identify IKBKE as a breast cancer oncogene. *Cell* **129**, 1065-1079, doi:S0092-8674(07)00532-6 [pii]10.1016/j.cell.2007.03.052 (2007).
214 Zhang, J. *et al.* Whole-genome sequencing identifies genetic alterations in pediatric low-grade gliomas. *Nat Genet* **45**, 602-612, doi:10.1038/ng.2611 (2013).
215 Wu, G. *et al.* The genomic landscape of diffuse intrinsic pontine glioma and pediatric non-brainstem high-grade glioma. *Nat Genet* **46**, 444-450, doi:10.1038/ng.2938 (2014).
216 Paugh, B. S. *et al.* Integrated molecular genetic profiling of pediatric high-grade gliomas reveals key differences with the adult disease. *J Clin Oncol* **28**, 3061-3068, doi:10.1200/JCO.2009.26.7252 (2010).
217 Kwok, R. P. *et al.* Nuclear protein CBP is a coactivator for the transcription factor CREB. *Nature* **370**, 223-226, doi:10.1038/370223a0 (1994).
218 Goodman, R. H. & Smolik, S. CBP/p300 in cell growth, transformation, and development. *Genes Dev* **14**, 1553-1577 (2000).
219 Iyer, N. G., Ozdag, H. & Caldas, C. p300/CBP and cancer. *Oncogene* **23**, 4225-4231, doi:10.1038/sj.onc.1207118 (2004).
220 Koike-Yusa, H., Li, Y., Tan, E. P., Velasco-Herrera Mdel, C. & Yusa, K. Genome-wide recessive genetic screening in mammalian cells with a lentiviral CRISPR-guide RNA library. *Nat Biotechnol* **32**, 267-273, doi:10.1038/nbt.2800 (2014).
221 Zhou, Y. *et al.* High-throughput screening of a CRISPR/Cas9 library for functional genomics in human cells. *Nature* **509**, 487-491, doi:10.1038/nature13166 (2014).

222 Chen, S. *et al.* Genome-wide CRISPR screen in a mouse model of tumor growth and metastasis. *Cell* **160**, 1246-1260, doi:10.1016/j.cell.2015.02.038 (2015).
223 Inoue, D. & Sagata, N. The Polo-like kinase Plx1 interacts with and inhibits Myt1 after fertilization of Xenopus eggs. *EMBO J* **24**, 1057-1067, doi:10.1038/sj.emboj.7600567 (2005).
224 Kasahara, K. *et al.* PI 3-kinase-dependent phosphorylation of Plk1-Ser99 promotes association with 14-3-3gamma and is required for metaphase-anaphase transition. *Nat Commun* **4**, 1882, doi:10.1038/ncomms2879 (2013).
225 Maddika, S. *et al.* Akt-mediated phosphorylation of CDK2 regulates its dual role in cell cycle progression and apoptosis. *J Cell Sci* **121**, 979-988, doi:10.1242/jcs.009530 (2008).
226 Liu, P. *et al.* Cell-cycle-regulated activation of Akt kinase by phosphorylation at its carboxyl terminus. *Nature* **508**, 541-545, doi:10.1038/nature13079 (2014).
227 Nakanishi, M. *et al.* Identification and characterization of human Wee1B, a new member of the Wee1 family of Cdk-inhibitory kinases. *Genes Cells* **5**, 839-847 (2000).
228 Kumagai, A. & Dunphy, W. G. Regulation of the cdc25 protein during the cell cycle in Xenopus extracts. *Cell* **70**, 139-151 (1992).
229 De Witt Hamer, P. C., Mir, S. E., Noske, D., Van Noorden, C. J. & Wurdinger, T. WEE1 kinase targeting combined with DNA-damaging cancer therapy catalyzes mitotic catastrophe. *Clin Cancer Res* **17**, 4200-4207, doi:10.1158/1078-0432.CCR-10-2537 (2011).
230 Bao, S. *et al.* Glioma stem cells promote radioresistance by preferential activation of the DNA damage response. *Nature* **444**, 756-760, doi:nature05236 [pii] 10.1038/nature05236 (2006).
231 Liu, G. *et al.* Analysis of gene expression and chemoresistance of CD133+ cancer stem cells in glioblastoma. *Mol Cancer* **5**, 67, doi:10.1186/1476-4598-5-67 (2006).
232 Zhang, J., Stevens, M. F. & Bradshaw, T. D. Temozolomide: mechanisms of action, repair and resistance. *Curr Mol Pharmacol* **5**, 102-114 (2012).
233 Hirose, Y., Berger, M. S. & Pieper, R. O. p53 effects both the duration of G2/M arrest and the fate of temozolomide-treated human glioblastoma cells. *Cancer Res* **61**, 1957-1963 (2001).
234 Pokorny, J. L. *et al.* The Efficacy of the Wee1 Inhibitor MK-1775 Combined with Temozolomide Is Limited by Heterogeneous Distribution across the Blood-Brain Barrier in Glioblastoma. *Clin Cancer Res* **21**, 1916-1924, doi:10.1158/1078-0432.CCR-14-2588 (2015).
235 Rohe, A., Gollner, C., Erdmann, F., Sippl, W. & Schmidt, M. The glycoglycerolipid 1,2-dipalmitoyl-3-(N-palmitoyl-6'-amino-6'-deoxy-alpha-d-glucosyl)-sn-glycerol is no inhibitor of the human Myt1 kinase. *J Enzyme Inhib Med Chem*, 1-4, doi:10.3109/14756366.2014.926343 (2014).
236 Rohe, A., Henze, C., Erdmann, F., Sippl, W. & Schmidt, M. A fluorescence anisotropy-based Myt1 kinase binding assay. *Assay Drug Dev Technol* **12**, 136-144, doi:10.1089/adt.2013.534 (2014).
237 Lottaz, C. *et al.* Transcriptional profiles of CD133+ and CD133- glioblastoma-derived cancer stem cell lines suggest different cells of origin. *Cancer Res* **70**, 2030-2040, doi:0008-5472.CAN-09-1707 [pii] 10.1158/0008-5472.CAN-09-1707 (2010).
238 Cancer Genome Atlas, N. Comprehensive molecular characterization of human colon and rectal cancer. *Nature* **487**, 330-337, doi:10.1038/nature11252 (2012).

239 Bird, A. DNA methylation patterns and epigenetic memory. *Genes Dev* **16**, 6-21, doi:10.1101/gad.947102 (2002).
240 Noushmehr, H. *et al.* Identification of a CpG island methylator phenotype that defines a distinct subgroup of glioma. *Cancer Cell* **17**, 510-522, doi:10.1016/j.ccr.2010.03.017 (2010).
241 Szklarczyk, D. *et al.* STRING v10: protein-protein interaction networks, integrated over the tree of life. *Nucleic Acids Res* **43**, D447-452, doi:10.1093/nar/gku1003 (2015).
242 Chen, J., Bardes, E. E., Aronow, B. J. & Jegga, A. G. ToppGene Suite for gene list enrichment analysis and candidate gene prioritization. *Nucleic Acids Res* **37**, W305-311, doi:10.1093/nar/gkp427 (2009).
243 Subramanian, A. *et al.* Gene set enrichment analysis: a knowledge-based approach for interpreting genome-wide expression profiles. *Proc Natl Acad Sci U S A* **102**, 15545-15550, doi:0506580102 [pii] 10.1073/pnas.0506580102 (2005).
244 Mootha, V. K. *et al.* PGC-1alpha-responsive genes involved in oxidative phosphorylation are coordinately downregulated in human diabetes. *Nat Genet* **34**, 267-273, doi:10.1038/ng1180 (2003).
245 Trapnell, C. *et al.* Differential gene and transcript expression analysis of RNA-seq experiments with TopHat and Cufflinks. *Nat Protoc* **7**, 562-578, doi:10.1038/nprot.2012.016 nprot.2012.016 [pii] (2012).
246 Anders, S. *HTSeq: Analysing high-throughput sequencing data with Python*, < http://www-huber.embl.de/users/anders/HTSeq/> (2010).
247 Robinson, M. D. & Smyth, G. K. Moderated statistical tests for assessing differences in tag abundance. *Bioinformatics* **23**, 2881-2887, doi:btm453 [pii]10.1093/bioinformatics/btm453 (2007).
248 Robinson, M. D. & Smyth, G. K. Small-sample estimation of negative binomial dispersion, with applications to SAGE data. *Biostatistics* **9**, 321-332, doi:kxm030 [pii] 10.1093/biostatistics/kxm030 (2008).
249 Trapnell, C., Pachter, L. & Salzberg, S. L. TopHat: discovering splice junctions with RNA-Seq. *Bioinformatics* **25**, 1105-1111, doi:btp120 [pii] 10.1093/bioinformatics/btp120 (2009).
250 Anders, S., Pyl, P. T. & Huber, W. HTSeq--a Python framework to work with high-throughput sequencing data. *Bioinformatics* **31**, 166-169, doi:10.1093/bioinformatics/btu638 (2015).
251 Reiner, A., Yekutieli, D. & Benjamini, Y. Identifying differentially expressed genes using false discovery rate controlling procedures. *Bioinformatics* **19**, 368-375 (2003).
252 McKenna, A. *et al.* The Genome Analysis Toolkit: a MapReduce framework for analyzing next-generation DNA sequencing data. *Genome Res* **20**, 1297-1303, doi:10.1101/gr.107524.110 (2010).
253 Li, H. & Durbin, R. Fast and accurate short read alignment with Burrows-Wheeler transform. *Bioinformatics* **25**, 1754-1760, doi:btp324 [pii] 10.1093/bioinformatics/btp324 (2009).
254 Cingolani, P. *et al.* A program for annotating and predicting the effects of single nucleotide polymorphisms, SnpEff: SNPs in the genome of Drosophila melanogaster strain w1118; iso-2; iso-3. *Fly (Austin)* **6**, 80-92, doi:10.4161/fly.19695 (2012).
255 Barretina, J. *et al.* The Cancer Cell Line Encyclopedia enables predictive modelling of anticancer drug sensitivity. *Nature* **483**, 603-607, doi:10.1038/nature11003 (2012).

256 Trapnell, C. *et al.* Transcript assembly and quantification by RNA-Seq reveals unannotated transcripts and isoform switching during cell differentiation. *Nat Biotechnol* **28**, 511-515, doi:10.1038/nbt.1621 (2010).
257 Merico, D., Isserlin, R., Stueker, O., Emili, A. & Bader, G. D. Enrichment map: a network-based method for gene-set enrichment visualization and interpretation. *PLoS One* **5**, e13984, doi:10.1371/journal.pone.0013984 (2010).
258 Ritchie, M. E. *et al.* limma powers differential expression analyses for RNA-sequencing and microarray studies. *Nucleic Acids Res* **43**, e47, doi:10.1093/nar/gkv007 (2015).
259 Prados, M. D. *et al.* Toward precision medicine in glioblastoma: the promise and the challenges. *Neuro Oncol* **17**, 1051-1063, doi:10.1093/neuonc/nov031 (2015).
260 Jiang, H. *et al.* A microtubule-associated zinc finger protein, BuGZ, regulates mitotic chromosome alignment by ensuring Bub3 stability and kinetochore targeting. *Dev Cell* **28**, 268-281, doi:10.1016/j.devcel.2013.12.013 (2014).
261 Weaver, B. A. How Taxol/paclitaxel kills cancer cells. *Mol Biol Cell* **25**, 2677-2681, doi:10.1091/mbc.E14-04-0916 (2014).
262 Wang, S. A. *et al.* Phosphorylation of p300 increases its protein degradation to enhance the lung cancer progression. *Biochim Biophys Acta* **1843**, 1135-1149, doi:10.1016/j.bbamcr.2014.02.001 (2014).
263 Poon, C. L., Lin, J. I., Zhang, X. & Harvey, K. F. The sterile 20-like kinase Tao-1 controls tissue growth by regulating the Salvador-Warts-Hippo pathway. *Dev Cell* **21**, 896-906, doi:10.1016/j.devcel.2011.09.012 (2011).
264 Wu, J. N. & Roberts, C. W. ARID1A mutations in cancer: another epigenetic tumor suppressor? *Cancer Discov* **3**, 35-43, doi:10.1158/2159-8290.CD-12-0361 (2013).
265 Reilly, K. M., Loisel, D. A., Bronson, R. T., McLaughlin, M. E. & Jacks, T. Nf1;Trp53 mutant mice develop glioblastoma with evidence of strain-specific effects. *Nat Genet* **26**, 109-113, doi:10.1038/79075 (2000).
266 Biswas, S. *et al.* Transforming growth factor beta receptor type II inactivation promotes the establishment and progression of colon cancer. *Cancer Res* **64**, 4687-4692, doi:10.1158/0008-5472.CAN-03-3255 (2004).
267 Morales, F. C., Molina, J. R., Hayashi, Y. & Georgescu, M. M. Overexpression of ezrin inactivates NF2 tumor suppressor in glioblastoma. *Neuro Oncol* **12**, 528-539, doi:10.1093/neuonc/nop060 (2010).
268 Hanahan, D. & Weinberg, R. A. Hallmarks of cancer: the next generation. *Cell* **144**, 646-674, doi:10.1016/j.cell.2011.02.013 (2011).
269 Foley, E. A. & Kapoor, T. M. Microtubule attachment and spindle assembly checkpoint signalling at the kinetochore. *Nat Rev Mol Cell Biol* **14**, 25-37, doi:10.1038/nrm3494 (2013).
270 Harvey, S. L. *et al.* A phosphatase threshold sets the level of Cdk1 activity in early mitosis in budding yeast. *Mol Biol Cell* **22**, 3595-3608, doi:10.1091/mbc.E11-04-0340 (2011).
271 Mochida, S. & Hunt, T. Protein phosphatases and their regulation in the control of mitosis. *EMBO Rep* **13**, 197-203, doi:10.1038/embor.2011.263 (2012).
272 Lianga, N. *et al.* A Wee1 checkpoint inhibits anaphase onset. *J Cell Biol* **201**, 843-862, doi:10.1083/jcb.201212038 (2013).
273 Wengner, A. M., Siemeister, G., Koppitz, M., Schulze, V., Kosemund, D., Klar, U., Stoeckigt, D., Neuhaus, R., Lienau, P., Bader, B., Prechtl, S., Doehr, O., Raschke, M.,

von Ahsen, O., Elbi, C., Bruns, I., Michels, M., Kreft, B., von Nussbaum, F., Brands, M., Mumberg, D., & Ziegelbauer K. Novel Mps1 kinase inhibitors with potent anti-tumor activity [Abstract]. *In: American Association for Cancer Research Annual Meeting* **Abstract: 3090**, Philadelphia, PA (2015).

274 Liu, X. Targeting Polo-Like Kinases: A Promising Therapeutic Approach for Cancer Treatment. *Transl Oncol* **8**, 185-195, doi:10.1016/j.tranon.2015.03.010 (2015).

275 Pezuk, J. A. *et al.* Polo-like kinase 1 inhibition causes decreased proliferation by cell cycle arrest, leading to cell death in glioblastoma. *Cancer Gene Ther* **20**, 499-506, doi:10.1038/cgt.2013.46 (2013).

276 Dohner, H. *et al.* Randomized, phase 2 trial of low-dose cytarabine with or without volasertib in AML patients not suitable for induction therapy. *Blood* **124**, 1426-1433, doi:10.1182/blood-2014-03-560557 (2014).

277 Barre-Sinoussi, F., Ross, A. L. & Delfraissy, J. F. Past, present and future: 30 years of HIV research. *Nat Rev Microbiol* **11**, 877-883, doi:10.1038/nrmicro3132 (2013).

278 Quail, D. F., Bowman, R.L., Quick, M.L., Schuhmacher, A.J., Akkari, L., Huse, J.H., Sutton, J.C., & Joyce, J.A. Deciphering Mechanisms of Resistance to Microenvironment-Targeted Therapies [Abstract]. *In: Biology of Cancer: Microenvironment, Metastasis, and Therapeutics* **Abstract: 152**, Cold Spring Harbor Laboratory, Cold Spring Harbor, NY (2015).

279 Collins, F. S. & Varmus, H. A new initiative on precision medicine. *N Engl J Med* **372**, 793-795, doi:10.1056/NEJMp1500523 (2015).